Gamma-ray blazars as candidate sources of high-energy neutrinos

Dissertation
zur Erlangung des akademischen Grades
doctor rerum naturalium
(Dr. rer. nat.)

im Fach: Physik
Spezialisierung: Experimentalphysik

eingereicht an der
Mathematisch-Naturwissenschaftlichen Fakultät
der Humboldt-Universität zu Berlin

von
Simone Garrappa, M. Sc.

Präsident (komm.) der Humboldt-Universität zu Berlin
Prof. Dr. Peter Frensch

Dekanin der Mathematisch-Naturwissenschaftlichen Fakultät
Prof. Dr. Caren Tischendorf

Gutachter:
Prof. Dr. Anna Franckowiak, Ruhr Universität Bochum
Prof. Dr. David Berge, Humboldt-Universität zu Berlin
Prof. Dr. Elina Lindfors, University of Turku

Tag der mündlichen Prüfung: 8 September 2022

Colophon
This document was typeset with the help of KOMA-Script and LaTeX using the open-source kaobook template class.

Publisher
First printed in Sep 2022 by Humboldt Universität zu Berlin

Alla mia famiglia,

ancora una volta.

–Simone

Abstract

After the discovery of a diffuse flux of high-energy astrophysical neutrinos by the IceCube South Pole Neutrino Observatory in 2013, the sources responsible for the majority of this emission are still unknown. Blazars, those AGN with a relativistic jet pointing towards Earth, are considered prime candidates for cosmic-ray acceleration and the production of high-energy neutrinos. This thesis work is motivated by the detection of the flaring gamma-ray blazar TXS 0506+056 in spatial and temporal coincidence with the neutrino event IceCube-170922A, that represented a milestone for the new field of multi-messenger astronomy. This discovery was possible thanks to the *Fermi* Large Area Telescope, which performs an all-sky survey of the GeV gamma-ray sky since 2008.

In this thesis, I present the results of a detailed gamma-ray analysis of the blazar TXS 0506+056 over 9.6 years of *Fermi*-LAT observations. The source shows strong flux variability in the gamma-ray band at the arrival of IceCube-170922A, indicating a neutrino-gamma-ray connection, while is observed in a low state during an additional lower-energy neutrino signal detected from the same source by IceCube in 2014/15 in archival data.

This puzzling behaviour has motivated further studies on the blazar sources coincident with single high-energy neutrinos. As part of this thesis, a first systematic analysis was conducted on all the archival events satisfying the IceCube realtime trigger criteria prior to the detection of IceCube-170922A. Among these coincidences, a second gamma-ray blazar GB6 J1040+0617, is found in spatial and temporal coincidence with the high-energy neutrino event IceCube-141209A while showing enhanced activity in the gamma-ray and optical bands. Although the chance coincidence is at ~30%, the source was found to be a plausible neutrino source candidate based on its energetics and multiwavelength features simultaneous with the neutrino detection.

A second search for blazar counterparts to high-energy neutrinos is done through realtime follow-up of more than 60 IceCube alerts with the *Fermi*-LAT. The powerful blazar PKS 1502+106 found coincident with the event IceCube-190730A represents an outstanding science case. Despite the source was not found in a flaring state at the detection of the neutrino, the detailed analysis presented in this work shows that its multiwavelength properties can potentially explain the coincident neutrino detection.

The gamma-ray variability properties of these three candidates are then compared to those of a larger sample of blazars detected by *Fermi*-LAT. No striking features of the neutrino blazar candidates could be identified which would make them stand out in comparison to the entire sample. This indicates that the coincidences are either found by chance or all blazars should be capable to produce a small flux of high-energy neutrinos.

Lastly, a study to compare the average gamma-ray emission of the potential neutrino counterparts to the entire sample of gamma-ray blazars is presented. The results show possible indications of correlation between neutrino and gamma-ray energy fluxes.

Zusammenfassung

Nach der Entdeckung eines diffusen Flusses hochenergetischer astrophysikalischer Neutrinos durch das IceCube South Pole Neutrino Observatory im Jahr 2013 sind die Quellen, die für den Großteil dieser Emission verantwortlich sind, immer noch unbekannt. Blazare, jene AGN mit einem relativistischen Jet, der auf die Erde zeigt, gelten als Hauptkandidaten für die Beschleunigung der kosmischen Strahlung und die Produktion hochenergetischer Neutrinos. Diese Doktorarbeit ist motiviert durch den Nachweis des Gammastrahlen-Blazers TXS 0506+056 in räumlicher Koinzidenz mit dem Neutrino IceCube-170922A. Dass sich der Blazar zur selben Zeit in einem erhöhten Zustand seiner Gammastrahlenaktivität befand, stellt einen Meilenstein in dem neuen Gebiet der Multi-Messenger-Astronomie dar. Möglich wurde diese Entdeckung durch das *Fermi* Large Area Telescope, das seit 2008 eine Himmelsdurchmusterung des GeV-Gammastrahlenhimmels durchführt.
In dieser Arbeit präsentiere ich die Ergebnisse einer detaillierten Gammastrahlenanalyse des Blazars TXS 0506+056 über 9,6 Jahre *Fermi*-LAT-Beobachtungen. Die Quelle ist stark variabel im Gammastrahlenband zur Ankunftszeit des Neutrinos IceCube-170922A, was auf eine Neutrino-Gammastrahlen-Verbindung hindeutet. Die Quelle wird jedoch während eines zusätzlichen niederenergetischen Neutrinosignals, das 2014/15 von IceCube in Archivdaten von derselben Quelle entdeckt wurde, in einem niedrigen Zustand beobachtet.
Dieses rätselhafte Verhalten hat weitere Studien zu den Blazaren motiviert, die mit einzelnen hochenergetischen Neutrinos zusammenfallen. Im Rahmen dieser Arbeit wurde eine erste systematische Analyse aller gemessenen Neutrino Ereignisse durchgeführt, die die IceCube-Echtzeit-Triggerkriterien vor der Detektion von IceCube-170922A erfüllten. Unter diesen Koinzidenzen befindet sich ein zweiter Gammastrahlen-Blazar GB6 J1040+0617 in räumlicher und zeitlicher Übereinstimmung mit dem hochenergetischen Neutrino-Ereignis IceCube-141209A, während er eine erhöhte Aktivität im Gammastrahlen- und im optischen Band zeigt. Obwohl die zufällige Koinzidenz bei ∼30% liegt, wurde festgestellt, dass die Quelle ein plausibler Kandidat für eine Neutrinoquelle ist, basierend auf ihren Energetik- und Multiwellenlängenmerkmalen gleichzeitig mit der Neutrinodetektion.
Eine zweite Suche nach Blazar-Gegenstücken zu hochenergetischen Neutrinos erfolgt durch Echtzeit-Follow-up von mehr als 60 IceCube-Alerts mit dem *Fermi*-LAT. Der kräftige Blazar PKS 1502+106, der zusammen mit dem Ereignis IceCube-190730A gefunden wurde, stellt einen herausragenden wissenschaftlichen Fall dar. Obwohl die Quelle beim Nachweis des Neutrinos nicht in einem Zustand erhöhter Emission gefunden wurde, zeigt die in dieser Arbeit vorgestellte detaillierte Analyse, dass ihre Multiwellenlängeneigenschaften möglicherweise den gleichzeitigen Neutrinonachweis erklären können.
Die Gammastrahlen-Variabilitätseigenschaften dieser drei Kandidaten werden dann mit denen einer größeren Stichprobe von Blazaren verglichen, die vom *Fermi*-LAT entdeckt

wurden. Es konnten keine auffälligen Merkmale der Neutrino-Blazar-Kandidaten identifiziert werden, die sie im Vergleich zur gesamten Stichprobe hervorheben würden. Dies deutet darauf hin, dass die Koinzidenzen entweder zufällig gefunden werden oder alle Blazaren in der Lage sein sollten, einen kleinen Fluss hochenergetischer Neutrinos zu erzeugen.
Schließlich wird eine Studie zum Vergleich der durchschnittlichen Gammastrahlenemission der potenziellen Neutrino-Gegenstücke mit der gesamten Stichprobe von Gammastrahlen-Blazaren vorgestellt. Die Ergebnisse zeigen mögliche Hinweise auf eine Korrelation zwischen Neutrino- und Gammastrahlen-Energieflüssen.

Contents

Abstract i

Contents iv

1 Introduction 1

High-energy neutrinos from Blazars 7

2 Blazars and high-energy neutrinos 9
2.1 Unified model of Active Galactic Nuclei . . . 9
2.2 Blazars . . . 13
2.2.1 Black Holes: the central engine . . . 14
2.2.2 Relativistic jets . . . 18
2.3 High-energy neutrino production in Blazars . . . 26
2.4 Diffuse neutrino emission from blazars . . . 28

Gamma-ray and Neutrino Astronomy 31

3 *Fermi*-LAT 33
3.1 The Large Area Telescope detectors . . . 33
3.1.1 The precision converter-tracker . . . 34
3.1.2 Calorimeter . . . 35
3.1.3 Anticoincidence detector (ACD) . . . 36
3.2 LAT performance and survey strategy . . . 37
3.2.1 Pass 8 event selection . . . 38
3.3 The likelihood approach in LAT data analysis . . . 43
3.3.1 The Likelihood in *Fermi*-LAT data . . . 43
3.3.2 Source models . . . 44
3.4 *Fermi*-LAT gamma-ray catalogs . . . 46
3.4.1 The catalog of AGN detected by the *Fermi*-LAT . . . 47
3.5 Data analysis with *Fermi*-LAT data . . . 50

4 The IceCube South Pole Neutrino Observatory 57
4.1 An instrumented, cubic kilometer of Antartic ice . . . 57
4.2 Astrophysical neutrinos and atmospheric background . . . 62
4.3 The Realtime Alert System . . . 64

Blazar candidate sources to high-energy neutrinos **69**

5 TXS 0506+056 **71**
5.1 IceCube-170922A . . . 71
5.2 *Fermi*-LAT analysis of the TXS 0506+056 region . . . 73
5.2.1 Spectral analysis . . . 74
5.2.2 Light Curve Analysis . . . 76
5.3 Summary . . . 80

6 GB6 J1040+0617 **85**
6.1 IceCube-141209A . . . 86
6.2 *Fermi*-LAT analysis of the GB6 J1040+0617 region . . . 86
6.2.1 Light curve Analysis of GB6 J1040+0617 . . . 88
6.2.2 Lightcurve Analysis of 4C+06.41 . . . 91
6.2.3 Disentangling the Gamma-ray Emission of GB6 J1040+0617 and 4C+06.41 . . . 91
6.3 Evaluating the IceCube-141209A and GB6 J1040+0617 coincidence . . . 94
6.4 Summary . . . 95

7 PKS 1502+106 coincident with IceCube-190730A **97**
7.1 IceCube-190730A . . . 97
7.2 The blazar PKS 1502+106 . . . 98
7.3 *Fermi*-LAT analysis of PKS 1502+106 . . . 99
7.3.1 Spectral Analysis . . . 99
7.3.2 Light curve analysis . . . 100
7.4 Numerical modelling of PKS 1502+106 . . . 104
7.4.1 Contributions from radiative processes to the observed SED . . . 105
7.4.2 Neutrino spectra and expected event rates . . . 108
7.5 Summary . . . 110

Variability study of gamma-ray Blazars **113**

8 Blazar variability in gamma-rays **115**
8.1 A sample of bright blazars detected by *Fermi*-LAT . . . 115
8.1.1 The light curve sample . . . 116
8.2 Modelling the flaring activities . . . 124
8.3 Results . . . 129
8.4 Summary . . . 139

A population of neutrino blazar candidates **141**

9 *Fermi*-LAT realtime follow-up **143**
9.1 Follow-up observations with *Fermi*-LAT . . . 144
9.2 A population of neutrino blazar candidates . . . 148
9.3 Results and discussion . . . 155
9.4 Neutrino flare candidates . . . 158

Conclusion **163**

10 Summary and outlook **165**

Appendix **169**

A *Fermi*-LAT Analysis configurations **171**
A.1 TXS 0506+056 analysis in Chapter 5 171
A.2 GB6 J1040+0617 analysis in Chapter 6 172
A.3 Analyses in Chapters 7 and 9 173
A.4 Analyses in Chapter 8 174

B IceCube Realtime Alerts **175**
B.1 IceCube Realtime Stream 1.0 (April 2016 - May 2019) 175
B.2 IceCube Realtime Stream 2.0 (Up to June 2021) 176
B.3 Archival high-energy neutrino events 178

Acknowledgements **181**

Bibliography **183**

List of Figures

1.1 Composite multi-wavelength image of the Centaurus A galaxy from observations in radio, infrared, visible and X-ray light. Credit: ESA/NASA. 1
1.2 Differential cosmic ray spectrum from [3]. 2
1.3 *Top*: All-sky maps at different wavelengths and as seen in neutrinos. *Bottom*: Distance (in Mpc) vs photon energy (in eV) diagram. The black filled region indicates distances larger than the photon mean free path at a certain energy. Credit: IceCube Collaboration. 3
1.4 High-energy diffuse fluxes of the three messenger particles from [14]. . . . 4

2.1 Composite image of the FR II galaxy Cygnus-A 10
2.2 AGN unification diagram from [58]. 12
2.3 Spectral energy distribution of Mrk 421 from [59]. The legend shows the association between flux measurements and correspondent instrument. . . 13
2.4 The original blazar sequence from [63, 64]. 14
2.5 EHT image of M87* from observations collected in the 2017 campaign from [79]. 17
2.6 Illustration of jet formation by magnetic fields from [80]. 18
2.7 Multiwavelength image of the 3C 279 jet structure in April 2017 from [86]. The color bars show the pixel values in Jy/beam. 20
2.8 Sketch of the inner jet of a blazar from [94], explaining the fast minute-scale gamma-ray flares of 3C 273 with the jet-in-jet magnetic reconnection model. 21
2.9 Schematic representation of synchtron emission of an electron with pitch angle β (angle between the particle and magnetic field directions) from [45]. . . . 22
2.10 The synchrotron spectrum for an electron plasma within a uniform magnetic field as a function of frequency from [45]. The x-axis is in function of the synchrotron self-absorption frquency ν_{sa}. 22
2.11 Mean free path (in Mpc) as a function of the photon energy (eV) adapted from [97]. Three backround photon field are considered: infrared (IR), cosmic microwave background (CMB) and radio. 25
2.12 Broadband SED in lepto-hadronic scenario with contributions from the single processes adapted from [106]. 28

3.1 Schematic view of the *Fermi*-LAT with its main components. An exploded view of one of the 16 towers is shown with an artistic impression of a gamma ray interacting in the Silicon-tracker volume and producing an electron-positon pair that gets absorbed in the calorimeter. 34
3.2 Illustration of the LAT tracker design principles. The sketch shows the ideal conversion in Tungsten foil with detection already happening in the first Si layer, that minimizes the path for multiple scattering, whose effect on the reconstructed direction is shown after the passage of the charged particles in the second *W* foil. 35

3.3 Illustration of LAT calorimeter module from [124]. The 96 CsI(Tl) scintillator crystal detector elements compose the core structure and are arranged in 8 layers of 12 bars each. Crystals in adjacent layers are hodoscopically arranged to measure x and y in alternate layers. The readout electronics is placed in side cells to be directly connected to both ends of each scintillator bar. The calorimeter has a total depth of 8.6 X_0, at normal incidence. 36
3.4 Illustration of the *Fermi*-LAT ACD from [124]. 37
3.5 Schematic of the LAT coordinate system from [127]. The z-axis corresponds to the LAT boresight, and the incidence (θ) and azimuth (ϕ) angles are defined with respect to the z and x axes, respectively. 38
3.6 Effective area as a function of energy for normal incidence photons ($\theta = 0$). Each curve shows the effective area for different event classes in the standard hierarchy of Pass 8 data. Adapted from https://www.slac.stanford.edu/exp/glast/groups/canda/lat_Performance.htm. 40
3.7 68% containment angles as a function of the energy for all PSF event types in Pass 8 data. Adapted from https://www.slac.stanford.edu/exp/glast/groups/canda/lat_Performance.htm. 41
3.8 Energy resolution (68% containment half width of the reconstructed incoming photon energy) as a function of energy for all EDISP event types in Pass 8 data. Adapted from https://www.slac.stanford.edu/exp/glast/groups/canda/lat_Performance.htm. 42
3.9 All-sky map in in Galactic coordinates with localizations of sources in [148]. The map background show one year of LAT data counts in greyscale color map. 48
3.10 Panels on the *left*: photon index for different blazar classes (and subclasses for BL Lacs) in 4LAC. Panels on the *right*: distributions of the sunchrotron peak frequency for different blazar classes in 4LAC. 49
3.11 Photon index vs. synchrotron peak frequency in the observer frame. Plot adapted from Fig. 7 in [148] 50
3.12 Energy Flux versus variability index of blazar objects in 4LAC. The black dashed line marks the $TS_{var} = 18.48$ threshold. 50
3.13 Differential point source sensitivity for 10 years of exposure in 4 bins per energy decade between 31.6 MeV and 1 TeV. Adapted from https://www.slac.stanford.edu/exp/glast/groups/canda/lat_Performance.htm. . . 55
3.14 All-sky map of integral point-source sensitivity in 10 years of sky survey. The integral sensitivity is calculated as the minimum required flux for a source with power-law spectrum with index 2 to reach a 5σ detection during 10 years of survey mode. The 5σ limit corresponds to a TS = 25 and at least 10 photons. Adapted from https://www.slac.stanford.edu/exp/glast/groups/canda/lat_Performance.htm. 55
3.15 Example of an adaptively-binned lightcurve computed with the method in [162] for the source 4FGL J0501.2-0158, associated with the FSRQ S3 0458-02. 56

4.1 Scaled representation of the IceCube South Pole Neutrino Observatory with its main components from [8]. 58
4.2 Schematic view of the Digital Optical Module (DOM) from [8]. 58
4.3 Feynman diagrams of the two high-energy neutrinos interaction channels: charged current (CC, left) mediated by a W boson and neutral current (NC, right) mediated by a Z^0 boson. 59

4.4 Event displays of the Cherenkov light pattern measured in the IceCube DOMs for a track-like event (left) and a cascade-like event (right). Each sphere represents a DOM, with its size proportional to the number of detected photons and the colormap describing the arrival time from the earliest hits in red to the latest in green. The event displays are from https://icecube.wisc.edu/gallery/. 60
4.6 Schematic view of the event definitions by their arrival direction from [175]. 62
4.5 Neutrino cross sections (*left*) and interaction lengths (*right*) for DIS interactions in water of neutrinos with a nucleus as a function of the neutrino energy from [175]. CC and NC interactions for neutrinos (solid lines) and anti-neutrinos (dashed lines) are shown, along with the Glashow resonance (purple dashed lines). 62
4.7 Comparison between astrophysical neutrino flux measurements from [178]. The best fit spectral index and flux normalization at 100 TeV are shown on the x and y axes, respectively, along with their 95% CL. The results are from measurements using the 7.5 years HESE sample from the full-sky [179], the 9.5 years sample of through-going tracks from the northern hemisphere [178] and the 6 years sample of cascade events from the full-sky [181]. 64
4.8 Distribution of alert rates (events per year) in declination bins from [16]. Starting tracks are events from the HESE selection, while through-going tracks are events that pass either the GFU or EHE selections. 67

5.1 Event display of IceCube-170922A from [186]. The red arrow shows the reconstructed directions, and the colormap indicates the time lag between the time of the first radiation detected in the first optical module and the subsequent detections along the radiation path of the event, in nanoseconds. The lower left panel shows the top view of the event. 72
5.2 Counts map of *Fermi*-LAT (E>100 MeV) of the region centered on TXS 0506+056 from [38]. The 90% neutrino angular uncertainty is shown as green contour and the best-fit neutrino position is marked by a green cross. 73
5.3 Time-dependent analysis results from [37]. The orange curve shows the results from the Gaussian-shaped time profile, while the blue curve shows the results from the box-shaped time profile. 73
5.4 TXS 0506+056 spectral comparison using 2014-15 neutrino flare time window from [38]. 75
5.5 Residual map of the TXS 0506+056 region from [38]. The dashed square indicates the portion of ROI shown in the counts map of Fig. 5.2. The colorbar measures the significance of the deviations of the model from data. 76
5.6 Adaptive binned light curve for TXS 0506+056 from [38]. Panel 1 shows the gamma-ray flux integrated above 300 MeV including the Bayesian Block representation shown in black, panel 2 shows the power-law spectral index and panel 3 shows the gamma-ray flux integrated above 800 MeV. The average spectral index is shown as horizontal dashed green line in panel 2. The third panel additionally includes photons above 10 GeV shown with red stars. . . 77
5.7 Zoomed view of the 2017 TXS 0506+056 outburst between MJD 57881-58130 extracted from Fig. 5.6. The dashed orange line shows the arrival time of IceCube-170922A, while the shaded coloured areas highlight the three distinct flares. 78

5.8 Broadband SED of TXS 0506+056 adapted from [186]. The grey points are the multiwavelength data collected in [186], while the *Fermi*-LAT SED from the 2017 flare (blue points) and the one simultaneous to the 2014-15 neutrino flare (orange points) are from [38]. 81

6.1 Counts map (E>100 MeV) of the region centered on GB6 J1040+0617 from [38]. The 90% neutrino angular uncertainty is shown as green contour and the best-fit neutrino position is marked by a green cross. The grey crosses indicate the gamma-ray emitters identified in the region by our analysis. 87
6.2 Residual map of the GB6 J1040+0617 region from [38]. The dashed square indicates the portion of ROI shown in the counts map of Fig. 6.1. The colorbar measures the significance of the deviations of the model from data. 88
6.3 Adaptively-binned light curve of GB6 J1040+0617 from [38]. The first panel shows gamma-ray flux integrated above 300 MeV including the Bayesian block representation shown in black. The second panel shows the power-law spectral index. The average spectral index is overlaid as a horizontal green dashed line. The third panel shows optical data obtained from the All-Sky Automated Survey for Supernovae (ASAS-SN), the Palomar Transient Factory, and the Catalina Sky Survey. ASAS-SN upper limits are displayed as gray triangles. The arrival of IceCube-141209A is indicated as an orange dashed line. The purple shaded region marks the bright and hard gamma-ray state, while the green shaded region indicates the gamma-ray flare in coincidence with the neutrino arrival time. 89
6.4 Spectral energy distributions of GB6 J1040+0617 and 4C+06.41 from [38]. *Fermi*-LAT data of the respective time ranges when each source is significantly detected are shown as black crosses, arrows indicate 95% upper limits, and the best-fit spectral model including statistical uncertainties is overlaid as a black band. *Left*: average spectrum of GB6 J1040+0617 compared to the spectrum during the 93 day gamma-ray excess coincident with the neutrino detection and the bright hard state during MJD 55753–56474. *Right*: average spectrum of 4C+06.41 compared with the spectrum during the bright gamma-ray flare during MJD 57729–57824. 90
6.5 Adaptively-binned light curve for 4C+06.41 from [38]. The first panel shows the gamma-ray flux above 170 MeV including the Bayesian block representation shown in black. The second panel shows the power-law spectral index. The average spectral index is overlaid as dashed green line in the second panel, where the light curve of the spectral index is shown in blue points with correspondent error bars. The third panel shows optical data obtained from ASAS-SN, and the fourth panel shows radio data from the Owens Valley Radio Observatory (OVRO). The arrival of IceCube-141209A is indicated as a vertical, dashed orange line. 92
6.6 Gamma-ray best-fit positions from [38]. *Left panel:* the blue and black circles indicate the 99% containment radius of the gamma-ray positions of the two putative sources GB6-Fermi and 4C-Fermi. The 90% neutrino uncertainty region is shown as a dashed gray line for reference. Orange, green, and violet crosses indicate the radio positions of the blazars located in the region. *Right panel:* the bright hard state and modest flare at the arrival of IceCube-141209A are shown in red and blue respectively, while the late flare attributed to 4C+06.41 is shown in brown. The circles indicate the 99% containment radius of the gamma-ray position. 92

6.7 Zommed-in optical light curve of GB6 J1040+0617 around the arrival time of IceCube-141209A from [38]. The solid black line is the Bayesian Blocks representation for the ASAS-SN V-band data set from Fig. 6.3 94
6.8 Multi-wavelength SED in the observer's frame for GB6 J1040+0617 using archival data, which are not contemporaneous. 96

7.1 *Fermi*-LAT countmap of the PKS 1502+106 region with the IceCube-190730A contour (*left*) and the average gamma-ray SED from 11 years of *Fermi*-LAT data (*right*). The gray line shows the best-fit log-parabola model and uncertainty (shaded area). The model does not account for EBL absorption, that starts to become significant in the SED above ∼20 GeV. 98
7.2 *Fermi*-LAT lightcurve of PKS 1502+106 from [228] with data from [227]. The shaded colored areas indicate the three characteristic states: *quiescent* (blue), flaring with a hard gamma-ray spectrum (*hard flares*, yellow) and flaring with a soft gamma-ray spectrum (*soft flares*, pink). The green line in the *top* panel shows the average flux used in the flare definition. The *bottom* panel shows the *Fermi*-LAT spectral index across the same 11 year time period. The green line shows the average spectral index ($\bar{\Gamma} = 2.31$), from where we draw the distinction between hard ($\Gamma < \bar{\Gamma}$) and soft ($\Gamma > \bar{\Gamma}$) flares, and the green band is its respective 1σ uncertainty. The red lines show the average spectral index in the time window of each flare. 101
7.3 Zoom view of the time windows chosen for the representative datasets of the hard flares (*left*) and soft flares (*right*). The upper panels show the *Fermi*-LAT integral flux in the 0.1-800 GeV band, the middle panels the corresponding light curve for the spectral index and the lower panels the *Swift*-XRT integral flux in the 0.3-10 KeV band. 103
7.4 *Fermi*-LAT SED of the representative states for the quiescent state simultaneous to the neutrino observation (*left* panel, blue) and flaring states (*right* panel) reflecting the colours used in Figure 7.2. The black SED shows the average spectrum of the low-activity state. 103
7.5 PKS 1502+106 lightcurve with data from [227]. The high-energy photons (E > 10 GeV) are shown as red stars and the y-axis on the right side shows their energy. 104
7.6 Gamma-ray cosmic horizon from [242]. 104
7.7 Numerical modelling results from [228]. The coloured curves show the predicted multi-wavelength fluxes and all-flavor neutrino spectra from PKS 1502+106 obtained with the leptohadronic model *(left)* and the proton synchrotron model *(right)* under three different parameter sets, indicated in Tab. 7.2. The shaded areas correspond to the uncertainty in the non-thermal proton power, also indicated in Tab. 7.2. The colored data points represent multi-wavelength flux observations during each of the three states (see Figure 7.2 and Tab. 7.1). The gray points show archival radio data from the source. 106
7.8 Breakdown of the spectrum from [228], during the different states into the different radiative processes for the leptohadronic model *(left)* and the proton synchrotron model *(right)*. 107

7.9 Neutrino expectations from the numerical modelling in [228]. *Left*: total muon neutrino fluence from PKS 1502+106 predicted by the leptohadronic (solid) and proton synchrotron model (dashed) in the total duration of each of the three activity states. *Right*: total, time-integrated number of IceCube events from PKS 1502+106, expected from the leptohadronic and protons synchrotron models, in the IceCube point source analysis, in the entire duration of each of the three states indicated in Figure 7.2. 109

8.1 Distribution of the average detection significance of blazars listed in 4LAC. The dashed orange line marks the selection cut at $\sigma_{av} = 40$. 116
8.2 Distributions of the energy fluxes (*left*) and redshift (*right*) of the selected sample. Only 210 sources out of 257 have a measured redshift in [148]. . . . 117
8.3 Distribution of the number of adaptive bins for each source in the sample (*left*) and time durations of each adaptive bin (*right*). The orange dashed lines indicate the median value of each distribution. 118
8.4 Distributions of the doubling (*upper row*) and halving (*lower row*) timescales divided by optical class (*left column*) and synchrotron peak frequency (*right column*). The dashed coloured lines mark the median value of each distribution. 120
8.5 Scatter plots of the doubling (upper row) and halving (lower row) timescales in the comoving frame, versus redshift. The distributions are divided following the optical classification (left column) and synchrotron peak classification (right column). The solid and dashed black lines mark the decision boundaries of the SVMs classifier best-fit results. The star-shaped markers are used for the three candidate neutrino blazars. 122
8.6 Active states in the light curve of GB6 J1040+0617. The green horizontal line and shaded area represent the threshold F_{th} and its uncertainty, while the orange shaded areas mark the BBs selected as active states. 123
8.7 Distributions of duty cycles divided following the optical classification (left panel) and the synchrotron peak classification (right panel). The dashed colored lines mark the median value of each distribution. 124
8.8 HOP blocks (shaded coloured areas) identified in the light curve of MG1 J123931+0443. The solid black line shows the BB representation of the light curve. 125
8.9 Best fit from Gaussian Process regression (solid purple curve) and 95% confidence level from the posterior distribution (shaded area). 127
8.10 Global fit of the HOP block from Figure 8.9. The solid orange curve shows the best-fit total model, while the green and red dashed curves show the single-flare models and constant background, respectively. 129
8.11 Flare duration distributions of the 3322 modelled flares in the comoving frame for each optical class. The black dashed line marks the median value of the total sample at 20.4 days. 129
8.12 Distribution of the symmetry parameter ξ for flares with $T'_{dur} < 1$ day. The solid and dashed vertical lines marks the average value and 1σ uncertainty calculated with the bootstrap method. 131
8.13 Average symmetry parameter ξ (and error) for sources with at least 3 flares with $T'_{dur} < 1$ day as a function of redshift. 131
8.14 Distribution of the symmetry parameter ξ for flares with $T'_{dur} < 20.4$ days for FSRQs (left panel) and BL Lacs (right panel). The solid and dashed vertical lines marks the average value and 1σ uncertainty calculated with the bootstrap method. 132

8.15 Distribution of the symmetry parameter ξ for flares with T'_{dur} > 20.4 days for FSRQs (left panel) and BL Lacs (right panel). The solid and dashed vertical lines marks the average value and 1σ uncertainty calculated with the bootstrap method. 132
8.16 Distributions of the blob radius size R'_b (in the comoving frame) of each flare, for each optical class. The dashed coloured lines mark the median values of each distribution. 133
8.17 Best-fit model for the HOP block of TXS 0506+056 coincident with the arrival of IceCube-170922A (purple dashed line). The solid orange curve shows the best-fit total model, while the green and red dashed curves show the single-flare models and constant background, respectively. 135
8.18 Distribution of ξ (*left*) and emission region size R'_b (*right*) for all the modelled flares in the light curve of TXS 0506+056. The orange dashed line marks the emission blob size of the flare coincident with the detection of IceCube-170922A. 136
8.19 Best-fit model for the HOP block of GB6 J1040+0617 coincident with the arrival of IceCube-141209A (purple dashed line). The solid orange curve shows the best-fit total model, while the green and red dashed curves show the single-flare model and constant background, respectively. 137
8.20 Distribution of ξ (*left*) and emission region size R'_b (*right*) for all the modelled flares in the light curve of PKS 1502+106. 138
8.21 Distribution of the distance of the gamma-ray emission region from the central SMBH. The solid black line marks the median value of the distirbution, while the orange dashed line marks the radius of the BLR derived in Chapter 7. . . 138

9.1 Scheme of the follow-up pipeline developed for *Fermi*-LAT data. The upper panel shows the synchronization and preprocessing of events (FT1) and spacecraft pointings (FT2) files, with the production of the *livetime cubes*. The lower panel shows the analysis workflow. 145
9.2 All-sky map in in Galactic coordinates from [271] showing the best-fit positions and 90% containment regions (approximated to circles) of the new IceCube Realtime Alert Stream in Galactic coordinates. *Gold* alerts are shown in orange and *Bronze* alerts in blue. 146
9.3 Distribution of the 90% containment regions (*left*) and number of 4FGL sources coincident (*right*) divided by alert type from [271]. The black dashed line in the *left* plot shows the median extension for the full sample, while the orange and blue dashed lines show the median extensions for the Gold and Bronze alerts, respectively. 147
9.4 *Fermi*-LAT counts map of IceCube-100608A with the 90% angular uncertainty. 151
9.5 Multiwavelength lightcurves of MG3 J225517+2409 152
9.6 *Fermi*-LAT countmap of the IceCube-201114A with its best-fit localization (green x) and 90% angular uncertainty (green circle). The bright diffuse emission in the lower right corner is due to the Galactic Plane. 153
9.7 *Fermi*-LAT counts map of the IceCube-201130A with its best-fit localization (green x) and 90% angular uncertainty (green circle). 154
9.8 *Fermi*-LAT counts map of the IceCube-210210A with its best-fit localization (green x) and 90% angular uncertainty (green circle). 155
9.9 p-values from the KS tests in function of the index α from Eq. 9.1. The solid lines show the results for the neutrino blazar candidates sample for each class. The dashed lines show the results for the test performed on the control samples, with the shaded areas marking the 1σ uncertainty regions from the N = 1000 Monte Carlo samples drawn for each α and source class. 156

9.10 Comparison of candidate neutrino blazars with all blazars in the 4LAC AGN sample adapted from [227]. Star-shaped markers indicate candidate neutrino blazars already studied in the literature and black circles show the new coincident sources (with an identified counterpart) from Table 9.1 158
9.11 *Fermi*-LAT countmap of the nlsy1 galaxy 1H 0323+342 (4FGL J0324.8+3412). 160
9.12 Multi-wavelength light curve of 1H 0323+342 from [227]. The duration of the neutrino flare is short ($T_w = 147$ s) and its arrival time is shown as an orange line. An excess in gamma rays is found coincident with the neutrino arrival time and an excess in X-ray emission is visible roughly one month before the neutrino arrival time. The *Fermi*-LAT gamma-ray light curve covers the energy range from 100 MeV to 800 GeV, the *Swift* X-ray light curve from 0.3 to 10 keV and the OVRO radio data is at 15 GHz 161

List of Tables

3.1 Table of FGL catalog releases from 0FGL to the latest 4FGL-DR2. 46

4.1 Expected and observed alert rates (events per year) from [16]. The total values of *Gold* alerts takes into account the overlap between the GFU and EHE event selections. 67

5.1 Significance of spectral variations during the box time window of the neutrino flare from [38]. 79
5.2 High-energy photons associated with TXS 0506+056 with a probability of $> 80\%$ detected during the neutrino flare time interval from [38] 80

6.1 Best fit localizations for the gamma-ray emitters associated with GB6 J1040+0617 and 4C+06.41. Coordinates are in J2000 equinox. 88

7.1 Time windows for the three representative states identified in Figure 7.2 and highlighted in Figure 7.3 for the flaring states of PKS 1502+106. The datasets are the same as used in [228]. 102
7.2 Parameter values from [228] underlying the results of the leptohadronic and proton synchrotron models, for each of the states identified in Figure 7.2. Primed quantities refer to the rest frame of the jet. The ranges in the values of the proton luminosity correspond to the uncertainties of the model, resulting in the shaded regions in Figure 7.7. We also report the reduced χ^2 values for the multi-wavelength SEDs predicted by each model, describing the goodness of fit. In the two bottom rows, we list the predicted number of neutrino events per year in IceCube, as well as the total expected number of events integrated over the eleven-year period. The yearly rates correspond to the IC86 configuration of the IceCube detector, since they were calculated using the effective area of that configuration. For the total number of events, we take into account the different detector configurations over the years, as depicted by the dashed vertical lines in Figure 7.2. 108

8.1 Sources with $p > 1\%$ from variability test. 119
8.2 Doubling and halving time scales (in the comoving frame) and duty cycle (DC) of the three neutrino blazar candidates. 124
8.3 Best fit parameters and derived quantities of the six flares in the HOP block of TXS 0506+056 coincident with the arrival of IceCube-170922A. 136

9.1 Selection of 4FGL-DR2 sources coincident with well-reconstructed realtime events from [271]. 148
9.2 The p-values from the K-S test on the different classes and the whole sample of candidate neutrino blazars from [227]. 149
9.3 Neutrino flare candidates from [289]. 159

B.1 Alerts from the IceCube Realtime Stream 1.0. Alerts that have been retracted are not shown. 175
B.2 Alerts from the IceCube Realtime Stream 2.0. Alerts that have been retracted are not shown. 176

B.3 (Continuing of Tab B.2) Alerts from the IceCube Realtime Stream 2.0. Alerts that have been retracted are not shown. 177
B.4 Archival high-energy neutrino events from https://icecube.wisc.edu/science/data/TXS0506_alerts. 178
B.5 (Continuing of Tab. B.4). Archival high-energy neutrino events from https://icecube.wisc.edu/science/data/TXS0506_alerts. 179

1 Introduction

The observation of the sky has been one of the main driving forces of human knowledge already since the naked eye was the only available tool for its investigation. Until the last century, the main probe for the study of the Universe has been the electromagnetic radiation in the visible part of the spectrum emitted by cosmic sources. The development of powerful technology and the enormous improvements in the knowledge of the properties of electromagnetic radiation across all the frequencies has opened new windows for astronomy, and an incredible new amount of information was revealed about astrophysical sources compared to the limited information accessible in the visible portion of the electromagnetic spectrum. Figure 1.1 shows a composite multi-wavelength image of the Centaurus A galaxy obtained from observations at radio, infrared, optical and X-ray frequencies. The image at visible light shows a bright nucleus surrounded by a dusty region and the infrared light provides an amazing resolution of the distribution of this matter. Observations in the X-ray and radio reveal features hardly accessible in the visible spectrum, like the morphology of the powerful relativistic jet of plasma developing from the galaxy center.

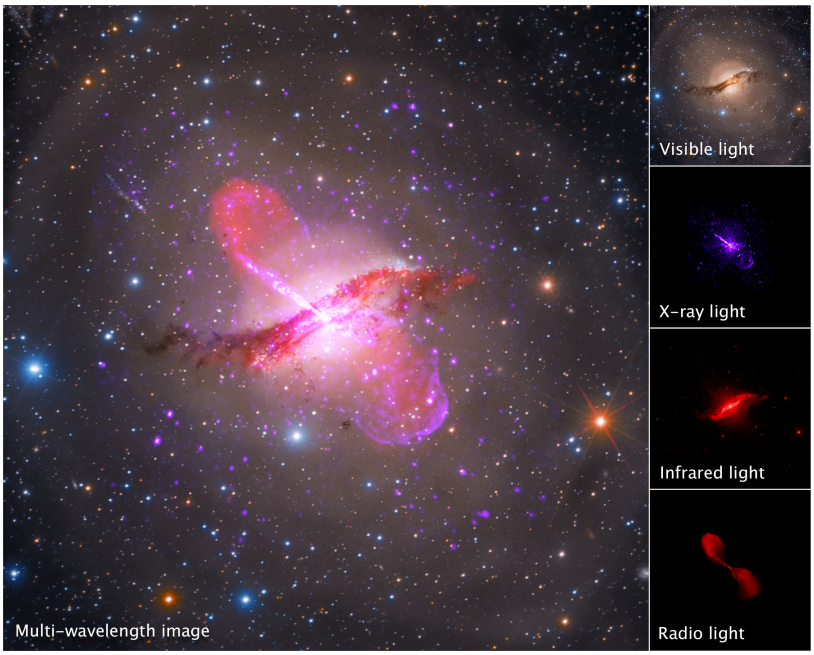

Figure 1.1: Composite multi-wavelength image of the Centaurus A galaxy from observations in radio, infrared, visible and X-ray light. Credit: ESA/NASA.

At the beginning of the last century, another major discovery was laying the foundation for another revolution in astrophysics. After the discovery of radioactivity by Henri Becquerel in 1896, Victor Hess [1] and Domenico Pacini [2] independently provided evidences of an isotropically distributed radiation getting through the atmosphere in the early 1910s. While Pacini's measurements were performed at sea level and underwater, Hess' measurements took place on balloon flights up to an altitude of 5200 m and allowed to reach two important conclusions about this radiation. The first one was that the origin of the radiation was

[1]: Hess (1912), 'Über Beobachtungen der durchdringenden Strahlung bei sieben Freiballonfahrten'

[2]: Pacini (1912), 'La radiazione penetrante alla superficie ed in seno alle acque'

outside of the atmosphere, and the second one was that the Sun was not the direct source because of the lack of day/night effects.
After more than 100 years of observations, several experimental results helped to identify this radiation as a flux of highly energetic particles and nuclei that constantly hit the Earth with energies up to more than 10^{20} eV, now referred to as *Cosmic Rays* (CRs) . Figure 1.2 shows the differential CR spectrum collecting the contributions from a multitude of experiments from small particle detectors launched on balloons to surface detectors with an area of > 3000 km^2. The steep energy dependence of the spectrum shows how low the fluxes measured for the most energetic events are, which can get as low as 1 particle/century/km^2 for events with energy > 10^{20} eV. The discovery of CRs has identified a new *messenger* that can reveal new insights into cosmic sources. One of the main goals of the study of CRs is to understand the origin of those observed at the highest energies, that require powerful acceleration mechanisms and strongly magnetized environments.

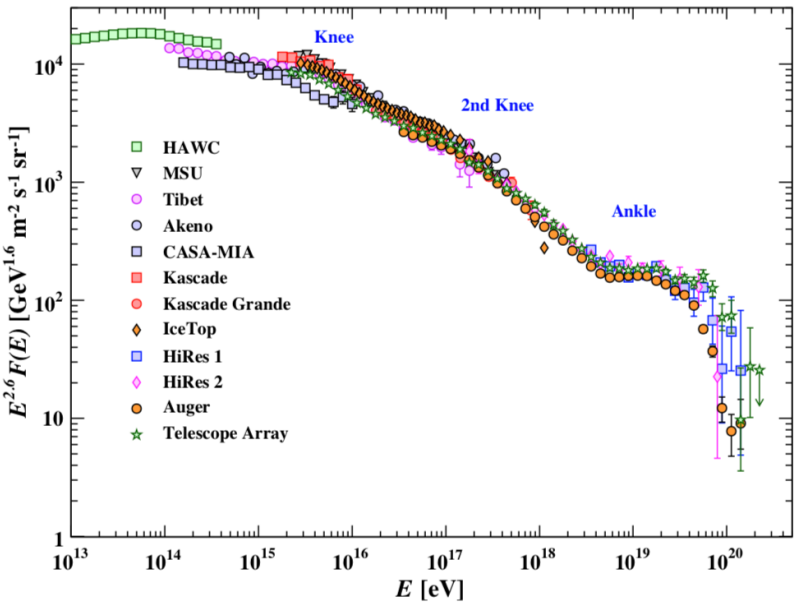

Figure 1.2: Differential cosmic ray spectrum from [3].

Identifying cosmic accelerators cannot be easily achieved by measuring the spectrum and the arrival directions of cosmic-ray particles, because of the influence of the interstellar magnetic fields on their trajectories. The curvature radius for the trajectory of a charged particle in a magnetic field is proportional to its energy, and therefore large surface detectors like the *Pierre Auger Observatory* and the *Telescope Array* use cosmic-ray events above high-energy thresholds (> 10^{18} eV) to reduce the effect of magnetic deflection and study anisotropies in their arrival directions. The events are called *ultra-high energy cosmic rays* (UHECRs) and constitute the tail of the spectrum in Figure 1.2. Recent results show evidence of anisotropy up to 4σ significance when tested to populations of high-energy nearby sources [4].
Gamma-rays are an ideal messenger to pinpoint the sources of cosmic rays, because are produced in radiative processes of CR inside the source and don't get deflected by magnetic fields. However, photons may suffer from absorption inside the source or during their journey from the source to Earth because of their interaction with low-energy fields like the cosmic microwave background (CMB) or the extragalactic

[4]: Aab et al. (2018), 'An Indication of Anisotropy in Arrival Directions of Ultra-high-energy Cosmic Rays through Comparison to the Flux Pattern of Extragalactic Gamma-Ray Sources'

background light (EBL). This absorption is stronger as the photon energy increases and Figure 1.3 shows an example of the distances at which the universe becomes opaque to gamma rays. Gamma-ray emission expected by Pevatron sources suffers already from strong absorption at distances larger than the Galactic radius, and therefore PeV gamma-ray detections at these energies can only be achieved for nearby objects.

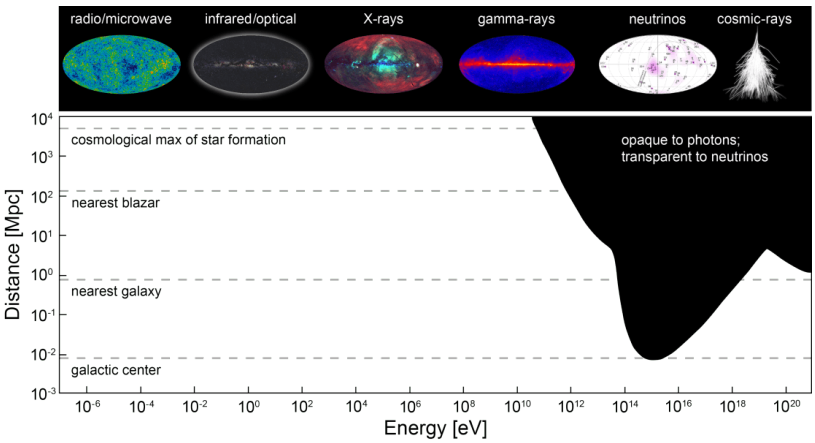

Figure 1.3: *Top*: All-sky maps at different wavelengths and as seen in neutrinos. *Bottom*: Distance (in Mpc) vs photon energy (in eV) diagram. The black filled region indicates distances larger than the photon mean free path at a certain energy. Credit: IceCube Collaboration.

Another messenger that is abundant in the Universe, electrically neutral and weakly interacting is the neutrino. Neutrinos are considered smoking guns for cosmic-ray acceleration, since they can only be produced by hadronic interactions and can travel almost unabsorbed from the source, even from the largest cosmic distances.

A first major milestone in the observation of astrophysical neutrinos was the measurements of solar neutrinos by the Davis experiment in the Homestacke Mine in the 1960s [5]. Extraterrestial MeV neutrinos were first detected from the supernova SN1987A in the Large Magellanic Cloud, one of the satellite galaxies of the Milky Way.

Of special interest for cosmic-ray physics are high-energy neutrinos at GeV to PeV energies. At the present day, three major neutrino detectors are devoted to the study of high-energy neutrino astronomy. In the Northern hemisphere, the ANTARES [6] Neutrino Telescope is operating underwater in the Mediterranean Sea, and Baikal-GVD under the surface of lake Baikal in Russia [7]. The IceCube South Pole Neutrino Observatory (SPNO) is operating inside the ice at the South Pole[8] and is the largest neutrino detector with 1 km^3 of instrumented volume.

In 2013, a diffuse flux of high-energy neutrinos has been detected by IceCube in the energy range from 30 TeV to 2 PeV [9–11]. However, for several years after this breakthrough discovery, no compelling evidence for spatial or temporal clustering of events had been identified and the origin of the neutrinos was unknown [12, 13]. The isotropic arrival directions of IceCube neutrinos suggest a predominantly extra-galactic origin of the cosmic neutrinos.

One of the most peculiar features of the diffuse neutrino emission is that in the 0.1 - 1 PeV range its energy flux is comparable to those observed for the diffuse sub-TeV gamma-ray flux and the UHECR flux (see Figure 1.4 for a comparison). Even though the energy ranges of these three messengers span over ten orders of magnitude, they show comparable energy budgets and therefore suggest that they might have a common origin [14].

[5]: Davis (1964), 'Solar Neutrinos. II. Experimental'

[6]: Brown (2009), 'The ANTARES neutrino telescope: Status and first results'

[7]: Allakhverdyan et al. (2021), 'The Baikal-GVD neutrino telescope: search for high-energy cascades'

[8]: Aartsen et al. (2017), 'The IceCube Neutrino Observatory: instrumentation and online systems'

[9]: IceCube Collaboration (2013), 'Evidence for High-Energy Extraterrestrial Neutrinos at the IceCube Detector'

[10]: Aartsen et al. (2015), 'Atmospheric and astrophysical neutrinos above 1 TeV interacting in IceCube'

[11]: Aartsen et al. (2016), 'Observation and Characterization of a Cosmic Muon Neutrino Flux from the Northern Hemisphere using six years of IceCube data'

[12]: Aartsen et al. (2017), 'All-sky Search for Time-integrated Neutrino Emission from Astrophysical Sources with 7 yr of IceCube Data'

[13]: Aartsen et al. (2015), 'Searches for Time-dependent Neutrino Sources with IceCube Data from 2008 to 2012'

[14]: Murase (2019), 'Multi-Messenger Connections among High-Energy Cosmic Particles'

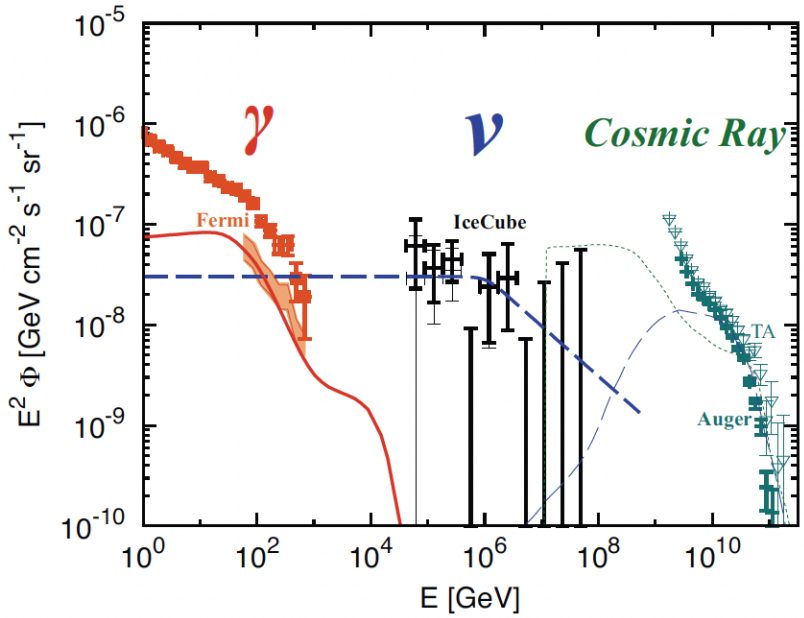

Figure 1.4: High-energy diffuse fluxes of the three messenger particles from [14].

To improve the search for electromagnetic counterparts to the high-energy astrophysical neutrinos, IceCube has implemented a realtime program [15, 16] in 2016, that selects high-energy neutrinos ($\gtrsim$ 60 TeV) with high probability of being of astrophysical origin. Information about the reconstructed neutrino direction are distributed to a network of follow-up instruments within seconds of the detection at the South Pole.

On September 22, 2017, the detection of the neutrino event IceCube-170922A with estimated energy of >100 TeV, and good angular resolution was distributed to the network of observatories. Shortly after, the *Fermi* Large Area Telescope (LAT) collaboration reported the detection of the gamma-ray blazar TXS 0506+056 in spatial coincidence with the neutrino event [17]. At the time of the IceCube trigger, the source was in a state of enhanced activity [17, 18]. Subsequently, the first-ever detection of TXS 0506+056 was reported by the Major Atmospheric Gamma Imaging Cherenkov Telescopes (MAGIC, [18, 19]) at energies >100 GeV and was later confirmed by the Very Energetic Radiation Imaging Telescope Array System (VERITAS, [20]). The chance probability of the coincidence between the neutrino and the flaring blazar was excluded at 3σ significance [18], making it the first compelling evidence of an extragalactic neutrino source.

Blazars are the most powerful class of active galactic nuclei (AGN) and have been suggested in several studies as good candidates for high-energy cosmic-ray acceleration sites and, in turn, sources of astrophysical neutrinos [21–35]. The production of $\mathcal{O}$(100 TeV) neutrinos in blazar jets would be accompanied by $\mathcal{O}$(200 TeV) gamma rays, implying a simultaneous production of neutrinos and gamma rays at the source [36]. However, the interaction of photons within the source or during their propagation could alter the connection between neutrinos and gamma rays. This might have been the case for the 3.5σ [37] detection of an excess of >100 GeV neutrinos from the location of TXS 0506+056 between September 2014 and March 2015. The detection of this neutrino flare was not accompanied by an enhanced activity in gamma rays [38], and rose questions about the gamma ray / neutrino connection.

[15]: Aartsen et al. (2017), 'The IceCube realtime alert system'
[16]: Blaufuss et al. (2019), 'The Next Generation of IceCube Real-time Neutrino Alerts'

[17]: Tanaka et al. (2017), 'Fermi-LAT detection of increased gamma-ray activity of TXS 0506+056, located inside the IceCube-170922A error region.'

[18]: Aartsen et al. (2018), 'Multi-messenger observations of a flaring blazar coincident with high-energy neutrino IceCube-170922A'
[19]: Ansoldi et al. (2018), 'The Blazar TXS 0506+056 Associated with a High-energy Neutrino: Insights into Extragalactic Jets and Cosmic-Ray Acceleration'

[20]: Abeysekara et al. (2018), 'VERITAS Observations of the BL Lac Object TXS 0506+056'

Since this remarkable identification of the first high-energy neutrino source candidate, several astrophysical sources coincident with high-energy neutrino events or clusters of >100 GeV neutrinos have been proposed as candidate neutrino sources. Some of these belonging to the blazar class of active galaxies will be presented in this thesis, while other interesting results include the association of single high-energy neutrinos with Tidal Disruption Events [39–41] and the coincidence of the Seyfert 2 galaxy NGC 1068 with the hottest spot (2.9σ) in the all-sky time integrated point-source search with 10 years of IceCube data [42]. I had the privilege of starting this thesis work only few months after the observation of the coincidence between the high-energy neutrino IceCube-170922A and the flaring blazar TXS 0506+056. My work was focused on the study of candidate gamma-ray blazar counterparts to high-energy neutrinos, mainly through observations done with the *Fermi*-LAT. This thesis is organized as follows:

- In Chapter 2 I give an overview of the physics of AGN with a focus on the blazar class and the properties of the accretion of their supermassive black hole, the relativistic jet, acceleration mechanisms and radiative processes of leptonic and hadronic nature.
- In Chapter 3 I give an overview of gamma-ray astronomy with *Fermi*-LAT, the main instrument used for the observations reported in this work. I focus on the instrument characteristics and performance, gamma-ray analysis techniques and main results in the detection of blazar sources.
- In Chapter 4 I give an overview of the IceCube SPNO, with a focus on the program of realtime alerts for high-energy neutrino events.
- In Chapter 5 I present the results on the analysis of *Fermi*-LAT data in the region of TXS 0506+056, focusing on the data simultaneous to the neutrino detections.
- In Chapter 6 I present the results on the analysis of GB6 J1040+0617, the second candidate gamma-ray blazar coincident with a track-like neutrino event found for the first time in this work in gamma-ray outburst at the arrival of the high-energy neutrino IceCube-141209A.
- In Chapter 7 I present the results on the analysis of PKS 1502+106, a powerful gamma-ray blazar coincident with the high-energy neutrino IceCube-190730A.
- In Chapter 8 I present the results on the caracterization of the variability of 256 bright blazars detected by *Fermi*-LAT, and I compare the variability of the neutrino blazar candidates from Chapters 5, 6 and 7 with that of the selected sample of bright blazars.
- In Chapter 9 I present the results of the follow-up activities of more than 3 years of IceCube neutrino alerts and the comparison of the population of gamma-ray blazars spatially coincident with single high-energy neutrinos with the whole population of blazars detected by *Fermi*-LAT.
- In Chapter 10 I summarise the main results of this thesis work and I outline the future perspectives for the multi-messenger studies of neutrino sources.

[21]: Stecker et al. (1991), 'High-energy neutrinos from active galactic nuclei'
[22]: Protheroe et al. (1992), 'High energy cosmic rays from active galactic nuclei'
[23]: Mannheim (1993), 'The proton blazar'
[24]: Szabo et al. (1994), 'Implications of particle acceleration in active galactic nuclei for cosmic rays and high energy neutrino astronomy'
[25]: Mannheim (1995), 'High-energy neutrinos from extragalactic jets'
[26]: Mastichiadis (1996), 'The Hadronic Model of Active Galactic Nuclei'
[27]: Protheroe (1999), 'High energy neutrino astrophysics'
[28]: Bednarek et al. (1999), 'Gamma-ray and neutrino flares produced by protons accelerated on an accretion disc surface in active galactic nuclei'
[29]: Mücke et al. (2001), 'A proton synchrotron blazar model for flaring in Markarian 501'
[30]: Mannheim et al. (2001), 'Cosmic ray bound for models of extragalactic neutrino production'
[31]: Atoyan et al. (2001), 'High-Energy Neutrinos from Photomeson Processes in Blazars'
[32]: Dermer et al. (2009), 'Ultra-high-energy cosmic rays from black hole jets of radio galaxies'
[33]: Böttcher et al. (2013), 'Leptonic and Hadronic Modeling of Fermi-detected Blazars'
[34]: Halzen (2013), 'Pionic photons and neutrinos from cosmic ray accelerators'
[35]: Kadler et al. (2016), 'Coincidence of a high-fluence blazar outburst with a PeV-energy neutrino event'
[36]: Ahlers et al. (2018), 'Opening a New Window onto the Universe with IceCube'
[37]: Aartsen et al. (2018), 'Neutrino emission from the direction of the blazar TXS 0506+056 prior to the IceCube-170922A alert'
[38]: Garrappa et al. (2019), 'Investigation of Two Fermi-LAT Gamma-Ray Blazars Coincident with High-energy Neutrinos Detected by IceCube'
[39]: Stein et al. (2021), 'A tidal disruption event coincident with a high-energy neutrino'
[40]: Reusch et al. (2021), 'The candidate tidal disruption event AT2019fdr coincident with a high-energy neutrino'
[41]: van Velzen et al. (2021), 'Establishing accretion flares from massive black holes as a major source of high-energy neutrinos'
[42]: Aartsen et al. (2020), 'Time-Integrated Neutrino Source Searches with 10 Years of IceCube Data'

High-energy neutrinos from Blazars

Blazars and high-energy neutrinos

2

2.1 Unified model of Active Galactic Nuclei

2.1 Unified model of Active Galactic Nuclei 9
2.2 Blazars 13
2.2.1 Black Holes: the central engine 14
2.2.2 Relativistic jets 18
2.3 High-energy neutrino production in Blazars . . . 26
2.4 Diffuse neutrino emission from blazars 28

Blazars are a subclass of powerful active galaxies, observed throughout the whole electromagnetic spectrum from the lowest radio frequencies to the highest gamma-ray energies. Before focusing on this specific class of astrophysical sources, it is necessary to have an overview of active galaxies to understand what makes blazars special among them.
Active Galactic Nuclei (AGN) are a peculiar class of astrophysical objects, namely galaxies that host a supermassive black hole ($M_{BH} > 10^6\ M_\odot$) in their center, which accretes matter and converts gravitational potential energy into radiation. About 1 over 100 galaxies in the Universe host an AGN, and their characteristic observational signatures can be detected over a wide range of the electromagnetic spectrum and, in some rare cases, up to the very-high-energy (VHE) gamma-ray band (>10^{11} eV). In addition to the central black hole, the typical structure of an AGN includes (see also Figure 2.2):

- An *accretion disk* formed by the matter captured by the black hole creating an equatorial flow around it, at distances smaller than a parsec[i] (pc).
- A region populated by high-density gas clouds (> 10^9 cm^{-3}) orbiting with velocities of the order of several thousands of km s^{-1} at typical distances of 0.01 - 1 pc from the black hole. The high velocity of these clouds is reflected in a large width of the correspondent emission lines observed in the optical spectra of AGN, as a consequence of the Doppler effect. This region is referred to as *Broad Line Region* (BLR).
- A *dusty torus*, typically at distances of 1 - 10 pc from the central black hole. Being at a distance larger than the sublimation radius of the black hole, this is the closest region containing molecular and atomic dust.
- A *Narrow Line Region* (NLR), formed by gas clouds at lower density of 10^3-10^5 cm^{-3} and lower velocities compared to the BLR ($\leq$ 1000 km s^{-1}). This region is typically located at hundreds of pc from the central black hole and along the torus axis.
- Around 10% of all AGN show a relativistic outflow of plasma, highly collimated up to kpc distances from the black hole and with larger, broadened structures up to Mpc scales.

Already from the groundbreaking observations made by Carl Seyfert in 1943 [43], the first 12 active galaxies were identified by their central core being brighter than the host galaxy and by the presence of high-excitation nuclear emission lines in their optical spectra (*Seyfert galaxies*). The properties of these emission lines were already discussed by Seyfert. 30 years later they led to the first classification scheme based on their relative widths of emission lines and those of the Balmer series [44]. In

[43]: Seyfert (1943), 'Nuclear Emission in Spiral Nebulae.'

[44]: Khachikian et al. (1974), 'An atlas of Seyfert galaxies.'

[i] Parsec (pc): unit of lenght for astronomical distances. 1pc = 3.086×10^{18} cm.

their atlas of 71 Seyfert galaxies, they divided the sources into two classes [45]:

- *Seyfert 1 galaxies* where the Balmer lines (mainly Hα, Hβ, and Hγ) appear broader than the forbidden lines (OII, OIII, N II, Ne III and Ne IV). In addition, they also show a strong Fe [II] line at 4570 Å.
- *Seyfert 2 galaxies* where both the Balmer and forbidden lines show the same narrow width. For objects in this class, the AGN core is usually less dominant with respect to the host galaxy compared to the Seyfert 1 objects.

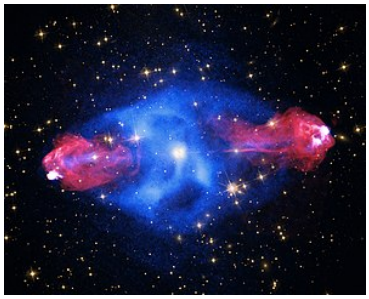

Figure 2.1: Composite image of the FR II galaxy Cygnus-A .

However, there is no clear separation between these classes, and observations of several objects show properties that fall in between these two categories. For this purpose, several intermediate classes are also defined for Seyfert galaxies, named as Seyfert 1.2, 1.5, 1.8 and 1.9 following the classification scheme in [46]. Another example are narrow-line Seyfert 1 galaxies (NLS1) that have very bright X-ray emission and, while their Hα line is broad, their Hβ line is narrow (equivalent to v < 2000 km s^{-1}), which makes them fall close to the Seyfert 1.9 class [47].
Another binary classification of active galaxies was introduced by Fanaroff and Riley in 1974 [48] for sources that where not exhibiting a bright central region but bright, extended radio jets and large radio luminosities. In this case, the presence of an AGN at the core of the host galaxy is assumed to explain the presence of the radio jets, and the classification scheme is based on the morphology of the radio emission. These so-called *radio galaxies* are divided in

- *Fanaroff-Riley class I* which show a rather compact emission arising from the vicinity of the core.
- *Fanaroff-Riley class II* which show extended lobes and the majority of the radio emission is measured at the termination shocks visible at their extremities. An example of an FR II galaxy is Cygnus A shown in a multi-wavelength composite view in Figure 2.1.

From the observation of the AGN cores in radio galaxies, both Seyfert 1 and 2 type of spectra are found, including the intermediate variants. Cygnus A in Figure 2.1 is known to have a Seyfert 2 core.
Radio observations play a very important role in the study of AGN already since the first large radio surveys in the 1960s, when the third Cambridge catalog of radio sources detected at 159 MHz was compiled [49]. Among the 471 sources in the catalog, a large number appeared in the optical images like blue stars and revealed strong emission lines in their spectra. These objects were called *quasi-stellar radio sources* (quasars) and one of their most important specimens is 3C 273, that was found to have strong Balmer lines redshifted by 16% (z = 0.15834) [50] where z is the source redshift defined as the relative shift of the spectral line to its true value

$$z = \frac{\lambda_{observed} - \lambda_{emitted}}{\lambda_{emitted}} \tag{2.1}$$

where λ indicates the peak wavelength of a spectral line. More quasars after 3C 273 were found to have significant redshift, reaching to the conclusion that those objects were indeed very distant Seyfert galaxies.

[46]: Osterbrock (1977), 'Spectrophotometry of Seyfert 1 galaxies.'

[47]: Osterbrock et al. (1985), 'The spectra of narrow-line Seyfert 1 galaxies.'

[48]: Fanaroff et al. (1974), 'The morphology of extragalactic radio sources of high and low luminosity'

[49]: Bennett (1962), 'The revised 3C catalogue of radio sources.'

[50]: Schmidt (1963), '3C 273 : A Star-Like Object with Large Red-Shift'

Another important feature in the identification of quasars is the observation of a prominent emission in the optical-UV range called *big blue bump*, likely due to the accretion disk thermal emission. Comparison between multiwavelength observations in radio and optical surveys showed that 90% of the optically detected quasars do not show strong radio emission, and therefore are more difficult to be found. Unlike the classification in Seyfert 1 and 2, that include several intermediate classes, the separation between radio-loud and radio-quiet quasars is sharp. Quasars are identified as radio-quiet when

$$R^{\star} = log \frac{f_{radio}}{f_B} < 1 \tag{2.2}$$

where f_{radio} and f_B are the radio and optical flux, respectively [45]. Radio-quiet quasars therefore have not to be considered radio-silent, and their weaker radio emission might be explained with the presence of small-scale jets, less powerful than in the case of the extended powerful jets observed in radio-loud objects [51].

[51]: Ulvestad et al. (2005), 'VLBA Imaging of Central Engines in Radio-Quiet Quasars'

Radio-loud quasars are further classified as *Flat Spectrum Radio Quasar* (FSRQ) and *Steep Radio Spectrum Quasar* (SRSQ) according to the spectral index shown in the radio band. A class of sources with inverted spectra that peak in the GHz range are also observed, and are named *GigaHertz Peaked Spectrum* sources (GPS) [45].

A revolution in the study of quasars happened in 1968 when John L. Schmitt [52] proposed a new classification for the irregular variable star BL Lacertae into a flat spectrum radio galaxy, while discussing the radio observations of the source reported in [53]. In his research note [52] he describes a *"marginal nebulosity about the star"* to outline the difficulty in resolving the host galaxy of the quasar, but the peculiar radio properties and the strong variability in the optical band suggested similar properties to other powerful FSRQs, like 3C 273 and 3C 454.3. The optical spectrum of BL Lacertae shows only weak lines and no prominent features, unlike the case of FSRQ objects. Because of the common features shown in radio observations, quasars with properties similar to those observed in BL Lacertae (BL Lac objects) and FSRQs were grouped in a single class called *blazar*, from a combination of the name of the two sub-classes.

[52]: Schmitt (1968), 'BL Lac identified as a Radio Source'

[53]: MacLeod et al. (1968), 'The Radio Source VRO 42.22.01'

The overview of AGN classifications given in this section is focused on setting the basis for the definition of the blazar class, which is the focus of this thesis work. The landscape of AGN classifications in astronomy is much broader, and several classes have been left out from this overview, like *Low Luminosity AGN* (LLAGN), *Ultraluminous Infrared Galaxies* (ULIRGs) and more. The recent review [54] gives a comprehensive description of the complex ensemble of AGN classes in each energy band.

[54]: Padovani et al. (2017), 'Active galactic nuclei: what's in a name?'

To conclude this section, it is worth to mention the efforts towards a unified model to explain the different AGN classes. A noteworthy step towards unification was made by Blandford and Rees in 1978 [55] when they introduced the interpretation of the different types of active galaxies according to the beaming angle shown towards the observer. In this model, blazars are sources showing the smallest beaming angles towards the observer and radio-quiet quasars are also hosting a radio jet but pointing away from the observer. This model however was not fully explaining the difference between radio-loud and radio-quiet AGN, until

[55]: Blandford et al. (1978), 'Extended and compact extragalactic radio sources: interpretation and theory.'

[56]: Antonucci (1993), 'Unified models for active galactic nuclei and quasars.'

Antonucci in 1993 added a fundamental piece to the puzzle [56]. In Antonucci's unified model, there are two types of AGN: radio-loud and radio-quiet. All the observed differences between each subclass would be explained by the orientation of the galaxy/jet axis. For example, radio galaxies are observed to have weaker emission compared to blazars because their jet is at large angle with respect to the line of sight. In addition, Antonucci introduced the presence of an optically thick torus sorrunding the central SMBH at typical distances of 1-100 pc that could hide the BLR when the AGN is observed edge-on, and therefore explain the lack of broad lines in Seyfert 2 galaxies. This occultation does not happen for the NLR since is located along the galactic plane axis, away from the shade of the torus.

[57]: Urry et al. (1995), 'Unified Schemes for Radio-Loud Active Galactic Nuclei'

A further attempt of unification was done by Urry and Padovani in 1995 [57]. They suggested that BL Lacs are evolutions of FSRQ sources, that gradually become weak-lined in their spectra by virtue of increased beaming of the continuum emission.

Figure 2.2 shows a diagram of AGN unification following the viewing-angle model.

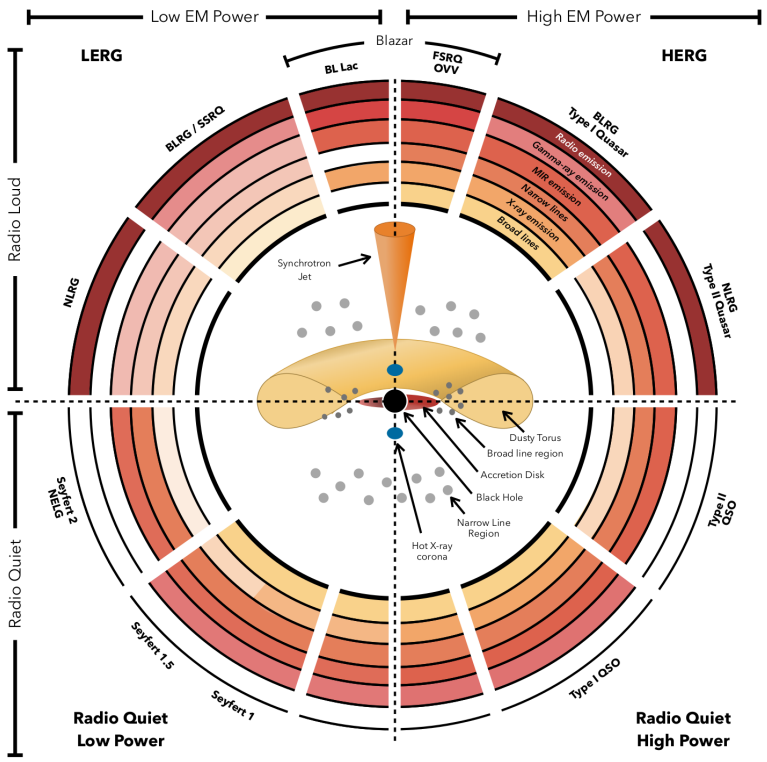

Figure 2.2: AGN unification diagram from [58].

2.2 Blazars

As from the properties highlighted in the unified model of AGN, blazars constitute a special class of radio-loud active galaxies with the relativistic jet pointing at a small angle ($\leq 10°$) toward the observer. They constitute roughly 10% of the jetted-AGN population and only 1% of the entire AGN population.
Blazars are detected across the whole electromagnetic spectrum, spanning about 15 decades in energy from radio frequencies to the most energetic gamma rays of > TeV. Their spectral energy distribution (SED) shows a typical two-humps structure (Figure 2.3): the first hump, that spans from radio to X-rays is commonly explained as synchrotron radiation from relativistic electrons accelerated in the jet, while the mechanisms behind the second hump depend on the composition of the particles in the emission region. In scenarios where the particle population that is being accelerated in the jet is dominated by electrons and positrons (*leptonic scenario*), the second hump can be explained as Inverse Compton scattering of electrons with the low-energy photon fields in the environment, which can get boosted up to gamma-ray energies. In the case where an hadronic population (protons and ions) starts to contribute significantly, the second peak can be explained as contribution of hadronic and leptonic models (*leptohadronic scenario*).

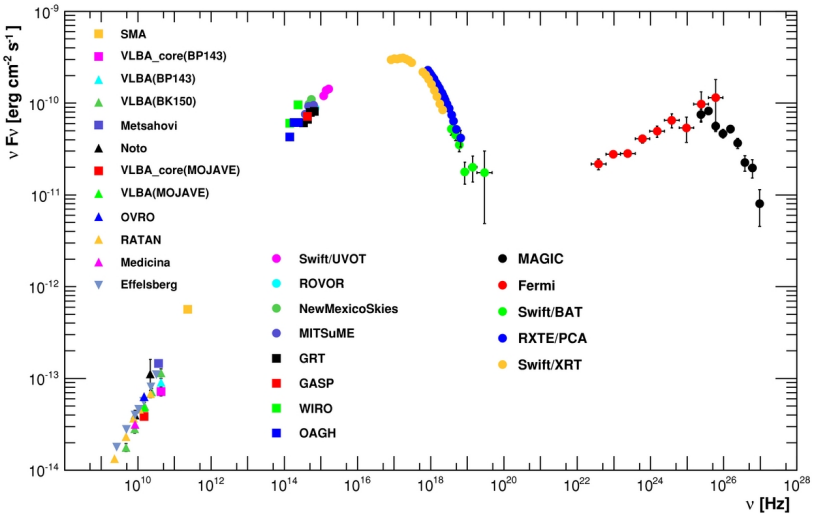

Figure 2.3: Spectral energy distribution of Mrk 421 from [59]. The legend shows the association between flux measurements and correspondent instrument.

As already mentioned in the previous section, blazars are classified in FSRQ and BL Lac objects based on the properties of their optical spectrum. FSRQs show lines with equivalent width > 5 Å in their optical spectrum. In BL Lacs, the spectrum is often featureless or shows only weak lines, with a consequent challenging estimation of the source redshift. According to observations from [60], bright BL Lac objects display weak and narrow Lyα lines, that might point to the fact that also BL Lacs have a NLR and BLR that are usually not seen in the spectra due to the dominance of the underlying nonthermal continuum [45]. Similar considerations have been made for the tentative identification of a sub-class of BL Lac objects called *masquerading BL Lacs* [61], which should group sources that are intrinsically FSRQs with hidden broad lines.
Another classification for blazars is based on the spectral localization of

[60]: Stocke et al. (2011), 'Broad Lyα Emission from Three Nearby BL Lacertae Objects'

[61]: Padovani et al. (2019), 'TXS 0506+056, the first cosmic neutrino source, is not a BL Lac'

the peak of their synchrotron emission ν^S_{peak}, and is outlined in [62]. It defines three classes based on the SED:

- *Low synchrotron peaked (LSP)*: $\nu^S_{peak} < 10^{14}$ Hz.
- *Intermediate synchrotron peaked (ISP)*: 10^{14} Hz $< \nu^S_{peak} < 10^{15}$ Hz.
- *High synchrotron peaked (HSP)*: $\nu^S_{peak} > 10^{15}$ Hz.

[62]: Abdo et al. (2010), 'The Spectral Energy Distribution of Fermi Bright Blazars'

Almost all gamma-ray detected FSRQ sources are LSP, with few ISP and HSP objects, while BL Lacs are observed evenly distributed in all 3 classes. From the study of this distribution of the observed peak frequencies in blazar SEDs, Fossati *et al.* [63] proposed the existence of an empirical relationship between the luminosity of blazars and the peak frequency ν^S_{peak} of their synchrotron spectrum (Figure 2.4). According to the sequence, sources with the highest luminosities tend to have the synchrotron peak ν^S_{peak} at the lowest frequencies (down to ~10^{12} Hz) and the corresponding peak of the Inverse Compton emission in the MeV band. With the decreasing of luminosity, ν^S_{peak} shifts to higher frequencies falling between the optical and X-ray range. This trend was confirmed by Ghisellini in 2017 [64] using the blazars detected in gamma rays by *Fermi*-LAT in 4 years of observations. Recently, the blazar sequence has been used as underlying hypothesis for the sources evolution in [65] to study the UHECR acceleration and neutrino emission in blazars, and a strong connection with objects at the extreme side of the sequence has been found. According to their results, low-luminosity BL Lacs of the HSP class tend to be good sites for UHECRs production, while FSRQs turn out to be more efficient neutrino emitters.

[63]: Fossati et al. (1998), 'A unifying view of the spectral energy distributions of blazars'

[64]: Ghisellini et al. (2017), 'The Fermi blazar sequence'

[65]: Rodrigues et al. (2018), 'Neutrinos and Ultra-high-energy Cosmic-ray Nuclei from Blazars'

In order to better understand the nature of blazars, it is necessary to focus on two key elements: the central black-hole and the relativistic jet. In the following sections, I will give a brief overview of some of their main properties, with a focus on those that will be relevant in the following chapters of this thesis.

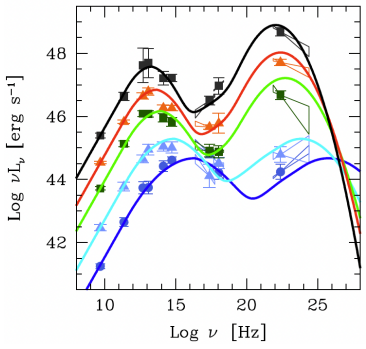

Figure 2.4: The original blazar sequence from [63, 64].

2.2.1 Black Holes: the central engine

Among the most fascinating objects in the universe, Black Holes were not the result of serendipitous discoveries but their existence has already been suggested in 1794, when John Mitchell discussed the possible existence of very massive objects whose gravity would be able to trap even the electromagnetic radiation. Pierre-Simon Laplace (independently in 1796) assumed this was possible for a particular category of objects that he named *dark stars* [45]. This concept was then rediscussed in 1916, when Karl Schwarzschild derived the solutions of Einstein's theory of General Relativity [66] for a point-source object of mass M. The solutions accounted for a spherical surface around the point-like object (black hole) that defined a distance at which the escape velocity from the gravitational field of the black hole is equal to the speed of light. This surface was named *event horizon* and its distance from the black hole in the middle is called *Schwarzschild radius* and depends on the black hole mass M_{BH} as

[45]: Beckmann et al. (2012), *Active Galactic Nuclei*

[66]: Einstein (1915), 'Die Feldgleichungen der Gravitation'

$$R_S = \frac{2GM_{BH}}{c^2} \tag{2.3}$$

where G is the gravitational constant and c the speed of light. A more general solution for the event horizon radius that extend to rotating black holes was found by Kerr in 1963 [67]

$$R_H = \frac{GM_{BH}}{c^2}\left(1+\sqrt{1-j^2}\right) \tag{2.4}$$

where j is the dimensionless spin of the black hole ($|j| < 1$), with a correspondent angular velocity of $\Omega_H = jc/2R_H$.
The first experimental evidences for the existence of black holes can be traced back to 1972, when the first source identified as a system containing a black hole was Cygnus X-1, a binary system formed by a ninth magnitude blue supergiant star and an invisible companion emitting in the X-rays, whose mass was estimated to be around 20 $M_\odot$[ii] [68, 69].
After these first experimental evidences, black holes have been observed over a wide range of masses, from values comparable to the solar mass (stellar-mass black holes) [70] up to supermassive black holes (SMBH) with masses from 10^6 to more than 10^9 $M_\odot$. This extremely massive category was thought to be responsible of the majority of the energy budget of AGN [71, 72], powered by the accretion of matter onto the central SMBH.
Although the exact nature of this accretion flow in the core of AGN is still matter of study, some basic dynamic and energetic considerations can be made on the accretion process in simple configurations. A first example is the so-called *Bondi-Hoyle* accretion [73], that considers an approximately spherically symmetric accretion flow onto the black hole, in terms of a uniform ambient wind. The accretion rate in this case would be

$$\dot{M} = \pi r^2 \rho v \tag{2.5}$$

where ρ and v are the density and velocity of the wind. The effective capture radius for accretion can be rewritten as the distance where the wind velocity is equal to the escape velocity from the black hole, and the accretion rate becomes

$$\dot{M} = \frac{4\pi\rho G^2 M_{BH}^2}{v^3}. \tag{2.6}$$

An important limit to the accretion onto a compact object was posed by Arthur Eddington, and is due to the effects of the radiation pressure experienced by the plasma falling onto the black hole, and depends to its mass and the mean opacity of the in-falling material. From the equation of the pressure gradient of the in-falling matter and the radiation pressure, it is easy to obtain the luminosity corresponding to the critical mass-accretion rate [45]

$$L_{Edd} = \frac{4\pi\rho G^2 M_{BH}^2 m_p c}{\sigma_T} \simeq 1.3\times10^{38}\frac{M_{BH}}{M_\odot}\,\mathrm{erg\,s^{-1}} \tag{2.7}$$

[67]: Kerr (1963), 'Gravitational Field of a Spinning Mass as an Example of Algebraically Special Metrics'

[68]: Bolton (1972), 'Identification of Cygnus X-1 with HDE 226868'
[69]: Webster et al. (1972), 'Cygnus X-1-a Spectroscopic Binary with a Heavy Companion ?'

[70]: Remillard et al. (2006), 'X-Ray Properties of Black-Hole Binaries'

[71]: Salpeter (1964), 'Accretion of Interstellar Matter by Massive Objects.'
[72]: Lynden-Bell (1969), 'Galactic Nuclei as Collapsed Old Quasars'

[73]: Bondi (1952), 'On spherically symmetrical accretion'

[ii] $M_\odot \simeq 2\times10^{30}$ kg is the mass of the Sun

where m_p is the proton mass (in the simplest case where the accreted matter is hydrogen) and σ_T is the *Thomson* cross-section[iii]. L_{Edd} is called *Eddington luminosity* and the *Eddington limit* is reached when the bolometric luminosity of the object (L_{bol}[iv]) is equal to L_{Edd}. In light of this limit, accretion rates are usually expressed in terms of normalised Eddington accretion rate

$$\dot{m} = \frac{\dot{M}}{\dot{M}_{Edd}}. \tag{2.8}$$

Bondi's accretion process is based on simple assumptions but turns out to be not efficient enough in the conversion from gravitational potential energy into radiative energy to explain the powering of AGN[45]. A more realistic geometry for the system formed by the accreted material would be more towards a flat-disk shape than a spherical distribution. The standard accretion disk model capable to explain the accretion process of very luminous AGN was introduced by Shakura and Sunyaev in 1973 [74], and consisted in a geometrically thin optically thick disk. The disk is formed by a series of rings, with radius between the inward and outward radii (r_{in} and r_{out}, respectively) of the distribution of accreted matter, and the viscous interactions between adjacent rings within the disk transfer angular momentum outwards, compensating for the loss of angular momentum due to matter falling onto the center (angular momentum transport) [45]. With this mechanism, gravitational potential energy is thus converted into thermal radiation that follows a black body spectrum of characteristic effective temperature

[74]: Shakura et al. (1973), 'Black holes in binary systems. Observational appearance.'

$$T_{eff}(r) = \left[\frac{3GM\dot{M}}{8\pi\sigma r^3}\left(1 - \sqrt{\frac{r_{in}}{r}}\right)\right]^{1/4} \tag{2.9}$$

where σ is the Stefan-Boltzmann constant. The disk surface is hotter in the inner regions where gravity is stronger, and for $r \gg r_{in}$ the temperature goes as $r^{-3/4}$. By deriving the total black body spectrum, for typical AGN parameters the emission from the inner part of the disk peaks at the frequency

$$\nu_{max} = \frac{2.82kT_{eff}}{h} \simeq 5.9 \times 10^{15}\left(\frac{T_{eff}[K]}{10^5}\right) \text{ Hz} \tag{2.10}$$

that explains the *big blue bump* feature observed in the optical/UV part of the Spectral Energy Distribution (SED). Among blazars, only FSRQs show the big blue bump feature.

As the Shakura-Sunyaev accretion disk model falls in the class of cooling-dominated flow, i.e. high density stream of gas in which the cooling time is much smaller than the inflow time [75], it is not applicable in systems with low accretion rate. In these systems, the densities can be so small that the cooling time scale becomes larger than the inflow time, corresponding to a geometrically thick, optically thin disk. This is the case of *radiatively inefficient accretion flows* (RIAF) where heating becomes dominant over cooling and most of the energy is stored in the flow and

[75]: Netzer (2013), *The Physics and Evolution of Active Galactic Nuclei*

[iii] $\sigma_T \simeq 6.65 \times 10^{-25}$ cm^{-2}

[iv] Bolometric luminosity: total energy radiated per second in the whole energy spectrum.

advected in the central object. A model consisting in a two-temperatures *advection dominated accretion flow* (ADAF) was introduced by Narayan and Yi in 1994 [76, 77]. In this model, the accretion rate is $\dot{m} \leq 0.05\text{-}0.1$ and together with the low particle density allows the Coulomb coupling between ions and electrons to break, with the viscous energy being mostly responsible for the ion heating. Typical temperatures reached by the ions are $\sim 10^{12}$K and are responsible for the pressure, while the electrons are typically at lower temperatures $\sim 10^{9}\text{-}10^{11}$K and are responsible for the majority of the radiation. The total luminosity of ADAF disks is lower than for Shakura-Sunyaev disks, with $L_{ADAF} \propto \dot{M}^2$ (instead of $\dot{M}$ as for the thin disk), and results in the description of the SED of AGN with low luminosity. In the next section I will show the role of accretion in the formation of relativistic jets in AGN.

[76]: Narayan et al. (1994), 'Advection-dominated Accretion: A Self-similar Solution'
[77]: Narayan et al. (1995), 'Advection-dominated Accretion: Underfed Black Holes and Neutron Stars'

Since no significant feature of thermal emission is observed in BL Lacs, there is a common agreement on the fact that the accretion regime in this class of objects is not radiatively efficient, and the disk should have a sub-Eddington luminosity $L_{disk} \leq 10^{-2}\text{-}10^{-3}\ L_{Edd}$, typical of the ADAF regime. A scarcity of ionizing UV photons in ADAF disks able to photo-ionize the clouds of gas of the BLR was also proposed to explain the lack of broad lines in the spectra of BL Lacs [78]. On the contrary, analysis of FSRQ observation from the optical to the X-ray band has shown that the accretion could occurs through a thin and hot accretion disc, surrounded by a hot thermal corona (typically emitting in the X-rays) and by the NLR and BLR.

[78]: MAGIC Collaboration et al. (2018), 'Detection of the blazar S4 0954+65 at very-high-energy with the MAGIC telescopes during an exceptionally high optical state'

After decades of observations of AGN at multiple wavelengths, the groundbreaking observations at the wavelength of 1.3 mm by the Event Horizon Telescope (EHT), a Very Long Baseline Interferometer (VLBI) global array of radio telescopes, provided the first image showing the structures around the SMBH candidate in the galaxy M87 at the scale of its event horizon [79] (See Figure 2.5). The image shows a ring structure with a diameter of 42 ± 3 μarcsec[v] with a central brightness depression (more than 10 times fainter) identified as the black hole shadow. The brightness of the ring is due to the emission of the plasma accreting close to the event horizon. The precision achieved with this imaging allowed to estimate a mass for the SMBH candidate M87* of $M_{BH} = (6.5 \pm 0.7) \times 10^9\ M_\odot$ [79].

[79]: Event Horizon Telescope Collaboration et al. (2019), 'First M87 Event Horizon Telescope Results. IV. Imaging the Central Supermassive Black Hole'

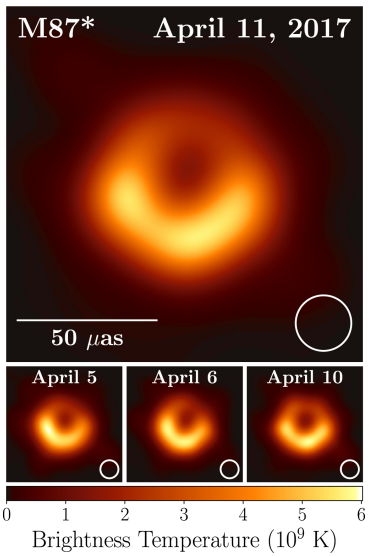

Figure 2.5: EHT image of M87* from observations collected in the 2017 campaign from [79].

[v] *arcsecond*, is a unit of angular measurement equal to 1/3600 of a degree.

2.2.2 Relativistic jets

A characteristic feature of blazars is given by the powerful jets aligned at very small angles towards the line of sight of the observer and originating from the region near the SMBH. These highly collimated outflows of plasma are observed in radio-loud AGN from scales comparable to distances in our solar system (≤ 1 AU[vi] to typical extensions of giant galaxies (≥ 1 Mpc).
In the previous section, I have described the role of the central SMBH in the formation of the accretion disk and some of the models for the structure and the mechanisms of this important power source for the AGN. There is a strong link between the accretion process of the central SMBH and the lunch of the relativistic jets, and the connection between the spinning black-hole, the accretion and the jet is still one of the main fields of study and is principally investigated through massive magneto-hydrodynamic simulations (MHD).

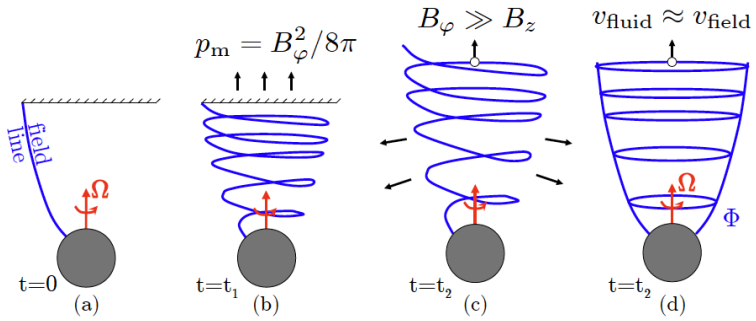

Figure 2.6: Illustration of jet formation by magnetic fields from [80].

[80]: Davis et al. (2020), 'Magnetohydrodynamics Simulations of Active Galactic Nucleus Disks and Jets'

An effective description of the jet formation principles is given in [80] and depicted in Figure 2.6. It assumes for simplicity a perfectly conducting spinning sphere (the SMBH in our case, but can be a neutron star or white dwarf in other systems), and models the ambient medium as a perfectly conducting *ceiling*. Picture *(a)* in Figure 2.6 shows a first magnetic field line connecting the sphere to the ceiling and shows the rotation axis of the sphere with angular frequency Ω. As the sphere rotates, it develops a number of toroidal loops forming a magnetic spring that pushes against the ceiling with an effective pressure

$$p_m \sim \frac{B_\phi^2}{8\pi} \tag{2.11}$$

generated by the toroidal magnetic field B_ϕ (Figure 2.6, *b*). As the magnetic field pressure p_m becomes stronger with the increasing of the toroidal field loops, at some point is able to push the ceiling away and accelerates the plasma along the rotation axis, forming a jet (Figure 2.6, *c*). Figure 2.6 (*d*) shows the final structure of the jet, that can be thought as a collection of toroidal field loops continuously generated by the reprocessing of vertical field lines from the rotating sphere and accelerate along the jet under the action of their own pressure gradient and tension. Even though a black hole does not have a physical surface, their spinning

[vi] Astronomical Unit (AU): is roughly the distance between Earth and Sun. 1AU = 1.5×10^8 km.

leads to the dragging of the inertial frames near the black hole, causing the magnetic field lines to rotate in a similar way to that described above in the toy model.
The formal mechanism behind this simplified representation was introduced by Blandford and Znajek (BZ mechanism) in 1977 [81], and has important implications on the disk-jet connection that links the accretion physics to the black hole magnetic flux Φ_{BH}. According to the famous *no hair theorem* the black hole can only have three hairs: mass, spin and charge [82], therefore the accretion disk is responsible for the magnetic field around the black hole. The pressure of the magnetic flux on the black hole is balanced by the pressure of the accretion flow, and thus a dimensionless black hole magnetic flux can be defined as function of the accretion rate. Such system is called *Magnetically arrested disk* (MAD) and defines a particular accretion state where the magnetic flux inside the disk is strong enough to balance the accretion flow. For systems like this, the jet luminosity produced by a spinning black hole (with spin j) can be written in function of the accretion rate $\dot{M}$ (see [80] for a more detailed overview)

[81]: Blandford et al. (1977), 'Electromagnetic extraction of energy from Kerr black holes.'

[82]: Misner et al. (1973), *Gravitation*

$$L_{BZ,j} = \eta_j \dot{M} c^2 \simeq 1.3 \times 10^{46} \eta_j \dot{m} \left(\frac{M_{BH}}{10^8 M_\odot} \right) \text{ erg s}^{-1} \tag{2.12}$$

where η_j is the jet efficiency, which ranges between $\eta_j \sim 0.3$ - 1 for MAD disks [83].
Thanks to the high resolution of single-dish radio telescopes of the *Very Long Baseline Arrays* (VLBA) we can resolve the relativistic plasma jets from μas to degree extensions. A characteristic signature is the presence of superluminal knots, that is areas of enhanced flux intensities within the jet mostly ascribed to the presence of shocks in the plasma outflow. The apparent superluminal motion measured for these components is an effect that was predicted already by Rees in 1966 [84] is based on a geometrical effect due to the angle between the jet and our line of sight θ_{obs} [85].
The combination of relativistic speeds and viewing angles θ_{obs} introduces relativistic beaming effects that have to be taken in account. Once defined the bulk Lorentz factor

[83]: McKinney et al. (2012), 'General relativistic magnetohydrodynamic simulations of magnetically choked accretion flows around black holes'

[84]: Rees (1966), 'Appearance of Relativistically Expanding Radio Sources'

[85]: Blandford et al. (1977), 'Superluminal expansion in extragalactic radio sources'

$$\Gamma_b = \frac{1}{\sqrt{1-\beta^2}} \tag{2.13}$$

where β is the jet velocity in units of the speed of light c, the energy of the radiation emitted from the region comoving with the jet will appear blue-shifted by the Doppler factor δ given by

$$\delta(\theta_{obs}) = \frac{1}{\Gamma_b(1-\beta cos\theta_{obs})}. \tag{2.14}$$

The Doppler boost is strongest for observations at small angles and weakens as the angle θ_{obs} increases. In the case of blazars and other sources where most of the emitted radiation is concentrated due to beaming, the opening angle of the jet can be approximated by $\theta_{obs} = 1/\Gamma_b \leq 5°$, for which $\delta \sim \Gamma_b$.
A recent remarkable result comes again from the 2017 campaign of the

EHT, where the prominent radio jet of the archetypal blazar 3C 279 was resolved with ultra-high angular resolution thanks to the VLBI technique [86]. Figure 2.7 shows the illustration of the 3C 279 jet structure observed during 3 days on April 2017 at the frequencies of 43 GHz, 86 GHz and 230 GHz. Two main components have been identified in the inner jet other than the central steady VLBI *core*, with non-radial apparent superluminal velocities of ~15 c and ~ 20 c that support the scenario of traveling shock region or instabilities in a bent, possibly rotating jet [86].

[86]: Kim et al. (2020), 'Event Horizon Telescope imaging of the archetypal blazar 3C 279 at an extreme 20 microarcsecond resolution'

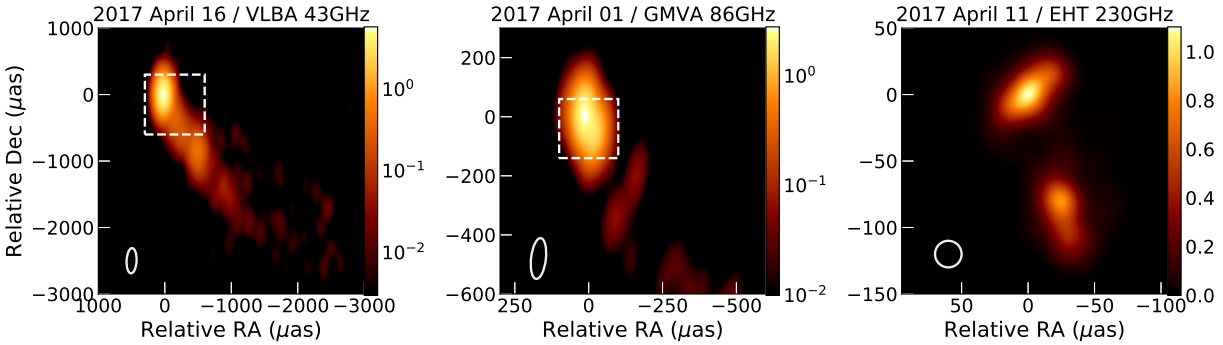

Figure 2.7: Multiwavelength image of the 3C 279 jet structure in April 2017 from [86]. The color bars show the pixel values in Jy/beam.

To account for other relativistic effects such as time dilatation, it is useful to derive some quantities in the comoving frame of the emitting source (primed quantities). An useful quantity is the comoving size of the blob, from which the blazar emission is radiated

$$R'_b = \frac{\delta c t_{var}}{1+z} \tag{2.15}$$

where t_{var} is the variability time scale, and the approximation $\delta \sim \Gamma_b$ valid for blazars can be used.

Particle acceleration in jets

An important aspect in relativistic jets is the mechanism of particle acceleration in their inner region. It is important to understand how particles are accelerated and how their are transported within the jet before they cool down, since the expected energies to be reached already for the lightest particles (electrons and positrons) in order to explain the observed X-ray and gamma-ray emissions can reach levels ≥ 100 TeV.
Particle acceleration in an electric field in the SMBH magnetosphere would be the first candidate, but energetics argument likely exclude this mechanism to be the one explaining the majority of observed jet power (see [87] and references therein).

[87]: Blandford et al. (2019), 'Relativistic Jets from Active Galactic Nuclei'

Diffusive Shock Acceleration

A first, more sophisticated mechanism often involved in relativistic jets is *diffusive shock acceleration*, that already efficiently explains particle accelerations in supernova remnants (SNR). Even in their most basic concept of planar shock, relatively small compression ratios would be able to explain most of the Synchrotron and Inverse Compton spectra observed in jetted sources. These shocks can powerfully accelerate up to high energies also because intense magnetic fields are created at the shock front by the accelerating particles, and the maximum acceleration energy should be just determined by the shock width or its radius of

curvature in the more realistic cases. A complication of this mechanism is that particles with the highest energies can escape upstream from a curved shock front, although most of them would lose energy during the shock region expansion and cooling by radiative processes[87].

Recent studies [88, 89] discuss the limitations of the shock acceleration, that may result not efficient in the magnetically dominated relativistic plasma of blazar jets. A second acceleration mechanism able to overcome these limitations and explain the broadband SED of blazars along with their rapid and strong variability is *magnetic reconnection*. This mechanism is based on compact magnetized structures, called plasmoids, that move at relativistic speeds with respect to the co-moving frame of the jet [90, 91]. These plasmoids can accelerate because of magnetic stresses, and the magnetic energy is transferred to the plasma and converted in kinetic energy. The idea of very compact structures like plasmoids in the jet comes from the observation of minute-scale variability in the gamma-ray emission of bright FSRQs (see [92] for a recent study) that would correspond to sizes emission region comparable or smaller than the Schwarzschild radius (R_S) of the SMBH, that gives an approximate size of the crossing-region size at the base of the jet. Results from the analytical model in [93] show that a jet collimated to the light-cylinder radius will start developing shock waves with a radius not smaller than 10 R_S.

A model of so-called *jet-in-jet* magnetic reconnection used in [94] to interpret some of the fast gamma-ray flares of the bright FSRQ 3C 279 is depicted in Figure 2.8. The inner jet of a blazar is divided in two parts, one believed to be magnetically dominated at distances < 0.1 pc (within the BLR radius) and one kinetically dominated (at d > 0.1 pc). At distances right outside the BLR, the helical magnetic field of the jet becomes unstable and tends to fragment into small plasmoids that interact by magnetic reconnection multiple times, creating reconnection chains that lead to bigger plasmoids (*monster plasmoids*). Subsequently, these massive plasmoids form mini-jets that are supposed to produce optically thin minute-scale gamma-ray flares. Shocks are then supposed to become dominant in the jet only at larger distances.

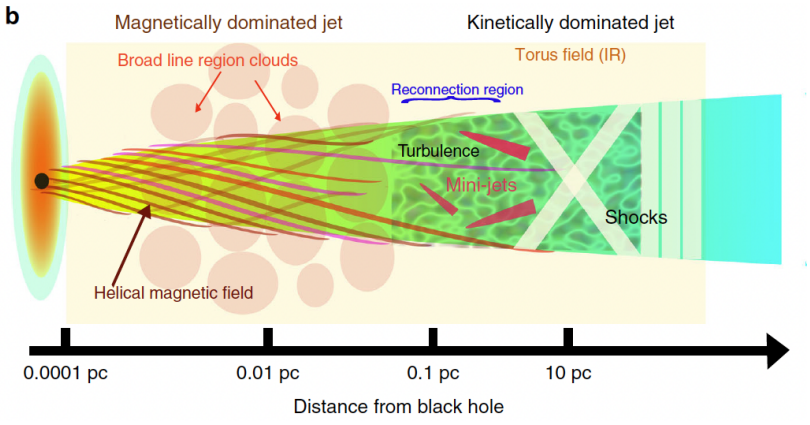

Figure 2.8: Sketch of the inner jet of a blazar from [94], explaining the fast minute-scale gamma-ray flares of 3C 273 with the jet-in-jet magnetic reconnection model.

Acceleration mechanisms in blazars jets are very challenging to be probed by experimental data, and represent one of the biggest open questions in the physics of the jets. Likely, different mechanisms act at the different temporal and spatial scales of jet dynamics and improvements in the observations will help disentangle the different contributions and finally probe the real mechanisms behind these powerful accelerations.

Magnetic Reconnection

[88]: Sironi et al. (2013), 'The Maximum Energy of Accelerated Particles in Relativistic Collisionless Shocks'

[89]: Bell et al. (2018), 'Cosmic-ray acceleration by relativistic shocks: limits and estimates'

[90]: Meyer et al. (2021), 'The Observability of Plasmoid-powered γ-Ray Flares with the Fermi Large Area Telescope'

[91]: Loureiro et al. (2012), 'Magnetic reconnection and stochastic plasmoid chains in high-Lundquist-number plasmas'

[92]: Meyer et al. (2019), 'Characterizing the Gamma-Ray Variability of the Brightest Flat Spectrum Radio Quasars Observed with the Fermi LAT'

[93]: Appl et al. (1993), 'The structure of relativistic MHD jets: a solution to the nonlinear Grad-Shafranov equation.'

[94]: Shukla et al. (2020), 'Gamma-ray flares from relativistic magnetic reconnection in the jet of the quasar 3C 279'

Leptonic radiative processes

As mentioned in Section 2.2, the mechanism responsible for the first hump of the observed SED in blazars is *synchrotron radiation* of non-thermal electrons. This process occurs in general when charged particles are accelerated in a magnetic field B′, and emit radiation while moving over a helical trajectory because of the Lorentz force perpendicular to the magnetic field direction (see scheme in Figure 2.10). For a population of electrons with number density N'_e with isotropic momentum distribution, in a region with magnetic field energy density of $U'_B = B'^2/8\pi$, the luminosity of the synchrotron radiation in the monochromatic approximation is given by [95]

[95]: Tavecchio et al. (2016), 'On the magnetization of BL Lac jets'

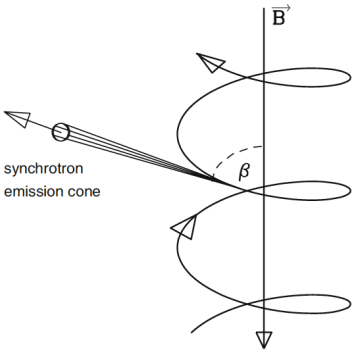

Figure 2.9: Schematic representation of synchtron emission of an electron with pitch angle β (angle between the particle and magnetic field directions) from [45].

$$L_\gamma^{syn}(\gamma'_e) = \frac{4}{3}\sigma_T c U'_B \gamma'_e V' N'_e \Gamma_b^4 \tag{2.16}$$

where V′ is the comoving volume of the emission region, σ_T is the Thomson cross-section and γ'_e is the electron's Lorentz factor in the comoving frame. The bulk Lorentz factor Γ_b is equal to the doppler factor and accounts for the relativistic boosting of the emission due to the beaming. Each electron emits a synchrotron spectrum that peaks at the energy measured in the observer's frame

$$E_{\gamma,max}^{syn} \sim 5\frac{\Gamma_b}{10}\frac{B'}{10G}\left(\frac{E'_e}{GeV}\right)^2 \text{ eV} \tag{2.17}$$

In the simple assumption of the electrons following a simple unbroken power-law distribution

$$n(E)dE = kE^{-p}dE \tag{2.18}$$

then the synchrotron spectrum in the radio band will be a power law with spectral index in the radio band α_R given by

$$\alpha_R = \frac{p-1}{2}. \tag{2.19}$$

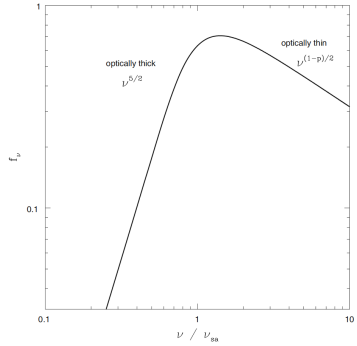

Figure 2.10: The synchrotron spectrum for an electron plasma within a uniform magnetic field as a function of frequency from [45]. The x-axis is in function of the synchrotron self-absorption frquency ν_{sa}.

In the case of FSRQs, where the radio continuum has a slope of $\alpha_R = 0.5$, the electron energy distribution satisfies $n(E) \propto E^{-2}$.
In a real-case scenario, however, the spectrum may show a spectral break at a certain frequency ν_a due to the absorption within the plasma of the compact emitting region. This effect is called *synchrotron self-absorption* and causes a break in the spectrum at the frequency ν_{sa} that is a function of the magnetic field strength, the observed flux at the break frequency ν_{sa} and the observed angular size of the emitting region [45]. Below this frequency, the spectrum follows a power-law shape of $\nu^{5/2}$, independently from the spectral shape of the electron distribution. Figure 2.10 shows the synchrotron spectrum for an electron plasma within a uniform magnetic field. The spectral transition between α_R = -5/2 to α_R = (p - 1)/2 can be physically interpreted as the transition from a range of frequencies where the source is optically thick to synchrotron radiation to a range where is optically thin.
A peculiar property of the synchrotron radiation is its polarization. The

degree of polarization depends on the ratio between the power per unit frequency emitted in the directions parallel and perpendicular to the projection of the magnetic field on the plane of the sky

$$\Pi = \frac{L_{\perp(\nu)} - L_{\parallel(\nu)}}{L_{\perp(\nu)} + L_{\parallel(\nu)}} = \frac{p+1}{p+7/3} \tag{2.20}$$

where the last term of the equations shows the empirical dependence from the power-law spectral index p of the energy distribution of the electrons [45].
In the pure leptonic scenario for the composition of the particle population accelerated in the blazar jet, the second hump of the broadband SED can be explained by the up-scattering of low-energy photons by the relativistic electrons. This process is called *Inverse Compton* (IC) and can bust photons in the radio and infrared band to X-ray or gamma-ray energies. If the relativistic charged particles have a Lorentz factor γ, a photon of energy E_1 can be up-scattered to a higher energy $E_2 \simeq \gamma^2 E_1$. In more general terms, for a photon field with energy density U_{ph} the luminosity of IC radiation is [45]

$$L_{IC} \propto \gamma^2 U'_{ph}. \tag{2.21}$$

A common scenario considered for blazars is when the synchrotron radiation produced by the population of relativistic electrons is upscattered by the same electrons via IC. This is called *synchrotron self-Compton* (SSC) process. A useful quantity used to estimate the ratio between the energy densities of electrons and magnetic field in SSC models is the so called *Compton dominance*, given by the ratio of the IC and synchrotron luminosities

$$\frac{L_{SSC}}{L_{syn}} = \frac{U_{rad}}{U_B}. \tag{2.22}$$

The Compton dominance is a redshift-independent quantity useful to interpret, among other things, the nature of blazar classes in light of the blazar sequence. This was interpreted as a sequence of radiative cooling within the blazar class [96] with the underlying concept that the acceleration of electrons at the highest energies becomes more inefficient as the radiative cooling processes (Synchrotron, Inverse Compton) become more severe. According to this picture, the presence of BLR and the dust torus is an essential source of seed photon fields (external Compton, EC). In these environments, the IC process becomes dominant with respect to the Synchrotron emission, and therefore they show a large Compton dominance. The high-energy peak of these objects is in the MeV band, while the Synchrotron peak falls in the sub-mm band. In BL Lacs, where the radiative cooling is less severe due to the scarcity of external fields, only the SSC process contributes to the high-energy emission, and therefore they show lower Compton dominance. The electrons can achieve SEDs peaking at higher energies, with the Synchrotron peak showing up in the UV to X-ray band and the high-energy peak in the GeV-TeV band.

[96]: Ghisellini et al. (1998), 'A theoretical unifying scheme for gamma-ray bright blazars'

Interaction with the Extragalactic Background Light: the gamma-ray horizon.

Gamma-rays are not traveling from the source to Earth undisturbed. To a certain degree, the Universe is opaque to gamma-rays but it was possible to study this effect only after a large population of distant blazars was observed at high-energies. The dominant process for the absorption of gamma-rays at very-high energies (VHE) consists in the interaction with the lower-energy photons of the *extragalactic background light* (EBL) [97]

[97]: Spurio (2015), *Particles and Astrophysics*

$$\gamma_E + \gamma_\epsilon \rightarrow e^+ \; e^- \tag{2.23}$$

where E is the energy of the VHE gamma-ray and ϵ the one of the EBL photon, that can span from energies from far-infrared to near-ultraviolet bands ($\sim 10^{-3}$ eV to 10 eV). The EBL is a diffuse photon field made of light emitted by stars, galaxies and hot dust across the cosmological time, with spectral emission modified by the redshift due to the expansion of the universe. From the mid-IR to sub-millimetric wavelengths, it consists of re-emitted light from dust particles, and its spectrum shows as well continuum thermal radiation and emission from molecules. From near-IR to UV most of the EBL is due to direct light emission from stars, with a subdominant contribution from AGN.
The cross-section for the pair-production process is described by the Bethe-Heitler formula

$$\sigma(E, \epsilon) \simeq 1.25 \times 10^{-25} (1 - \zeta^2) \text{ cm}^2 \tag{2.24}$$

where $\zeta = \sqrt{1 - \frac{(m_e c^2)^2}{E\epsilon}}$ and the maximum cross-section at

$$\epsilon = 2\frac{(m_e c^2)^2}{E} \simeq \frac{520 GeV}{E} \text{eV} \tag{2.25}$$

and a threshold for the process at $E_{th} \sim \epsilon/2$.
The measurement of the EBL energy density is a challenging task in astrophysics, due to several contaminations from nearby object to this diffuse emission. Several models have been developed in the last decade and, because of the different results obtained by various approaches, a common agreement on the EBL spectrum is still far to be reached (see [98–100] for some recent results).

[98]: Finke et al. (2010), 'Modeling the Extragalactic Background Light from Stars and Dust'
[99]: Dominguez et al. (2011), 'Extragalactic background light inferred from AEGIS galaxy-SED-type fractions'
[100]: Gilmore et al. (2012), 'Semi-analytic modelling of the extragalactic background light and consequences for extragalactic gamma-ray spectra'

An important quantity that can be calculated from EBL models is the *optical depth* $\tau_{\gamma\gamma}(E, z)$ for a photon of energy E emitted by a source at redshift z. It is a dimensionless quantity that can be used to estimate the survival probability for the photon or, equivalently, as attenuation factor of the source flux at the observer with the expression

$$I(E, z) = I_0 e^{-\tau_{\gamma\gamma}(E,z)} \tag{2.26}$$

where I_0 it the flux at source. Figure 2.11 shows the mean free path (expressed in Mpc) of photons for EBL absorption, as function of the energy. It can be noticed how the so called *gamma-ray horizon* gets closer to the observer as the energy of the photon increases. Gamma-rays from galactic sources (e.g. the Galactic Center at $\sim$ 8.5 kpc) start to be

significantly attenuated at energies ~ 100 TeV, while emission from the nearby universe (≤ 10 Mpc) starts to be attenuated already above ~ 10 TeV.

EBL absorption poses important limitation to gamma-ray astronomy, in particular for the highest energies covered by *Fermi*-LAT and for the Imaging Atmospheric Cherenkov Telescopes (IACT). However, the imprint given from EBL absorption to the spectra of distant sources is used as a tool to study the properties of the EBL itself. A recent example is a study from the *Fermi*-LAT collaboration [] where with the large sample of detected blazars it was possible to reconstruct the EBL evolution and the determine the star-formation history of the Universe up to a redshift of z = 3.1 . Other recent works from gamma-ray observatories were published by HESS [101], MAGIC [102], VERITAS [103].

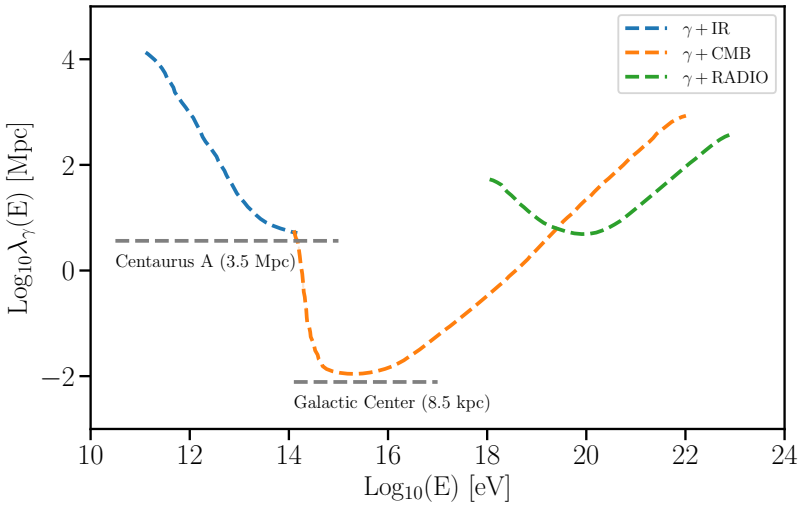

[101]: H. E. S. S. Collaboration et al. (2017), 'Measurement of the EBL spectral energy distribution using the VHE gamma-ray spectra of H.E.S.S. blazars'

[102]: Acciari et al. (2019), 'Measurement of the extragalactic background light using MAGIC and Fermi-LAT gamma-ray observations of blazars up to z = 1'

[103]: Abeysekara et al. (2019), 'Measurement of the Extragalactic Background Light Spectral Energy Distribution with VERITAS'

Figure 2.11: Mean free path (in Mpc) as a function of the photon energy (eV) adapted from [97]. Three backround photon field are considered: infrared (IR), cosmic microwave background (CMB) and radio.

2.3 High-energy neutrino production in Blazars

The production of neutrinos would necessarily require radiative processes that involve populations of accelerated hadronic particles. In this case, high-energy neutrinos and gamma rays are mainly produced in the decay of the charged and neutral pions, and therefore their simultaneous observation could represent a signature of CR acceleration in the source. A first class of hadronic interactions is the *astrophysical beam dump*, namely inelastic proton-proton collisions with the surrounding gas, that have mesons and barions as products [97]

[97]: Spurio (2015), *Particles and Astrophysics*

$$p + p \rightarrow \pi^{\pm}\ ,\ \pi^{0}\ ,\ K^{\pm}\ ,\ K^{0}\ ,\ p\ ,\ n\ ,\ \ldots \tag{2.27}$$

A second class of processes is defined by leptohadronic interactions. Leptohadronic interactions of high-energy protons with soft target photons in the environment happen through the intermediate production of Δ^+ resonance that can decay in two main different ways according to the branching ratios[vii] (BR).

$$p + \gamma \rightarrow \Delta^{+} \rightarrow p\pi^{0}\ \ (BR = 1/3) \tag{2.28}$$

Neutral pions (π^0) are produced with a BR of 1/3 and decay in two gamma rays ($\pi^0 \rightarrow \gamma\gamma$) with a lifetime of $\tau_{\pi^0} = (8.52 \pm 0.18)\times10^{-17}$ s, and the . This channels doesn't produce neutrinos but is important for the contribution to the gamma-ray emission observed in the SED.
The channel of interest for high-energy neutrino production is the Δ^+ decay in charged pions(π^+)

$$p + \gamma \rightarrow \Delta^{+} \rightarrow n\pi^{+}\ \ (BR = 2/3). \tag{2.29}$$

The charged pion decays with a mean life of $\tau_{\pi^+} = (2.6033 \pm 0.0005)\times10^{-8}$ s as

$$\pi^{+} \rightarrow \mu^{+}\nu_{\mu} \rightarrow e^{+}\nu_{e}\overline{\nu}_{\mu}\nu_{\mu}. \tag{2.30}$$

The threshold energy for this $p\gamma$ interaction can be calculated from the Lorentz-invariant square of the center-of-momentum energy of the interaction (s) [104]

[104]: Murase et al. (2022), 'High-Energy Neutrinos from Active Galactic Nuclei'

$$s = m_p^2c^4 + 2m_pc^2\overline{\epsilon}_{th} = (m_p + m_\pi)^2c^4 \tag{2.31}$$

where m_p and m_π are the proton and pion mass, respectively. The resulting energy threshold for the process is $\overline{\epsilon} \simeq 0.145$ GeV.
The fraction of the proton energy taken by the pion in both channels is ~20% (f_π, inelasticity). The energy of the charged pion is shared almost equally among the four light products (Eq. 2.30), and therefore the average neutrino energy is ~5% that of the parent proton. The two gamma-rays produced by the π^0 decay have instead 10% of the initial proton energy. The energy ratio between gamma-rays and neutrinos from

[vii] Branching ratio: is the fraction of time a particle decays to a particular final state.

this process is therefore $E_\gamma \sim 2E_\nu$.
Depending on environment crossed by the emission region, the gamma-rays produced via π^0 may re-interact with lower-energy photon fields through photon annihilation and produce electron-positron pairs ($\gamma\gamma \rightarrow e^+e^-$ with a threshold equal to twice the electron mass ($\sim$ 1 MeV). Electrons and positrons produced in these photon annihilations will eventually start electromagnetic cascades, and, while accelerated, also cool down via synchrotron radiation and IC scattering. The result is that the initial energy budget for gamma-rays produced in the π^0 decay that would be expected to contribute in the GeV-TeV gamma-ray band will be re-distributed to energy below the MeV. This effect can be even more incisive in sources with external photon fields (e.g. BLR in FSRQs) where gamma-rays $\geq$ GeV can be strongly suppressed. In optically-thick environments where high neutrino production efficiency is required, it might happen that the GeV band covered by *Fermi*-LAT might not be ideal to identify simultaneous signatures of enhancement in the gamma-ray emission, and X-Ray/MeV observations could provide better constraints to models [105].

[105]: Rodrigues et al. (2019), 'Lepto-hadronic Blazar Models Applied to the 2014-2015 Flare of TXS 0506+056'

Another interaction channel of high-energy protons with the environment radiation is the photo-production of electron-positron pairs

Bethe-Heitler pair production

$$p + \gamma \rightarrow p\ e^+\ e^- \tag{2.32}$$

and is called *Bethe-Heitler* pair production and needs a center-of-mass threshold energy of only $2m_e \simeq 1$ MeV. This is a smaller threshold compared to the ~150 MeV needed for photo-meson production, and it has also a higher cross-section. This process can therefore become the dominant cooling process for protons below the photo-meson production threshold [106].

[106]: Rodrigues (2019), 'Blazars as Sources of Neutrinos and Ultra-high-energy Cosmic Rays'

A class of hadronic models that does not require the interaction with photon fields is the *proton-synchrotron* discussed in [107]. Compared to the synchrotron radiation from electrons, if we consider populations accelerated at he same energies, tthe proton-synchrotron radiation will peak at energies lower by a factor $(m_e/m_p)^3 \sim 5{\times}10^9$. This process therefore requires much stronger (> 10×) magnetic fields compared to the values commonly adopted in pure leptonic models, and challenges the energy budget estimations derived from multi-wavelength observations of blazar jets, as shown in a recent study [108] on gamma-ray detected blazars.

Proton-synchrotron

[107]: Mücke et al. (2001), 'A proton synchrotron blazar model for flaring in Markarian 501'

[108]: Liodakis et al. (2020), 'Proton Synchrotron Gamma-Rays and the Energy Crisis in Blazars'

Figure 2.12 shows the processes described above as single components of a broadband SED and the correspondent neutrino spectrum.

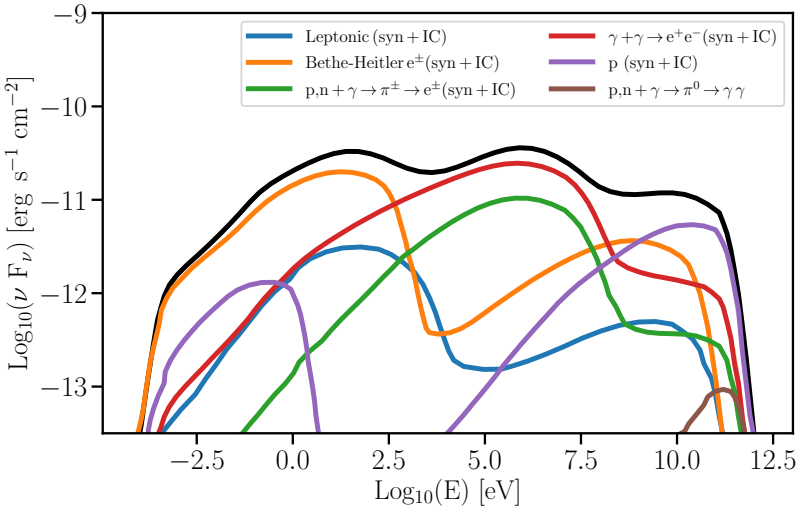

Figure 2.12: Broadband SED in lepto-hadronic scenario with contributions from the single processes adapted from [106].

2.4 Diffuse neutrino emission from blazars

Blazars are among the brightest sources in the gamma-ray sky and, as I will show in Chapter 3, constitute the majority of the extra-galactic objects detected by *Fermi*-LAT. The emission from resolved and unresolved blazars contribute to most of the *extragalactic gamma-ray background* (EGB) in the GeV-TeV range, with a contribution of 50% only from resolved sources [109]. The rest of the emission from unresolved sources is often referred as *isotropic gamma-ray background* (IGRB) and its composition is believed to be dominated by the contribution of FSRQs, BL Lacs, misaligned AGN and star-forming galaxies [110].
This blazar dominance over the EGB in the GeV-TeV band might link to a dominant contribution from blazars also in the neutrino sky. As shown in the overview of radiative processes, high-energy neutrinos are produced in lepto-hadronic models, where the gamma-rays are produced in either in leptonic and hadronic processes. The efficiency of photomeson production differs in FSRQs and BL Lacs, since the former possess the external fields provided by the BLR and the dusty torus, while the principal photon field in BL Lacs is is the synchrotron radiation emitted by the ultra-relativistic population of electrons. This leads to global picture that someway follows the correlation observed for the blazar sequence, and sources with higher luminosity are those where the photomeson efficiency is higher. This correlation is expressed in [111] as

$$L_\nu \propto L_\gamma^{\gamma_{LW}} \tag{2.33}$$

where γ_{LW} is the luminosity-weighting index, that has different expected values depending on the source class considered [111–114]. I will discuss and test this relation in Chapter 9 on the population of candidate high-energy neutrino blazars observed so far.
An estimation of the blazar contribution to the all-sky neutrino intensity given in [113], shows that a blazar-dominated scenario could in principle saturate the observed level of diffuse neutrino flux. The majority of the contribution would come from FSRQs, assuming a fixed level of

[109]: Ajello et al. (2015), 'The Origin of the Extragalactic Gamma-Ray Background and Implications for Dark Matter Annihilation'
[110]: Di Mauro et al. (2015), 'Composition of the Fermi-LAT isotropic gamma-ray background intensity: Emission from extragalactic point sources and dark matter annihilations'
[111]: Murase et al. (2016), 'Constraining high-energy cosmic neutrino sources: Implications and prospects'
[112]: Tavecchio et al. (2015), 'High-energy cosmic neutrinos from spine-sheath BL Lac jets'
[113]: Murase et al. (2014), 'Diffuse neutrino intensity from the inner jets of active galactic nuclei: Impacts of external photon fields and the blazar sequence'
[114]: Petropoulou et al. (2015), 'Photo-hadronic origin of γ -ray BL Lac emission: implications for IceCube neutrinos'
[113]: Murase et al. (2014), 'Diffuse neutrino intensity from the inner jets of active galactic nuclei: Impacts of external photon fields and the blazar sequence'

cosmic-ray loading factor ξ_{cr}, defined as the ratio between the isotropic-equivalent cosmic-ray luminosity L_{cr} and the bolometric non-thermal luminosity from the jet L_{rad}

$$\xi_{cr} = \frac{L_{cr}}{L_{rad}}. \tag{2.34}$$

The assumption of constant cosmic-ray loading is reasonable if its considered that all blazar have the same acceleration mechanism. The blazar contribution is however unlikely to be dominant to the diffuse neutrino flux for three main constraints (See [104] and references therein):

[104]: Murase et al. (2022), 'High-Energy Neutrinos from Active Galactic Nuclei'

1. The first constraint comes from the IceCube limits placed in the analysis of the extremely high-energy (EHE) neutrinos sample [115]. These limits exclude models that interpret the EGB as the result of proton-induced cascade emission, with the direct consequence that hadronic processes in blazars might not be the dominant emission mechanism or limited to only a subsample of the blazar population. In addition, blazar models predict hard neutrino spectra that are not consistent with the limits, and therefore blazar models cannot describe properly neutrino data in the 10-100 TeV range.
2. Stacking limits on the contribution from gamma-ray detected blazars reported from the IceCube Collaboration pose the second limit for the blazar population. The limits were calculated using the second *Fermi*-LAT Catalog of AGN (2LAC) [116] and limited the contribution of gamma-ray detected blazars to < 27% of the diffuse neutrino flux from 10 TeV to 2 PeV, assuming a single power-law spectrum with index -2.5. Recent studies in [117] extended the sample to unresolved blazar sources and found similar results.
3. The last constraint comes from the lack of multiplet neutrino sources in IceCube data, and places strong limits on the local density of sources (See [111] for a detailed discussion).

[115]: Aartsen et al. (2018), 'Differential limit on the extremely-high-energy cosmic neutrino flux in the presence of astrophysical background from nine years of IceCube data'

[116]: Aartsen et al. (2017), 'The contribution of Fermi-2LAC blazars to the diffuse TeV-PeV neutrino flux'

[117]: Yuan et al. (2020), 'Complementarity of Stacking and Multiplet Constraints on the Blazar Contribution to the Cumulative High-energy Neutrino Intensity'

These three constraints indicate that the astrophysical diffuse neutrino flux cannot be explained by the sole contribution of the blazar population, that is limited to a fraction up to $\leq 30\%$ of the total flux. These limits are quite solid in the range of medium-energy neutrinos (10 - 100 TeV) but can be relaxed to a larger contribution ($\leq 50\%$) in the PeV range, either considering an harder spectral index for the neutrino spectrum or by considering the sub-sample of high-luminosity FSRQs. As shown in [116], when this sample of FSRQs is considered, the multiplet constraints can be significantly weakened and can contribute to a larger fraction of the neutrino flux.

Gamma-ray and Neutrino Astronomy

The *Fermi* Large Area Telescope

3

3.1 The Large Area Telescope detectors 33

3.2 LAT performance and survey strategy 37

3.3 The likelihood approach in LAT data analysis . . . 43

3.4 *Fermi*-LAT gamma-ray catalogs 46

3.5 Data analysis with *Fermi*-LAT data 50

The Large Area Telescope (LAT) is the main instrument on board of the *Fermi* satellite. Formerly named *Gamma-ray Large Area Space Telescope* (GLAST), it was launched by NASA on 2008, June 11 and then renamed as *Fermi*. The mission follows the successful exploration of the gamma-ray sky by the EGRET instrument [118] on board of the *Compton Gamma-Ray Observatory* (CGRO), which performed the first all-sky survey above 50 MeV and outstanding observations of several astrophysical gamma-ray sources, e.g. blazars, pulsars and high-energy solar flares. Going further back in time, the first observations of the gamma-ray sky from space started already in 1968 with the *Explorer XI* mission, with the first 22 photons detected above 50 MeV [119]. Only 7 years later, the *Third Orbiting Solar Observatory* (OSO-3) detected 621 photons in the same energy range, obtaining the first evidence of a gamma-ray diffuse background emission [120]. The first dedicated gamma-ray mission was the *Second Small Astronomy Satellite* (SAS-2) launched in 1972 [121], followed by the *Cos-B* mission [122], that conducted the first dedicated observations of gamma-ray point sources such as the Geminga pulsar.
Along with the LAT, the *Fermi* satellite hosts the Gamma-ray Burst Monitor (GBM), devoted to the spectral and temporal analysis of Gamma-Ray Bursts (GRBs), covering the low-energy range from 8 keV up to 40 MeV [123]. At the time of this dissertation, the LAT is observing the gamma-ray sky and delivering data after more than 13 years of operations, and still represents the only operative instrument capable of covering the energy range from 20 MeV to more than 300 GeV with high sensitivity and exceptional performance in resolving the gamma-ray sky.
In this chapter, I present the the main instrument that provided the data for the works presented in this thesis. I will start by describing the detector in Sec.3.1, and its performance in Sec. 3.2. In Sec. 3.3.1, I will describe the likelihood approach used to analyse photon data, along with a typical analysis configuration.

[120]: Kraushaar et al. (1972), 'High-Energy Cosmic Gamma-Ray Observations from the OSO-3 Satellite'

[121]: Fichtel et al. (1975), 'High-energy gamma-ray results from the second Small Astronomy Satellite.'

[122]: Scarsi et al. (1977), 'The Cos-B Experiment and Mission'

[123]: Meegan et al. (2009), 'The Fermi Gamma-ray Burst Monitor'

3.1 The Large Area Telescope detectors

The core mechanism for the gamma-ray detection at the energies covered by the LAT is the conversion of the gamma rays into e^+e^- pairs from the interaction with a high-Z material. In this process, the energy transferred to the e^+e^- pair is

$$E_p = E_\gamma - 2m_e c^2 \tag{3.1}$$

and from the reconstruction of the development of the e^+e^- pair, it is possible to trace back the original direction of the primary gamma ray. The detector schematics of the LAT is designed to exploit this detection mechanism maximizing the efficiency obtainable with the limitations of a space-based detector.
The detector structure consists of a 4×4 array of converting-tracking

modules followed by a calorimeter at the bottom and with a segmented shield of plastic scintillators surrounding the whole structure to serve as anti-coincidence detector (ACD). The data acquisition system (DAQ) uses prompt signals available from all the sub-detectors to form a trigger. An exploded schematics of the whole detector is shown in Fig. 3.1.

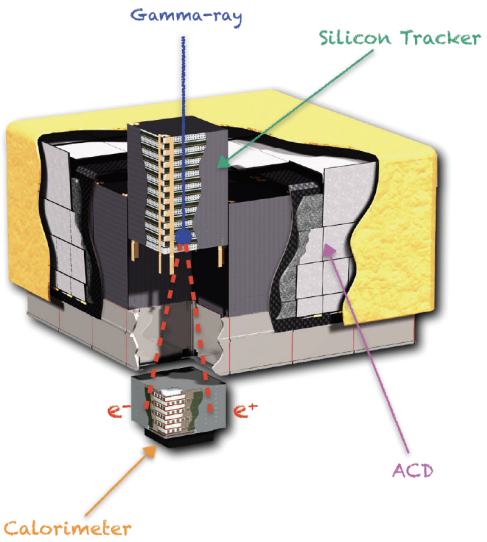

Figure 3.1: Schematic view of the *Fermi*-LAT with its main components. An exploded view of one of the 16 towers is shown with an artistic impression of a gamma ray interacting in the Silicon-tracker volume and producing an electron-positon pair that gets absorbed in the calorimeter.

3.1.1 The precision converter-tracker

The converter-tracker module consists of 18 tracking planes, each one made of 2 layers arranged orthogonally (to measure the x and y coordinates of the interaction points) of single-sided Silicon Strip Detectors (SSDs). Each single-sided SSD is Alternating Coupling (AC)-coupled, with 384 56-μm wide aluminium readout strips spaced at 228 μm pitch (distance between the centers of adjacent strips). The 16 layers at the top of the tracker module are interleaved with Tungsten (W) foils that, with its high atomic number ($Z = 74$), increases drastically the conversion efficiency of gamma rays into e^+e^- pairs compared to the sole Silicon (Si) structure ($Z = 14$).
After the pair conversion, that mostly happens inside the W foils, the signature of the two charged particles is recorded by the SSDs and allows to reconstruct the direction of the incident gamma ray. This peculiar signature is also fundamental for the rejection of the large background of charged cosmic rays. A major limit in the resolution of the direction of the incident photon is due to multiple scattering of e^+ and e^- and bremsstrahlung radiation. In order to minimize these effects, the SSDs are held close to the converter foils, minimizing the inactive regions and the presence of any passive material. Optimal results are indeed obtained when the e^+ and e^- directions are measured immediately after the conversion. At energies around 100 MeV, missing one of the first hits results in a penalty of a factor two in resolution, resulting in large tails of the probability distribution for the reconstructed direction (Point Spread Function, PSF). In order to minimize missing hits in the first layer following a conversion vertex, the Tungsten foils only cover the active areas of SSDs.
The use of thin converters is motivated by the need of preserving the PSF

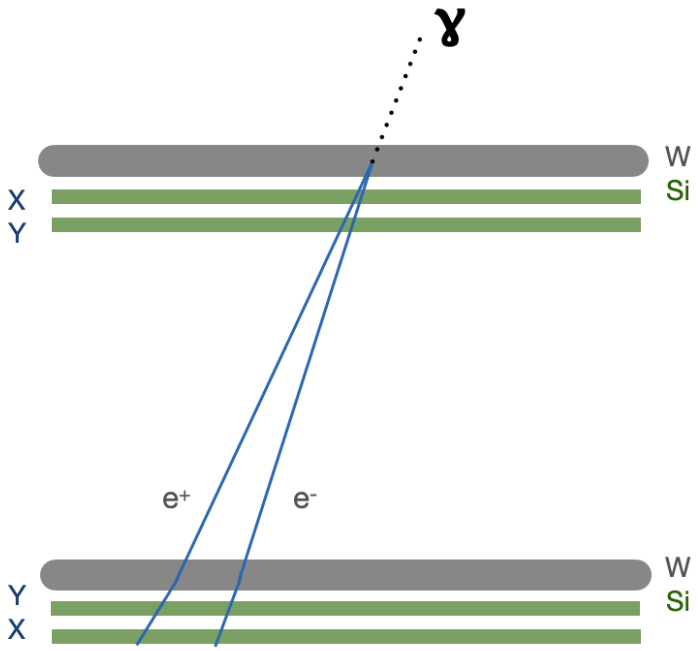

Figure 3.2: Illustration of the LAT tracker design principles. The sketch shows the ideal conversion in Tungsten foil with detection already happening in the first Si layer, that minimizes the path for multiple scattering, whose effect on the reconstructed direction is shown after the passage of the charged particles in the second *W* foil.

quality but at the same time this would affect the detector effective area at high energies. As a trade-off between these two factors, the LAT tracker has been divided into 2 regions, namely *front* and *back*. The front region, that includes the first 12 tracking planes, has thin converters of 0.03 X_0[i] each, while the subsequent 4 planes (back region) have converters about 6 times thicker, to maximize the effective area, with a factor two penalty in the angular resolution at 1 GeV for photons that convert in this region. A schematic view of the LAT Silicon tracker is shown in Fig. 3.2.

3.1.2 Calorimeter

The calorimeter module on board of the LAT is composed of 96 CsI(Tl) crystals of size 2.7 cm × 2.0 cm × 32.6 cm. These crystals are arranged in an hodoscopic structure (with each layer aligned 90° with respect to its neighbors) of 8 layers with 12 crystals each.
The hodoscopic structure enables the imaging capabilities of the calorimeter, allowing to obtain the shower development profile in the (x,z) and (y,z) planes, and thereby providing an important feature for background rejection and an estimator for the energy leakage of the shower produced by the interaction of the charged particles in the scintillator crystals. The total depth of the calorimeter structure corresponds to 8.6 X_0 (over a total instrument radiation length of 10.1 X_0). The section of each crystal is comparable to the CsI radiation length $X_{0,CsI} = 1.86$ cm and Molière radius[ii] for electromagnetic showers $R_{M,CsI} = 3.8$ cm.

[i] *Radiation length* (X_0): for high-energy photons, it is defined as $\frac{7}{9}$ of the mean free path for pair production. For high-energy electrons, it is the mean distance over which a particle looses all but $1/e$ of it energy by bremsstrahlung radiation. It is measured in g cm^{-}2.
[ii] *Molière radius* (R_M): measure of the lateral development of an electromagnetic shower in a specific material. On average, only 10% of the shower energy is deposited outside the

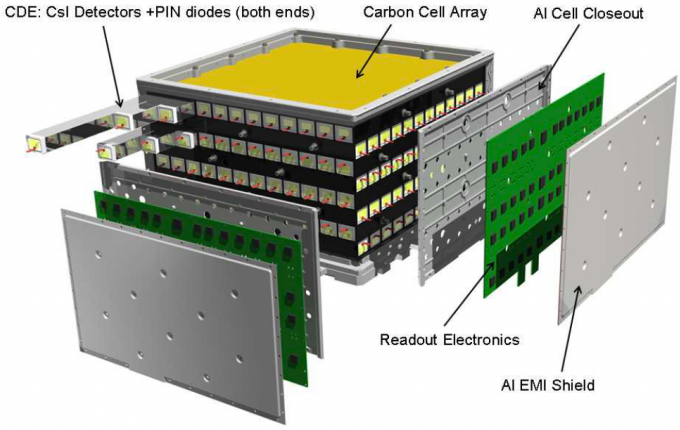

Figure 3.3: Illustration of LAT calorimeter module from [124]. The 96 CsI(Tl) scintillator crystal detector elements compose the core structure and are arranged in 8 layers of 12 bars each. Crystals in adjacent layers are hodoscopically arranged to measure x and y in alternate layers. The readout electronics is placed in side cells to be directly connected to both ends of each scintillator bar. The calorimeter has a total depth of 8.6 X_0, at normal incidence.

From the readout of the light yielded in each crystal, one spatial coordinate is derived from the asymmetry of the continuous profile of the light from the two opposite ends of the crystal (along its longest dimension) in addition to the two spatial coordinates from the location of the crystal in the module. The position resolution achieved with this double readout system at the ends of each crystal scales with the deposited energy and varies from few mm for depositions at ~10 MeV to a fraction of a mm for depositions >1 GeV. The end-to-end readout technique and the segmentation of the calorimeter allow to reach a great resolution of the development of the particle showers and the energy measurements up to few TeV.
A schematics of the module is shown in Fig. 3.3. Further details can be found in [124].

[124]: Atwood et al. (2009), 'The Large Area Telescope on the Fermi Gamma-Ray Space Telescope Mission'

3.1.3 Anticoincidence detector (ACD)

The *ACD* is designed as veto detector to reject charged cosmic-rays particles and has a segmented structure for a total of 89 plastic scintillator tiles arranged in a 5×5 array on the top and 16 tiles on each of the 4 sides of the LAT. The tiles overlap in one dimension to minimize gaps. The remaining gaps are covered with 2 sets of 4 scintillating fiber ribbons. A schematics of the LAT ACD is shown in Fig. 3.4.
The efficiency for each scintillator tile for detecting a Minimum Ionizing Particle (MIP) is >0.9997, that is fundamental to achieve the required cosmic-ray rejection efficiency of 0.99999 when combined with the other subsystems. Measured in radiation lengths, its total thickness is 0.06 X_0, and includes the thickness of a low-mass shield (0.39 g cm^{-2}), that completely surrounds the ADC, to protect from micrometeoroid.
The main challenge in the ACD is to deal with the light yield contamination introduced by the backsplash effect due to the calorimeter mass. The backsplash effect is an isotropic production of secondary particles (mostly 100 keV -1 MeV photons) from the electromagnetic shower induced by the incident high-energy gamma ray that can interact by Compton scatter

cylinder with radius R_M and 99% of the energy is deposited, on average, within 3.5 R_M.

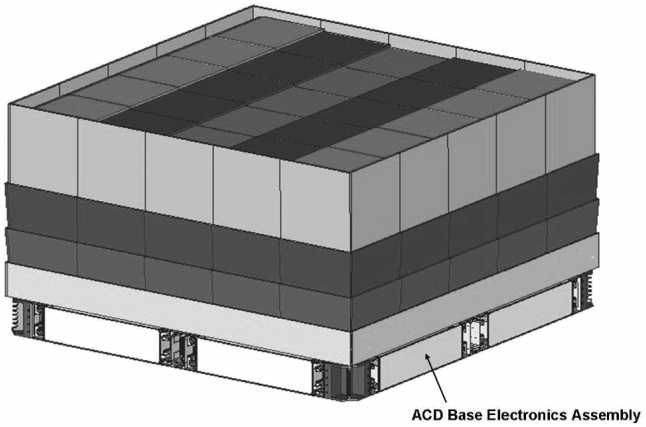

Figure 3.4: Illustration of the *Fermi*-LAT ACD from [124].

in the ACD and create false veto signals from the recoiling electrons. It was already observed in EGRET that false vetoes can cause a drop in the detection efficiency of about a factor two above 10 GeV with respect to the efficiency level at 1 GeV. The segmented structure of the ACD on board of the LAT suppresses the backsplash effect, reducing the amount of scintillation units considered for each event to only those closest to its reconstructed direction, reducing the amount of detector area affected by contaminations from the backsplash effect [125].

[125]: Moiseev et al. (2004), 'Observation and simulations of the backsplash effects in high-energy γ-ray telescopes containing a massive calorimeter'

3.2 LAT performance and survey strategy

The LAT performance is the result of a combination of the detector design, algorithms for event reconstruction and signal/background efficiency. The products of the performance analysis are the Instrument Response Functions (IRFs), that describe the performance as a function of photon energy, incidence angle and other parameters. This section presents an overview of the principal components of the LAT IRFs and does not review in details the event reconstruction and selection algorithms, that can be found in [126].
The LAT IRFs can be factorized into three parts:

[126]: Atwood et al. (2013), 'Pass 8: Toward the Full Realization of the Fermi-LAT Scientific Potential'

1. The *Effective area*, $A_{eff}(E, \hat{v}, s)$, is the product of the geometrical collection area, the gamma-ray conversion probability and the efficiency of a given event selections for a photon of energy E and direction $\hat{v}$ in the detector frame.
2. The *Point Spread Function* (PSF), $P(\hat{v}'; E, \hat{v}, s)$, is the probability density to reconstruct a true incident direction $\hat{v}'$ for a photon with $(E, \hat{v})$ belonging to the event selection s.
3. The *Energy dispersion*, $D(E'; E, \hat{v}, s)$, is the probability density to measure a true event energy E' for a photon with $(E, \hat{v})$ belonging to the event selection s.

The evaluation of the LAT response is made through a comparison with a dedicated Monte Carlo simulation performed on the full detector, that includes the simulation of a large number of gamma-ray events in order to cover all possible photon energies and inclination angle with high

statistics. In some cases, an in-flight calibration method using data from the Vela pulsar and the Earth limb is used for small corrections on the LAT response, in order to improve the data/model agreement. A schematic of the LAT with its coordinates frame from [127] is shown in Fig. 3.5.

[127]: Ackermann et al. (2012), 'The Fermi Large Area Telescope on Orbit: Event Classification, Instrument Response Functions, and Calibration'

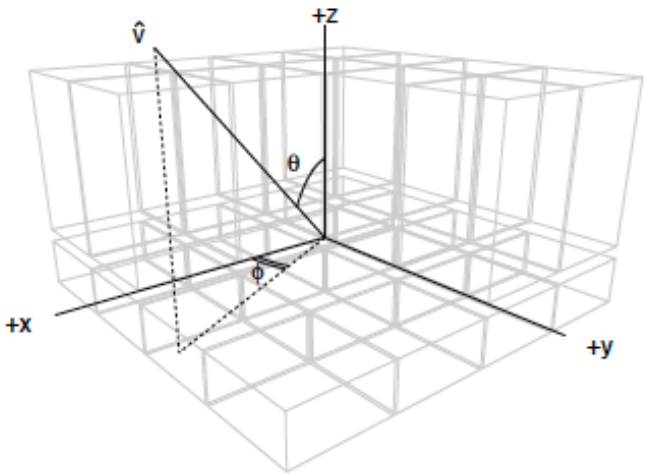

Figure 3.5: Schematic of the LAT coordinate system from [127]. The z-axis corresponds to the LAT boresight, and the incidence (θ) and azimuth (ϕ) angles are defined with respect to the z and x axes, respectively.

3.2.1 Pass 8 event selection

Since the beginning of the mission, the event selections of LAT data have been constantly improved following a better understanding of the instrument performance and the background properties. Four main event selections (Passes) have been released since 2008, these are Pass 6, Pass 7, Pass 7 Reprocessed and Pass 8. The last (and currently used) Pass 8 selection [126] marks a significant improvement in the LAT data quality compared to the previous Passes. All the analyses presented in this thesis work use Pass 8 data, so all the performances presented in this section are evaluated on this event selection.

[126]: Atwood et al. (2013), 'Pass 8: Toward the Full Realization of the Fermi-LAT Scientific Potential'

The events are classified as part of the event reconstruction process, and the classification is based on their probability of being photon events and on the quality of their reconstruction. The selection cuts divide events into classes, and for each class a set of IRFs is calculated. For each class, there is an additional classification into event types that uses selections based on the individual event topologies. One example is the different classification for events that undergo convertion in the Front or Back section of the Silicon Tracker.

In Pass 8, the event classes are divided in three nested hierarchies: *Standard*, *Extended* and *no-ACD*. The *Extended* and *no-ACD* hierarchies include classes that are defined with a less restrictive fiducial selection, such as events with projected trajectories that do not cross the Calorimeter section (TRANSIENT classes). The *Standard* hierarchy includes all the classes recommended for LAT analysis, among which there is the SOURCE class (recommended for point source analysis) and its nested variants with stricter selection cuts and therefore lower contamination (ULTRACLEAN, ULTRACLEANVETO, SOURCEVETO). The *Standard* hierarchy also includes two TRANSIENT classes with higher background rate, typically used for the short-timescales analysis of GRBs.

In addition to the Front and Back types (according on the conversion

vertex in the Silicon Tracker), Pass 8 divides events into two more event types:

- *PSF event type*: indicates the quality of the reconstructed direction, with data divided into quartiles, from the lowest quality quartile (PSF0) to the best quality quartile (PSF3).
- *EDISP event type*: indicates the quality of the energy reconstruction. The lowest quality quartile is EDISP0 and the best quality quartile is EDISP3.

In the following sections, I will present in detail the different components of the IRFs, and I will focus mainly on the SOURCE event class that is the one used in all the point-source analyses presented in this thesis. A detailed description of all data selections can be found in the Cicerone documentation[iii] of the Fermi-LAT Collaboration.

The Effective Area

The effective area A_{eff} depends on the geometrical cross section of the whole detector and the efficiency for converting and correctly identifying the incident gamma rays. Its calculation is done through a comparison with Monte Carlo simulations, where gamma rays are generated uniformly in log(E) and solid angle. When binning the parameter space, in each bin centered at the generic values (E_i,θ_j,ϕ_k) the effective area can be expressed in terms of the total number of generated events N_{gen} and the number of events $n_{i,j,k}$ passing the event selection:

$$A_{eff}(E_i, \theta_j, \phi_k) = (6\mathrm{m}^2)\left(\frac{n_{i,j,k}}{N_{gen}}\right)\left(\frac{2\pi}{\Delta\Omega_{j,k}}\right) \times \left(\frac{log_{10}E_{max} - log_{10}E_{min}}{log_{10}E_{max,i} - log_{10}E_{min,i}}\right) \tag{3.2}$$

where $\Delta\Omega_{j,k}$ is the solid angle subtended by the bin j,k in θ and ϕ. The energy boundaries $E_{min/max}$ and $E_{min/max,i}$ are for the whole event selection energy range and for the i-th energy bin, respectively.
In the evaluation of the instrument performance, the more common way is to consider the effective area with its angular dependence for a given energy or its value at normal incidence as a function of the energy.
Another quantity that is usually considered is the acceptance, namely the integral of the effective area over the solid angle:

$$\mathscr{A}(E) = \int A_{eff}\left(E, \theta, \phi\right) d\Omega = \int_0^{\frac{\pi}{2}} \int_0^{2\pi} A_{eff}\left(E, \theta, \phi\right) sin\theta d\theta d\phi. \tag{3.3}$$

From the acceptance and the on-axis effective area, one can derive the Field of View (FoV):

[iii] https://fermi.gsfc.nasa.gov/ssc/data/analysis/documentation/Cicerone/Cicerone_Data/LAT_DP.html

$$FoV\,(E) = \frac{\mathscr{A}\,(E)}{A_{eff}\,(E, \theta = 0)} \tag{3.4}$$

The on-axis effective area and acceptance for all four event classes of the *Standard* hierarchy in Pass 8 are shown in Fig. 3.6.

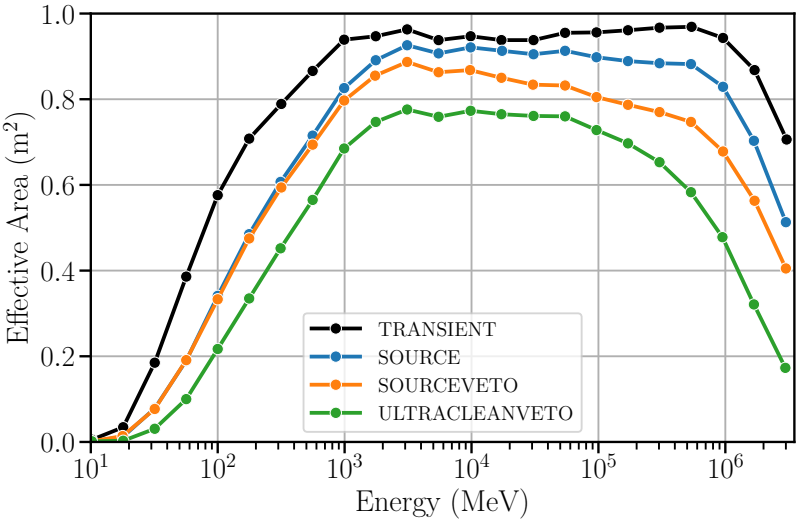

Figure 3.6: Effective area as a function of energy for normal incidence photons (θ = 0). Each curve shows the effective area for different event classes in the standard hierarchy of Pass 8 data. Adapted from https://www.slac.stanford.edu/exp/glast/groups/canda/lat_Performance.htm.

The Point Spread Function (PSF)

The point spread function (PSF) is a function of the photon energy, inclination angle and the event class and represents the likelihood to reconstruct a gamma ray with a given angular deviation:

$$\delta v = \left|\hat{v}' - \hat{v}\right| \tag{3.5}$$

To account for the first order variation of the PSF with energy, due to the dominance of multiple scattering at low energies (E < 1GeV) and the limits in the spatial resolution of the Silicon Tracker at higher energies, a scaling factor $S_P(E)$ is introduced in the PSF parametrization:

$$S_P\,(E) = \sqrt{\left[c_0 \cdot \left(\frac{E}{100MeV}\right)^{-\beta}\right]^2 + c_1^2} \tag{3.6}$$

and the scaled angular deviation x is defined as:

$$x = \frac{\delta v}{S_P\,(E)} \tag{3.7}$$

where E is the energy expressed in MeV, c_0 and c_1 are distinct values that depend on the event type and β is used as common, fixed value of 0.8 for all event types.
After accounting for the overall energy scaling, a base function is used to fit the PSF:

$$K(x,\sigma,\gamma) = \frac{1}{2\pi\sigma^2}\left(1-\frac{1}{\gamma}\right)\left[1+\frac{1}{2\gamma}\cdot\frac{x^2}{\sigma^2}\right]^{-\gamma} \tag{3.8}$$

known as *King function* [128] and to be isomorphic to the Student's t-distribution [129]. The *King function* also satisfies the normalization condition:

[128]: King (1962), 'The structure of star clusters. I. an empirical density law'

[129]: Student (1908), 'The probable error of a mean'

$$\int_0^\infty K(x,\sigma,\gamma)\,2\pi x dx = 1 \tag{3.9}$$

where the $2\pi x$ factor is derived from the integration over the solid angle

$$d\Omega = sin(x)dxd\phi \sim 2\pi x dx\,. \tag{3.10}$$

However, in the case of small angle approximation, is not valid anymore at very low energies because of the widening of the PSF and therefore $K(x)\,sin(x)$ has to be numerically normalized.
For a better description of the tails of the distribution, for a given incidence angle and energy, the sum of two *King* functions is used to describe the PSF as function of the scaled deviation:

$$P(x) = f_{core}K(x,\sigma_{core},\gamma_{core}) + (1-f_{core})\,K(x,\sigma_{tail},\gamma_{tail}) \tag{3.11}$$

The parameter of this function are stored in the IRF files in a tabular form. The value of f_{core} can be extracted from the N_{tail}, σ_{tail} and σ_{core}

$$f_{core} = \frac{1}{1+N_{tail}\cdot\sigma_{tail}^2/\sigma_{core}^2}. \tag{3.12}$$

The LAT PSF at 68% containment angle as a function of the energy is shown in Fig. 3.7 for each PSF event type.

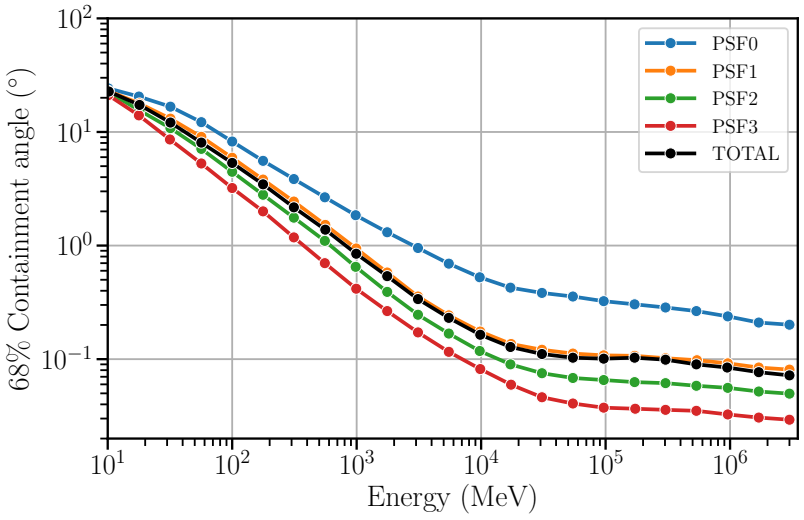

Figure 3.7: 68% containment angles as a function of the energy for all PSF event types in Pass 8 data. Adapted from https://www.slac.stanford.edu/exp/glast/groups/canda/lat_Performance.htm.

Energy dispersion

The energy dispersion of a particle detector is the difference between the reconstructed energy (E') and the true energy (E) of an event. A common way to define this quantity is in terms of fractional difference:

$$\frac{\delta E}{E} = \frac{E' - E}{E} \tag{3.13}$$

The energy dispersion parameterization depends on two quantities, the energy (E) and the inclination angle (θ). The 2-dimensional space described by these variables is binned in 4 bins per decade for $log(E)$ (in the energy range from 5.6 MeV to 3.2 TeV) and 8 equally spaced bins in $cos(\theta)$ for the inclination angle (covering the range from 0.2 to 1.0). For each bin, the scaled energy dispersion

$$x = \frac{\delta E}{E \cdot S_D(E, \theta)} \tag{3.14}$$

is calculated, binned into a histogram and fitted. The scaling factor in 3.14 depends on the true energy (E) and the true incidence angle (θ) and is defined by:

$$x = \frac{\delta E}{E \cdot S_D(E, \theta)} \tag{3.15}$$

A comparison of the energy resolution for all the EDISP quartiles event types in Pass 8 data is shown in Fig. 3.8.

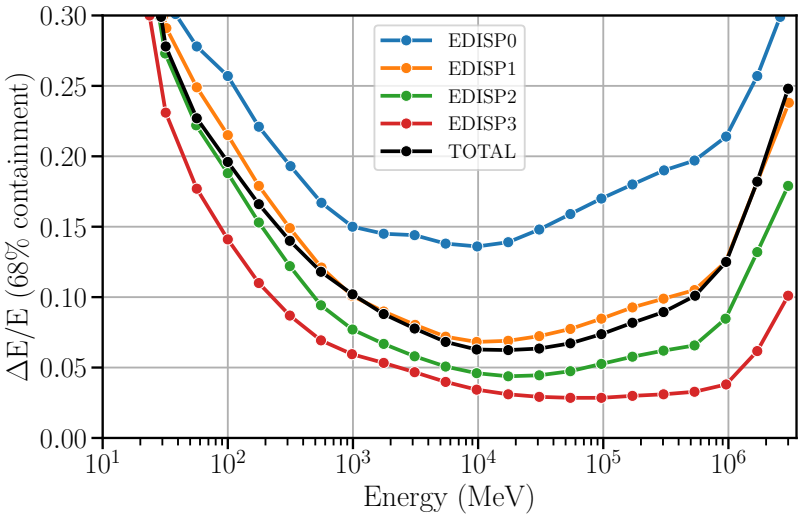

Figure 3.8: Energy resolution (68% containment half width of the reconstructed incoming photon energy) as a function of energy for all EDISP event types in Pass 8 data. Adapted from https://www.slac.stanford.edu/exp/glast/groups/canda/lat_Performance.htm.

Observing strategy

Since the beginning of the nominal scientific operations on August 4 2008, the *Fermi* satellite has an all-sky scanning survey strategy as primary observing mode. This survey mode is optimized to maximize the observing time while maintaining uniformity in the sky coverage. The *Fermi*-LAT countinously scans the sky, alternating between northern

and southern hemispheres each orbit, providing ~30 minutes of livetime on each point in the sky every two orbits (~3 hours).
The survey observations are regularly interrupted during passages of the orbit through the *South Atlantic Anomaly* (SAA), where the rate of cosmic-ray particles detected by the instrument is much higher than the average one observed during the rest of the orbit [130]. This interruption results in an exposure difference between the northern and southern sky of ~15%. Other occasional interruptions of the survey mode were performed in the first 10 years of operations for special observing strategies like the Target of Opportunity (ToO) observations of particularly interesting astrophysical events.
On March 16 2018, one of the two solar arrays of the spacecraft experienced an anomaly, and since then it can no longer be rotated by the motors. Since then, a new observing profile has been adopted, in order to maintain sufficient spacecraft power while also maintaining thermal control. The new observing mode[iv] depends on the angle between the orbital plane and the Sun (called β angle). Following the precession of the satellite's orbit, this angle varies on both a yearly timescale and with an approximate period of 46 days.
The new observing strategy still ensures a full coverage of the sky with an exposure similar to the one achieved before the anomaly, but variations of the pointing mode like ToOs are no longer supported.

[130]: Ginet et al. (2007), 'Proton Flux Anisotropy in Low Earth Orbit'

3.3 The likelihood approach in LAT data analysis

In this section, I will describe the general concepts behind the point-source data analysis with *Fermi*-LAT data. As for any particle detector that aims to reach enough precision to perform astronomical measurements, the data analysis presents several challenges due to the previously described limitations in the angular resolution, the low photon statistics and the detector performance, mostly sensitive to the energy of the measured photons. I will first describe the likelihood approach used in the *Fermi*-LAT data analysis, then I will describe the spectral models used to model blazars and I will conclude with a description of typical configurations that have been used for the analysis presented in this thesis work.

3.3.1 The Likelihood in *Fermi*-LAT data

The statistical concept of *likelihood* (i.e. the probability of obtaining the data given an input model) has a key role in the *Fermi*-LAT data analysis, since we use the approach of constructing a parametrized model of the selected region of the sky and we fit all the parameters with the very well known maximum-likelihood method [131].
When constructing a likelihood object, there is an implicit assumption that we sufficiently understand the response of our experiment. This is equally important as the choice of the model, which describes the gamma-ray sky we are observing.
The likelihood approach can be used in two different variants: binned

[131]: Cowan (2021), 'Statistics'

[iv] https://fermi.gsfc.nasa.gov/ssc/observations/types/post_anomaly/

and unbinned. In the binned case, the sample of photons is binned along different parameter space quantities (e.g. energy, space, time) and the likelihood is defined as the product of the probabilities of observing the detected number of counts in each bin. Given the relatively small photon statistics observed by the *Fermi*-LAT, it has been found that the best distribution to describe the number of counts in each bin is the Poissonian one:

$$p_i = e^{-m_i} \frac{m_i^{n_i}}{n_i!} \tag{3.16}$$

where n_i are the detected counts in the i-th bin, m_i is the predicted number of counts given the model and therefore p_i is the probability of detecting these counts given the model. The likelihood is then defined by the product of these probabilities

$$\mathcal{L} = e^{-N_{exp}} \prod_i \frac{m_i^{n_i}}{n_i!} \tag{3.17}$$

where $N_{exp} = \sum_i m_i$ is the total expected number of counts predicted given the model and $e^{-N_{exp}}$ is the product of all the e^{-m_i}, for all bins.
As previously mentioned, this is the case when the analysis is defined in a binned way. When binning a likelihood space, one has to achieve a good trade-off between the bin size (small enough to keep a good representation of data) and a reasonable number of counts per bin (to have the fit statistically reliable).
In the limit where the bin size tends to 0, in which case the bin can be empty or $n_i = 1$, we are in the unbinned regime, and the likelihood becomes

$$\mathcal{L} = e^{-N_{exp}} \prod_i m^{n_i} \tag{3.18}$$

where i is the index over the photon counts. This unbinned approach is in general more accurate, since each photon is taken in account individually and not averaged in a bin, however it is more computationally expensive and often avoided especially when dealing with a large number of counts (i.e. long observation time). In this thesis work, I have performed the majority of the gamma-ray analyses using the binned likelihood method. I will however highlight when, in special cases, the unbinned likelihood method was used in order to perform a dedicated study on the individual high-energy photons observed from a source.

3.3.2 Source models

The observation of astrophysical sources in gamma rays, has shown that their spectra exhibit a variety of shapes, that can depend on the source class as well as the strength of the gamma-ray emission observed at Earth. The spectral models mostly used to describe the spectra of extragalactic gamma-ray point sources (i.e. sources with no resolved spatial extension) are:

- Power Law

$$\frac{dN}{dE} = N_0 \left(\frac{E}{E_0}\right)^{-\alpha} . \tag{3.19}$$

- Log Parabola

$$\frac{dN}{dE} = N_0 \left(\frac{E}{E_0}\right)^{-(\alpha+\beta\log(E/E_0))} . \tag{3.20}$$

where N_0 represents the normalization parameter, that coincides with the flux at the pivot energy E_0 for the power law. E_b is a scale factor for the log parabola as described in [132].

Power law: The simplest spectral model used to describe point-like gamma-ray sources is the power law (only 2 parameters, Eq. 3.19). It is not an analytical model used just to describe the spectra of astrophysical sources, but is indeed found to be a good analytical description of empirical data in several fields of knowledge like economics, biology, social sciences and basically all branches of physics. It is fascinating the huge variety of systems that can be described in nature by power laws, that find a possible connection in the intrinsic properties of dynamical systems, in particular in the concept of self-organized criticality [133, 134]. In particular, for the subjects of our studies, the power-law description of the observations comes from the acceleration mechanisms that produce the electromagnetic emission that we measure. The general acceleration mechanism used to describe the acceleration of particles in astrophysical sources is based on an idea originally proposed by E. Fermi [135], called the "first order Fermi acceleration". In this model, particles are accelerated in environments similar to the ones generated by supernova explosions, where the key elements are strong shock regions and magnetized plasma. Key features of the power-law distribution are the spectral index (α, model parameter for which I will present an overview of the observed values in the blazar population in the next sections) and the so called "pivot energy" (E_0 in Eq. 3.19, not a parameter), that is the energy where the error on the absolute flux reaches its minimum.

Log Parabola: In the presence of a curvature in the energy distribution of the gamma-ray emission observed from a point source, an alternative model is the log parabola (Eq. 3.20). This model has 3 parameters (one more than a power law) and is the simplest model used to describe spectral curvatures in absence of a sharp break in the spectrum. The name comes from the parabolic shape shown by the model in a log-log space, that is conserved also when the spectrum is represented in the form $\log(E^n \frac{dN}{dE})$ versus log(E) [134].

In the analytical expression 3.20, N_0 is the flux normalization and E_0 the pivot energy, respectively, as in the case of the power law. The parameter α is the spectral index at the pivot energy E_0 while the parameter β describes the curvature of the spectrum. Instead of treating the two parameters α and β distinctly, they can be grouped in the definition of an energy-dependent spectral index from the log-derivative of Eq. 3.20 [132]

$$\alpha' = \alpha + 2\beta \log \frac{E}{E_0} \tag{3.21}$$

from which one can calculate the peak energy E_p (i.e. the energy where

[132]: Massaro et al. (2004), 'Log-parabolic spectra and particle acceleration in the BL Lac object Mkn 421: Spectral analysis of the complete BeppoSAX wide band X-ray data set'

[133]: Bak et al. (1987), 'Self-organized criticality: An explanation of the 1/f noise'

[134]: Lipari (2021), 'The origin of the power-law form of the extragalactic gamma-ray flux'

[135]: Fermi (1949), 'On the Origin of the Cosmic Radiation'

the spectrum is flat with α(E) = 2)

$$E_p = E_0\, e^{(2-\alpha)/2\beta}. \tag{3.22}$$

The first applications of the log-parabola model to the spectra of high-energy astrophysical sources dates back to 2000, where it was used to describe the spectrum of the Crab pulsar [136]. Shortly after, it was used to describe a subsample of X-ray Blazar SEDs observed by *Beppo*SAX [137, 138].
The log parabola and the power law are, by definition, *nested* models. This is because the power law can be obtained by setting the parameter β to 0 in the log parabola analytical expression. This will be a useful property for statistical tests that I will describe in the next chapters. I will present more models used for point sources outside the blazar class in the next section where I will describe the latest *Fermi*-LAT gamma-ray catalogs of sources.

[136]: Massaro et al. (2000), 'Fine phase resolved spectroscopy of the X-ray emission of the Crab pulsar (PSR B0531+21) observed with BeppoSAX'

[137]: Giommi et al. (2002), 'A Catalog of 157 X-ray Spectra and 84 Spectral Energy Distributions of Blazars Observed with BeppoSAX'

[138]: Boella et al. (1997), 'BeppoSAX, the wide band mission for X-ray astronomy'

3.4 *Fermi*-LAT gamma-ray catalogs

Already after only 3 months since the start of observations, the *Fermi*-LAT collaboration released the first list of bright gamma-ray sources (0FGL,[139]), that counted only 205 significantly detected objects. Since then, a progressive series of catalogs has been released covering always longer observing periods and different energy ranges. At the moment of the preparation of this manuscript, the most recent version of the catalog is the 4FGL, in his second data release that covers 10 years of *Fermi*-LAT operations (4FGL-DR2, [140]), and includes now 5788 sources. The first published version of 4FGL was covering 8 years of observations in the energy range 50 MeV - 1 TeV [141].
The energy range investigated by the 4FGL is not the only one used historically to build *Fermi*-LAT catalogs. Dedicated catalog works have been performed for the detection of sources at low energies, below 100 MeV [142] or in the high-end of the energy range, like the "Catalog of Hard *Fermi*-LAT Sources" that lists detections in the 10 GeV - 2 TeV range in its first and third issues (1FHL, 3FHL [143, 144]) and in the 50 GeV - 2 TeV range in its second issue (2FHL, [145]). Table 3.1 summarizes the main *Fermi*-LAT catalogs with their energy ranges and integration times.

[139]: Abdo et al. (2009), 'Fermi/Large Area Telescope Bright Gamma-Ray Source List'

[140]: Ballet et al. (2020), 'Fermi Large Area Telescope Fourth Source Catalog Data Release 2'

[141]: Abdollahi et al. (2020), 'Fermi Large Area Telescope Fourth Source Catalog'

[142]: Principe et al. (2018), 'The first catalog of Fermi-LAT sources below 100 MeV'

[143]: Ackermann et al. (2013), 'The First Fermi-LAT Catalog of Sources above 10 GeV'

[144]: Ajello et al. (2017), '3FHL: The Third Catalog of Hard Fermi-LAT Sources'

[145]: Ackermann et al. (2016), '2FHL: The Second Catalog of Hard Fermi-LAT Sources'

The 4FGL-DR2 includes all the 5064 sources that have been detected in the first version of 4FGL above a 4σ significance over 8 years of data, plus

Table 3.1: Table of FGL catalog releases from 0FGL to the latest 4FGL-DR2.

Name	Energy range	Integration time	Sources
0FGL	0.1 - 100 GeV	3 months	205
1FGL	0.1 - 100 GeV	11 months	1451
2FGL	0.1 - 100 GeV	2 years	1873
1FHL	10 GeV - 2 TeV	3 years	514
3FGL	0.1 - 300 GeV	4 years	3033
2FHL	50 GeV - 2 TeV	7 years	360
3FHL	10 GeV - 2 TeV	7 years	1556
4FGL	0.05 GeV - 1 TeV	8 years	5064
4FGL-DR2	0.05 GeV - 1 TeV	10 years	5788

newly detected sources from two additional years of data, for a total of 5788 objects.
A large variety of source classes have been associated with the gamma-ray objects listed in the catalog. The most represented sources in the catalog are blazars, classified in their subclasses (see Ch. 2), followed by pulsars, supernova remnants and radio galaxies. Interestingly, still 1667 sources remain unassociated in the catalog, corresponding to about 29% of the whole sample.
The spectrum of 3986 of the detected sources (approximately 69% of the sample) is modelled with a simple power-law function, while 1572 (approximately 27% of the sample) show a curved spectrum for which a log-parabola model is statistically preferred. The remaining 230 sources are modelled with a power law with a super exponential cutoff

$$\frac{dN}{dE} = N_0 \left(\frac{E}{E_0}\right)^{-\alpha} e^{-E/Ec}. \tag{3.23}$$

where E_c is the cutoff energy and N_0 and E_0 are the normalization and the pivot energy, like in the simple power law. Among these 230 sources, 227 are associated with pulsars, one with a normal galaxy and two with blazar objects. The two blazars are 3C 454.3 (z = 0.86 [146]) and CTA 102 (z = 1.03 [147]), both belonging to the FSRQ class and among the brightest detected in the whole *Fermi*-LAT sample of sources of this kind.

[146]: Healey et al. (2008), 'CGRaBS: An All-Sky Survey of Gamma-Ray Blazar Candidates'
[147]: Monroe et al. (2016), 'The UV-bright Quasar Survey (UVQS): DR1'

3.4.1 The catalog of AGN detected by the *Fermi*-LAT

Since in this thesis the main objects of interest are blazars, in this section I will focus on the catalog of AGN detected by the *Fermi*-LAT, that is compiled at every issue of the main FGL catalog.
At the time of the preparation of this manuscript, the latest published version is the 4LAC-DR2 [148, 149], that includes all AGN-type sources detected in 4FGL-DR2. For each source, in addition to the information already present in 4FGL, the catalog lists (whenever available) the source classification (optical and SED-based class), redshift, synchrotron-peak frequency and νF_ν in the observer frame, and the VLBI and Gaia counterparts listed in the Radio Fundamental Catalog (RFC [150]). The census of sources counts a large variety of classes, dominated by blazar-type objects (~98% of the sample) divided in their optical classes of FSRQ and BL Lac objects, in addition to a significant fraction (~41%) of blazar candidates of uncertain type objects (BCU). These objects represent tentative classifications to sources that are considered candidate blazars because of their multiwavelength spectrum (two-humped, blazar-like SED) or high-confidence associations with blazar objects observed in other wavelengths (e.g. BZCAT [151], RFC[150], CRATES [152] and more). In the remaining 2% of non-blazar AGN sources listed in the 4LAC-DR2, the largest component is of radio galaxies (~1.3%) followed by other AGN of non-specific classification (~0.3%), Narrow-line Seyfert 1 galaxies (NLSy1, ~0.3%), compact steep spectrum radio sources (CSS, ~0.2%) and steep-spectrum radio quasars (SSRQ, ~0.1%). A classification based on the synchrotron peak frequency (ν^S_{peak} from [62] is also provided for blazar objects, where 3 additional classes divide the sample in

[148]: Ajello et al. (2020), 'The Fourth Catalog of Active Galactic Nuclei Detected by the Fermi Large Area Telescope'
[149]: Lott et al. (2020), 'The Fourth Catalog of Active Galactic Nuclei Detected by the Fermi Large Area Telescope – Data Release 2'
[150]: Petrov et al. (2019), 'The Second LBA Calibrator Survey of southern compact extragalactic radio sources - LCS2'
[151]: Massaro et al. (2015), 'The 5th edition of the Roma-BZCAT. A short presentation'
[152]: Healey et al. (2007), 'CRATES: An All-Sky Survey of Flat-Spectrum Radio Sources'
[62]: Abdo et al. (2010), 'The Spectral Energy Distribution of Fermi Bright Blazars'

- Low-synchrotron-peaked blazars (LSP, with $\nu^S_{peak} < 10^{14}$ Hz)
- Intermediate-synchrotron-peaked blazars (ISP, with 10^{14} Hz $< \nu^S_{peak} < 10^{15}$ Hz)
- High-synchrotron-peaked blazars (HSP, with $\nu^S_{peak} > 10^{15}$ Hz)

with quantities measured in the observer frame.
The localizations of all 3027 sources in 4LAC-DR2 (2863 at high galactic latitudes $|b| > 10°$and 344 at $|b| < 10°$) are shown in Fig. 3.9 in galactic coordinates, with FSRQ objects in blue circles, BL Lacs in orange squares, BCUs in green diamonds and the remaining AGN in the catalog with red triangles.

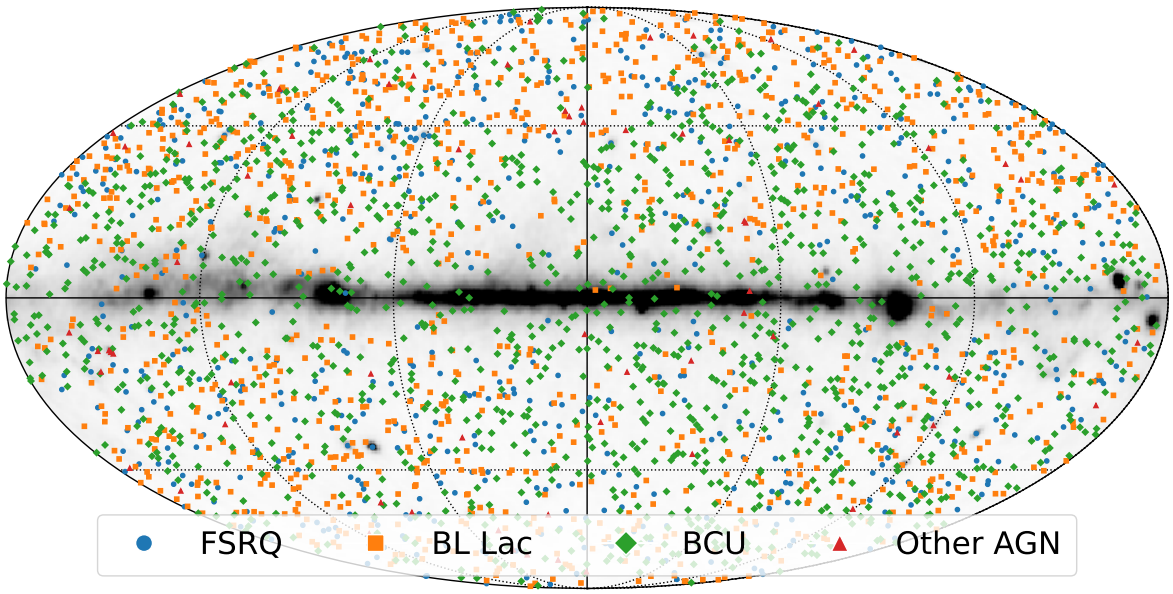

Figure 3.9: All-sky map in in Galactic coordinates with localizations of sources in [148]. The map background show one year of LAT data counts in greyscale color map.

Focusing on the subsample of blazar objects, an interesting picture comes from the spectral properties of the different blazar classes. The first column of panels in Fig. 3.10 shows the distributions of the spectral index for the different optical classes, with overlayed medians and root mean square (rms) for each distribution (dashed and dotted lines, respectively). There is a marked difference between the distributions of spectral indices in FSRQ and BL Lac sources, with median and rms of 2.44 ± 0.21 for FSRQs and 2.03 ± 0.21 for BL Lacs. This difference in the distributions has a good separation power between the two classes. The index distribution for the BCU objects spans over a wide range, up to photon index values of 3. This subsample of still unclassified blazars is likely a mixture of FSRQ and BL Lac objects, and therefore has a distribution compatible with a linear correlation of the distributions of the two classes [148].
This separation between the two classes might be due to the fact that

[148]: Ajello et al. (2020), 'The Fourth Catalog of Active Galactic Nuclei Detected by the Fermi Large Area Telescope'

differently from the FSRQ that are observed with synchroton spectra peaking at low frequencies (LSP), while the BL Lac objects are observed peaking also at higher frequencies, and include several ISP and HSP sources. The second column of panels in Fig. 3.10 shows the distributions of the synchroton-peak frequencies divided by class.

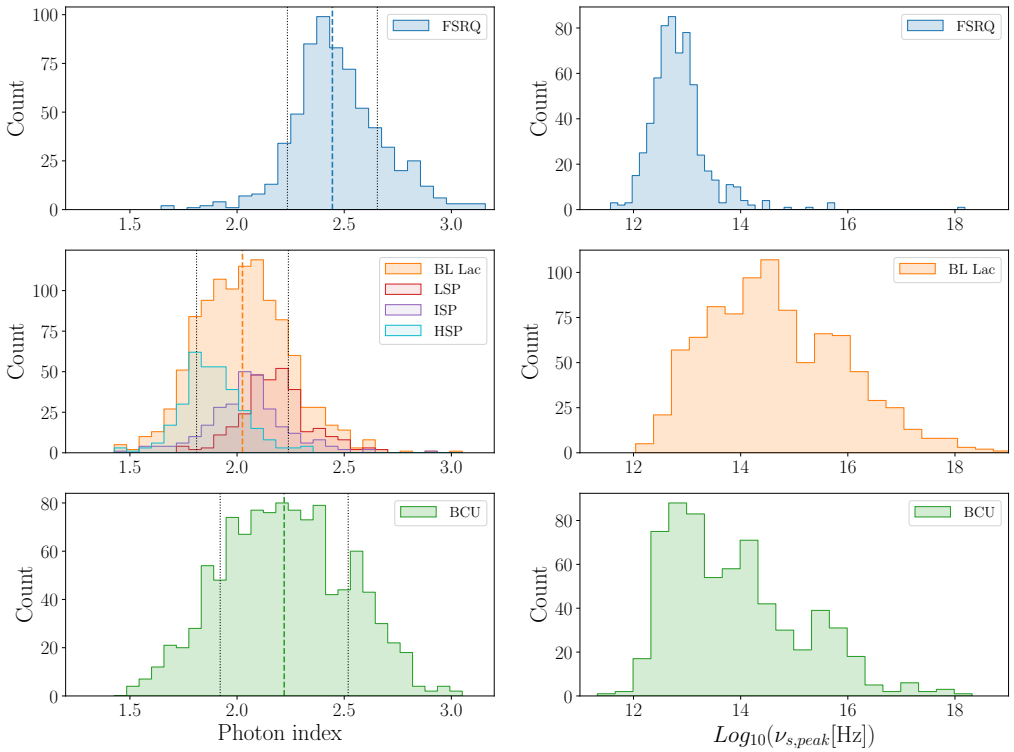

Figure 3.10: Panels on the *left*: photon index for different blazar classes (and subclasses for BL Lacs) in 4LAC. Panels on the *right*: distributions of the sunchrotron peak frequency for different blazar classes in 4LAC.

Another interesting picture comes from the representation of the photon index and synchrotron-peak frequency in a two-dimensional space. The scatter plot in Fig. 3.11 shows the photon index as a function of the synchrotron-peak frequency for the whole FSRQ sample and for the BL Lac sample divided into the SED subclasses. The correlation that arises from this two-dimensional distribution was already observed in previous catalogs. In particular, the one observed in the 3LAC catalog [153] was reproduced theoretically by [154] and found to be compatible with an equipartition blazar model where the primary electrons follow a log-parabolic energy distribution [148]. Another feature of interest in this plot is the region where the FSRQs and the BL Lac LSPs overlap, and their spectral indices are also very similar. In this region, is it possible to find objects that could be in a transition phase between the FSRQ and the BL Lac classes. Some of these objects have already been identified, and a systematic search for this peculiar class of blazars can be found in [155].

One last feature of 4LAC which is important for this thesis is the variability

[153]: Ackermann et al. (2015), 'The Third Catalog of Active Galactic Nuclei Detected by the Fermi Large Area Telescope'

[154]: Dermer et al. (2015), 'Near-equipartition Jets with Log-parabola Electron Energy Distribution and the Blazar Spectral-index Diagrams'

[155]: Ruan et al. (2014), 'The Nature of Transition Blazars'

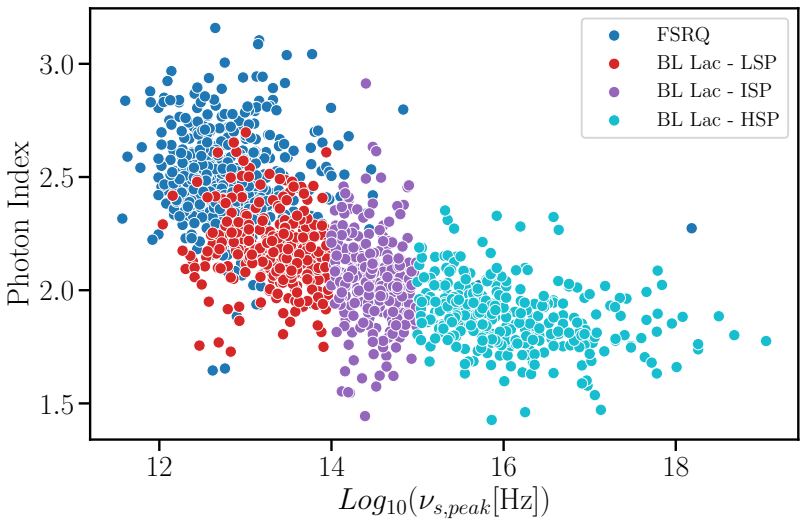

Figure 3.11: Photon index vs. synchrotron peak frequency in the observer frame. Plot adapted from Fig. 7 in [148]

quantified for each source. The variability of each catalog object is measured by means of a variability index that is computed in the 4FGL after producing light curve samples with 1-year and 2-month binning and covering 10 years of observations. It is defined as the test statistics (TS_{var}) of a likelihood ratio test between the light curve and the constant flux model. Figure 3.12 shows the Energy Flux versus the variability index of blazar objects in 4LAC. The black dashed line indicates the variability index value of TS_{var} =18.48 above which a source has < 1 % chance of being a steady source [141, 149].

[141]: Abdollahi et al. (2020), 'Fermi Large Area Telescope Fourth Source Catalog'
[149]: Lott et al. (2020), 'The Fourth Catalog of Active Galactic Nuclei Detected by the Fermi Large Area Telescope – Data Release 2'

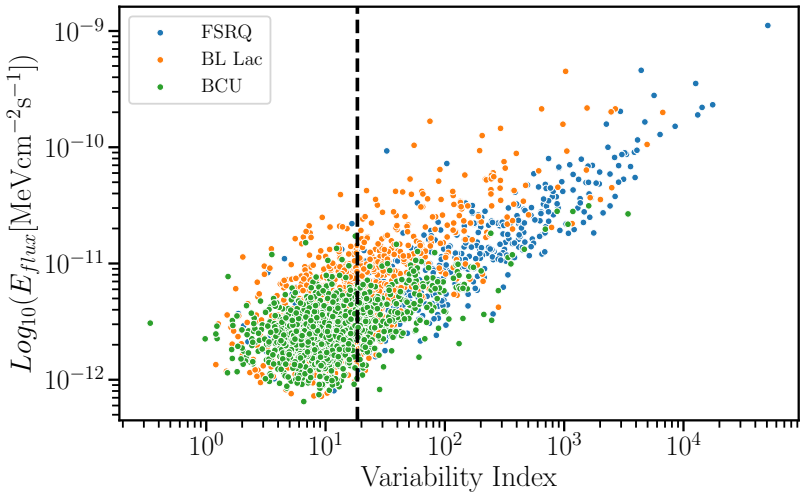

Figure 3.12: Energy Flux versus variability index of blazar objects in 4LAC. The black dashed line marks the TS_{var} = 18.48 threshold.

3.5 Data analysis with *Fermi*-LAT data

After introducing the Likelihood methods in Sec. 3.3.1 and the source models in Sec. 3.3.2, in this section I will give an overview of the main steps of a typical analysis of *Fermi*-LAT data, with a focus on the methods used in the analysis included in this thesis. The official analysis tools developed by the *Fermi*-LAT collaboration are the *Fermi Science Tools*[v],

[v] https://fermi.gsfc.nasa.gov/ssc/data/analysis/software/

also available in the python package named *fermitools*[vi]. An alternative way to use the fermitools, is via their official python wrapper called *fermipy*[156], that was extensively used in the analyses included in this thesis.

[156]: Wood et al. (2018), 'Fermipy: An open-source Python package for analysis of Fermi-LAT Data'

Data selection

As for any experimental data analysis, the selection of data is the first step and its configuration is very sensitive to the case of study.
The data from *Fermi*-LAT observations are publicly available from the Fermi Science Support Center (FSSC[vii]) and divided in two different types:

- **FT1**: also known as *event files*, contain a list of all events classified as photons with measured and reconstructed parameters. These include, among others, the detection time, reconstructed energy and arrival direction in celestial and detector-based coordinate system.
- **FT2**: also known as *spececraft files*, contain spacecraft locations, pointings and the instrument-related informations necessary for the data analysis, in 30-seconds intervals.

As first step of the analysis, a selection of events is performed in a region of interest (ROI) centered at the coordinates of the target source, with a typical extension of $10°\times10°$ or $15°\times15°$, depending on the region and source considered. This selection is done by the routine `gtselect`, that allows also to select a specific time interval and energy range (typically starting from 100 MeV for point-source analysis). An additional cut is on the zenith angle θ_Z, allowing typical values < 90°-100°in order to reduce the contamination from the emission due to the gamma-rays produced by the interaction of cosmic rays in the Earth's atmosphere [157]. Another routine that performs the data selection in the preparatory stage of the analysis is `gtmktime`, that selects the *Good Time Intervals* (GTI) within our integration period, namely intervals where the instrument is in normal data-taking mode and no other factor (internal or external) is altering the data quality. An example of external altering factor is the passage of the satellite through the SAA.

[157]: Abdo et al. (2009), 'Fermi large area telescope observations of the cosmic-ray induced γ-ray emission of the Earth's atmosphere'

Source models

An additional component of the analysis is a starting configuration model for the already known sources in the ROI. Three kind of sources are included: point sources, extended sources and background components. The point source spectral properties are usually taken directly from a catalog, and included in the ROI model. In the case of extended sources in the ROI, dedicated templates are included in *fermitools*. Two background models are also provided[viii] by the *Fermi*-LAT collaboration

[vi] https://github.com/fermi-lat/Fermitools-conda/wiki
[vii] https://fermi.gsfc.nasa.gov/cgi-bin/ssc/LAT/LATDataQuery.cgi
[viii] https://fermi.gsfc.nasa.gov/ssc/data/access/lat/BackgroundModels.html

- **Galactic diffuse** (also known as Interstellar Emission Model, IEM) is a spatial and spectral template for the Galactic diffuse emission. Developed using spectral line surveys of HI and C0 (as tracer of H_2) to derive the distribution of interstellar gas in Galactocentric rings. The diffuse model of the gamma-ray emission was derived fitting the gamma-ray emissivities of the rings in several energy bands to the *Fermi*-LAT observations. Included in the fit, there is also a model of the Inverse Compton emission calculated with GALPROP [158] and a model for the diffuse isotropic emission. The latest version of the IEM is $gll_iem_v07.fits$.
- **Isotropic spectral template**: Derived fitting the all-sky emission in the energy range 30 MeV to 10 TeV, excluding the Galactic plane region ($b < 10°$) and regions around the celestial poles (Dec > 60°), in order to exclude the Galactic diffuse emission and the gamma-rays produced in the Earth's atmosphere. This isotropic diffuse emission is due to yet unresolved extra-galactic sources and residual contamination from cosmic rays in the instrument.

[158]: Porter et al. (2021), 'The GALPROP Cosmic-ray Propagation and Non-thermal Emissions Framework: Release v57'

Binning, Livetime and exposure

In a binned likelihood analysis, data must be arranged in a three-dimensional counts map, where the third axis describes the energy. This map is called *counts cube*, and is produced with the routine `gtbin` with a typical configuration of

- Ten logarithmically spaced bins per decade in energy;
- Spatial binning of 0.1°size.

There are two quantities that are pre-computed in the analysis after the data selection and binning. These are the *livetime* (i.e. the time spent by the LAT observing any given position of the ROI at any given inclination angle) and the *exposure map* (i.e. the effective area multiplied by live time). They have a key role in speeding up the likelihood optimization in the model fit. Instead of calculating these quantities at any optimization of the likelihood, they are calculated only once, and stored in multidimensional arrays to cover the analysis parameter space.
As we have seen before in Sec. 3.2, the IRFs are a function of the angle between the direction to a source and the normal to the instrument. Therefore, the calculation of the expected number of counts that goes in the likelihood (Sec. 3.3.1) depends on the amount of time that the source spends at a given inclination angle with respect to the LAT during an observation. The *livetime cube* is an array that collects these livetimes at all points on the sky, and its structured on a healpix [159] grid in celestial coordinates and inclination angle bins. The *livetime cube* is computed with the routine `gtltcube` and it only depends on the list of satellite pointings in the FT2 file. A peculiar property of the *livetime cubes* is the additivity, so they can be summed up to cover contiguous time periods. This will be a key feature for the setup of the fast-updating follow-up pipeline described in Chapter 9.
The *exposure maps* used in the likelihood method consist of an integral of the total set of IRFs over the entire ROI data-space

[159]: Górski et al. (2005), 'HEALPix: A Framework for High-Resolution Discretization and Fast Analysis of Data Distributed on the Sphere'

$$\varepsilon(E,\hat{p}) = \int_{ROI} dE' d\hat{p}' dt R(E',\hat{p}';E,\hat{p},t) \ , \tag{3.24}$$

where E' and $\hat{p}'$ are the measured energies and directions, respectively. Given $S_i(E,\hat{p})$ the photon intensity from a source i in the model

$$N_{pred} = \int dE d\hat{p} S_i(E,\hat{p}\,\varepsilon(E,\hat{p})) \ . \tag{3.25}$$

Unlike the calculation of livetimes that is only dependent on the specific time period but valid for the whole sky, the calculation of N_{pred} must be repeated at any change of ROI configuration. The exposure map is computed by the `gtexpcube2` routine and it requires a list of object located also 5°-10°outside the ROI, in order to account properly for the large PSF of low-energy events emitted from sources located just outside the region considered with `gtselect`.
Once obtained the *exposure map*, a *model counts map* is created with the routine `gtsrcmaps`. This tool makes use of Eq. 3.25 to evaluate the product between the source spectrum and the exposure at the target position, and then does the convolution with the effective PSF.

Likelihood optimization

Once all the factors that will enter in the likelihood have been pre-calculated, the fit can be performed. The likelihood fit is handled by the routine `gtlike`, that can use a wide range of optimizers, among which the commonly used `MINUIT` [160]. As already mentioned in Sec. 3.3.1, two types of likelihoods can be used: binned and unbinned. The standard method used in the analyses described in this thesis work is the binned likelihood, that is also the only one handled by *fermipy* and the ideal approach for long timescales or high-density data (i.e. bright sources or crowded region of the sky) in terms of computational stability.
The unbinned method (or at least part of its approach) will be used only in special applications within the analysis. In the study of the gamma-ray emission detected from a particular object, it is sometimes interesting to identify the high-energy photons with high probability of being associated to a target source giving the spectral behaviour shown in a specific period. For these specific periods, I have also performed the analysis with the unbinned approach, that differs from the standard use of `gtlike` for the application of two additional routines: `gtdiffrsp` and `gtsrcprob`. The former computes the integrals over the spatial distribution of diffuse sources, that must be performed over the whole sky and are computationally expensive. These integrals are precomputed for each diffuse model component and stored in new columns of the FT1. The second routine `gtsrcprob` assigns a probability for each photon event of being associated to each of the sources in the model.
During the likelihood fit, an arbitrary subset of the model parameters (or all of them) can be set free and being allowed to vary with the fit, otherwise they will be set to the catalog (or template) values.
After the likelihood optimization, the next step is to quantify the detection (or not) of each source in the model.

[160]: James et al. (1975), 'Minuit - a system for function minimization and analysis of the parameter errors and correlations'

Source detection and sensitivity

To quantify the detection of a source in the model, we define a Test Statistics (TS) following the prescriptions in [161]

[161]: Mattox et al. (1996), 'The Likelihood Analysis of EGRET Data'

$$TS = 2 \ln \frac{L_{max,1}}{L_{max,0}} \tag{3.26}$$

that is the maximum likelihood ratio between the likelihood for the model to be tested ($\mathcal{H}_1$) and the *null hypothesis* ($\mathcal{H}_0$). In the case of source detection, the model $\mathcal{H}_0$ differs from the model $\mathcal{H}_1$ only for the exclusion of the source of interest.
For a large number of counts, the TS behaves asymptotically as a χ^2 distribution, and therefore, if the two models differ by only 1 *dof*, the significance can be calculated as $\sqrt{TS}$. For a larger number of *dof* (i.e. more free parameters, e.g. localization) the correspondent significance must be calculated in the rigorous way, considering the χ^2 distribution with the adequate number of *dof* and converting the p-value to the number of σ relative to a normal distribution.
Another interesting application is to quantify possible detections of sources not already included in the catalog (and therefore in the ROI model). This can be done in an efficient way using the `find_sources()`[ix] method. Differently from the strongly time-consuming routine `gtfindsrc` in fermitools, the *fermipy* implementation tests point sources in each spatial bin of the ROI by means of likelihood ratio creating a so-called *TS-map*. The algorithm then iterates over the most prominent peaks of TS in the map to perform more accurate spatial and spectral tests for point sources at these localizations.
Figure 3.13 shows a comparison between the differential sensitivities for 10 years of exposure in 4 bins per energy decade between 31.6 MeV and 1 TeV. The model assumed for the putative source is a power law with index 2.0 and only diffuse backgrounds are considered. A threshold of minimum 10 photons per energy bin is required for the detection. The curves are calculated for 4 different directions in the sky labeled in Galactic coordinates: Galactic center (l,b) = (0°,0°), intermediate Galactic latitude (l,b) = (0°,30°), North Galactic pole (l,b) = (0°,90°) and North Celestial pole (l,b) = (120°,45°).

Figure 3.14 shows the integral flux sensitivity map for an isolated point source with 10 years of exposure. The integral sensitivity is calculated as the minimum required flux for a source with a power-law spectrum with index 2 to reach a 5σ detection during 10 years of data taken in survey mode. The 5σ limit corresponds to a TS = 25 and at least 10 photons.

Spectral Energy Distribution

The spectral energy distribution (SED) is computed with the `sed()` method in *fermipy* by performing independent fits for the flux normalization of a source in bins of energy. The flux normalization in each energy bin is fitted using a power-law spectrum with a fixed index. The default

[ix] https://fermipy.readthedocs.io/en/latest/advanced/detection.html

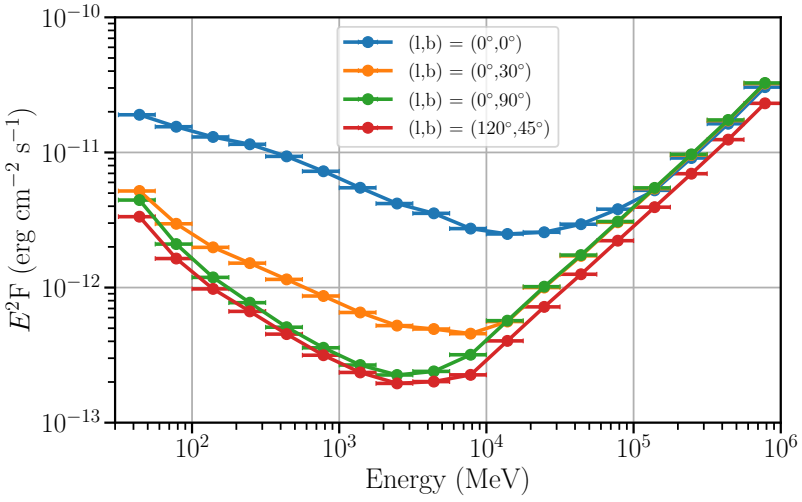

Figure 3.13: Differential point source sensitivity for 10 years of exposure in 4 bins per energy decade between 31.6 MeV and 1 TeV. Adapted from https://www.slac.stanford.edu/exp/glast/groups/canda/lat_Performance.htm.

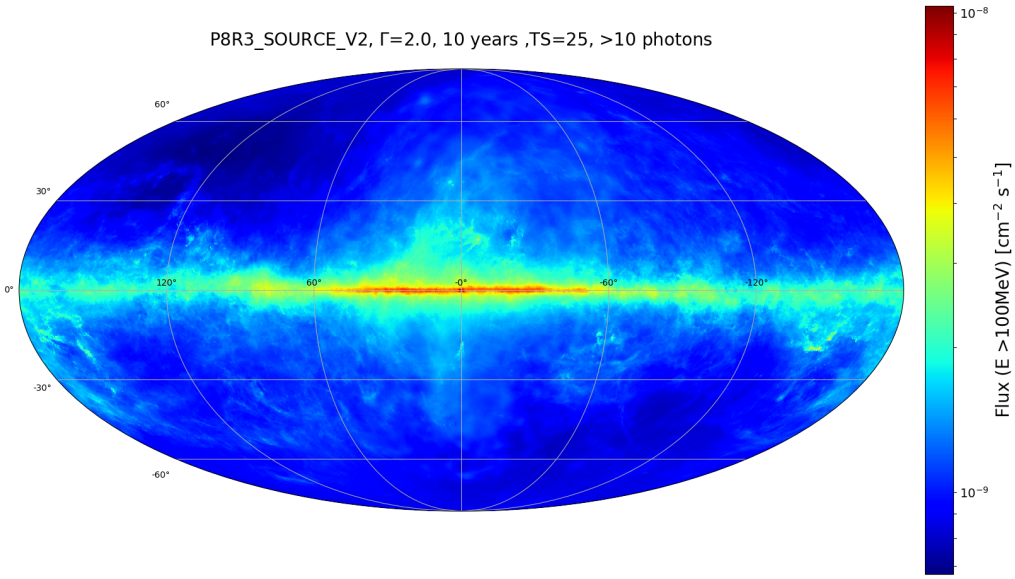

Figure 3.14: All-sky map of integral point-source sensitivity in 10 years of sky survey. The integral sensitivity is calculated as the minimum required flux for a source with power-law spectrum with index 2 to reach a 5σ detection during 10 years of survey mode. The 5σ limit corresponds to a TS = 25 and at least 10 photons. Adapted from https://www.slac.stanford.edu/exp/glast/groups/canda/lat_Performance.htm.

index used is $\alpha = 2.0$, but alternatively any value can be used (e.g. the best-fit spectral index from the global fit).

Light curves and adaptive binning

The computing of the so-called *light curve* of a source is a standard practice in astronomy. This technique consists in fitting the spectral parameters of a target source in a sequence of time bins, in order to study the evolution of these parameters with time. The `lightcurve()` method in *fermipy* performs these multiple fits for a given set of time bins. The

standard choice for the time binning consists in a fixed size that generally depends on the timescale of interest for the observer to be investigated, the intensity of the source or the availability of the observations.
An interesting method that I chose to adopt for the binning of the light curves in the analyses presented in this thesis is the *adaptive bins* algorithm [162]. This method produces a temporal binning for the light curve with a variable binning size that depends on the intensity of the source and the precision of the flux measurement. The condition that is satisfied for each bin is a constant relative flux uncertainty

[162]: Lott et al. (2012), 'An adaptive-binning method for generating constant-uncertainty/constant-significance light curves with Fermi-LAT data'

$$\frac{\sigma_{F_i}}{F_i} = const. \tag{3.27}$$

where F_i is the flux in the bin i and σ_{F_i} is its uncertainty. The method is iterative, and starting from a time T_0 freezes the width of the bin once the condition is satisfied, to then start with the next bin. The width of each bin will be therefore smaller during periods of enhanced activity from the source, while it will be longer during periods of low activity. The short duration of each bin in the periods of bright emission from the source is essential to significantly resolve the smallest variability timescales and have a detailed picture of the flares development in time. This will be a key feature in our analyses, in particular in Chapter 8 where I will present the characterization of a large number of gamma-ray flares from the brightest blazars detected by *Fermi*-LAT. An example of adaptively binned light curve is shown in Fig. 3.15.

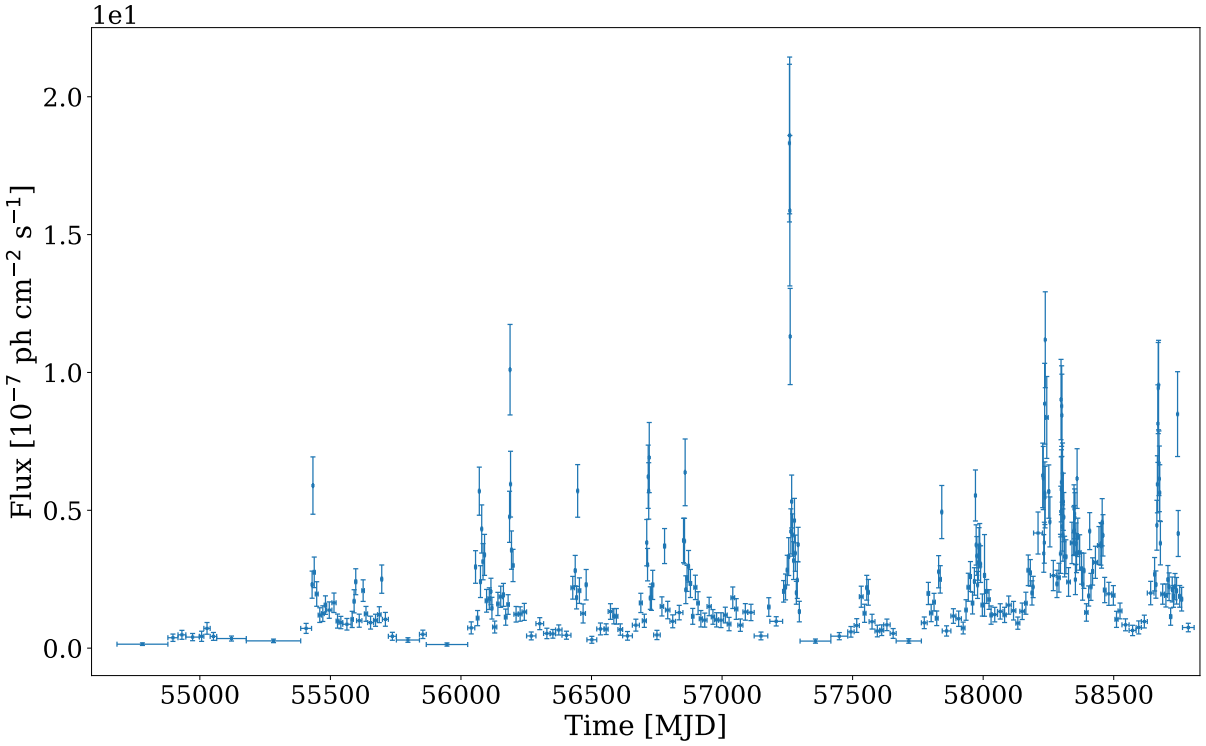

Figure 3.15: Example of an adaptively-binned lightcurve computed with the method in [162] for the source 4FGL J0501.2-0158, associated with the FSRQ S3 0458-02.

The general analysis configurations for the main *Fermi*-LAT analyses presented in the next chapters are described in Appendix A.

The IceCube South Pole Neutrino Observatory

4

4.1 An instrumented, cubic kilometer of Antartic ice

4.1 An instrumented, cubic kilometer of Antartic ice . . 57

4.2 Astrophysical neutrinos and atmospheric background 62

4.3 The Realtime Alert System 64

The detection of neutrino events is one of the most challenging measurements in cosmic-ray physics. The main difficulty comes from the fact that neutrinos interact only via the weak force, and their low cross sections ($\sim 10^{-33}$ cm^2 at 1 PeV [163]) require either a substantial flux of events at Earth or a massive detector. Therefore, it was immediately clear that to move the first steps towards neutrino astronomy at high energies, massive detectors of cubic-kilometer scale were needed [164].

A first milestone in developing such a cubic-kilometer scale detector was the instrumentation of 0.01 km^3 of natural ice with optical sensors in the Antarctic Muon And Neutrino Detector Array (AMANDA) project [165]. The ice serves as a target for neutrino interactions and medium for Cherenkov radiation. In its years of operations, even after its full deployment in 1998, AMANDA was only able to perform measurements of atmospheric neutrinos. For the first significant detection of an astrophysical flux of neutrinos, the scientific community had to wait until the year 2013 when the IceCube South Pole Neutrino Observatory (SPNO) [9], the successor of AMANDA, discovered a diffuse flux of high-energy neutrinos.

The IceCube SPNO consists of 1 km^3 of natural Antartic ice converted into a particle detector by means of optical sensors distributed deeply under the glacier surface, constructed between 2004 and 2011. The in-ice array of instrumentation is composed of a total of 86 vertical strings equipped with optical sensor enclosed in so-called digital optical modules (DOMs). The primary array consists of 78 strings with a vertical separation between DOMs of 17m. The first DOMs are located at a depth of 1450m below the surface, and are arranged in series up to a depth of 2450m, for a total of 60 DOMs per string. The arrangement of the strings follows an hexagonal footprint on a triangular grid with 125 m horizontal separation, resulting in a total volume of 1 km^3 of ice delimited by the instrumental grid. This design is a compromise between the optimization of the low-energy threshold and the effective area for high-energy astrophysical neutrinos in the energy range of $\mathcal{O}$(TeV)-$\mathcal{O}$(PeV) [8]. An artistic representation of the in-ice array is shown in Fig. 4.1, showing also the arrangement of the IceTop array for cosmic-ray measurements and the IceCube Lab (ICL), the central building where the data processing units are hosted.

Each DOM contains both light-sensor and data acquisition modules, enclosed in a glass pressure sphere. The light-sensor is a 10-inch PhotoMultiplier Tube (PMT) sensitive to single-photon measurements in the 300 to 650 nm range, with a photon detection efficiency (PDE) that peaks at 25% for standard DOMs and at 35% for high-quantum efficiency DOMs equipped on a subset of 8 strings, closely spaced in the center of IceCube called *DeepCore* (see Fig. 4.1). The higher quantum-efficiency of the DeepCore's DOMs and the closer spacing of these 8 strings allow

[163]: Cooper-Sarkar et al. (2011), 'The high energy neutrino cross-section in the Standard Model and its uncertainty'

[164]: Roberts (1992), 'The birth of high-energy neutrino astronomy: A personal history of the DUMAND project'

[165]: Andres et al. (2000), 'The AMANDA neutrino telescope: principle of operation and first results'

[9]: IceCube Collaboration (2013), 'Evidence for High-Energy Extraterrestrial Neutrinos at the IceCube Detector'

[8]: Aartsen et al. (2017), 'The IceCube Neutrino Observatory: instrumentation and online systems'

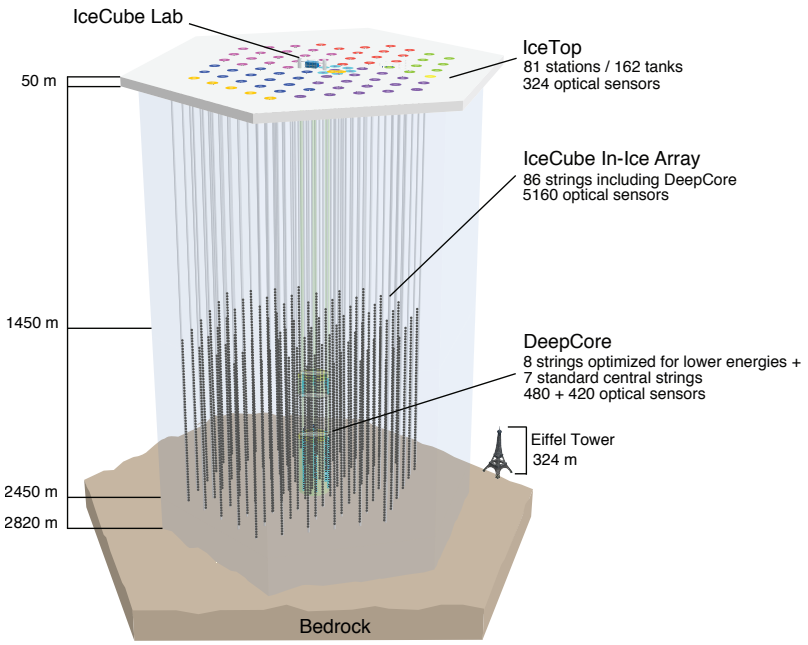

Figure 4.1: Scaled representation of the IceCube South Pole Neutrino Observatory with its main components from [8].

for an improved sensitivity down to 10 GeV, covering the energy scale for atmospheric neutrino oscillation measurements. Around the PMT, an anular-shaped circuit board hosts the signal digitizer and a flasher board with UV/optical LEDs used for calibration purposes. A micro-metal grid surrounds the PMT to shield it from the Earth magnetic field, improving the electron collection performance in the PMT dynodes [166]. A schematic representation of the DOM is shown in Fig. 4.2.

[166]: Abbasi et al. (2010), 'Calibration and characterization of the IceCube photomultiplier tube'

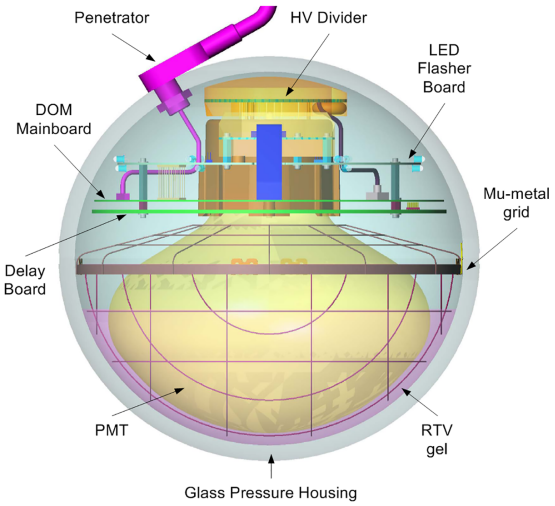

Figure 4.2: Schematic view of the Digital Optical Module (DOM) from [8].

At the glacier surface, an array of 162 tanks arranged in pairs containing ice forms the *IceTop* cosmic-ray detector. Each tank of *IceTop* is equipped internally with two DOMs, and the whole array serves as main instrument for the study of cosmic-ray air showers and as veto detector for the in-ice IceCube array [167].

[167]: Abbasi et al. (2013), 'IceTop: The surface component of IceCube'

High-energy neutrino interactions and event topologies

Typical neutrino interactions in the ice at energies >100 GeV happen mainly via Deep Inelastic Scattering (DIS) where by the exchange of a $W^{\pm}$ (charged current interaction, CC) or a Z^0 (neutral current interaction, NC) boson the neutrino can scatter on individual quarks in a nucleon N[168]. Fig. 4.3 shows the Feynman diagrams of the two possible neutrino interactions and their products.

[168]: Formaggio et al. (2012), 'From eV to EeV: Neutrino cross sections across energy scales'

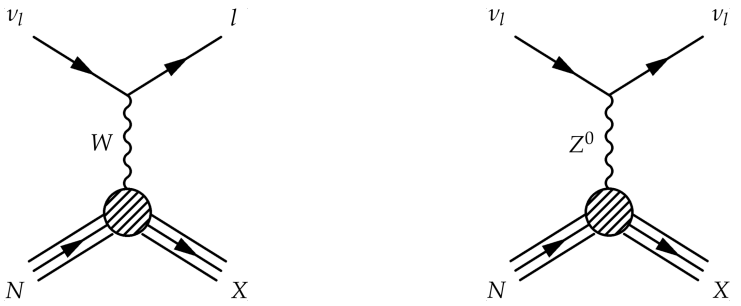

Figure 4.3: Feynman diagrams of the two high-energy neutrinos interaction channels: charged current (CC, left) mediated by a W boson and neutral current (NC, right) mediated by a Z^0 boson.

In CC interactions, a charged lepton is produced, conserving the flavor of the primary neutrino (ν_μ, ν_e or ν_τ), accompanied by a hadronic cascade (X). The cascade is produced by secondary particles from the reaction and the products of their decay and interaction chains. In NC interactions, instead, only momentum is transferred to the nucleus and the outgoing lepton is a neutrino (ν_l) of the same flavor, accompanied by a hadronic cascade (X).
The main radiative process that is detected by optical sensors placed in the instrumented volume of ice is the *Cherenkov radiation*, namely the radiation emitted by a particle that travels faster than the speed of light in a certain medium. This is the case of the secondary charged particles produced in the CC and NC interactions, that are usually relativistic. Indeed, given the velocity $\beta = v/c$ for a particle travelling in a medium with refractive index n, the Cherenkov light is emitted in a cone that forms an angle θ_C with the particle trajectory. The known relation describes the dependency of the emission angle from the refractive index

$$cos\theta_C = \frac{1}{n\beta} \tag{4.1}$$

where $\beta \sim 1$ for relativistic particles, $n \sim 1.32$ for the ice, resulting in an angle of θ_C ~41°. The spectrum of this emitted radiation, namely the number of photons per unit wavelength λ and unit distance x travelled in the medium is given by

$$\frac{dN}{dxd\lambda} = \frac{2\pi\alpha Z^2}{\lambda^2}\left(1 - \frac{1}{n^2(\lambda)\beta^2}\right), \tag{4.2}$$

known as *Frank-Tamm* formula, where Z is the electric charge of the emitting particle, $n(\lambda)$ the refractive index that is a function of the wavelength, and $\alpha \sim 1/137$ is the fine-structure constant. The spectrum of the Cherenkov emission peaks in the near ultra-violet band, and the average radiation produced in ice for a charged particle ($Z = 1$) is N ~ 250 photons/cm, integrating the light in the range 300-500 nm where

the DOMs are most sensitive.
Although the amount of detected photons is used as proxy for the energy deposited by the particles in the detector, the pattern of the Cherenkov light deposition in the detector is also used to classify the events given their topologies. Three different topologies are expected in IceCube after the interaction of astrophysical neutrinos: *Tracks* (Figure 4.4, *left*), *Cascades* (Figure 4.4, *right*) and a combination of the two, called *Double Bangs*.

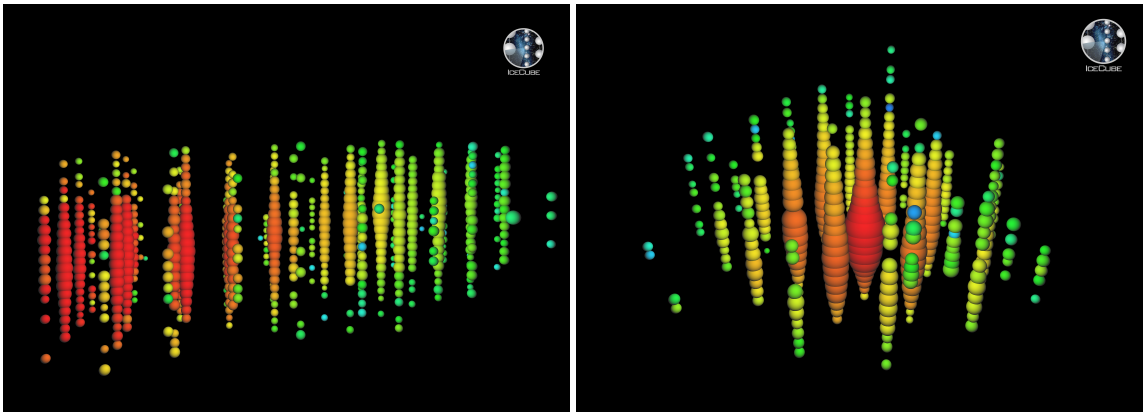

Figure 4.4: Event displays of the Cherenkov light pattern measured in the IceCube DOMs for a track-like event (left) and a cascade-like event (right). Each sphere represents a DOM, with its size proportional to the number of detected photons and the colormap describing the arrival time from the earliest hits in red to the latest in green. The event displays are from https://icecube.wisc.edu/gallery/.

Tracks: Track-like events are tracers of CC interactions of ν_μ, where the muon produced traverses the detector loosing energy mostly by ionization in the ice. About 1% of its total energy is lost by means of Cherenkov radiation, therefore the energy resolution of such events is quite poor. On the other hand, their direction can be very well reconstructed, with a resolution of the order of ~1°that allows to perform astronomical studies on the search of sources of cosmic neutrinos. This is also possible because of the small interaction angle Ψ between the incoming ν_μ and the outgoing muon that has a dependency with the primary neutrino energy given by

$$\Psi = 0.7^\circ \cdot \left(\frac{E_\nu}{\text{TeV}}\right)^{-0.7} \tag{4.3}$$

that is smaller, at all energies, than the angular uncertainty from the reconstruction of the muon track.
The muons that create the track-like pattern inside IceCube can be the result of neutrino interactions that happen outside the instrumented volume (*through-going tracks*), or interactions that happen inside the cubic kilometer of instrumented ice (*starting tracks*). Both topologies of track-like events are used for single-event astronomical studies, but the starting track have a lower angular resolution due to the shorter lever-arm of the muon path inside the detector. Already for energies above 300 GeV, the interaction length of the muon is larger than the kilometer-scale of IceCube, and therefore these events leave a trace that traverse the whole detector and its resolved size depends only on its arrival direction. The light pattern is produced by the cone of Cherenkov radiation emitted by the muon and, since it undergoes also several other kind of energy losses (bremsstrahlung, photo-nuclear interactions, pair production), also

by the superimposition of Cherenkov emission by secondary charged particles produced in these additional interactions. The measurement of all these energy losses by the muon can however only give a lower limit on the energy of the parent neutrino. I will present a deeper overview on track-like events in Sec. 4.3.

Cascades: Cascade-like events can be either traces of CC or NC interactions. In CC interactions this is the case of ν_e producing a secondary electron that interacts almost immediately producing an electromagnetic shower initiated by its bremsstrahlung photons ($X_{0,ice}$ = 39.31 cm). The radiation pattern can be approximated by a spherical shape and, differently from a starting-track event that shows a similar cascade-like pattern near the interaction vertex, in the case of ν_e no track-like pattern is expected outside the cascade region. In the majority of cases, the cascade is pretty-well contained inside the detector volume, and since the majority of energy losses is through the electromagnetic and hadronic showers, it is possible to have a good calorimetric measurement and a fairly good energy resolution of ~15% at TeV energies [169], even if the shower is partially contained. In fact, given the high energy of the events observed, secondary particles in these showers have a high multiplicity and the Cherenkov light undergoes multiple scattering in the ice, resulting in an extension of tens of meter for the light pattern.The resulting angular resolution, however, is on the order of ~10°(median) for energies above 60 TeV[169], and therefore not suitable to pinpoint a single candidate high-energy counterpart in the sky.
Cascade-like radiation patterns are also tracers of NC interactions, and are initiated by the charged particles produced in the hadronic showers mentioned above (X in the Feynman diagram of Fig. 4.3). Because of the coarse arrangement of DOMs within IceCube, the light-pattern of these hadronic showers cannot be distinguished from the one produced by electromagnetic showers in ν_e CC interactions, but their capability of reconstructing the energy of the neutrino is consequently worse.

[169]: Aartsen et al. (2014), 'Energy reconstruction methods in the IceCube neutrino telescope'

Double-bang: In case of ν_τ CC interactions, the topology of the light pattern is a combination of the previous two, presenting both cascade-like and track-like features. These are called *double-bangs* [170] and are composed of two cascades connected by a track-like pattern. The first cascade is created by the hadronic shower from the ν_τ CC interaction and the τ lepton produced travels in the ice creating a track-like pattern similar to the one of a muon. However, the τ has a decay length of about 50m per PeV of energy, that constrains the range for which the resolution of these tracks is possible to energies above ~100 TeV. In the case of τ decay into an electron, a second cascade is observed due to the electromagnetic shower initiated by the latter. In a sample of neutrino events observed by IceCube in 7.5 years, only two double-bang ν_τ candidates have been identified [171].
Another possible interaction is the scattering of the neutrino with the electrons instead of the nucleus. This process is usually rare, because of the small mass of the electron compared to the nucleons. However, in the peculiar case of the scattering of an anti-neutrino $\overline{\nu}_e$ with an electron, the center of mass energy equals the mass of the W boson at the *Glashow resonance* energy [172] given by

[170]: Learned et al. (1995), 'Detecting ν_τ oscillations at PeV energies'

[171]: Abbasi et al. (2020), 'Measurement of Astrophysical Tau Neutrinos in IceCube's High-Energy Starting Events'

[172]: Glashow (1960), 'Resonant Scattering of Antineutrinos'

$$E^{res}_{\bar{\nu}_e} = \frac{m_W^2}{2m_e} \sim 6.3\text{PeV}. \tag{4.4}$$

At the time of this manuscript, one *Glashow resonance* candidate has been identified by IceCube, with the observation of a shower-like event of energy 6.05 ± 0.72 PeV [173].

[173]: Aartsen et al. (2021), 'Detection of a particle shower at the Glashow resonance with IceCube'

[174]: Gandhi et al. (1998), 'Neutrino interactions at ultrahigh energies'

[175]: Bradascio (2021), 'Searches for cross-correlations between IceCube neutrinos and Active Galactic Nuclei selected in various bands of the electromagnetic spectrum'

The left panel of Fig. 4.5 shows the cross sections for the DIS interactions discussed above at the energies where IceCube is sensitive [174, 175]. The cross section for CC interactions is higher than for NC interactions through the whole energy band from 10^2 GeV to 10^{12} GeV of about a factor three. At energies around 10^4 GeV, the transition in the slope of the cross section is due to the propagator of the massive boson. The difference between the cross section of neutrinos (solid lines) and anti-neutrinos (dashed lines) in each interaction becomes negligible for energies above 10^6 GeV, because of the dominant scattering with the sea quarks. The cross section for electron anti-neutrinos is shown as purple dashed line, characterized by the sharp peak of the *Glashow resonance*. The right panel of Fig. 4.5 shows the correspondent interaction lengths. Notably here, is the transition point at $4{\times}10^4$ GeV, where the interaction length for CC interactions becomes smaller than the Earth's diameter, and the detection efficiency for events above such energies starts to suffer from severe absorptions inside the Earth for events coming from below the IceCube horizon.

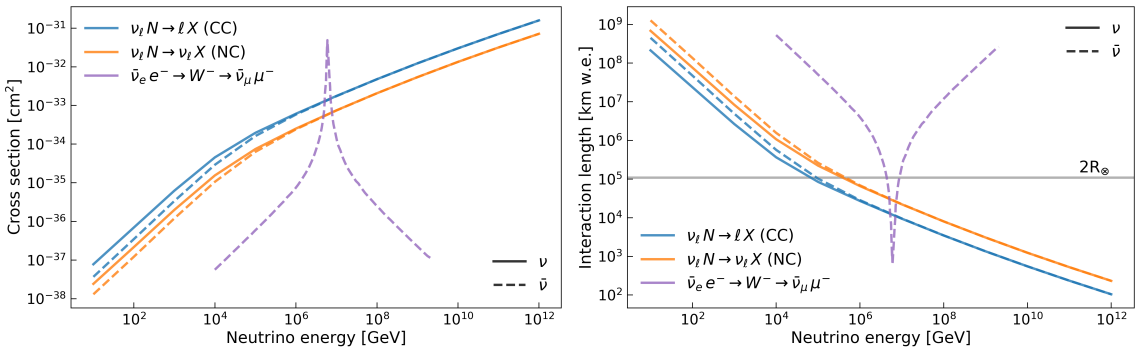

Figure 4.5: Neutrino cross sections (*left*) and interaction lengths (*right*) for DIS interactions in water of neutrinos with a nucleus as a function of the neutrino energy from [175]. CC and NC interactions for neutrinos (solid lines) and anti-neutrinos (dashed lines) are shown, along with the Glashow resonance (purple dashed lines).

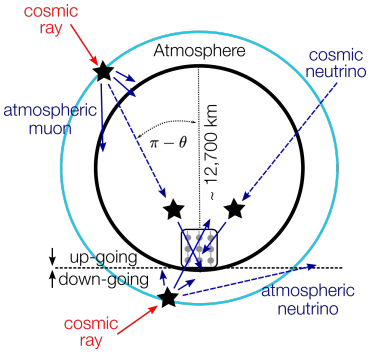

Figure 4.6: Schematic view of the event definitions by their arrival direction from [175].

4.2 Astrophysical neutrinos and atmospheric background

For the purpose of the work presented in this manuscript, I will focus in this chapter on the astrophysical component of neutrinos detected by IceCube.

The main challenge in the observation of astrophysical neutrinos is to remove the background of atmospheric neutrinos and muons produced by the interaction of cosmic rays in the atmosphere. The background component of muons produced in air showers is observed mainly in down-going tracks (see Figure 4.6 for a definition of up-going and down-going events). In the case of up-going and horizontal events, the muons

pass through enough material in the Earth to be efficiently absorbed, but for down-going events the situation is more critical since they only traverse ∼ 1.5 km of Antartic ice before entering the detector volume. A strict energy cut at approximately 10 TeV is necessary to reject a significant amount of atmospheric muons in the Southern hemisphere. Above these energies, a self veto from the identification of multiple, coincident track-like events and the use of IceTop as anti-coincidence detector for showers with axes close to the vertical allow for a good rejection of background events from the southern sky for energies above 10 TeV [176]. However, a critical component of background events remains from the so-called *muon-bundles*, namely multiple muons produced in cosmic-ray interactions in the atmosphere that travel with very similar direction and appear in IceCube as a single, high-energy muon [177].

[176]: Gaisser et al. (2014), 'Generalized self-veto probability for atmospheric neutrinos'

[177]: Vorobev et al. (2021), 'Review of Investigations of Muon Bundles Generated by Very-High-Energy Cosmic Rays'

The other component of background in IceCube is from neutrinos produced in the interaction of cosmic rays in the atmosphere. This is a dominant background that affects both up-going and down-going events in the same way since the path travelled through the Earth for up-going events is not contributing significantly to their interaction. Atmospheric and astrophysical neutrinos cannot be distinguished on an event-by-event basis in the detector, so the selection of the signal (astrophysical) component over the background (atmospheric) is based on their different spectral and arrival direction properties, that come from our knowledge of the well-measured spectrum of atmospheric neutrinos and the expectations for neutrinos accelerated in cosmic-rays sources. For energies below ∼ 300 TeV, the atmospheric component dominates the neutrino spectrum, following a power law $\propto E^{-3.7}$. This steep spectrum is due to the re-interactions of mesons in the air-shower, and the expected rate of atmospheric neutrinos above ∼ 300 TeV reduces to few events per year. The astrophysical neutrino component has a flatter shape following a power law $\sim E^{-2}$ as expected for Fermi acceleration in cosmic sources. Three main methods are used in IceCube to discriminate this component from the atmospheric one:

- Selection of through-going, track-like events from the Northern hemisphere (daughter muons from the interaction of astrophysical neutrinos in the Earth), with the Earth shielding the atmospheric muons and signal/background discrimination based on the different spectral shapes. This method cannot be applied to events arriving from the Southern hemisphere sky and is only sensitive to track-like events.
- Selection of both track-like and cascade-like events, requiring that the interaction happens within the detector volume. These events are called *High Energy Starting Events* (HESE) and for this selection, the peripheral strings of IceCube are used as additional veto region, to exclude e.g. through-going atmospheric muons. This method is sensitive to arrival directions from both hemispheres, but has a lower effective area for ν_μ compared to the selection of through-going events.
- Selection of only cascade-like events, from ν_e and ν_τ events. This method has a great advantage in the purity of the final sample but, as discussed before, the capability of pinpointing astrophysical sources is reduced by a lot given the worse angular resolution of cascade-like events.

[178]: Abbasi et al. (2021), 'Improved Characterization of the Astrophysical Muon-Neutrino Flux with 9.5 Years of IceCube Data'

[179]: Abbasi et al. (2021), 'IceCube high-energy starting event sample: Description and flux characterization with 7.5 years of data'

[180]: Aartsen et al. (2014), 'Observation of High-Energy Astrophysical Neutrinos in Three Years of IceCube Data'

[181]: Aartsen et al. (2020), 'Characteristics of the diffuse astrophysical electron and tau neutrino flux with six years of IceCube high energy cascade data'

Figure 4.7 shows a summary of astrophysical neutrino-flux measurements adapted from [178], the best fit and 95% confidence levels for the spectral index and flux normalization measurements are shown. The orange marker and contour show the measurement using the HESE selection [179] using 7.5 years of all-sky data. The HESE selection was also the one that led to the first discovery of the astrophysical flux using only 3 years of data [180]. The results from 9.5 years of through-going tracks observed from the Northern hemisphere [178] are shown in blue and the measurements from the cascades sample which include 6 years of data from the whole sky [181] are shown in green. A mild tension is observed between the measurements obtained with the HESE sample and those obtained with the through-going tracks and cascades. The measurements are still compatible within the $\sim 2\sigma$ confidence levels, and the mild tension observed could be due to the fact that different samples cover energy ranges which are not completely overlapping. The true shape of the astrophysical neutrino flux could be more complex than the simple power-law distribution that can be discovered with the present observations, and therefore this could lead to different spectral shapes observed in the different samples.

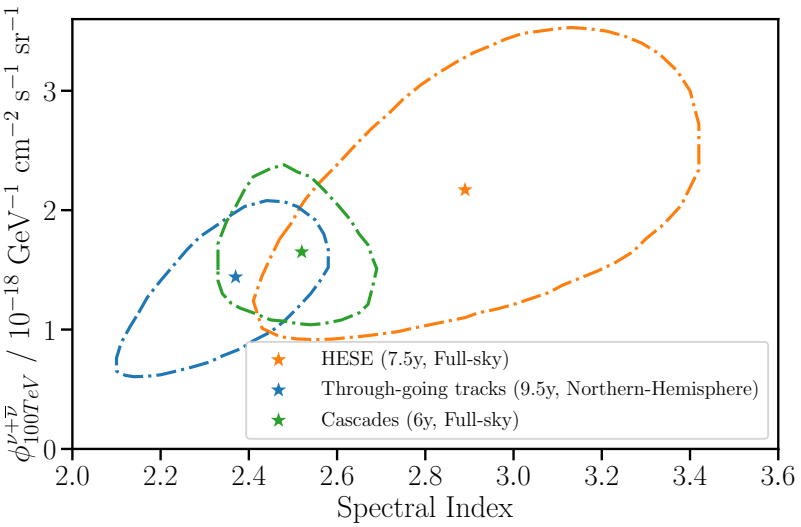

Figure 4.7: Comparison between astrophysical neutrino flux measurements from [178]. The best fit spectral index and flux normalization at 100 TeV are shown on the x and y axes, respectively, along with their 95% CL. The results are from measurements using the 7.5 years HESE sample from the full-sky [179], the 9.5 years sample of through-going tracks from the northern hemisphere [178] and the 6 years sample of cascade events from the full-sky [181].

4.3 The Realtime Alert System

After measuring the astrophysical component of the neutrino flux for the first time [180], the compelling interest in identifying the sources of cosmic neutrinos led to the development of a system that could alert the whole multi-messenger community immediately after the detection of rare neutrino events with a high probability of having an astrophysical origin.

[15]: Aartsen et al. (2017), 'The IceCube realtime alert system'

The IceCube Realtime System [15] selects track-like events from different event selections directly at the South Pole using an online event filter. The selected events are then sent to the IceCube Data Center in Madison

(WI) through the Iridium satellite system and then for each event their probability of being of astrophysical origin (*signalness*) is calculated following the definition in [16]

[16]: Blaufuss et al. (2019), 'The Next Generation of IceCube Real-time Neutrino Alerts'

$$Signalness(E,\delta) = \frac{N_{signal}(E,\delta)}{N_{signal}(E,\delta) + N_{background}(E,\delta)} \tag{4.5}$$

where N_{signal} and $N_{background}$ are the number of signal and background events at a declination δ that have an energy above the energy proxy E for the specific event selection.
At its start in 2016, the Realtime System was based only on the HESE and the *Extremely High Energy* (EHE) event selections [15] and the realtime alerts were issued in two separate streams according to their classification as HESE or EHE, both reporting events with a minimum signalness of 50%. After its upgrade in June 2019 (V2), the *Gamma-ray Follow-Up* (GFU) event selection for track-like signatures was added, and the streams were all unified under two new categories: *Gold* and *Bronze* events. *Gold* events belong to a sample that has an average signalness of 50%, while *Bronze* events belong to a sample with an average signalness of 30%. Here I give a brief overview of each of the three classes of track-like events.

[15]: Aartsen et al. (2017), 'The IceCube realtime alert system'

- **HESE track selection**: the starting-events in this class follow the technique described in the previous section, where the outer strings of IceCube are used as veto region to reject through-going muons and select only neutrino events with the interaction vertex inside the fiducial detector volume. An additional requirement for the HESE events selected in the Realtime Alert System is the requirement of an out-going muon track, to reject the majority of cascade-like HESE detections. The minimum required length of the measured track is 200 meters, to ensure enough lever-arm for good reconstruction of the arrival direction. A final cut introduced in V2 is on the total charge of photoelectrons (PE) recorded by the detector, to define the classification in the *Gold* or *Bronze* stream.
- **EHE track selection**: this selection targets events whose interaction vertex is outside the fiducial volume of the detector, requiring that a single muon track is observed crossing the detector. The energy range of these events is between 500 TeV and 10 PeV, with a selection threshold of 4000 on the number of photoelectrons (NPE) detected from the muon's Cherenkov pattern. To this minimum value of 4000 NPE, an additional declination-dependent cut is required, along with a χ^2 test for track-like hypothesis in order to achieve an average 50% signalness in the final sample. All EHE tracks are therefore classified as *Gold* alerts in V2.
- **GFU track selection**: the Gamma-ray Follow-Up selection has been added in V2 to select high-quality tracks by means of multi-variate classification. The selection algorithm is based on boosted decision trees (BDTs) trained on Monte Carlo simulations and the energy-dependent cuts are treated differently for the two hemispheres. The reconstructed muon energy is used for up-going events from the Northern sky, while a two-dimensional cut dependent on the total PE and declination is applied to down-going events from the Southern sky. These cuts are applied to select only events that

satisfy the 50% and 30% average signalness of the *Gold* and *Bronze* samples, respectively.

Track reconstruction

The event reconstruction during realtime detections requires computationally-efficient methods for the determination of the arrival direction. A first reconstruction method that is applied within the Realtime Alert System is the so-called *Spline Multi-Photo-Electron* (*SplineMPE*) reconstruction. This is a likelihood-based reconstruction based on a spline-interpolated ice propagation model. The assumption on the signal hypothesis is an infinite muon track with continuous energy losses (i. e. minimum ionizing particle), which describes well a significant portion of through-going events but gives a poor description in the case of starting events. Additionally, under this hypothesis stochastic energy losses from the muon are not considered. A detailed description of the SplineMPE method can be found in [182].

[182]: Abbasi et al. (2021), 'A muon-track reconstruction exploiting stochastic losses for large-scale Cherenkov detectors'

Another, more sophisticated (and hence more computationally-expensive) reconstruction method for the neutrino direction is *Millipede*, that was initially conceived as energy reconstruction method [169]. In *Millipede*, the muon track is considered as a sum of several shorter segments, with a typical length of ~10 m, and each of these segments is modelled as a point-like cascade depositing a certain amount of energy. This series of cascade-like emissions models both continuous and stochastic energy losses of the muon along the track. For each DOM, the sum of the expectation in the number of photoelectrons from each individual cascade is considered in a poissonian likelihood, that is maximized over the observed emission recorded in each sensor. The expected number of photoelectrons are initialized with a seed track, usually the one obtained with simple methods like $SplineMPE$. Although this approach was initially developed for energy reconstruction, it was generalized to be used over a grid of different track hypothesis, giving a simultaneous accurate guess on both energy and direction. The generalized method is applied iteratively on a grid all over the sky defined using the HEALpix [159] pixelisation scheme, starting from a coarse resolution and then increasing the grid resolution locally around the maximum of the likelihood landscape (in order to optimize the computational cost of each iteration and likelihood evaluation for each track hypothesis) [183].

[169]: Aartsen et al. (2014), 'Energy reconstruction methods in the IceCube neutrino telescope'

[159]: Górski et al. (2005), 'HEALPix: A Framework for High-Resolution Discretization and Fast Analysis of Data Distributed on the Sphere'

[183]: Kintscher (2018), 'Searching for Transient Neutrino Sources with IceCube in Real-Time'

Expected alert rate

To calculate the expected rates of astrophysical events passing the selections described above, a spectral shape must be assumed on the astrophysical neutrino flux. In the case of the current V2 alert stream, the spectral values measured in [184] are assumed, i.e. a power-law shape with normalization at 100 TeV of 1.01×10^{-18} GeV^{-1} cm^{-2}s^{-1}sr^{-1} and a spectral index of -2.19 . The expected and observed rates for each event selection are listed in Tab. 4.1.

[184]: Haack et al. (2017), 'A measurement of the diffuse astrophysical muon neutrino flux using eight years of IceCube data.'

The observed values are calculated applying the event selections to 7 years of IceCube data [16]. The majority of expected alerts comes from the detection of through-going tracks, and the starting events constitute

[16]: Blaufuss et al. (2019), 'The Next Generation of IceCube Real-time Neutrino Alerts'

	Gold			*Bronze*	
	HESE	EHE	GFU	HESE	GFU
Signal ($E^{-2.19}$)	0.5	2.1	5.1	0.3	2.5
Atmospheric backgrounds	0.4	1.9	4.7	0.9	13.8
Observed historical rate	1.1	4.3	7.8	0.9	18.4

Table 4.1: Expected and observed alert rates (events per year) from [16]. The total values of *Gold* alerts takes into account the overlap between the GFU and EHE event selections.

only a small fraction of the whole sample. Given the known declination dependence of background events discussed in the previous sections, also the arrival directions of realtime alerts are not expected to be isotropic. Figure 4.8 shows the distribution of the number of IceCube realtime alerts expected per year, binned in $sin(\delta)$, where δ is the declination in equatorial coordinates. The majority of alerts is expected for horizontal tracks in the range $0 < \delta < 30°$, just above the celestial equator where IceCube is most sensitive. Though-going tracks from the GFU and EHE selections are the dominant topology in the sample, while starting events from the HESE selection constitute only a minor fraction.

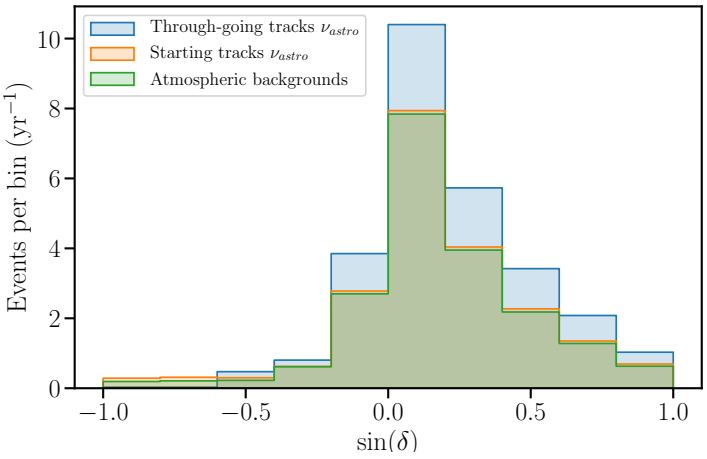

Figure 4.8: Distribution of alert rates (events per year) in declination bins from [16]. Starting tracks are events from the HESE selection, while through-going tracks are events that pass either the GFU or EHE selections.

Each alert is distributed in machine-readable format by the Astrophysical Multimessenger Observatory Network (AMON) [185] through Notices of the Gamma-ray Coordinates Network (GCN)[i], reporting basic informations about the event like the arrival time, signalness and estimated energy and the arrival direction of the event evaluated with the SplineMPE technique.

Immediately after issuing a GCN Notice for the alert, a more sophisticated event reconstruction is performed internally in IceCube using *Millipede*, that usually requires ~2 hours of computational time. Once obtained, the refined localization of the neutrino event is sent via GCN Circular (typically not machine readable) and via machine-readable update of the initial GCN Notice. Another channel used to report on these realtime alerts is the *Astronomer's Telegram* (ATEL) network [ii], which is especially used to report astronomical transients possibly connected with the neutrino detection. I will present a review of the realtime follow-up activities to neutrino alerts with *Fermi*-LAT in Chapter 9.

After the significant impact that the Realtime Alert stream of IceCube track-like events had since its beginning in 2016, new streams of alerts

[185]: Smith et al. (2013), 'The Astrophysical Multimessenger Observatory Network (AMON)'

[i] https://gcn.gsfc.nasa.gov
[ii] https://www.astronomerstelegram.org/

have been developed for the multimessenger community. Among these, there is the stream of alerts from cascade-like events detected by IceCube [iii] with a median angular resolution ~10° but an average signalness much higher compared to the track-like event sample, due to the better purity of the cascades sample. However, the angular resolution for these events is not ideal to obtain significant coincidences with astronomical transients, therefore only coincidences with the alert stream of track-like events will be presented in this thesis work. The full list of alerts from the old and current streams are reported in Appendix B.

[iii] https://gcn.gsfc.nasa.gov/doc/High_Energy_Neutrino_Cascade_Alerts.pdf

Blazar candidate sources to high-energy neutrinos

TXS 0506+056 coincident with IceCube-170922A

5

The observations of the extragalactic neutrino sky, unlike those of the visible sky first by Galileo Galilei and then with the first catalog by Charles Messier in the $17th$ and $18th$ centuries, are only a few years old. After the observations of the low-energy neutrino emission from the supernova SN1987A and the discovery of the astrophysical neutrino flux by IceCube in 2013, we have obtained the first evidence of extragalactic neutrino sources only in 2017. I had the privilege of starting my PhD studies only a few months after the detection of the remarkable event IceCube-170922A, that pointed at the first neutrino blazar candidate, TXS 0506+056. In this chapter, I present the studies I made on this source during the exciting times that followed the detection, using almost a decade of observations with the *Fermi*-LAT. The source revealed not only the coincidence with a single high-energy neutrino, but also with an additional bulk of lower-energy neutrino emission that was hidden in the observations until a dedicated a posteriori search was performed. In a timeframe of only a few weeks, this brought the entire field of neutrino astronomy from a lack of point sources to a fascinating big puzzle to be solved.

5.1 IceCube-170922A 71

5.2 *Fermi*-LAT analysis of the TXS 0506+056 region . . . 73

5.3 Summary 80

Contributions to the work presented in this chapter

The work presented in this Chapter is based on the publication *Garrappa et al. 2019* [38], where we first presented an analysis of two *Fermi*-LAT blazars spatially coincident with IceCube events, one of which was TXS 0506+056. My main technical contribution to this study was the analysis of *Fermi*-LAT data, with special focus on the periods coincident with the neutrino detections.

5.1 IceCube-170922A

As part of the IceCube realtime alert system started in 2016, the most compelling coincidence between a track-type high energy neutrino and an astrophysical source was observed on 2017 September 22 at 20:54:30.43 UTC (MJD 58018.87). The event was classified as an extremely high-energy (*EHE*) through-going muon-track event according to the classification in [15] and has a reconstructed direction of Dec = $5.72^{+0.50}_{-0.30}$ and RA = $77.43^{+0.95}_{-0.65}$ (°, J2000), with a 90% uncertainty area of 1.28 sq. deg. In its passage through the fiducial volume of the detector, IceCube-170922A deposited an energy of (23.7 ± 2.8) TeV and its primary neutrino energy was estimated to be ∼ 290 TeV (with a 90% confidence lower limit of 183 TeV), with a probability to have an astrophysical origin of 56.5% [186]. An event display of IceCube-170922A is shown in Fig.5.1, showing the side and top view of the detector and with the colormap following the temporal evolution of the radiation pattern inside the detector.

[15]: Aartsen et al. (2017), 'The IceCube realtime alert system'

[186]: IceCube Coll. et al. (2018), 'Multimessenger observations of a flaring blazar coincident with high-energy neutrino IceCube-170922A'

After IceCube issued the realtime alert for IceCube-170922A, it was soon observed that its arrival direction was consistent with the gamma-ray

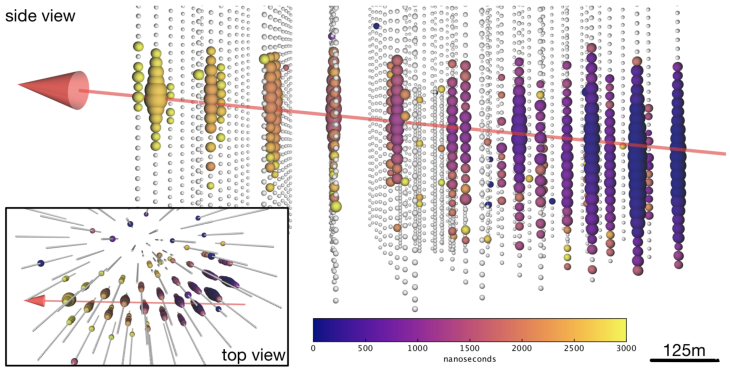

Figure 5.1: Event display of IceCube-170922A from [186]. The red arrow shows the reconstructed directions, and the colormap indicates the time lag between the time of the first radiation detected in the first optical module and the subsequent detections along the radiation path of the event, in nanoseconds. The lower left panel shows the top view of the event.

blazar TXS 0506+056 and, after IceCube released the refined reconstruction described in Chapter 4, no further high-energy sources were found coincident with the well contained 90% uncertainty region.
During the daily, all-sky monitoring of *Fermi*-LAT, the source was observed in a state of enhanced activity for several months before the neutrino detection and was subsequently reported as a potential electromagnetic counterpart of IceCube-170922A [187]. Fig. 5.2 shows a counts map of *Fermi*-LAT data with the best-fit neutrino localization and the 90% contour. Two weeks later, the source was detected at energies > 100 GeV for the first time by the *MAGIC* [186] [19], and later confirmed by *VERITAS* [20] Imaging Air Cherenkov Telescopes.

[187]: Tanaka et al. (2017), 'Fermi-LAT detection of increased gamma-ray activity of TXS 0506+056, located inside the IceCube-170922A error region.'

[19]: Ansoldi et al. (2018), 'The Blazar TXS 0506+056 Associated with a High-energy Neutrino: Insights into Extragalactic Jets and Cosmic-Ray Acceleration'

[20]: Abeysekara et al. (2018), 'VERITAS Observations of the BL Lac Object TXS 0506+056'

These detections of a coincident source at high energies triggered an extensive multi-wavelength campaign of the source with observations down to radio frequencies, providing an incredible amount of quasi-simultaneous data of the source for the interpretation of this remarkable coincidence. Dedicated searches for neutrino events were also performed with ANTARES (Astronomy with a Neutrino Telescope and Abyss environmental RE- Search) in the time window [T_0-1 day, T_0+1 day] (where T_0 is the time of the neutrino arrival), and no neutrino candidates were found [188]. This was not unexpected, since at the declination of the arrival direction of IceCube-170922A the effective area of ANTARES is smaller by about a factor 10 compared to IceCube. A comprehensive description of the multi-wavelength campaign that followed the detection of IceCube-170922A can be found in [186].

[188]: Dornic et al. (2017), 'Search for counterpart to IceCube-170922A with ANTARES'

The chance coincidence for the association of IceCube-170922A with the gamma-ray blazar TXS 0506+056 during its brightest flaring activity was excluded at 3σ level, making this the first compelling identification of an extragalactic source with a cosmic neutrino. This motivated a further search for additional neutrino emission observed from the direction of IceCube-170922A in the previous decade of IceCube archival data. Interestingly, a time-dependent analysis of about 9.5 years of IceCube data revealed an excess of low (~ 1-10 TeV) neutrinos consistent with the position of TXS 0506+056 clustered in space and time, with a post-trial significance of 3.5σ [37]. The excess was found testing time windows of variable width, and cross-checked using two different kernels of box and Gaussian shape. The findings of both kernels are shown in Fig. 5.3 and locate the excess in a period between 2014 September and 2015 March,

[37]: Aartsen et al. (2018), 'Neutrino emission from the direction of the blazar TXS 0506+056 prior to the IceCube-170922A alert'

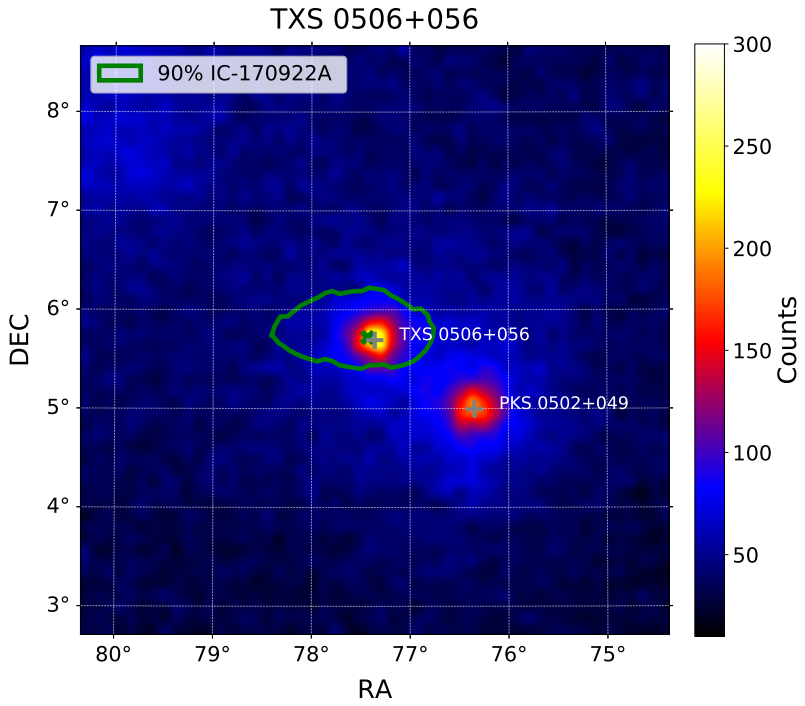

Figure 5.2: Counts map of *Fermi*-LAT (E>100 MeV) of the region centered on TXS 0506+056 from [38]. The 90% neutrino angular uncertainty is shown as green contour and the best-fit neutrino position is marked by a green cross.

with a duration of 110 days for the Gaussian kernel (orange solid line) and 158 days for the box-shaped window (blue solid line).

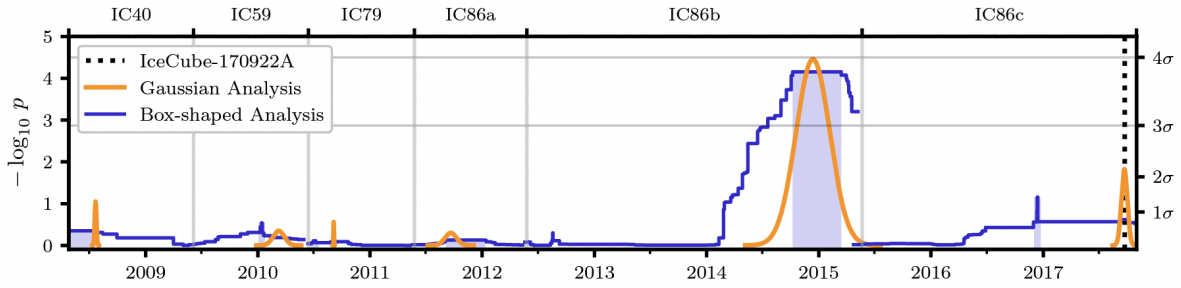

Figure 5.3: Time-dependent analysis results from [37]. The orange curve shows the results from the Gaussian-shaped time profile, while the blue curve shows the results from the box-shaped time profile.

In the following sections, I will describe the gamma-ray analysis I have performed on the region of IceCube-170922A [38]. The analysis uses 9.6 years of *Fermi*-LAT data and gives a detailed picture of the behaviour of TXS 0506+056 in the two periods coincident with the neutrino detection.

[38]: Garrappa et al. (2019), 'Investigation of Two Fermi-LAT Gamma-Ray Blazars Coincident with High-energy Neutrinos Detected by IceCube'

5.2 *Fermi*-LAT analysis of the TXS 0506+056 region

The gamma-ray source TXS 0506+056 at Dec= +5.69°, RA=77.36° is located within the 50% IceCube-170922A angular uncertainty region, at a distance of 0.1° from the best fit neutrino position (see Fig. 5.2). The source is listed in the 4FGL and 3FHL catalogs as 4FGL J0509.4+0541 and

[144]: Ajello et al. (2017), '3FHL: The Third Catalog of Hard Fermi-LAT Sources'

3FHL J0509.4+0541, respectively [144]. Its detection in the 3FHL catalog (that focuses on the energy range from 10 GeV to 2 TeV) identifies the source already as a potential target for very-high-energy gamma-ray emission. TXS 0506+056 is among the brightest 4.4% (5.9%) sources in the 4FGL (3FHL) in terms of gamma-ray energy flux integrated within the energy bounds of the corresponding catalogs [144]. The redshift was measured at $z = 0.336$ by [189] and later confirmed by [190] at $z = 0.3365 \pm 0.0010$. The source is classified as a BL Lac object [191] and recently tentatively associated to a new class of blazars called *masquerading BL Lac*, namely objects that are intrinsically FSRQs with hidden broad lines and a standard Shakura–Sunyaev accretion disk [61].

[191]: Véron-Cetty et al. (2006), 'A catalogue of quasars and active nuclei: 12th edition'

[61]: Padovani et al. (2019), 'TXS 0506+056, the first cosmic neutrino source, is not a BL Lac'

5.2.1 Spectral analysis

For this analysis, we consider 9.6 years of *Fermi*-LAT data in the region of the sky around IceCube-170922A [38]. The analyses performed have the same main configuration as described in Appendix A, except for specific approaches that are applied on specific cases that I will describe in these sections.

[38]: Garrappa et al. (2019), 'Investigation of Two Fermi-LAT Gamma-Ray Blazars Coincident with High-energy Neutrinos Detected by IceCube'

In the 3FGL catalog the gamma-ray spectrum of TXS 0506+056 was modelled with a simple power-law function. However, we can attempt to better describe the curved spectrum revealed by an increased set of data by exploring more complex spectral models. In this analysis we adopt a log-parabola function to describe the spectral energy distribution of TXS 0506+056, which contains one additional parameter compared to a power-law and is commonly used to describe curved spectra of gamma-ray blazars (See also Chapter 3):

$$\frac{dN}{dE} = N_0 \left(\frac{E}{E_b}\right)^{-(\alpha+\beta\log(E/E_b))} . \tag{5.1}$$

where β describes the curvature and α is the analogous of the spectral index in the power-law analytical expression (equivalent to a log-parabola with $\beta = 0$). Throughout this analysis, we will fix the value of the pivot energy to $E_b = 1.44$ GeV.

Given the analytical relation between the log-parabola and the power-law expressions, they can be considered as nested models[i] and therefore a likelihood-ratio test can be applied to check if a model with a larger number of free parameters (in our case, a log-parabola) is statistically preferred to a more simple model with less free parameters (i.e. a power law).

We find that, considering almost a decade of LAT data, a log-parabola model is preferred with a test statistic TS_{SS} for the different spectral shape models of

$$TS_{SS} = -2(\log \mathcal{L}_{PL} - \log \mathcal{L}_{LP}) = 374.3 \sim 19\sigma \tag{5.2}$$

[i] Two models are nested when the parameter space of one is a subset of the parameter space of the other.

(i.e. the log-parabola model describes the data better with an equivalent significance of 19σ for a normal distribution). Here, $\mathscr{L}_{PL}$ and $\mathscr{L}_{LP}$ are the maximum likelihoods for the power-law and log-parabola spectral model, respectively.
For TXS 0506+056 we obtain the best-fit model parameters of $\alpha = 2.03 \pm 0.02$, $\beta = 0.05 \pm 0.01$ and $N_0 = (4.16 \pm 0.08) \times 10^{-12}\,\mathrm{cm^{-2}\,s^{-1}\,MeV^{-1}}$ (gray spectrum in Fig. 5.4).

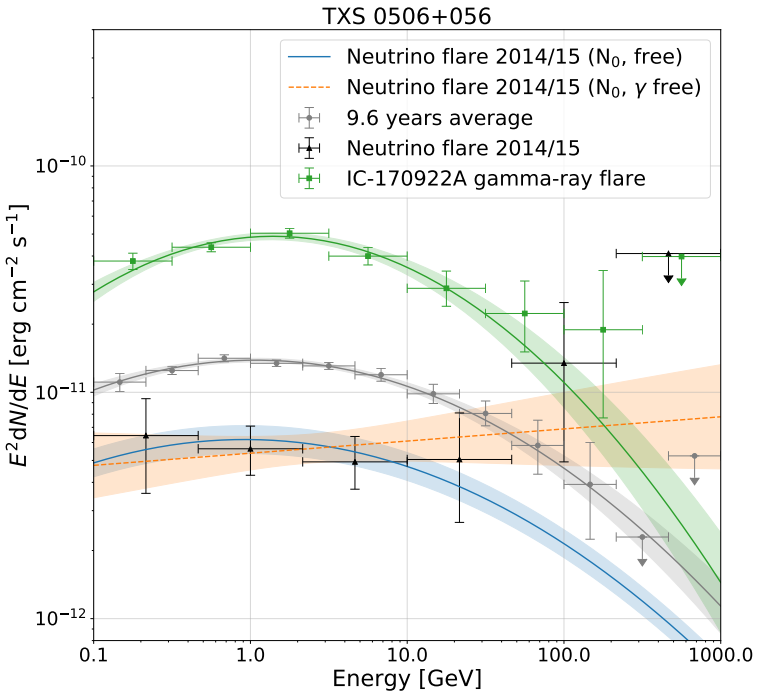

Figure 5.4: TXS 0506+056 spectral comparison using 2014-15 neutrino flare time window from [38].

A major challenge in the modelling of this region, is the presence of the bright, nearby FGL source PKS 0502+049 at Dec= +4.99 and RA= 76.35 (°, J2000) that is located only 1.23°away from TXS 0506+056. This relatively small distance, comparable to the PSF values of the LAT for energies < 1 GeV, requires the source model to be properly handled during the analysis, in order to disentangle the two bright emissions.
The spectrum of PKS 0502+049 is well-modeled by a log-parabola function with best fit values of $\alpha = 2.34 \pm 0.02$, $\beta = 0.10 \pm 0.01$ and $N_0 = (1.08 \pm 0.02) \times 10^{-11}\,\mathrm{cm^{-2}\,s^{-1}\,MeV^{-1}}$. Although TXS 0506+056 is less bright than PKS 0502+049 for energies below 1 GeV, its energy flux integrated over the whole analysis energy range results in $(8.17 \pm 0.29) \times 10^{-11}\,\mathrm{erg\,cm^{-2}\,s^{-1}}$ compared to $(6.70 \pm 0.13) \times 10^{-11}\,\mathrm{erg\,cm^{-2}\,s^{-1}}$ for the nearby source.
The gamma-ray sky region is well described by the best-fit model, as can be seen in the residual map shown in Fig. 5.5, which shows no significant structure that could arise from sources not properly modelled or diffuse components. Previous studies discussed a possible source confusion between PKS 0502+049 and TXS 0506+056 [192] and speculated if the archival neutrino flare originated in PKS 0502+049 [193]. However, based on the precision in the spacial and temporal localization provided by the present analysis, this hypothesis can be excluded.

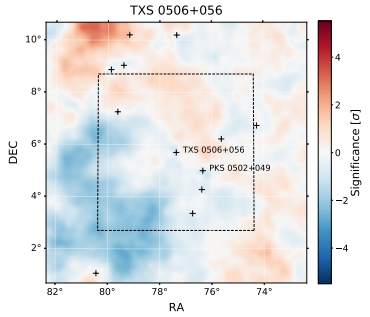

Figure 5.5: Residual map of the TXS 0506+056 region from [38]. The dashed square indicates the portion of ROI shown in the counts map of Fig. 5.2. The colorbar measures the significance of the deviations of the model from data.

At the time of the work, only the catalogs up to the 3FGL were available, that was limited to only 4 years of data. Using more than twice the observation time, it is not uncommon to detect new sources not listed in the published catalogs. This could be due to the awakening of sources at more recent times, or to their lower gamma-ray brightness and consequently longer integration time required to reach a significant detection. This is the case of the detection of a new gamma-ray excess with $TS_{det} > 25$, where

$$TS_{det} = \log \mathscr{L}(\mathscr{H}_1) - \log \mathscr{L}(\mathscr{H}_0) \tag{5.3}$$

describes the difference in the maximum log-likelihood of the whole ROI model with ($\mathscr{H}_1$) and without ($\mathscr{H}_0$) the source after running the source-finding algorithm of `fermipy`. The new gamma-ray emitter *Fermi* J0517.5+0858 is found with a best-fit localization at a distance of 2.37° from TXS 0506+056, and outside the neutrino contour. The source is now listed in the fourth LAT catalog as 4FGL J0517.5+0858, with no association.

5.2.2 Light Curve Analysis

In order to study the temporal behaviour of TXS 0506+056 in gamma rays, we produced an adaptively-binned (AB) light curve, following the procedure in [162] (See also Ch. 3). The adaptive binning method consists in the computation of optimal time intervals that satisfy a common criterion of detectability for the source. For this analysis, I chose a time binning that yields 15% flux uncertainty in an energy range from 300 MeV to 1 TeV. The lower cut on the energy range was chosen as the optimum energy where the flux and the spectral index are decorrelated in the source model, as shown in [162]. A likelihood fit was performed in each bin using a power-law model for TXS 0506+056 while allowing the spectral normalizations of the closest (< 3°) neighbouring sources detected with TS > 16 (> 4σ), to vary. The choice of using the power-law model instead of the log-parabola in the spectral analysis described in the previous section comes from the fact that with the increase in the statistics of observed photons, the adaptive bins can resolve very small timescales, with a bin-width that can get as small as hours or minutes. Therefore, at these short timescales, the source spectrum can be well described by a simple power-law, and the log-parabola model is generally not statistically preferred.The flux and spectral index variation are shown in Fig. 5.6 in the top and middle panel, respectively.
In order to identify and characterize statistically-significant variations in the light curve, we apply the Bayesian Block algorithm outlined in [194], using the `astropy` implementation [195, 196]. To determine the optimal value of the prior for the number of blocks, we use the empirical relation in [194] for the probability to falsely report a detection of a change point. This probability, which represents the relative frequency with which the algorithm reports the presence of a change point in data with no signal present, was set to 0.05. The Bayesian Blocks representation of the lightcurve is shown as a solid black line in the top panel of Fig. 5.6.

[162]: Lott et al. (2012), 'An adaptive-binning method for generating constant-uncertainty/constant-significance light curves with Fermi-LAT data'

[195]: Astropy Collaboration et al. (2013), 'Astropy: A community Python package for astronomy'

[196]: Price-Whelan et al. (2018), 'The Astropy Project: Building an Open-science Project and Status of the v2.0 Core Package'

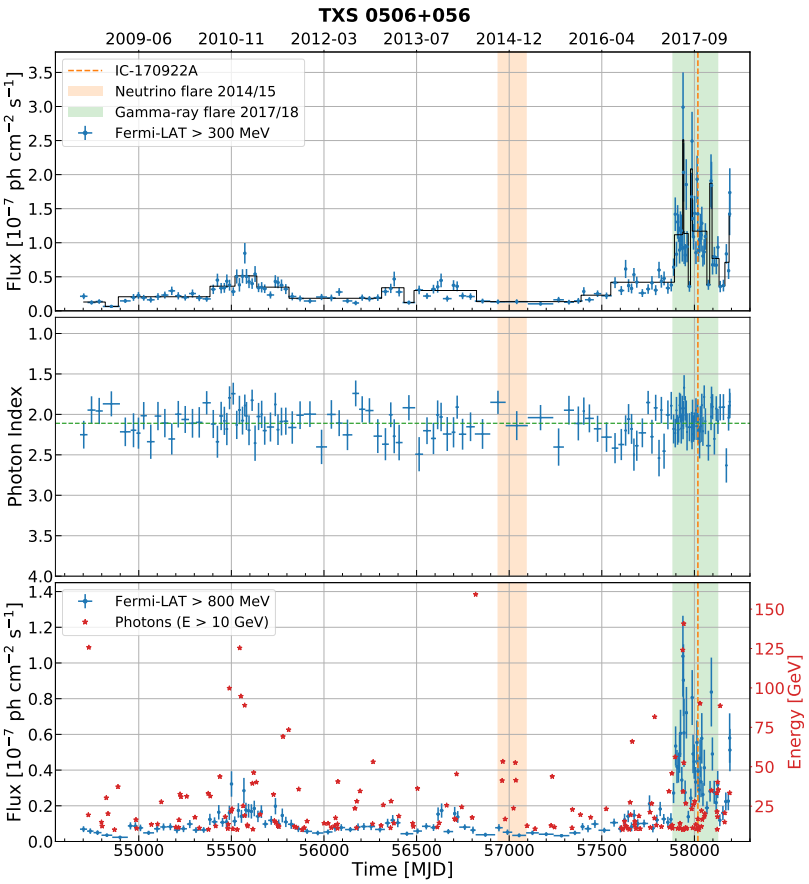

Figure 5.6: Adaptive binned light curve for TXS 0506+056 from [38]. Panel 1 shows the gamma-ray flux integrated above 300 MeV including the Bayesian Block representation shown in black, panel 2 shows the power-law spectral index and panel 3 shows the gamma-ray flux integrated above 800 MeV. The average spectral index is shown as horizontal dashed green line in panel 2. The third panel additionally includes photons above 10 GeV shown with red stars.

The 2017 outburst: The reader can immediately notice that the largest historical gamma-ray outburst for TXS 0506+056 occurred in 2017, and the detection of IceCube-170922A falls during this period of enhanced emission. A closer investigation to this flaring activity shows significant structures, which are highlighted by the Bayesian Block representation (see Fig. 5.7). This outburst lasted for about 9 months and can be modelled by three distinct flares, characterised by a typical exponential rise and fall of the flux (highlighted with shaded colored areas in Figure 5.7). These flaring windows range from MJD 57881-57963 (green shaded area), 57983-58062 (pink shaded area) and 58088-58130 (purple shaded area). The flux normalization during the sub-flares is 6.09, 6.37 and 5.1 times larger compared to the 700-days quiescent state selected between MJD 55800-56500. These sub-flares are characterized by fast variability, with the shortest timescale for significant variation detected by the Bayesian Block of ~1 week (in the observer frame). IceCube-170922A is detected during the second of these three substructures of the outburst, in which the Bayesian Blocks identify significant variations of the flux, happening also around the time of the neutrino arrival. A further characterization of these flaring activities is presented in Chapter 8.

The second panel of Fig. 5.6 shows the light curve of the spectral index for the power-law model used to fit the source in each bin. The spectral index shows, overall, small variations with respect to the average index of

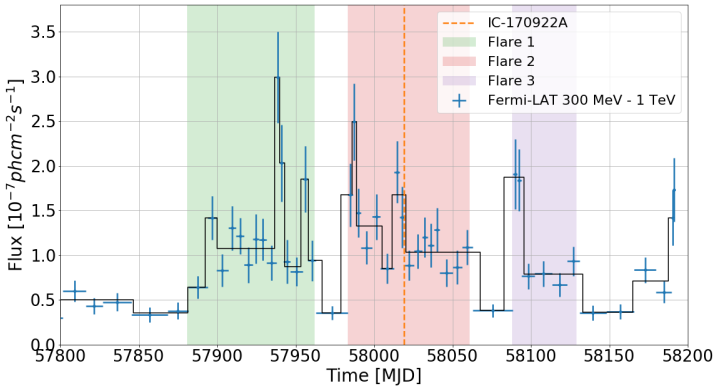

Figure 5.7: Zoomed view of the 2017 TXS 0506+056 outburst between MJD 57881-58130 extracted from Fig. 5.6. The dashed orange line shows the arrival time of IceCube-170922A, while the shaded coloured areas highlight the three distinct flares.

α=2.11 and the source is observed in no extended time periods of spectral hardening or softening over the full 9.6-year time range of observations.

The 2014-15 neutrino flare: During the 2014-15 neutrino flare, differently from the large gamma-ray outburst observed in 2017, the source displays no remarkable activity (see orange region in Fig. 5.6). The resulting adaptive bins in this period are quite large in width, and the flux level measured from the source is among the lowest in the history of LAT observations from this source. The source is in a persistent low state starting from mid-2014 up to the beginning of 2016, when the Bayesian Blocks start picking significant, moderate and slow flux enhancements that lead to the strong outburst in the beginning of 2017. The time window we select to isolate the period of the neutrino flare is the 158-day one from the box-shaped kernel (Fig. 5.3) between MJD 56928-57086, that gives a sharper definition for the start and stop time, compared to the gaussian time-window.
To further investigate the object's behaviour during the neutrino flare, we derive the best-fit model for the region in the 158 days of the neutrino flare and we then use the likelihood technique to robustly quantify any potential spectral change of the TXS 0506+056 gamma-ray spectrum with respect to the average one. The likelihood ratio tests the hypothesis $\mathcal{H}_0$ (i.e. the gamma-ray spectral shape is identical to the average one), against the hypothesis $\mathcal{H}_1$ (i.e. an alternative spectral shape). The two hypothesis in our specific application are defined as the following:

- The $\mathcal{H}_0$ model allows only the normalization of TXS 0506+056 to vary in the fit, while the spectral index is fixed to the average values obtained from the 9.6-years analysis;
- The $\mathcal{H}_1$ model has the spectral index of the power-law model for TXS 0506+056 as an additional free parameter, and is the alternative model to be compared to.

All the other sources in the ROI, along with the Galactic and isotropic diffuse models, have the spectral parameters (including the normalisation) fixed to the 9.6-years fit results for both the hypothesis, except for the nearby source PKS 0502+049 whose parameters are kept free in both hypothesis. We define the test statistic describing spectral change as

$$TS_{SC} = -2(\log \mathcal{L}_0 - \log \mathcal{L}_1), \tag{5.4}$$

where $\mathcal{L}_0$ is the likelihood for the null hypothesis $\mathcal{H}_0$, and $\mathcal{L}_1$ is the one corresponding to the alternative hypothesis $\mathcal{H}_1$, both for the whole ROI. We repeated the analysis for various low energy thresholds E_{min} (0.1, 0.5, 1, 2 and 10 GeV) and model TXS 0506+056 with two different spectral shapes (power-law and log-parabola). We adopt this approach to check for a possible bias in this test introduced by a specific choice of the low energy threshold.
The results are summarized in Table 5.1, showing the statistical metrics of the test performed for each E_{min} and for both the log-parabola and power-law models. Differently from the power-law model that introduces only 1 free parameter (α) the log-parabola spectral shape introduces two additional parameters (α and β) that are left free in the $\mathcal{H}_1$ model with respect to $\mathcal{H}_0$. The correspondent p-value of each test is calculated according to Wilks' theorem [197], according to which the distribution of TS_{SC} can be assumed to follow a χ^2 distribution with one and two degrees of freedom for the power-law or log-parabola spectral model, respectively [161]. The p-value obtained from the χ^2 distribution is converted to a Gaussian equivalent two-sided significance in units of sigma. For all tested cases, the lowest p-value found for the spectral change is 4% (corresponding to a significance of 2.06σ), for E_{min} = 2 GeV. For other values of E_{min}, the p-values reach values up to 27%. Given the fact that the highest significance is at 2σ level, we conclude that there is no significant evidence in favour of a hardening or softening of the spectrum during the detection of the neutrino flare.

[197]: Wilks (1938), 'The Large-Sample Distribution of the Likelihood Ratio for Testing Composite Hypotheses'

[161]: Mattox et al. (1996), 'The Likelihood Analysis of EGRET Data'

Table 5.1: Significance of spectral variations during the box time window of the neutrino flare from [38].

E_{min}	log parabola			power law			power law index
[GeV]	TS_{SC}	σ	p-value	TS_{SC}	σ	p-value	
0.1	2.49	1.06	0.29	1.28	1.13	0.26	1.95 ± 0.12
0.5	4.13	1.53	0.13	3.87	1.97	0.05	1.88 ± 0.13
1.0	2.33	1.01	0.31	1.20	1.09	0.27	1.98 ± 0.17
2.0	5.12	1.77	0.08	4.25	2.06	0.04	1.76 ± 0.20
10.0	3.64	1.40	0.16	2.19	1.48	0.14	1.77 ± 0.40

In the work [192], a spectral hardening was claimed during the neutrino flare with a 2% p-value, considering the energy range with $E_{min} > 2$ GeV. In their analysis, the threshold for E_{min} was chosen to avoid source confusion at lower energies with the neighbouring source PKS 0502+049. In our analysis, we overcome the problem of source confusion by including the PKS 0502+049 normalization as additional free parameter in our ROI model. As already shown in the previous section, the robustness of our results is confirmed by the absence of significant residuals in the region of the two sources (see Fig. 5.5).

[192]: Padovani et al. (2018), 'Dissecting the region around IceCube-170922A: the blazar TXS 0506+056 as the first cosmic neutrino source'

In the absence of TeV gamma-ray observations in the period coincident with the neutrino flare, we have investigated possible patterns in the high-energy emission (>10 GeV) observed in *Fermi*-LAT data. If we assume a simple correlation between gamma-ray and neutrino emission in blazars, an excess in high-energy photons observed by the *Fermi*-LAT may be the best tracer for neutrino emission, even in presence of a lack of enhanced

Table 5.2: High-energy photons associated with TXS 0506+056 with a probability of > 80% detected during the neutrino flare time interval from [38]

arrival time [MJD]	dist. [°]	energy [GeV]	prob. [%]
56961.908	0.18	41.19	97.18
56965.688	0.02	53.31	99.97
56978.261	0.20	16.77	95.12
57023.479	0.05	23.67	99.90
57033.211	0.09	52.56	99.57
57035.923	0.26	41.40	94.16

overall emission. A broader study on this correlation will be presented in Chapter 9, while for the moment I will focus on the analysis performed only during the neutrino flare period.
When we perform an unbinned likelihood analysis during the 158 days, in order to associate a probability for each observed photon to belong to a component in our model (i.e. a source or a diffuse component). We find only 6 photons with E > 10 GeV during the 158-days period with a probability to be associated with TXS 0506+056 higher than 80%. Their arrival time, distance from the source, energy and association probability are listed in Table 5.2.
To assess if there was some unexpected excess of high-energy emission in this period, we assume the quiescent state period of MJD 55800-56500. Assuming the average spectral shape of the source in this interval and refitting its normalization in the 158 days of the neutrino flare, we can calculate the expected number of high-energy photons. We obtain 4.44 (0.69) photons above 10 (50) GeV. Considering that we observe six photons above 10 GeV of which 2 above 50 GeV, we quantify this excess with a p-value of 15% from Poisson statistics, corresponding to a one-sided Gaussian equivalent significance of 1σ. These findings are fully compatible with the expectations in absence of a spectral change in the source. The bottom panel of Fig. 5.6 shows each high-energy photon (E > 10 GeV) observed from TXS 0506+056 (red star markers), overlayed to the flux light curve. The highest-energy photon associated with TXS 0506+056 over the 9.6-year period was detected on MJD 56819, has an energy of 159.3 GeV and is outside the neutrino flare time window.
We then repeat the same exercise to all the three substructures of the 2017 outburst, were we find TS_{SC} values (starting from 100 MeV) of 3.5, 3.4 and 1.77 using a log-parabola function with two extra degrees of freedom pointing to similar spectral shapes compared to the average 9.6-years spectrum. All results show that the spectral shape in all three substructures are compatible with the average spectrum within 1σ. Integrating over the whole 2017 outburst duration, we find 39 (5) photons above 10 GeV (50 GeV), which are compatible with the expected number of photons assuming the average spectral shape and a normalization fitted in the flare time window of 44.37 (4.16).

5.3 Summary

In this chapter, I have presented the results of a detailed gamma-ray analysis of the blazar TXS 0506+056 over 9.6 years of *Fermi*-LAT observations. With an association as counterpart of the high-energy neutrino IceCube-170922A at 3σ level, this is to date (at the time of the preparation of this manuscript) the extragalactic source with the highest association

significance with a single high-energy neutrino. This result has not only motivated the astronomical community to investigate the electromagnetic emission of the blazar after the neutrino detection, but also the IceCube Collaboration to look back into archival data from the direction of the blazar. This led to the discovery of a burst of lower-energy neutrinos back in 2014-15, where 13±5 events where found clustered in space and time with a significance of 3.5σ. These discoveries were the motivation behind the gamma-ray analysis presented in this chapter, which resulted in a detailed description of gamma-ray emission from TXS 0506+056 in the time periods surrounding the neutrino emission. Figure 5.8 shows the two gamma-ray SEDs from the work described in this chapter in comparison with multiwavelength observations collected in [186]. In the following, I summarize these results and their implications in light of other studies of this blazar as candidate neutrino source.

[186]: IceCube Coll. et al. (2018), 'Multimessenger observations of a flaring blazar coincident with high-energy neutrino IceCube-170922A'

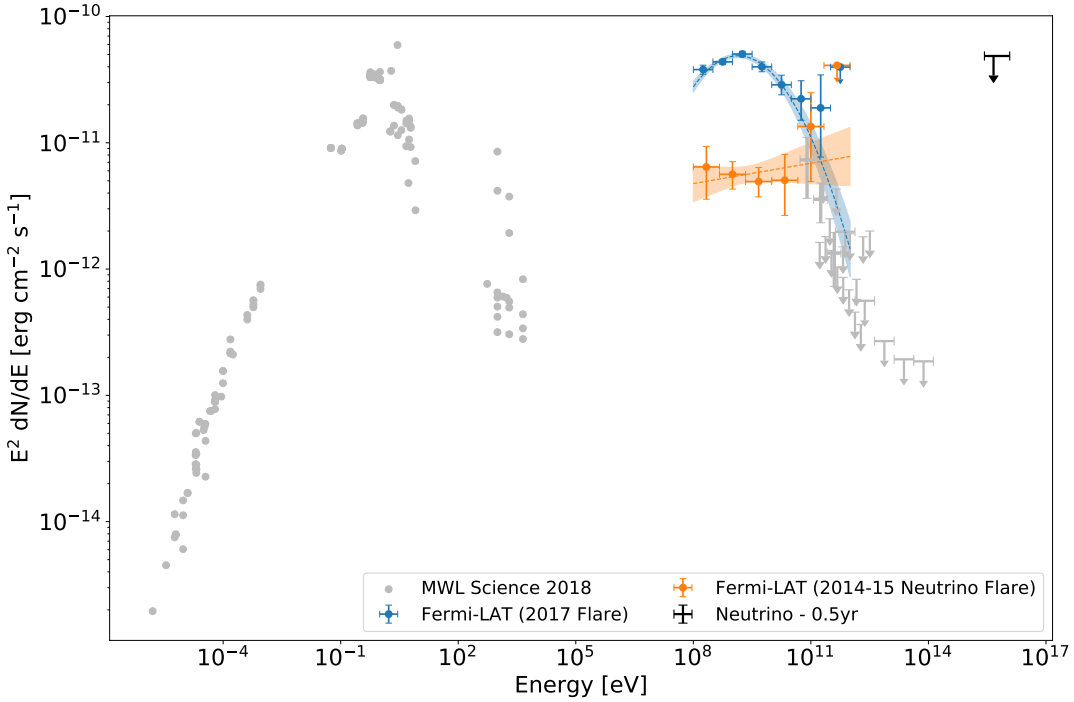

Figure 5.8: Broadband SED of TXS 0506+056 adapted from [186]. The grey points are the multiwavelength data collected in [186], while the *Fermi*-LAT SED from the 2017 flare (blue points) and the one simultaneous to the 2014-15 neutrino flare (orange points) are from [38].

The 2017 outburst: During the bright gamma-ray flare in 2017 coincident with IceCube-170922A, we detect the source with high significance over daily timescales in *Fermi*-LAT data, with the Bayesian Blocks representation able to resolve significant variations down to weekly timescales. Even shorter variability timescales were found in the >100 GeV band by MAGIC [19], which further support the existence of a compact emission region that found already evidences in *Fermi*-LAT data. The outburst structure can be dissected in three main bright flaring states, separated by two short quiescent periods (Fig. 5.7). IceCube-170922A is detected in the middle of the second one, while the source was showing significantly enhanced emission.

Several works attempted the numerical modelling of the broadband SED shown by TXS 0506+056 simultaneous to the neutrino detection. The one-zone model was the most commonly used approach, as in the case of [19, 198–200] where, despite the different assumption on the leading mechanisms behind the hadronic interactions, all agree with an expectation of ∼0.1 neutrino in 6-months (rough duration considered for the outburst). This is compatible with the detection of a single high-energy event due to the Eddington bias discussed in [201]. More exotic models consider multiple zones [202, 203] or interactions between jet and a star or gas cloud [204] but obtain anyway similar estimations.
Some interesting findings come from VLBA observations at 15 GHz, where the jet structure of TXS 0506+056 appears strongly curved, and has been interpreted with the interaction of two jets. The two jet components point to the presence of a merging system at the galaxy center and the interactions between jet material would explain the observation of IceCube-170922A [205]. However, the double-jet structure is not confirmed in VLBA observations at 43 GHz, and seems consistent with a single jet with spine-sheath structure [206].
The 2014-15 neutrino flare: The behaviour of the source during the period of the neutrino flare detection is totally different, and our light curve analysis shows the source in a long quiescent state, with a level of emission so low that the adaptive bins covering that period have a length of ∼70 days. Our detailed analysis on the spectral shape revealed also that no significant change is observed and therefore the gamma-rays appear not to be a tracer of this phenomenon. This brought several challenges in the numerical modelling of the emission during this period, where hybrid models were adopted trying to constrain the electromagnetic emission with the only constraints given by ASAS-SN (optical), Swift-BAT (upper limits in X-rays) and *Fermi*-LAT observations of the region [105, 207, 208]. From the attempts in the numerical modelling of the emission observed in this period, two main issues clearly arise:

- It is challenging to reproduce the expectation of 13 ± 5 neutrinos in 6 months without violating the few observational constraints available. The expectations vary from $N_{\nu_\mu} \leq 0.05$ evts/(6 months) in [207] to $N_{\nu_\mu} \leq 4.9$ evts/(6 months) in [105] with the introduction of external fields that enhance the proton luminosity and absorb the gamma-ray emission.
- The absence of MeV instruments, and thus of constraints in that band, leads to model results where the majority of the emission from the absorption of gamma rays shows up as prominent emission in the MeV band, that cannot be excluded with current observations.

The numerical results are in tension with the IceCube results. This tension could originate by the fact that the neutrino flare was measured under the assumption of a simple power-law neutrino spectrum that does not describe properly the more complex structure of the actual emitted spectrum, or to the lack of a better observational overview of the source during that period and hence a poor knowledge of the environment.
An interesting discussion in [209], based on our gamma-ray measurements, shows that the diffuse IceCube flux discovered in 2013 can be fully described by only a subsample of blazars, made of about 5% of the whole population, that shows sporadic neutrino flaring emission with the luminosity of the 2014-15 neutrino flare. This would indicate

[19]: Ansoldi et al. (2018), 'The Blazar TXS 0506+056 Associated with a High-energy Neutrino: Insights into Extragalactic Jets and Cosmic-Ray Acceleration'
[198]: Gao et al. (2019), 'Interpretation of the coincident observation of a high energy neutrino and a bright flare'
[199]: Keivani et al. (2018), 'A Multimessenger Picture of the Flaring Blazar TXS 0506+056: Implications for High-energy Neutrino Emission and Cosmic-Ray Acceleration'
[200]: Cerruti et al. (2019), 'Lepto-hadronic single-zone models for the electromagnetic and neutrino emission of TXS 0506+056'
[201]: Strotjohann et al. (2018), 'Eddington Bias for Cosmic Neutrino Sources'
[202]: Liu et al. (2019), 'Hadronuclear interpretation of a high-energy neutrino event coincident with a blazar flare'
[203]: Xue et al. (2019), 'A Two-zone Model for Blazar Emission: Implications for TXS 0506+056 and the Neutrino Event IceCube-170922A'
[204]: Wang et al. (2018), 'Jet-cloud/star interaction as an interpretation of neutrino outburst from the blazar TXS 0506+056'
[205]: Britzen et al. (2019), 'A cosmic collider: Was the IceCube neutrino generated in a precessing jet-jet interaction in TXS 0506+056?'
[206]: Ros et al. (2020), 'Apparent superluminal core expansion and limb brightening in the candidate neutrino blazar TXS 0506+056'
[105]: Rodrigues et al. (2019), 'Lepto-hadronic Blazar Models Applied to the 2014-2015 Flare of TXS 0506+056'
[207]: Petropoulou et al. (2020), 'Multi-epoch Modeling of TXS 0506+056 and Implications for Long-term High-energy Neutrino Emission'
[208]: Reimer et al. (2019), 'Cascading Constraints from Neutrino-emitting Blazars: The Case of TXS 0506+056'
[209]: Halzen et al. (2019), 'On the Neutrino Flares from the Direction of TXS 0506+056'

that TXS 0506+056 is part of a special sub-population of blazars that shows a different and characteristic behaviour during the emission of these neutrino flares. I will discuss the behaviour of neutrino blazars as a population in Chapter 9 from an observational point of view.
With TXS 0506+056 we found the first compelling evidence of a candidate neutrino source among the blazar population, and with the lesson learned from this outstanding coincidence, we defined a strategy to search for more neutrino blazar candidates from coincidences with new realtime alerts and archival observations. The latter will be the subject of the next Chapter 6, while the new candidates identified from realtime follow-ups will be presented in Chapters 7 and 9.

GB6 J1040+0617 coincident with IceCube-141209A

6

6.1 IceCube-141209A 86

6.2 *Fermi*-LAT analysis of the GB6 J1040+0617 region . . 86

6.3 Evaluating the IceCube-141209A and GB6 J1040+0617 coincidence 94

6.4 Summary 95

After the extensive study of the first compelling candidate source to a high-energy neutrino, identified thanks to the prompt alert issued by the IceCube Realtime Alert Stream described in Ch. 4, the most pressing question was *"Are there more coincidences between flaring gamma-ray sources and high-energy neutrinos already observed in the past?"*. The question does not come naively, since the Realtime Alert Stream is operating only since mid 2016 and IceCube is operational at full detector setup (IC 86) since 2011 and therefore several high-energy neutrinos of all topologies have been observed without being sent to the astronomical community right after their detection. One famous example, is the case of the blazar PKS B1424-418 coincident with the PeV-energy neutrino event of cascade-type IC35 [35], part of the significant component of the astrophysical neutrino spectrum detected by IceCube in 2013 [9]. This was also found to be during a gamma-ray outburst at the time of the neutrino arrival, but only after the publication of the event detection few years later, with the consequent limitations in obtaining simultaneous data at different wavelengths.

In the work [38], we considered a sample based on the high-energy neutrino events observed by the IceCube detector from 2010 to 2017, and satisfying the IceCube realtime trigger criteria (see Appendix B for the full list). These events are all of the track-type and typically with an energy > 90 TeV. The sample includes ten published realtime alerts (up to and including IceCube-170922A) and forty archival events. In our search for coincident gamma-ray sources, in order to reduce the amount of chance coincidences due to the poor angular reconstruction of some events, we applied a selection cut and restricted the study to events with a 90% angular uncertainty smaller than 5 deg^2. Eight events did not satisfy this criteria and were thus discarded. The final neutrino sample consists of 37 well-reconstructed events. Each event was cross checked with the Third *Fermi*-LAT Point Source Catalog [210] and the Third *Fermi*-LAT Catalog of High-Energy Sources [144] to search for spatial coincidences with known gamma-ray sources.

Among the remaining 37 neutrino events, besides the IceCube-170922A / TXS 0506+056 occurrence, one additional spatial coincidence with a gamma-ray source is confirmed in this search (see also [18]). The gamma-ray source 3FGL J1040.4+0615 [153], which is associated with the BL Lac object GB6 J1040+0617. Interestingly, we found this source to be during one of its brightest flaring states at detection of the neutrino event IceCube-141209A, showing a picture similar to TXS 0506+056.

In the following sections, I will present my analysis published in the work [38] that identified for the first time GB6 J1040+0617 as the candidate counterpart of IceCube-141209A because of spatial and temporal coincidence in gamma rays.

[35]: Kadler et al. (2016), 'Coincidence of a high-fluence blazar outburst with a PeV-energy neutrino event'

[9]: IceCube Collaboration (2013), 'Evidence for High-Energy Extraterrestrial Neutrinos at the IceCube Detector'

[38]: Garrappa et al. (2019), 'Investigation of Two Fermi-LAT Gamma-Ray Blazars Coincident with High-energy Neutrinos Detected by IceCube'

[210]: Acero et al. (2015), 'Fermi Large Area Telescope Third Source Catalog'

[144]: Ajello et al. (2017), '3FHL: The Third Catalog of Hard Fermi-LAT Sources'

[18]: Aartsen et al. (2018), 'Multi-messenger observations of a flaring blazar coincident with high-energy neutrino IceCube-170922A'

[153]: Ackermann et al. (2015), 'The Third Catalog of Active Galactic Nuclei Detected by the Fermi Large Area Telescope'

Contributions to the work presented in this chapter

The work presented in this Chapter is from the publication *Garrappa et al. 2019* [38], in which I have performed the search for coincidences with archival neutrino events, the entire *Fermi*-LAT spectral and temporal analysis of the IceCube-141209A region and contributed to the collection of multiwavelength data.

6.1 IceCube-141209A

The High-Energy Starting (HESE) muon-track Event IceCube-141209A [211] was detected on 2014 December 9 at 03:26:04.704 UTC (MJD 57000.14311). Given the interest in this specific archival event that was triggered during the preparation of our work, a dedicated full reconstruction using *Millipede* (see Chapter 4) was performed to include the proper systematics in the estimation of its arrival direction. The resulting map of the likelihood landscape allowed us to find the global minimum and the uncertainty contours at a given confidence level. The final best fit position and the 90% confidence region are shown in Fig. 6.1 . The best estimate of the event direction is Dec= 6.84 deg and RA= 159.70 deg (J2000 equinox) with a 90% containment angular uncertainty region of 2.24 sq. deg. This more sofisticated reconstruction slightly shifted the best fit position of IceCube-141209A by 0.44°, and its 90% uncertainty region is 0.02 sq. deg smaller compared to the values published in [18] and the published event list. This is due to updated low-level re-calibrations and an event-by-event treatment of the systematic uncertainties, which are applied to events of special interest such as IceCube-170922A and this one. After the refined reconstruction, the best-fit location remained within the original 50% localisation contour.

The event deposited an energy of $97.4^{+9.6}_{-9.6}$ TeV in the detector and has a 29% probability of being of astrophysical origin, following the criteria and procedure in [15]. This means that, considering in the HESE alert sample a selection of events with a similar or larger deposited charge and with a similar arrival direction in the detector, about 29% of them are astrophysical. Therefore there is still a non-negligible probability that the event is of atmospheric origin.

Within the 90% uncertainty region of IceCube-141209A, we have identified only one cataloged gamma-ray source (among all 3FGL and 3FHL sources), 3FGL J1040.4+0615. This source is located at a distance of 0.70°from the best-fit neutrino position.

[211]: IceCube Collaboration et al. (2017), 'The IceCube Neutrino Observatory - Contributions to ICRC 2017 Part II: Properties of the Atmospheric and Astrophysical Neutrino Flux'

[18]: Aartsen et al. (2018), 'Multi-messenger observations of a flaring blazar coincident with high-energy neutrino IceCube-170922A'

[15]: Aartsen et al. (2017), 'The IceCube realtime alert system'

6.2 *Fermi*-LAT analysis of the GB6 J1040+0617 region

The gamma-ray source 3FGL J1040.4+0615, coincident with IceCube-141209A, was included as well in the 3FHL [144] catalog as 3FHL J1040.5+0618. We noted that it was not included in 2FHL[212], and so it was never significantly detected at energies > 50 GeV. It is among the brightest 26.1% (47.0%) 3FGL (3FHL) sources in terms of gamma-ray energy flux for the 4-year (8-year) integration time. We find that the most

[144]: Ajello et al. (2017), '3FHL: The Third Catalog of Hard Fermi-LAT Sources'

[212]: Ackermann et al. (2016), '2FHL: The Second Catalog of Hard Fermi-LAT Sources'

likely counterpart for this gamma-ray source is the low-synchrotron-peaked (LSP) BL Lac object GB6 J1040+0617, whose likely optical counterpart is SDSS J104031.62+061721.7, located 1′ from the 3FHL position. The source has a measured redshift of $z = 0.7351 \pm 0.0045$ [213, 214], and recently confirmed at $z = 0.74$ [215].
The most challenging feature about this LAT source, is that the gamma-ray emitter that is listed in the catalog as a single source is instead the contribution of two different known candidate blazars at very close relative distance in the sky, unresolved by the catalog routines. An additional significant gamma-ray emission offset from the direction of GB6 J1040+0617, is indeed consistent with the blazar 4C+06.41, at redshift 1.27 [216].

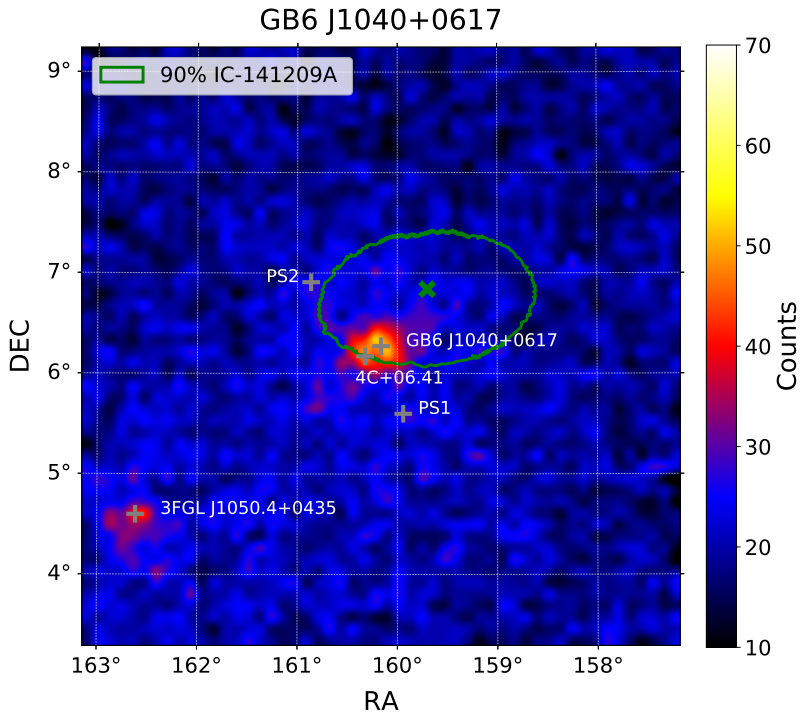

Figure 6.1: Counts map (E>100 MeV) of the region centered on GB6 J1040+0617 from [38]. The 90% neutrino angular uncertainty is shown as green contour and the best-fit neutrino position is marked by a green cross. The grey crosses indicate the gamma-ray emitters identified in the region by our analysis.

To analyse the LAT data in the region of GB6 J1040+0617, we performed the likelihood analysis described in Ch. 5 in a ROI centered on the catalog position of 3FGL J1040.4+0615. When investigating 9.6-years of gamma-ray events observed by *Fermi*-LAT in the region, and trying to pinpoint the radio counterpart of this object, we note that a significant amount of gamma-ray emission is clustered offset from the direction of GB6 J1040+0617, and positionally consistent with the radio position of the bright flat-spectrum radio quasar 4C+06.41 (see the *Fermi*-LAT counts map in Fig. 6.1).
This object is only 0.22°apart from GB6 J1040+0617 and is not reported in the 3FGL or any other subsequent catalogs with longer integration. We noted that in the second *Fermi*-LAT source catalog of AGN [210], 4C+06.41 was tentatively associated with the gamma-ray object 2FGL J1040.7+0614, probably due to the low statistics of the emission from the sources and the consequently poor localisation of the emitter, that resulted therefore consistent also with the position of 4C+06.41. In this case, 4C+06.41 was probably preferred as candidate counterpart given its stronger radio emission compared to GB6 J1040+0617.

[213]: Ahn et al. (2012), 'The Ninth Data Release of the Sloan Digital Sky Survey: First Spectroscopic Data from the SDSS-III Baryon Oscillation Spectroscopic Survey'

[214]: Maselli et al. (2015), 'New blazars from the cross-match of recent multi-frequency catalogs'

[215]: Paiano et al. (2021), 'The spectra of IceCube neutrino candidate sources - I. Optical spectroscopy of blazars'

[216]: Snellen et al. (2002), 'Automated optical identification of a large complete northern hemisphere sample of flat-spectrum radio sources with S_{6cm}>200 mJy'

[210]: Acero et al. (2015), 'Fermi Large Area Telescope Third Source Catalog'

In our ROI model, we therefore replace the single source 3FGL J1040.4+0615 with two point-like sources modelled with power-law spectra, located at the radio positions of GB6 J1040+0617 and 4C+06.41 [217, 218]. After an integration over the whole 9.6-year LAT dataset, 4C+06.41 is detected with a TS_{det} of 36 (correspondent to a ~6σ detection), while GB6 J1040+0617 dominates the bulk of the observed gamma-ray emission with a TS_{det} of 277 (> 16σ). Table 6.1 lists the best-fit positions and TS_{det} of the two sources.

[217]: Gregory et al. (1996), 'The GB6 Catalog of Radio Sources'
[218]: Lambert et al. (2009), 'On radio source selection to define a stable celestial frame'

Table 6.1: Best fit localizations for the gamma-ray emitters associated with GB6 J1040+0617 and 4C+06.41. Coordinates are in J2000 equinox.

Source	Localization			TS_{det}
	Ra (°)	Dec (°)	r_{99} (°)	
GB6 J1040+0617	160.13	6.29	0.04	277
4C+06.41	160.36	6.17	0.13	36

Furthermore, two additional new sources are found in the region, now named Fermi J1039.7+0535 and Fermi J1043.4+0654 [38]. This is not surprising given the longer integration time of this study with respect to the *Fermi*-LAT catalog (more than double the 3FGL one). In the counts map of Fig. 6.1 we refer to these sources as PS1 and PS2, respectively. In the 4FGL-DR2 (published 2 years after the results shown here) PS1 is listed as 4FGL J1039.6+0535, and tentatively associated with the BCU object NVSS J103940+053608. PS2 is also included in 4FGL-DR2 as 4FGL J1043.6+0654 and associated with the BL Lac object NVSS J104323+065307 (also known as 5BZB J1043+0653). PS1 and PS2 are dim sources with TS_{det} values of 36.85 and 26.27 in the 9.6-year data set. They are adequately modelled by power-law spectra with best-fit spectral indices of 2.11 ± 0.17 and 1.80 ± 0.21, respectively. Both gamma-ray sources lie outside of the IceCube 90% uncertainty contour. Based on the faintness of these sources and distance from the IceCube event, we did not investigate them further in this work.

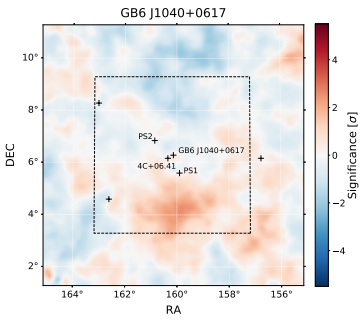

Figure 6.2: Residual map of the GB6 J1040+0617 region from [38]. The dashed square indicates the portion of ROI shown in the counts map of Fig. 6.1. The colorbar measures the significance of the deviations of the model from data.

In the analysis of the gamma-ray region of IceCube-141209A, we find two bright additional catalog sources: 3FGL J1050.4+0435 detected with TS_{det} = 463, 3FGL J1058.5+0133 detected with a TS_{det} = 8619, located 3.0°and 6.5°and away from GB6 J1040+0617, respectively. They are both located outside the 90% angular uncertainty of the neutrino localisation, but since their gamma-ray flux is comparable to the one of GB6 J1040+0617, we let their spectral parameters free to vary in the likelihood fit to obtain a better fit of the global model. The residuals map resulting from the best global fit of the region is shown in Fig. 6.2.

6.2.1 Light curve Analysis of GB6 J1040+0617

As first approach to disentangle the gamma-ray emission observed from the two blazar candidate counterparts GB6 J1040+0617 and 4C+06.41, we perform a temporal analysis of *Fermi*-LAT data, fitting the models of both sources at the same time during the computation of each light curve.
As in the analysis of TXS 0506+056, we use the adaptive-binning method starting at the optimum energy of 300 MeV for GB6 J1040+0617. The resulting light curve, shown in the top panel of Fig. 6.3, highlights several flux variations, observed throughout the 9.6 years and that can be grouped in two major temporal windows. The first one is a long-lasting

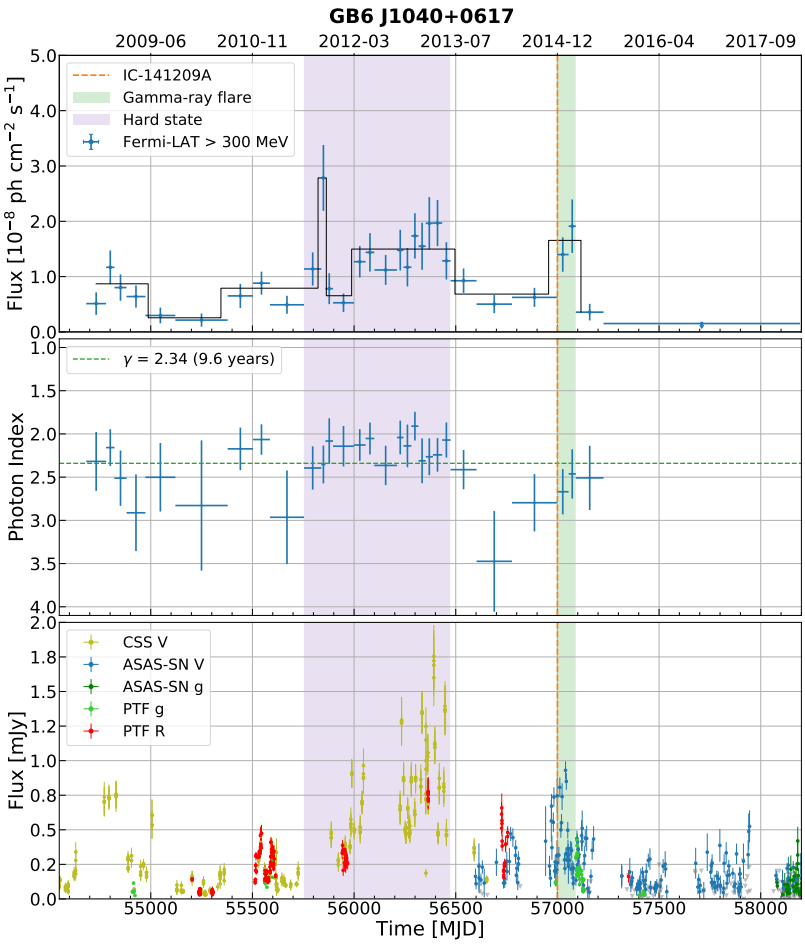

Figure 6.3: Adaptively-binned light curve of GB6 J1040+0617 from [38]. The first panel shows gamma-ray flux integrated above 300 MeV including the Bayesian block representation shown in black. The second panel shows the power-law spectral index. The average spectral index is overlaid as a horizontal green dashed line. The third panel shows optical data obtained from the All-Sky Automated Survey for Supernovae (ASAS-SN), the Palomar Transient Factory, and the Catalina Sky Survey. ASAS-SN upper limits are displayed as gray triangles. The arrival of IceCube-141209A is indicated as an orange dashed line. The purple shaded region marks the bright and hard gamma-ray state, while the green shaded region indicates the gamma-ray flare in coincidence with the neutrino arrival time.

period of flaring activity with a harder spectrum compared to the average (purple shaded area, Fig. 6.3). The second one is a shorter flaring activity that starts shortly before the neutrino arrival (green shaded area, Fig. 6.3).
The hard flare: The first feature that can be identified is a bright, long-lasting hard-spectral state with a total duration of 721 days, from MJD 55753 to MJD 56474. During this period the source reaches a peak flux value of $(2.8 \pm 0.6 \times 10^{-8})$ ph cm^{-2} s^{-1} integrated in the energy range from 300 MeV to 1 TeV (a factor of 2.5 increase compared to the average flux) with an average power-law index of 2.08 ± 0.04 and an energy flux of $(2.84 \pm 0.94) \times 10^{-11}$ erg cm^{-2} s^{-1}.
Fig. 6.4 (left) shows the SED averaged over the time window from MJD 54633 to 57227 (where we have a significant detection of GB6 J1040+0617 with TS_{det} of 451) compared to the hard bright state and to the spectrum observed during the 93 days around the neutrino arrival time. The average gamma-ray emission is well modelled by a power law with $\gamma = 2.33 \pm 0.06$ and $N_0 = (1.77 \pm 0.08) \times 10^{-12}$ cm^{-2} s^{-1} MeV^{-1}. A likelihood ratio test similar to the one performed in Sec. 5.2.2, shows a hardening of the spectrum during the hard bright state at 4.1σ significance. Furthermore, we find that the spectral shape during the hard state favours a log-

parabola instead of a power-law model, with best-fit spectral parameters $\alpha = 2.03 \pm 0.06$ and $\beta = 0.10 \pm 0.03$ (E_b is fixed to 1 GeV) with the null hypothesis of power-law model rejected at 19σ. We also noted that, during the bright hard state, there is an increase of at least a factor of 10 in the energy at which the high-energy component of the SED peaks. After performing an unbinned analysis like the one performed for TXS 0506+056 in Ch. 5, we find 10 photons above 10 GeV during this flaring period, which is compatible with 9.56 expected photons from the average spectral shape. We did not find an excess of high-energy photons because the spectral change is mainly due to a lack in low-energy photons caused by a shift in the high-energy SED peak to higher energies.

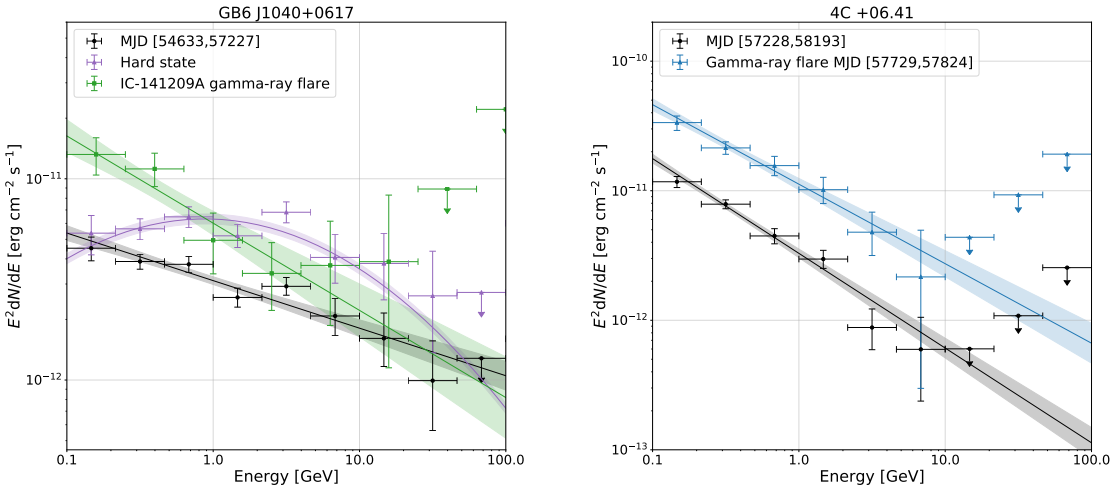

Figure 6.4: Spectral energy distributions of GB6 J1040+0617 and 4C+06.41 from [38]. *Fermi*-LAT data of the respective time ranges when each source is significantly detected are shown as black crosses, arrows indicate 95% upper limits, and the best-fit spectral model including statistical uncertainties is overlaid as a black band. *Left*: average spectrum of GB6 J1040+0617 compared to the spectrum during the 93 day gamma-ray excess coincident with the neutrino detection and the bright hard state during MJD 55753–56474. *Right*: average spectrum of 4C+06.41 compared with the spectrum during the bright gamma-ray flare during MJD 57729–57824.

The 93-day flare: the second identified time window, and the most relevant for the neutrino/gamma-ray connection in this source, is a flaring activity that starts a few days before the IceCube-141209A detection and lasts 93 days from MJD 56997 to 57090. The flare is significantly detected by the Bayesian Blocks and is defined by the bin edges of the two high-flux adaptively-binned time bins.

During the 93-day window around the neutrino arrival time the source is brighter by a factor of 2.4 compared to the average integrated energy flux with a spectral shape compatible to the average one at 1-σ level. The best fit spectral parameters during this time are $\gamma = 2.43 \pm 0.11$ and $N_0 = (3.76 \pm 0.55) \times 10^{-12}\,\mathrm{cm^{-2}\,s^{-1}\,MeV^{-1}}$.

For this flaring period coincident with the neutrino arrival, we only find one photon with energy larger than 10 GeV, which is consistent with the expectation of 1.54 photons obtained assuming the average spectral shape observed during the whole 93 days.

For the whole 9.6 years dataset, we do not find photons with energy above 50 GeV in the whole 9.6 years dataset that could be associated to GB6 J1040+0617, consistent with the fact that the source was not included in the 2FHL.

6.2.2 Lightcurve Analysis of 4C+06.41

The same adaptively binned lightcurve analysis, applied to the gamma-ray emitter coincident with 4C+06.41 is shown in Fig. 6.5, and is computed using the optimum energy of 170 MeV beginning at MJD 57228 (because of the different spectral shape compared to the one of GB6 J1040+0617). At the earliest time of the *Fermi*-LAT mission, we can find no significant emission from the source, so we can instead calculate the upper limit for the integral flux in a single time bin spanning from MJD 54682-57228. The emission in the time window spanning from MJD 57228-58193 is significantly detected, and the average spectrum is well modelled by a power law with best-fit parameters of $\gamma = 2.73 \pm 0.05$, $N_0 = (2.05 \pm 0.16) \times 10^{-13}\,\mathrm{cm^{-2}\,s^{-1}\,MeV^{-1}}$ with TS_{det} of 322.

At the arrival time of IceCube-141209A the gamma-ray flux of 4C+06.41 is below $1.44 \times 10^{-9}\,\mathrm{ph\,cm^{-2}\,s^{-1}}$ at 95% confidence level, integrated between 300 MeV and 1 TeV. In the 25 bins that resolve the emission in the 95-day period between MJD 57729 to 57824, the Bayesian Blocks identify a bright, distinct flare for the source that outshines GB6 J1040+0617 which is not significantly detected in the joint analysis. During the flaring activity, the source is described as a power-law spectrum with best-fit parameters $\gamma = 2.61 \pm 0.07$ and $N_0 = (7.01 \pm 0.75) \times 10^{-12}\,\mathrm{cm^{-2}\,s^{-1}\,MeV^{-1}}$. Given the soft spectrum of these sources, increasing the energy threshold to GeV energies to improve the PSF and disentangle the two emissions during the outburst of 4C+06.41 is significantly reducing the photon statistics, already limited by the short observation time, and GB6 J1040+0617 is still not significantly detected. A detailed analysis to disentangle the two distinct emissions is described in the next section.

6.2.3 Disentangling the Gamma-ray Emission of GB6 J1040+0617 and 4C+06.41

From the lightcurve analyses shown in Fig. 6.3 and Fig. 6.5, we observed that the gamma-ray emission from GB6 J1040+0617 dominates at earlier times, up to ~mid-2015 when it entered a quiescent gamma-ray state. The missing of persistent, significant detection after the outburst coincident with IceCube-141209A, could be mostly attributed to a quiescent state of the source (well below the detection sensitivity for *Fermi*-LAT) and the outburst shown by the nearby 4C+06.41 that, given the small relative distance between the two emitters and the soft spectra (with consequently majority of low-energy emission with broad PSF) makes the subsequent detection of GB6 J1040+0617 challenging.
As a second approach to disentangle the emission of the two gamma-ray emitters, we perform a dedicated analysis testing the localisation of the gamma-ray emission of the two objects for the whole 9.6-year dataset and the single flaring activities.

Full dataset: Using the full 9.6-year dataset, we find that the best-fit gamma-ray position and 99% uncertainty of the two putative sources called GB6-Fermi and 4C-Fermi (blue cross for the first and black for the second in Fig. 6.6) to coincide well with the radio positions of

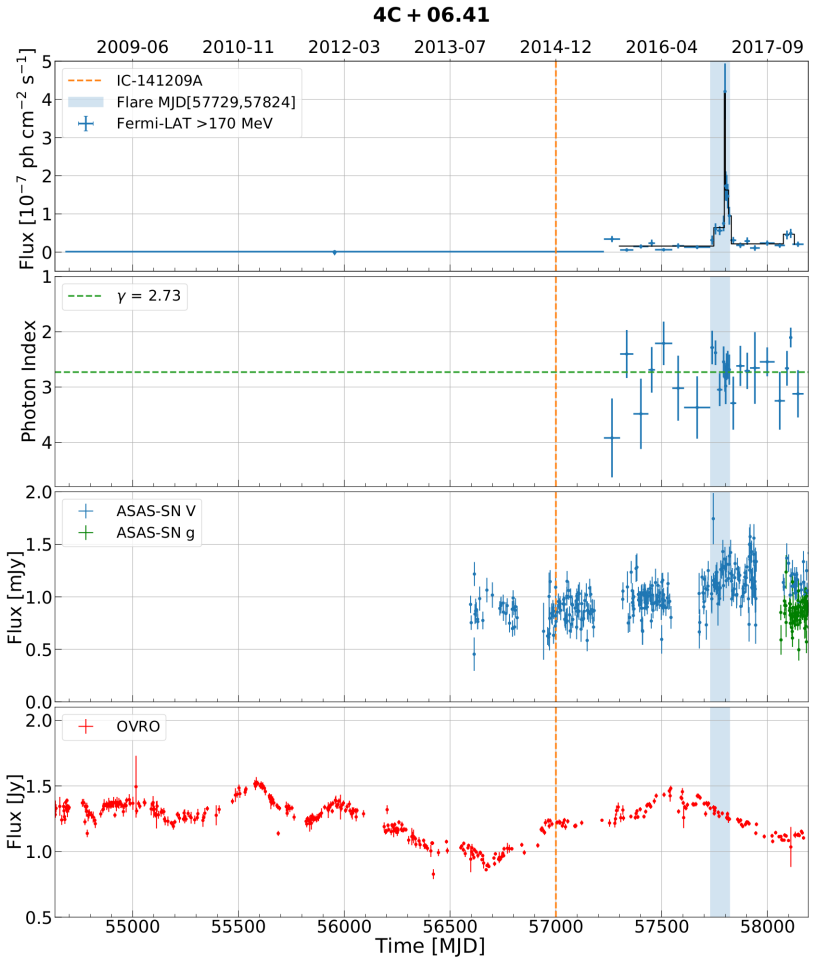

Figure 6.5: Adaptively-binned light curve for 4C+06.41 from [38]. The first panel shows the gamma-ray flux above 170 MeV including the Bayesian block representation shown in black. The second panel shows the power-law spectral index. The average spectral index is overlaid as dashed green line in the second panel, where the light curve of the spectral index is shown in blue points with correspondent error bars. The third panel shows optical data obtained from ASAS-SN, and the fourth panel shows radio data from the Owens Valley Radio Observatory (OVRO). The arrival of IceCube-141209A is indicated as a vertical, dashed orange line.

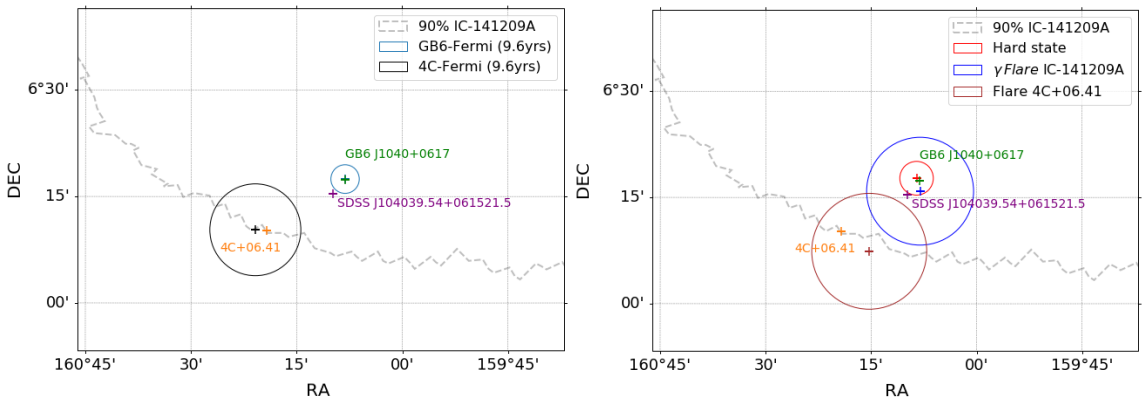

Figure 6.6: Gamma-ray best-fit positions from [38]. *Left panel:* the blue and black circles indicate the 99% containment radius of the gamma-ray positions of the two putative sources GB6-Fermi and 4C-Fermi. The 90% neutrino uncertainty region is shown as a dashed gray line for reference. Orange, green, and violet crosses indicate the radio positions of the blazars located in the region. *Right panel:* the bright hard state and modest flare at the arrival of IceCube-141209A are shown in red and blue respectively, while the late flare attributed to 4C+06.41 is shown in brown. The circles indicate the 99% containment radius of the gamma-ray position.

GB6 J1040+0617 and 4C+06.41 respectively (green and orange cross). From archival searches in the multiwavelenght catalogs of the region, we find another radio-loud object, SDSS J104039.54+061521.5 located at RA = 160.16475°and Dec = 6.2558°(J2000), just 1′ away from the radio catalog position of GB6 J1040+0617. Adding another putative source at the radio position of SDSS J104039.54+061521.5 in our ROI does not significantly improve our model, yielding a significance of $TS_{det} = 0$ for SDSS J104039.54+061521.5, and we find that its position is located outside the 99% uncertainty circle of GB6 J1040+0617 (blue circle) and is thus excluded as being responsible for the majority of the prolonged gamma-ray emission observed by the LAT. We also calculate a 95% flux upper limit for SDSS J104039.54+061521.5 of 8.8×10^{-10}ph cm^{-2} s^{-1} for a power-law spectral shape with index of 2.0 integrated over the energy range from 100 MeV to 1 TeV.

Flaring periods: We can also perform the same dedicated analysis for the flaring time intervals to derive the best-fit localisation of the gamma-ray emission. We find that the long-lasting, bright hard flare and the 93-days flare around the neutrino arrival time have the gamma-ray emission consistent with the position of GB6 J1040+0617, while the most recent enhanced gamma-ray emission is confirmed to be consistent with 4C+06.41 (see Fig. 6.6, *right* panel) and not with the position of GB6 J1040+0617, with very good accuracy. An additional observation that supports the association comes from the softer spectral shape observed during the most recent flare, that matches the one of 4C+06.41 (see Fig. 6.4, *right* panel).

An additional evidence for the association of the gamma-ray flaring activity contemporaneous to IceCube-141209A with GB6 J1040+0617 comes from archival optical observations. Collecting several years of observations from the All-Sky Automated Survey for Supernovae (ASAS-SN) [219, 220] in the V and g bands, from the Catalina Sky Survey (CSS) [221] in the V band and from the the Palomar Transient Factory (PTF) in the R and g bands [222, 223], we obtain a good monitoring for the source during the time spanned by *Fermi*-LAT observations. We find a good correlation between the main flaring activities in the optical and gamma-ray bands (purple and green shaded areas, Fig.6.3), as observed for a large sample of blazars in several works like [224], where the authors find the majority of time lags between gamma-ray and optical activity to span in a time window between (-10,+10) days. Given the higher spatial resolution of optical telescopes, this correlation strengthens the argument of GB6 J1040+0617 being the counterpart of the 93-day gamma-ray flare coincident with IceCube-141209A. Figure 6.7 shows a zoomed view of the ASAS-SN data of the optical flare coincident with IceCube-141209A, with superimposed Bayesian Blocks representation that indicates significant, rapid variability on daily timescales. The presence of slower variability in gamma-rays compared to optical observations could hint to a proton-synchrotron scenario as discussed in [225], however the lack of polarization measurements and the modest brightness of this source in gamma rays do not allow in this case to exclude completely a more canonical Inverse Compton scenario.

A similar correlation between the optical and gamma-ray band was also found in the light curves of 4C+06.41 (Fig. 6.5), that confirm the association of this more recent gamma-ray outburst to this different counterpart. The recurring periods of long discontinuity in optical observations are

[219]: Shappee et al. (2014), 'The Man behind the Curtain: X-Rays Drive the UV through NIR Variability in the 2013 Active Galactic Nucleus Outburst in NGC 2617'

[220]: Kochanek et al. (2017), 'The All-Sky Automated Survey for Supernovae (ASAS-SN) Light Curve Server v1.0'

[221]: Drake et al. (2009), 'First Results from the Catalina Real-Time Transient Survey'

[222]: Laher et al. (2014), 'IPAC Image Processing and Data Archiving for the Palomar Transient Factory'

[223]: Masci et al. (2017), 'The IPAC Image Subtraction and Discovery Pipeline for the Intermediate Palomar Transient Factory'

[224]: Liodakis et al. (2019), 'Probing Blazar Emission Processes with Optical/Gamma-Ray Flare Correlations'

[225]: Zhang et al. (2018), 'Variability and Optical Polarization Can Probe the Neutrino and Electromagnetic Emission Mechanisms of TXS˜0506+056'

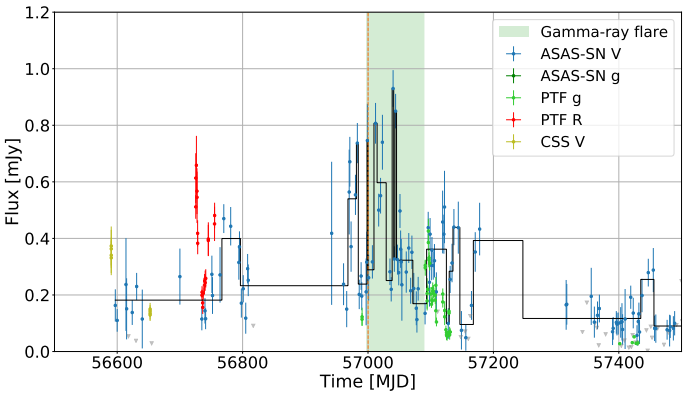

Figure 6.7: Zommed-in optical light curve of GB6 J1040+0617 around the arrival time of IceCube-141209A from [38]. The solid black line is the Bayesian Blocks representation for the ASAS-SN V-band data set from Fig. 6.3

due to the source being very close to the ecliptic. Luckily, this outburst was observed in a period of visibility for the source and we have a good sampling of observations. The contamination from solar emission is a critical point also in gamma-ray analyses even with its quiescent emission [226], therefore it is crucial in our *Fermi*-LAT analysis to remove the intervals with contamination from the quiet Sun as well as for the Solar flare intervals, as described in Ch. 3, to have a clean picture of the IceCube-141209A region.

[226]: Abdo et al. (2011), 'Fermi Large Area Telescope Observations of Two Gamma-Ray Emission Components from the Quiescent Sun'

6.3 Evaluating the IceCube-141209A and GB6 J1040+0617 coincidence

After the identification of GB6 J1040+0617 as the most likely counterpart of IceCube-141209A given the spatial localisation of the gamma-ray flaring activity at the arrival of the neutrino, we can now evaluate the *p*-value of the chance coincidence between the blazar and the neutrino. To evaluate such coincidence, we follow an approach similar to the one adopted for TXS 0506+056 in [18], considering the same sample of monthly binned light curves. The *p*-value is defined as

$$p = \frac{N_s A_\nu}{4\pi} \times N_{frac}, \tag{6.1}$$

were we consider N_s=2257 (number of extra-galactic *Fermi*-LAT sources of the light curves sample used in [18]). We find that N_{frac} = 9.5% of all monthly bins considered show a gamma-ray energy flux higher than the one of GB6 J1040+0617 in the energy range from 1–100 GeV. We considered the area of the 90% neutrino position uncertainty region A_ν=2.24 square degrees and obtained a p-value of 1%, that corresponds to a Gaussian equivalent, one-sided probability of 2.3σ. The search for associations, however, introduces a number of trials equivalent to the 37 well-reconstructed high-energy neutrino events in the sample. After correcting for this look-elsewhere effect, the final *p*-value is 30 %.

[18]: Aartsen et al. (2018), 'Multi-messenger observations of a flaring blazar coincident with high-energy neutrino IceCube-170922A'

6.4 Summary

This chapter concludes the description of the work published in [38], with the identification of GB6 J1040+0617 as the most likely counterpart of IceCube-141209A. In the hypothesis of IceCube-141209A being of astrophysical origin, this represents the second identified astrophysical counterpart to a high energy neutrino among the gamma-ray blazar population. The gamma-ray analysis of this region presents several challenges, starting from the presence of two very close (0.2°apart) emitters, that even in catalog searches have been listed as a single source and reaches the limit of *Fermi*-LAT's capability to disentangle point sources with the PSF achievable at energies as low as 100 MeV. Another challenging element for the region, is the vicinity to the ecliptic and the necessity to remove the contamination from the quiet Sun and solar flares happened when the star was in the proximity of the ROI.

[38]: Garrappa et al. (2019), 'Investigation of Two Fermi-LAT Gamma-Ray Blazars Coincident with High-energy Neutrinos Detected by IceCube'

Given that we found this second candidate right after the realtime discovery of the IceCube-170922A and TXS 0506+056 association (despite IceCube-141209A was detected already 3 years before) some comparison with the first neutrino blazar candidate should be drawn. Assuming the redshift of 0.73, GB6 J1040+0617 has rest-frame energetics similar to those of TXS 0506+056, with an average gamma-ray luminosity between 100 MeV and 100 GeV of 4.1×10^{46} erg s^{-1}, 1.5 times larger than TXS 0506+056. Both sources are classified as BL Lac objects, with a difference in the frequency of the synchrotron peak, with TXS 0506+056 classified as intermediate synchrotron peak (ISP) and GB6 J1040+0617 as low synchrotron peak (LSP). A collection of multiwavelength archival data for GB6 J1040+0617 from radio to gamma rays (Fig. 6.8) shows the typical double hump structure without additional features, as expected for BL Lac objects.

They are also located at similar declinations, near the equatorial plane, that defines at the south pole the portion of the Sky along the horizon, where IceCube is most sensitive to high-energy neutrinos. From a simple, rough estimate of expected neutrino events based uniquely on the measured levels of emission in X-ray and gamma rays and, assuming the effective area published for TXS 0506+056, we find a range of events per year that goes from a pessimistic lower limit of $3{\times}10^{-3}$ to an optimistic rate of 0.7 events per year in the energy range 100 TeV - 10 PeV. A value of expected high-energy neutrinos much smaller than 1 is consistent with the Eddington bias effect [201] that predicts the observation of a single event as statistical fluctuation in a broad population of weak neutrino sources (or at least well below our current instrument sensitivity). This makes GB6 J1040+0617 a plausible neutrino source candidate and, even if the association with IceCube-141209A cannot be made at levels as significant as for TXS 0506+056, this multiwavelength study indicates GB6 J1040+0617 as the most likely counterpart to this event and one of the most credited neutrino blazar candidates so far.

[201]: Strotjohann et al. (2018), 'Eddington Bias for Cosmic Neutrino Sources'

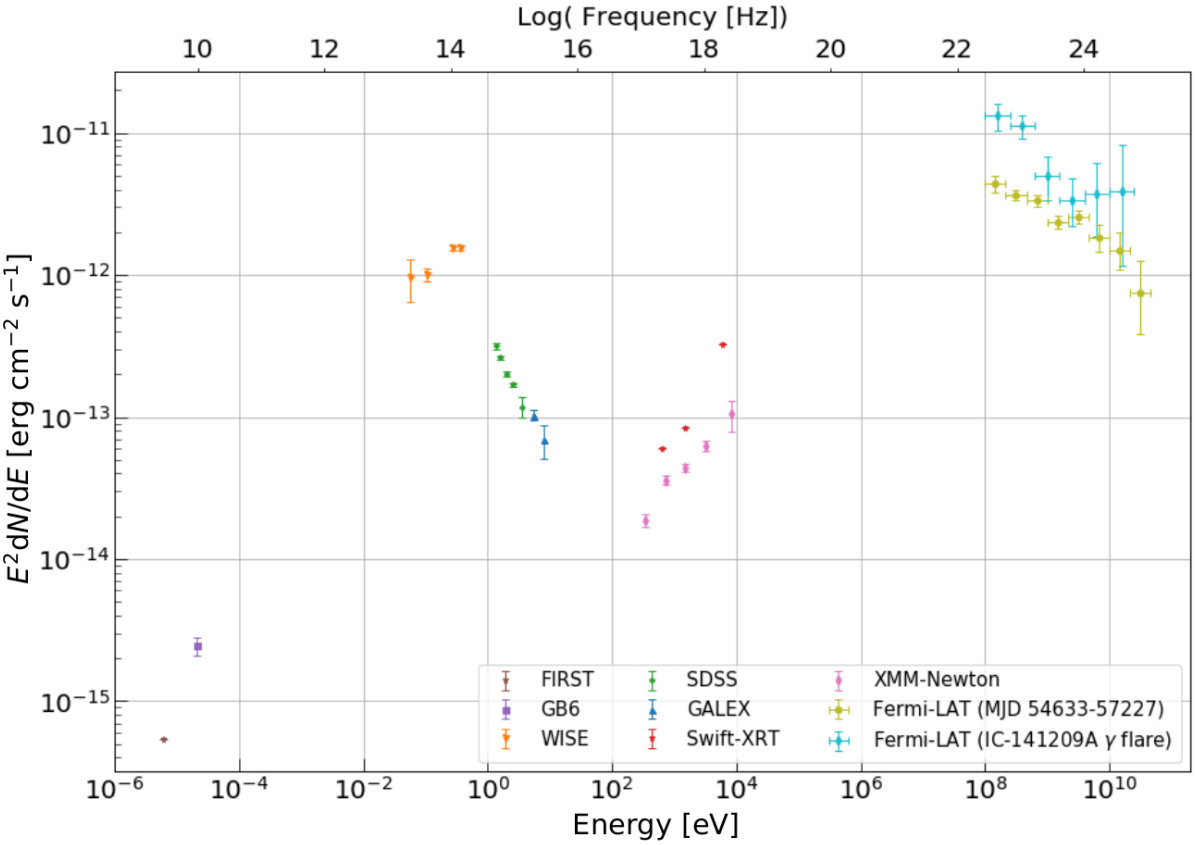

Figure 6.8: Multi-wavelength SED in the observer's frame for GB6 J1040+0617 using archival data, which are not contemporaneous.

PKS 1502+106 coincident with IceCube-190730A

7

After the identification of TXS 0506+056 and GB6 J1040+0617 as candidate counterparts of high-energy neutrinos, another interesting coincidence was reported between a high-energy neutrino and a *Fermi*-LAT source during the operations of the IceCube Realtime System 2.0. Although the event reconstruction identifies the powerful gamma-ray blazar PKS 1502+106 as the only spatially-coincident candidate, at the arrival of IceCube-190730A the behaviour of the source is different from the one previously shown by TXS 0506+056 and GB6 J1040+0617. However, the energetics of the source make PKS 1502+106 an outstanding candidate for neutrino emission.
In this chapter, I will present an analysis of the gamma-ray blazar PKS 1502+106 and its coincidence with IceCube-190730A.

7.1 IceCube-190730A 97
7.2 The blazar PKS 1502+106 98
7.3 *Fermi*-LAT analysis of PKS 1502+106 99
7.4 Numerical modelling of PKS 1502+106 104
7.5 Summary 110

Contributions to the work presented in this chapter

The work presented in this Chapter is from two publications for which I am corresponding author. The first part is from the paper *Franckowiak et al. 2020* [227] in which my contribution was the full *Fermi*-LAT spectral and temporal analysis of PKS 1502+106. The second paper of which results are presented here is *Rodrigues et al. 2021* [228]. The paper focuses on the numerical modelling of the source, that was done by the leading author X. Rodrigues. My contributions were a detailed temporal analysis of the gamma-ray emission from the source, a characterization of different relevant activity states, and the estimation of the number of IceCube events during each of these states, based on the emission rates predicted by the model. I am presenting in this chapter also the results from the numerical modelling because of their importance in the interpretation of the source's high-energy emission and, more in generally, for future strategies in the identification of the multi-wavelength features expected in neutrino blazar candidates.

7.1 IceCube-190730A

On July 30, 2019 at 20:50:41.31 UTC (MJD 58694.86) the high-energy neutrino IceCube-190730A of the Gold class was observed with a best-fit arrival direction of Dec= $10.47^{+1.14}_{-0.89}$ deg and RA= $225.79^{+1.28}_{-1.43}$ deg (J2000 equinox) with a total 90% uncertainty region of 5.5 sq. deg after the Millipede reconstruction (see Chapter 4).
The signalness calculated for this event was 67%, making this one of the alerts with the highest probability of being of astrophysical origin in the Gold sample and even higher than the one calculated for IceCube-170922A. The estimated neutrino energy was ~300 TeV.
This event would not fulfill the conditions for *well-reconstructed event* described in the previous selection of archival alerts in Chapter 6. As I will show in Chapter 9, the set of alerts belonging to the IceCube Realtime Stream 2.0 shows a slightly larger median extension of the angular error. That requires a different selection threshold for *well-reconstructed events*

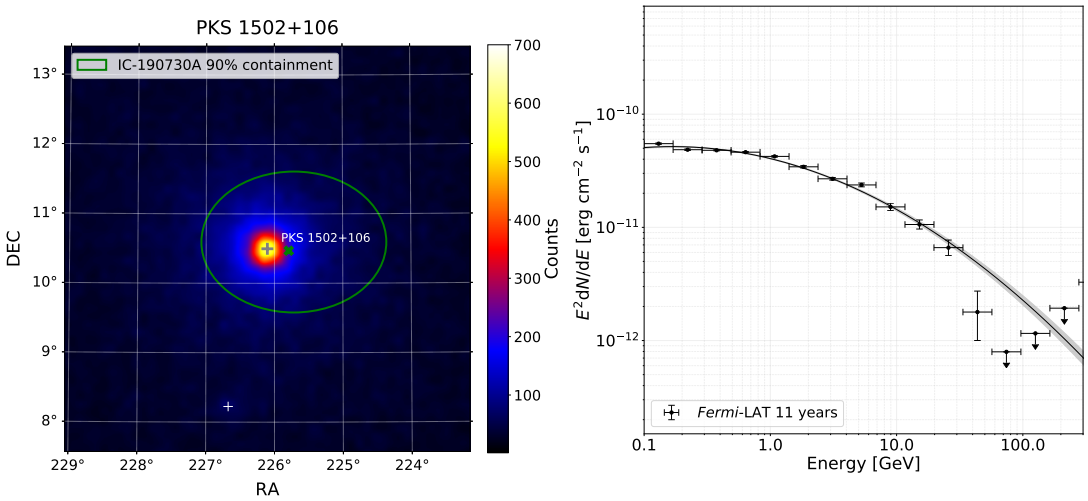

Figure 7.1: *Fermi*-LAT countmap of the PKS 1502+106 region with the IceCube-190730A contour (*left*) and the average gamma-ray SED from 11 years of *Fermi*-LAT data (*right*). The gray line shows the best-fit log-parabola model and uncertainty (shaded area). The model does not account for EBL absorption, that starts to become significant in the SED above ~20 GeV.

to be consistent with the criterium we adopted in the previous studies, that considers the median angular error of the specific alerts stream. IceCube-190730A is considered part of the *well-reconstructed events* of the new Realtime Alert Stream 2.0 and, because of the remarkable properties of PKS 1502+106, was considered a coincidence of high scientific interest already at the time of the realtime follow-up with observations with the *Fermi*-LAT. A gamma-ray countmap of *Fermi*-LAT photons with the IceCube-190730A 90% contour is shown in the left panel of Figure 7.1.

7.2 The blazar PKS 1502+106

The blazar PKS 1502+106 was originally discovered with the 178 MHz pencil beam survey from the Mullard Radio Astronomy Observatory (Cambridge, UK) [229, 230] and was further classified as a flat-spectrum radio quasar (FSRQ) due to the broad lines resolved with optical spectroscopy observations and its flat radio spectrum [152]. Its designation as PKS 1502+106 comes from observations published in 1966 by the Australian National Radio Astronomy Observatory of Parkes (NSW, Australia) [231] and its second common designation as OR 103 was listed by the "Big Ear" Radio Observatory of the Ohio State University in Delaware (OH) [232].
Its redshift was measured with high precision from the spectral observation of the Sloan Digital Sky Survey (SDSS) with the best-fit value given at $z = 1.8385 \pm 0.0024$, corresponding to a luminosity distance of 14176.8 Mpc [233]. The source hosts a supermassive black hole (SMBH) in its center with a mass estimated in the range 0.5-1$\times 10^9 M_\odot$ and an accretion rate of 2 $M_\odot$ yr^{-1} [234]. It is straightforward to derive the correspondent Schwarzschild radius of the SMBH from:

[229]: Crowther et al. (1966), 'A pencil-beam radio telescope operating at 178 Mc/s'
[230]: Williams et al. (1966), 'A survey of radio sources and background radiation at 38 Mc/s'
[152]: Healey et al. (2007), 'CRATES: An All-Sky Survey of Flat-Spectrum Radio Sources'
[231]: Day et al. (1966), 'The Parkes catalogue of radio sources, declination zone 0° to +20°'
[232]: Fitch et al. (1969), 'A high-sensitivity 1415-MHz survey between declinations of 0 and 20 north.'
[233]: Adelman-McCarthy et al. (2008), 'The Sixth Data Release of the Sloan Digital Sky Survey'
[234]: D'Elia et al. (2003), 'The disc-jet relation in strong-lined blazars'

$$R_S = \frac{2GM}{c^2} \simeq 3 \times 10^{14}\,\mathrm{cm} \tag{7.1}$$

assuming a $10^9 M_\odot$ mass. Additional information about the system in the vicinity of the black hole come from [235]. From the fit of the Mg II emission line profile, the authors estimate the total bolometric luminosity of the Broad Line Region (BLR) at $L_{BLR} = 2{\times}10^{46}$ erg s^{-1} from which the distance of the BLR from the black hole [236] can be derived as

[235]: Shen et al. (2011), 'A Catalog of Quasar Properties from Sloan Digital Sky Survey Data Release 7'

[236]: Ghisellini et al. (2009), 'Canonical high-power blazars'

$$R_{BLR} = 5 \times 10^{17} \sqrt{\frac{L}{10^{16}}} \simeq 7 \times 10^{17}\ \mathrm{cm}\ \simeq 0.23\mathrm{pc}. \tag{7.2}$$

In terms of gamma-ray energy flux, PKS 1502+106 is the 15th brightest blazar observed by *Fermi*-LAT according to [148], and it was significantly detected already in the first year of *Fermi*-LAT operations as the second-brightest source in the gamma-sky [237, 238] because of a prolonged outburst observed in 2008-2010. Being the exceptional detection of the first distant blazar in gamma rays, the *Fermi*-LAT observations triggered the first successful multi-wavelength campaign from the daily monitoring of the Flare Advocates. Results from the multi-wavelength campaign during the 2008-10 outburst are presented in [239] and identify for the first time PKS 1502+106 as the counterpart of the bright gamma-ray point source observed by *Fermi*-LAT, giving a first estimation of the physical parameters of the jet environment in a Synchrotron Self-Compton scenario that connects observations from radio to gamma rays.

[148]: Ajello et al. (2020), 'The Fourth Catalog of Active Galactic Nuclei Detected by the Fermi Large Area Telescope'

[237]: Ciprini (2008), 'GLAST LAT detection of a possible new gamma-ray flaring blazar: PKS 1502+106'

[238]: Horan et al. (2009), 'Fermi-LAT detection of renewed activity from the blazar PKS 1502+106'

[239]: Abdo et al. (2010), 'PKS 1502+106: A New and Distant Gamma-ray Blazar in Outburst Discovered by the Fermi Large Area Telescope'

More works have studied the physical properties of PKS 1502+106 at different wavelengths, exploiting the synergies between simultaneous multi-wavelength observations. An example is given in [240], where with VLBI imaging at frequencies up to 86 GHz and the gamma-ray observations of *Fermi*-LAT revealed the compact, core-dominated morphology of the sources and the one-sided parsec-scale jet structure. These are resolved with unprecedented resolution, constraining the location of the gamma-ray emitting region at $\leq$5.9 pc away from the SMBH at the base of the jet.

[240]: Karamanavis et al. (2016), 'PKS 1502+106: A high-redshift Fermi blazar at extreme angular resolution. Structural dynamics with VLBI imaging up to 86 GHz'

7.3 *Fermi*-LAT analysis of PKS 1502+106

7.3.1 Spectral Analysis

At the time of the detection of IceCube-190730A, PKS 1502+106 was found in a very low activity state in gamma-rays. During the realtime follow-up with *Fermi*-LAT observations, we found no significant detection of the source at timescales of 1-day and 1-week prior to the neutrino arrival [241].

[241]: Garrappa et al. (2019), 'Fermi-LAT Gamma-ray Observations of IceCube-190730A'

In the work [227], I analyze almost 11 years of *Fermi*-LAT data collected between 2008 August and 2019 August, in the energy range from 100 MeV to 800 GeV. In the analysis, the diffuse templates, IRFs and ROI configurations described in Appendix A are used.

[227]: Franckowiak et al. (2020), 'Patterns in the Multiwavelength Behavior of Candidate Neutrino Blazars'

In the 15°$\times$ 15° ROI centered at the catalog position of PKS 1502+106, the gamma-ray emitter 4FGL J1504.4+1029 (identified as the gamma-ray counterpart of PKS 1502+106 in [239]) is by far the brightest source in the

region, with a TS_{det} two orders of magnitude higher than the second and third-brightest sources in the region, 4FGL J1505.0+0326 (associated with the NLSy1 galaxy PKS 1502+036, at 7.1°distance) and 4FGL J1506.6+0813 (associated with the BL Lac object PMN J1506+0814, at 2.3°distance).
We found a best-fit localisation for 4FGL J1504.4+1029 of RA (°, J2000) = 226.1072 ± 0.0022 and Dec (°, J2000) = 10.4939 ± 0.0021, consistent within the uncertainties with the previously reported catalog positions.
A log-parabolic model for the source was significantly preferred over the simple power law to describe the spectral energy distribution (SED):

$$\frac{dN}{dE} = N_0 \left(\frac{E}{E_b}\right)^{-(\alpha+\beta\log(E/E_b))} \tag{7.3}$$

with best-fit values $\alpha = 2.12 \pm 0.01$, $\beta = 0.10 \pm 0.01$, $N_0 = (1.19 \pm 0.01) \times 10^{-10}$ cm^{-2} s^{-1} MeV^{-1} and E_b fixed to 497 GeV. The gamma-ray SED averaged over 11 years is shown in the right panel of Figure 7.1. The errors on the differential flux bins and the best fit model include only statistical uncertainties. The curvature observed in the spectrum could point to the interaction of gamma rays produced in the jet with low-energy photons from the surrounding BLR, thus producing electron-positron pairs and cascading to lower energies [239]. Alternatively, it can also indicate a transition from the Thomson to the Klein-Nishina regime. In the case where protons are also accelerated in the jet, the same photon fields from the BLR should also be efficient targets for neutrino production, which provides a strong motivation for lepto-hadronic models such as our study in [228].

[239]: Abdo et al. (2010), 'PKS 1502+106: A New and Distant Gamma-ray Blazar in Outburst Discovered by the Fermi Large Area Telescope'

[228]: Rodrigues et al. (2021), 'Multi-wavelength and Neutrino Emission from Blazar PKS 1502 + 106'

7.3.2 Light curve analysis

To study the temporal behaviour of the source, we performed a light curve analysis for the whole 11 years of data used for the spectral analysis in the previous section. To compute the duration of each bin, we used once again the adaptive binning technique described in [162] with a constant 15% relative flux error. In the analysis of each time bin, the gamma-ray emission of the target source is modelled with a power law instead of a log parabola, because the photon statistics in each of the computed adaptive bins are generally not high enough for the log parabola model to be statistically preferred over the power law. The resulting light curve consists of 435 bins with durations that span from as short as ~10 hours during some of the brightest flaring activities, to as long as ~150 days during long, persistent quiescent states. A representation of the final light curve after applying a full likelihood analysis to each bin is shown with black points in Figure 7.2, where in the upper panel the integral fluxes and correspondent 1-σ error bars are shown, while in the lower panel the power-law spectral index of each bin together with its 1-σ error is shown.
At the beginning of the *Fermi*-LAT observations, we can see the bright and long-lasting gamma-ray outburst of the source that spanned from 2008-2010 as mentioned in the previous sections of this chapter, while from 2010-2015 the source experienced sporadic and mild flaring activities. On 2008 August 7, only 3 days after the start of the scientific operations of *Fermi*-LAT, the source was observed at its highest flux level, reaching the

[162]: Lott et al. (2012), 'An adaptive-binning method for generating constant-uncertainty/constant-significance light curves with Fermi-LAT data'

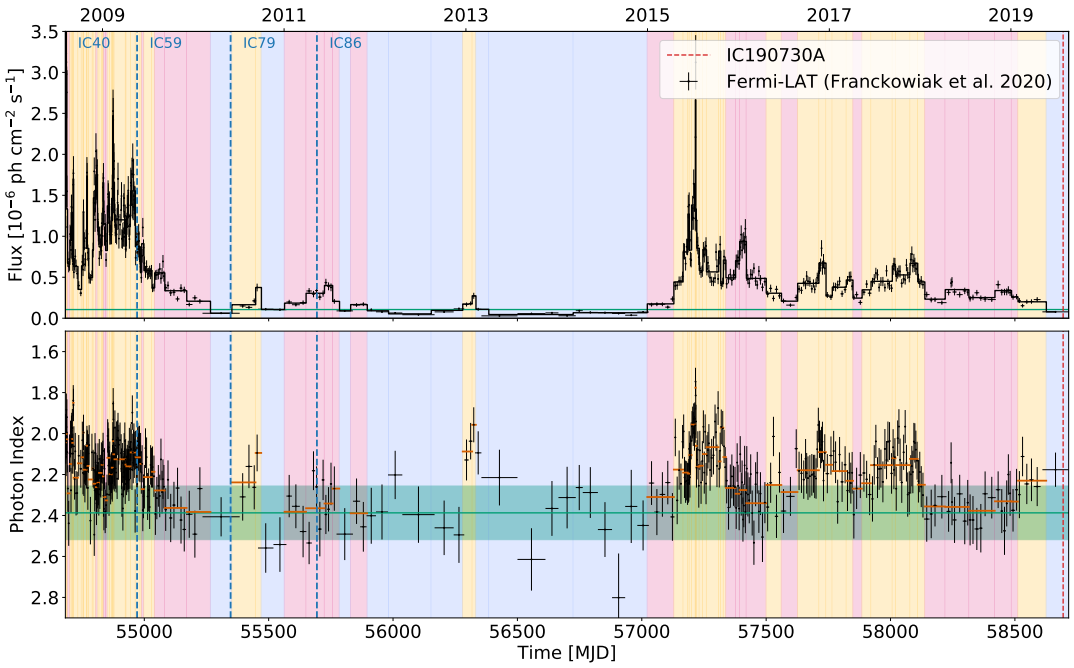

Figure 7.2: *Fermi*-LAT lightcurve of PKS 1502+106 from [228] with data from [227]. The shaded colored areas indicate the three characteristic states: *quiescent* (blue), flaring with a hard gamma-ray spectrum (*hard flares*, yellow) and flaring with a soft gamma-ray spectrum (*soft flares*, pink). The green line in the *top* panel shows the average flux used in the flare definition. The *bottom* panel shows the *Fermi*-LAT spectral index across the same 11 year time period. The green line shows the average spectral index ($\bar{\Gamma} = 2.31$), from where we draw the distinction between hard ($\Gamma < \bar{\Gamma}$) and soft ($\Gamma > \bar{\Gamma}$) flares, and the green band is its respective 1σ uncertainty. The red lines show the average spectral index in the time window of each flare.

value of $F = (4.5 \pm 0.6) \times 10^{-6}$ ph cm^{-2} s^{-1} over an integration timescale of ~16 hours. Several lower flaring activities characterized the source from 2016-2019 until a few months before the observation of IceCube-190730A, when the source entered again in a quiescent state similar to the one observed between 2013-2015.

In order to identify the different flaring activities observed for the source and disentangle them from the windows of quiescent state, we first compute the Bayesian Blocks representation of the light curve following the method described in [194], shown as a black curve in the upper panel of Figure 7.2.

We define a simple method to exploit the Bayesian Blocks representation and isolate flares from the quiescent states. Given that there is no standard reference flux level that would define the transition between quiescent and flaring state, we consider the average of the measured fluxes in the low activity period from 2010 March to 2014 December, weighted by the time duration of each bin. This average value of $\bar{F} = (2.97 \pm 0.02) \times 10^{-7}$ ph cm^{-2} s^{-1} is represented as a green line in the upper panel of Figure 7.2). Its uncertainty, represented by a thin green band, was calculated from the propagation of the errors of the single-flux bins. We use this average value as a proxy tolerance band for the quiescent state of the source. All the Bayesian Blocks above this band are identified as flaring states of the source.

From the light curve of the correspondent spectral indices (lower panel,

Figure 7.2) it is interesting to notice how the spectral shape of the source changes significantly during the transitions of the several flaring activities. Following the same approach used for the proxy of the quiescent flux, we can compute the average value of the observed spectral index and the relative uncertainty from the error propagation, and we obtain the value $\bar{\Gamma} = (2.39 \pm 0.13)$. From this proxy for the average spectral index (and error) we define three different gamma-ray states for PKS 1502+106:

- a quiescent state, with low gamma-ray flux ($F \leq \bar{F}$);
- a gamma-ray flaring state with hard spectral index (hard flares, $\Gamma < \bar{\Gamma}$);
- a gamma-ray flaring state with spectral index larger or consistent with the average proxy within the uncertainty band (soft flares, $\Gamma \geq \bar{\Gamma}$).

In the lower panel of Figure 7.2 the average spectral index during the quiescent state and its uncertainty are displayed as green horizontal line and shaded area, and the average index of all the bins belonging to the same bayesian block is shown as a red horizontal line. The shaded areas across both panels of Figure 7.2 identify the nature of the different states in the bayesian blocks representation, with blue areas for the quiescent states, pink for the soft flares and yellow for the hard flares. The cumulative durations of these states is of about 3.8 years for the quiescent state, 3.7 and 3.5 years for the hard and soft flaring states, respectively. Already from our first multi-wavelength study of the source reported in [227], we found a good correlation between the temporal evolution in the gamma-ray and optical band, while in the radio band the variability of the source is much slower and the sporadic X-ray observations cannot give a comprehensive picture of the behaviour in the time domain. In order to have a simultaneous picture of the SED across the energy spectrum, we have selected intervals from the time windows covered by *Swift*-XRT pointings (coloured areas in Figure 7.3), since they have the poorest sampling among all the multiwavelength data collected for the source. The selected representative datasets are shown in Tab. 7.1 and Figure 7.3 for the gamma-ray and X-ray data. The gamma-ray SEDs corresponding to each representative observation are displayed in both panels of Figure 7.4, compared to the average quiescent state considered a priori the flares selection. The colours used for each SED reflect those used to mark each classified interval in Figure 7.2.

Table 7.1: Time windows for the three representative states identified in Figure 7.2 and highlighted in Figure 7.3 for the flaring states of PKS 1502+106. The datasets are the same as used in [228].

State	Total duration [yr]	Representative dataset
Quiescent (ν)	3.8	MJD 58664-58724
Hard Flare	3.7	MJD 57210-57219
Soft Flare	3.5	MJD 58107-58125

From an unbinned analysis like the one used in Chapters 5 and 6, we find that the highest photon energy observed from PKS 1502+106 during more than a decade of observations with *Fermi*-LAT is 51.1 GeV, observed on 2015 September 18 while the source was in a one of its brightest flaring states. This is consistent with the expectations for the cosmic gamma-ray horizon [242] for a source at z = 1.8385 (see Figure 7.6), and is the only gamma-ray observed from the source above 50 GeV. Figure 7.5 shows the adaptively binned light curve (black points) overlayed with the single high-energy (E > 10 GeV) photons associated with the source at p > 80%

[242]: Fermi-LAT Collaboration et al. (2018), 'A gamma-ray determination of the Universe's star formation history'

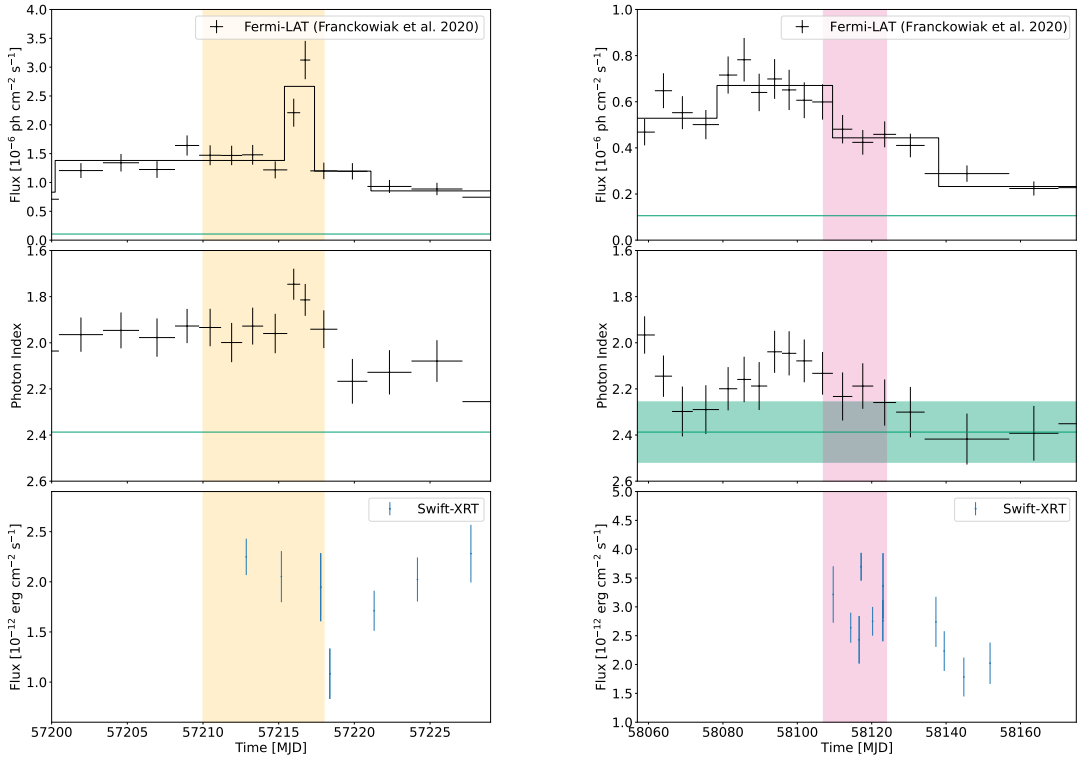

Figure 7.3: Zoom view of the time windows chosen for the representative datasets of the hard flares (*left*) and soft flares (*right*). The upper panels show the *Fermi*-LAT integral flux in the 0.1-800 GeV band, the middle panels the corresponding light curve for the spectral index and the lower panels the *Swift*-XRT integral flux in the 0.3-10 KeV band.

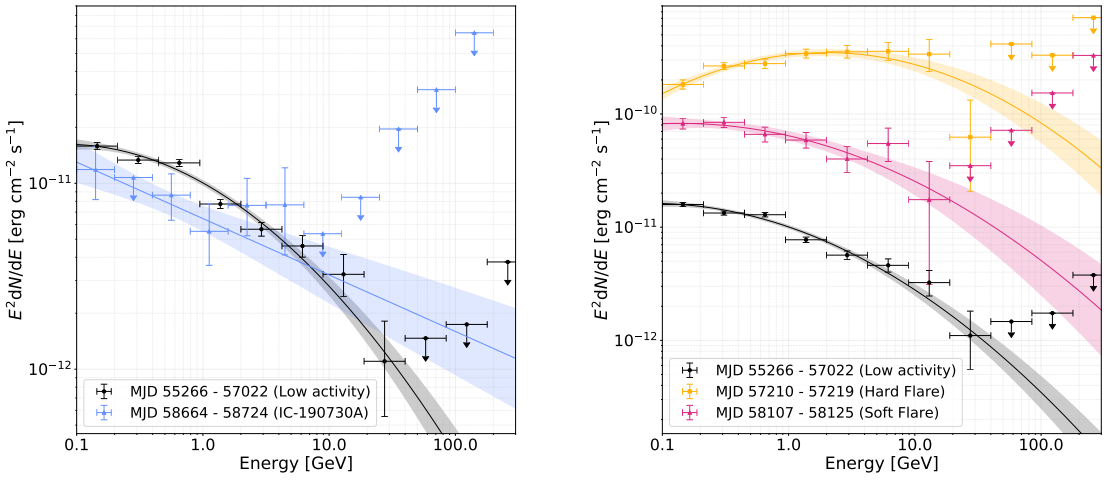

Figure 7.4: *Fermi*-LAT SED of the representative states for the quiescent state simultaneous to the neutrino observation (*left* panel, blue) and flaring states (*right* panel) reflecting the colours used in Figure 7.2. The black SED shows the average spectrum of the low-activity state.

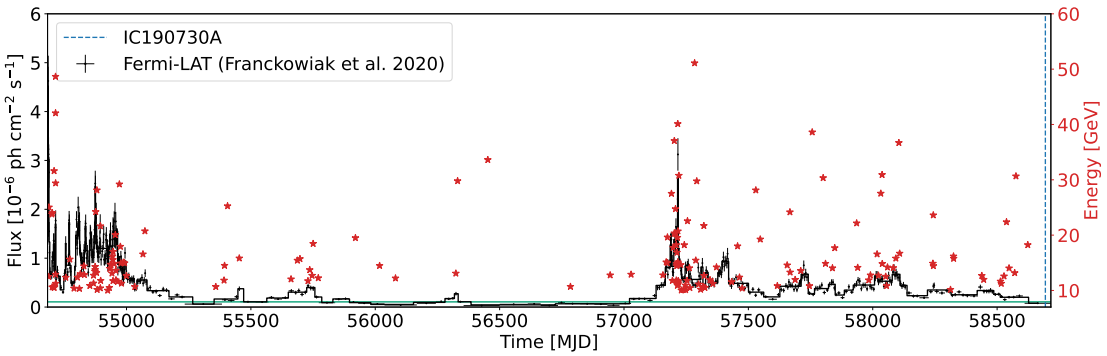

Figure 7.5: PKS 1502+106 lightcurve with data from [227]. The high-energy photons (E > 10 GeV) are shown as red stars and the y-axis on the right side shows their energy.

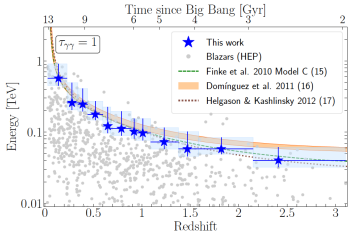

Figure 7.6: Gamma-ray cosmic horizon from [242].

[228]: Rodrigues et al. (2021), 'Multi-wavelength and Neutrino Emission from Blazar PKS 1502 + 106'

(red stars). The bulk of the observed high-energy emission is between 10-20 GeV, and is mainly observed during the flaring states of the source. No high-energy photon is observed around the time of IceCube-190730A (dashed blue line).

7.4 Numerical modelling of PKS 1502+106

Based on my analysis presented in the previous section, a numerical model can then be used to explain this gamma-ray data, together with other multi-wavelength observations of the source. These models can also shed light on the potential connection with the observed IceCube event. In this section I will summarize the physics behind the models and the conclusions that can be taken, as presented first in [228]. The emission region is modelled as a single radiative zone in the jet, geometrically described as an homogeneous, spherical blob in its co-moving frame (with comoving radius denoted as R'_b). In the source frame, the blob is moving away from the SMBH at relativistic speed with a Lorentz factor Γ_b, from which we assume the observation angle of the jet relative to its axis $\theta_{obs} = 1/\Gamma_b$. The dissipation radius R_{diss} is the quantity that measures the distance between the blob and the SMBH. We assume an homogeneous randomly-oriented magnetic field within the blob with strength B'.
We also assume that this magnetic field accelerates electrons and protons inside the jet, which are then injected into the blob. For what concerns the particle populations, we assume the electrons to be accelerated to a simple power-law distribution

$$\frac{dN_e}{d\gamma_e} \propto \gamma_e^{-p_e} \tag{7.4}$$

where γ_e is the Lorentz factor $1/\sqrt{(1-\beta^2)}$, β being the electron speed in units of c. In the case of protons, we describe their injection as a broken power law function. This allows additional degrees of freedom, crucial for a detailed description of the emitted spectra of neutrinos and hadronic photons

$$\frac{dN_p}{d\gamma_p} \propto \begin{cases} \gamma^{-p_p^{low}} & \gamma < \gamma_{break} \\ \gamma^{-p_p^{high}} & \gamma > \gamma_{break} \end{cases} \tag{7.5}$$

where p_p^{low} and p_p^{high} are the two spectral indices below and above γ_{break}. Another important component of the model are the external radiation fields. As previously described in Chapter 2, FSRQ objects are characterized by a BLR that sorrounds the accretion disk. The emission that comes from the powerful accretion happening around the SMBH is reprocessed and partially isotropized by the BLR. As shown in [227], during the quiescent state of PKS 1502+106, the emission from the disk can be identified by the thermal bump in the optical/ultraviolet (UV) band, at ~ 5 eV. As for BLR properties, we assume the values for luminosity and radius that come from the measurements in Sec. 7.2 and that about 10% of the power output by the accretion disk is reprocessed as estimated in [243], and re-emitted isotropically in the rest frame of the black hole. Within the volume confined by the BLR, the target photon field has a constant energy density proportional to $L_{disk} R_{BLR}^{-2}$ (that is relativistically boosted by a factor Γ_b^2 in the jet frame of rest), while outside the BLR it diminishes with distance following the analytical relations in [236]. An additional external field component used in the model is the thermal infrared emission from a dusty torus that surrounds the disk, that however has a negligible energy density compared to the BLR emission.
A more detailed description of the model and the parameter search can be found in our publication [228]. In the next section, I will focus on the model results and their implications on the observed neutrino-blazar coincidence and the peculiar multi-wavelength features that help inferring the possible scenarios.

[227]: Franckowiak et al. (2020), 'Patterns in the Multiwavelength Behavior of Candidate Neutrino Blazars'

[243]: Greene et al. (2005), 'Estimating Black Hole Masses in Active Galaxies Using the Hα Emission Line'

[236]: Ghisellini et al. (2009), 'Canonical high-power blazars'

[228]: Rodrigues et al. (2021), 'Multi-wavelength and Neutrino Emission from Blazar PKS 1502 + 106'

7.4.1 Contributions from radiative processes to the observed SED

I will now show how the model described in the previous section can be used to predict multi-wavelength and neutrino emission from PKS 1502+106, under two different scenarios:

- A *leptohadronic model* with the emission region blob located near the perimeter of the BLR and magnetic field strength $B' \leq 1$ G;
- A *proton synchroton model* with the emission region blob located far outside the BLR and magnetic field strength $B' \geq 10$ G.

As shown in [228], either of these scenarios can explain the simultaneous multi-wavelength emission during all three periods introduced in Sec. 7.3.2: *hard flare*, *soft flare* and the *quiescent state* during the neutrino arrival. The simulated fluxes during the three prototype states are shown in Figure 7.7, with the leptohadronic SEDs in the left panel and the proton synchrotron SEDs in the right panel. The three simultaneous gamma-ray spectra analysed in Sec. 7.3.2, as well as simultaneous X-ray observations from *Swift*-XRT and optical from ASAS-SN and CSS [227] can be well-explained by the model. The grey points from radio observations are archival observations not simultaneous with the selected periods. These points cannot be explained by the same one-zone model because the high radiation density necessary for hadronic processes in our compact

[227]: Franckowiak et al. (2020), 'Patterns in the Multiwavelength Behavior of Candidate Neutrino Blazars'

emitting region leads to efficient synchrotron self-absorption at low frequencies that suppresses the outgoing radio emission.

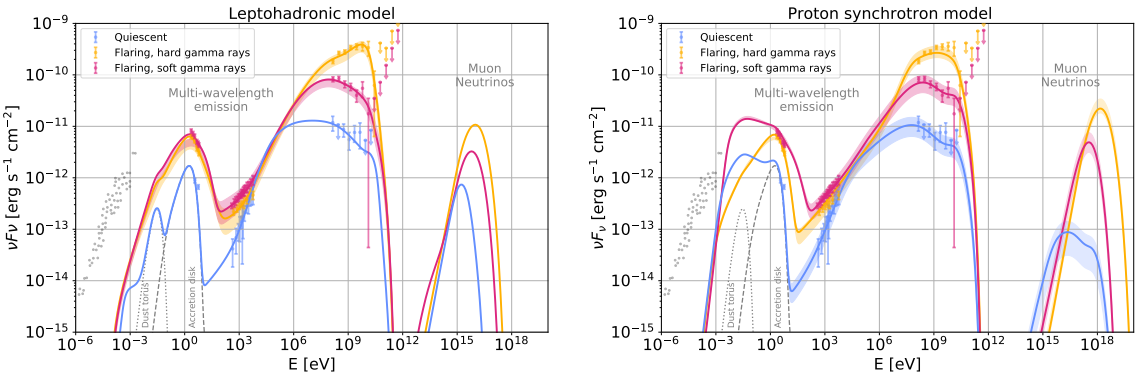

Figure 7.7: Numerical modelling results from [228]. The coloured curves show the predicted multi-wavelength fluxes and all-flavor neutrino spectra from PKS 1502+106 obtained with the leptohadronic model *(left)* and the proton synchrotron model *(right)* under three different parameter sets, indicated in Tab. 7.2. The shaded areas correspond to the uncertainty in the non-thermal proton power, also indicated in Tab. 7.2. The colored data points represent multi-wavelength flux observations during each of the three states (see Figure 7.2 and Tab. 7.1). The gray points show archival radio data from the source.

The uncertainty bands around each best-fit SED and neutrino spectrum were obtained by varying the power in accelerated protons until the predictions in X-rays or gamma rays give residuals larger than ±40%, covering approximately the 1 σ uncertainty on experimental data.
I will discuss now separately the relative contribution of the different subprocess to the overall SED in the three gamma-ray states of the source.
Quiescent state: Looking at the leptohadronic SED of the quiescent state in Figure 7.7 (*left*), the uncertainty band of the neutrino spectrum is consistent with a purely leptonic limit where the hadronic component is completely removed lowering down to zero the power in accelerated protons. If we consider the individual contributions of the subprocesses to the observed SED as shown in Figure 7.8 (upper row, left panel) we can notice that, when considering only the purely leptonic radiative components, the inverse Compton of relativistic electrons on the external thermal fields (blue line) can describe entirely the hard X-ray spectrum observed above 1 keV, while the Bethe-Heitler (orange line). Photon-photon pair production (green line) becomes more dominant for the X-ray emission below 1 keV and can explain the softening of the spectrum in soft X-rays (0.3 - 1 keV). Additional features to probe hadronic acceleration during the quiescent state is the gamma-ray emission above 1 GeV, that is dominated by photon-photon pair production, a sub-dominant contribution of photo-pion emission (yellow line) and Bethe-Heitler pair production. The high-energy part of the inverse Compton emission suffers of a sharp cutoff at ~1 GeV that cannot fully describe the gamma-ray observations until the interactions with the EBL become dominant above 50 GeV. Interestingly, the gamma-ray emission measured above 100 MeV (so for the full energy band of *Fermi*-LAT) is also important for the proton-synchrotron scenario (Figure 7.8, first line, right panel) where the dominant components are proton synchrotron emission (red line) and a minor contribution from Bethe Heitler pair production.

Flaring states: As the large uncertainties in the flux measurement of the quiescent state can still leave space to a compatibility with a fully (or at least dominant) leptonic scenario, the observations of flaring states

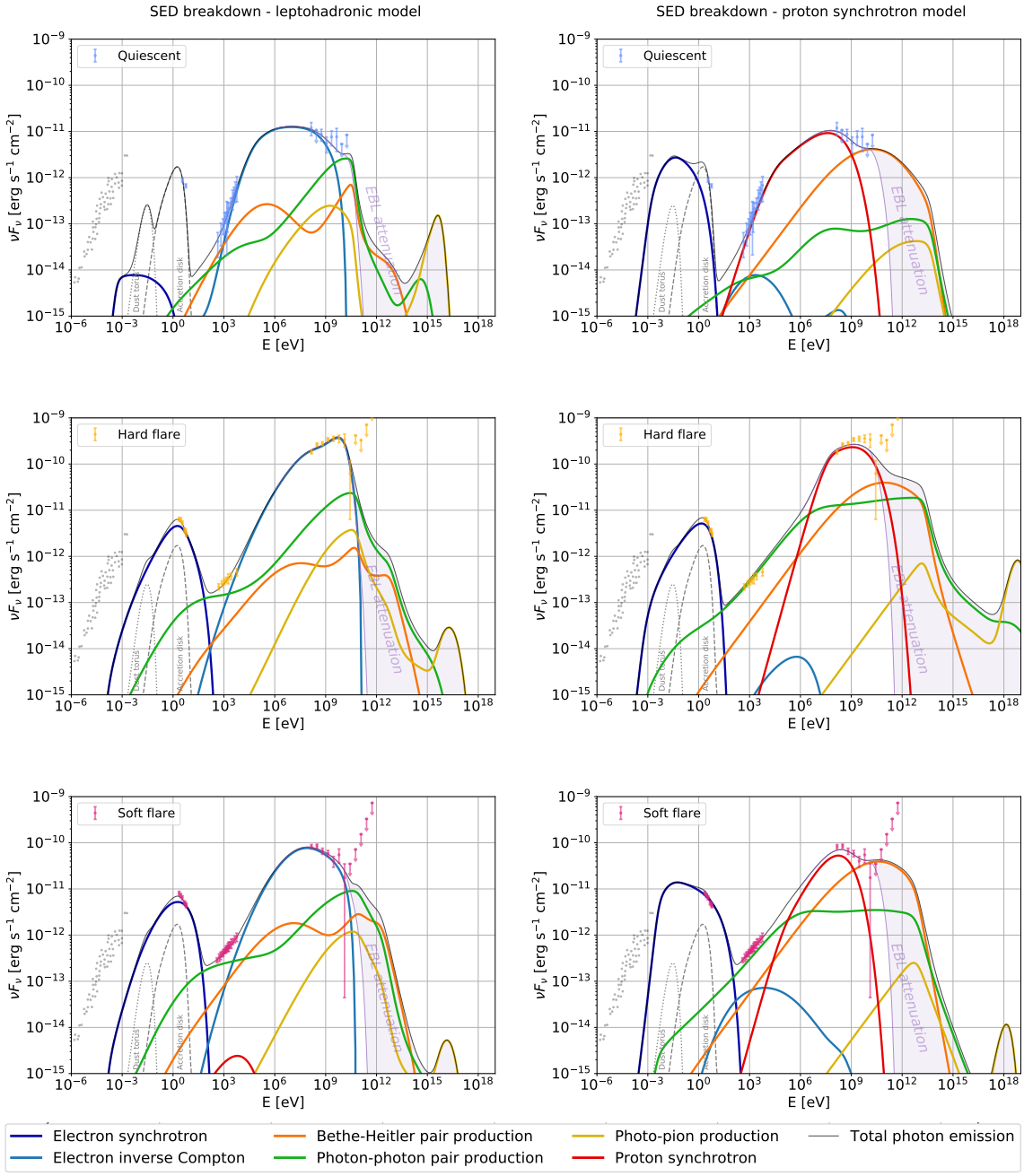

Figure 7.8: Breakdown of the spectrum from [228], during the different states into the different radiative processes for the leptohadronic model *(left)* and the proton synchrotron model *(right)*.

cannot easily be described without introducing an hadronic component. A key feature, in this case, can be found in X-ray observations. Compared to the quiescent state, the X-ray spectrum observed during flaring states is softer. This different spectral shape is well described by the cascade emission from photon-photon and Bethe-Heitler interactions, that give a resulting softer spectrum when added up to the inverse Compton emission from electrons (Figure 7.8, second and third lines, left panels). Observations in X-ray and gamma ray are also well described in the proton-synchrotron scenario by dominant contributions of the hadronic radiative processes (Figure 7.8, second and third lines, right panels).

Table 7.2: Parameter values from [228] underlying the results of the leptohadronic and proton synchrotron models, for each of the states identified in Figure 7.2. Primed quantities refer to the rest frame of the jet. The ranges in the values of the proton luminosity correspond to the uncertainties of the model, resulting in the shaded regions in Figure 7.7. We also report the reduced χ^2 values for the multi-wavelength SEDs predicted by each model, describing the goodness of fit. In the two bottom rows, we list the predicted number of neutrino events per year in IceCube, as well as the total expected number of events integrated over the eleven-year period. The yearly rates correspond to the IC86 configuration of the IceCube detector, since they were calculated using the effective area of that configuration. For the total number of events, we take into account the different detector configurations over the years, as depicted by the dashed vertical lines in Figure 7.2.

Model	Leptohadronic			Proton Synchrotron		
State	Quiescent	Hard Flare	Soft Flare	Quiescent	Hard Flare	Soft Flare
$R'_{\rm b}$ [cm, log]	16.0	15.9	15.9	16.0	16.0	16.0
B' [G]	0.3	0.3	0.6	10.0	12.6	15.8
Bulk Lorentz factor $\Gamma_{\rm b}$	27.6	28.7	26.2	40.0	49.2	42.6
$R_{\rm diss}/R_{\rm BLR}$	1.3	1.3	1.6	$\geq$2.5	$\geq$2.5	$\geq$2.5
L'_e [erg s^{-1}, log]	43.5	44.6	44.2	42.0	41.6	42.6
L'_p [erg s^{-1}, log]	$\leq 44.8^{+0.8}$	$45.6^{+0.2}_{-0.2}$	$46.0^{+0.2}_{-0.1}$	$45.5^{+0.4}_{-0.3}$	$45.3^{+0.0}_{-0.2}$	$45.1^{+0.1}_{-0.2}$
$\gamma_e'^{\rm min}$, log	1.0	3.8	3.3	2.0	3.0	1.9
$\gamma_e'^{\rm max}$, log	3.7	4.5	4.2	3.0	3.1	3.5
p_e	2.1	3.6	1.2	2.1	3.5	2.1
$\gamma_p'^{\rm min}$, log	5.4	5.2	4.6	2.0	8.1	6.8
$\gamma_p'^{\rm break}$, log	-	-	-	6.7	-	-
$\gamma_p'^{\rm max}$, log	6.1	7.1	6.9	8.5	9.2	8.3
$p_p^{\rm low}$	-	-	-	0.3	-	-
$p_p^{\rm high}$	1.5	1.5	1.5	2.3	2.4	1.5
$\chi^2_{\rm SED}$/d.o.f.	0.3	2.7	1.0	0.7	3.8	1.6
$N_{\rm events}$ per year	$0.47^{+2.19}_{-0.47}$	$3.19^{+1.90}_{-1.71}$	$1.27^{+0.8}_{-0.55}$	$0.02^{+0.01}_{-0.01}$	$0.05^{+0.02}_{-0.01}$	$0.05^{+0.02}_{-0.02}$
$N_{\rm events}$ (total)	$1.77^{+8.23}_{-1.77}$	$10.94^{+6.56}_{-5.84}$	$4.32^{+2.71}_{-1.87}$	$0.07^{+0.05}_{-0.04}$	$0.17^{+0.06}_{-0.03}$	$0.17^{+0.06}_{-0.04}$

7.4.2 Neutrino spectra and expected event rates

From the comparison of neutrino spectra simulated in the leptohadronic and proton synchrotron models (Figure 7.7) we can already observe some important differences. First, the peak energy in the two models differs significantly: in the proton synchrotron model the peak energy spans from 10 PeV to 1 EeV, while in the leptohadronic model it is located at lower energies, in the range from 1-10 PeV depending on the different state that we consider. This is due because of the major constraints of the two models, that reflect on the maximum achievable proton energy. The proton synchrotron model is constrained by the gamma-ray measurements, since the second SED hump is described almost entirely by proton synchrotron radiation, while the leptohadronic model is mainly constrained by X-ray measurements that are dominated by the emission of the electromagnetic cascades inside the blob.
Another difference is in the predicted neutrino flux. During the quiescent state, it is about 10 times higher in the leptohadronic model, while during flares the levels are similar. This is because in the leptohadronic model, the main target photons for neutrino production are the BLR photon fields, which are relativistically boosted into the jet frame and have therefore very high densities, regardless of jet activity. On the other hand, in the proton synchrotron model the blob lies outside the BLR, so the only UV photons available for neutrino production are non-thermal photons produced inside the jet. These photons are much more abundant during flares than during the quiescent state (see the difference in the

non-thermal photon emissions in the right-hand panels of Figure 7.8), leading to the large difference in the predicted neutrino fluxes.
Finally, the pronounced dip in the photon field between 10 eV and 1 keV during the quiescent state (upper right panel of Figure 7.8) leads to a characteristic double-hump neutrino spectrum (right panel of Figure 7.7) which is another particular feature of the proton synchrotron model. We do not find such structure in the neutrino spectrum simulated from the leptohadronic model because the external photon fields (i.e. the BLR and the accretion disk) are the main target for photo-pion interactions.

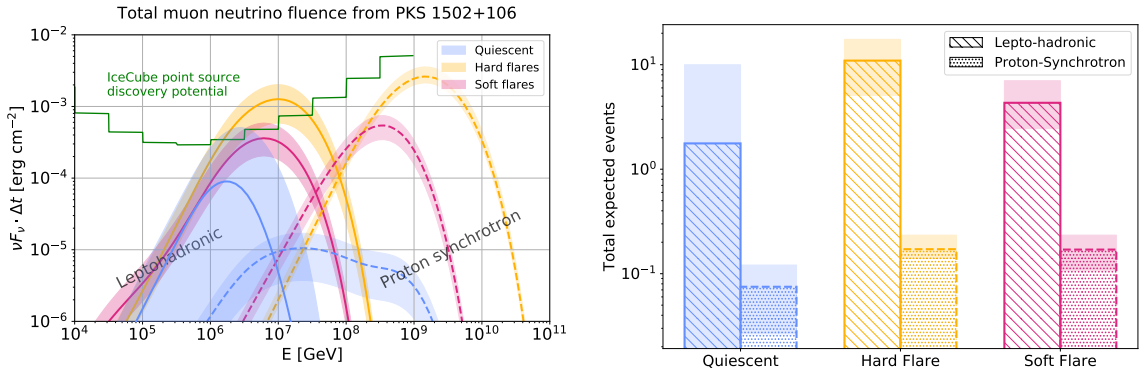

Figure 7.9: Neutrino expectations from the numerical modelling in [228]. *Left*: total muon neutrino fluence from PKS 1502+106 predicted by the leptohadronic (solid) and proton synchrotron model (dashed) in the total duration of each of the three activity states. *Right*: total, time-integrated number of IceCube events from PKS 1502+106, expected from the leptohadronic and protons synchrotron models, in the IceCube point source analysis, in the entire duration of each of the three states indicated in Figure 7.2.

Having obtained predictions for the neutrino spectra, we can now derive the number of expected neutrinos in different scenarios. This quantity is calculated using the following prescriptions:

- the IceCube effective area for the point-source analysis in the 86-string configuration, following the event selection in [244];
- a scaling for the effective area to account for the different IceCube string configurations from August 2008 to May 2011;
- a low-energy threshold of $E_\nu = 100$ TeV to emulate the selection criteria of the realtime stream [16].

[244]: Aartsen et al. (2017), 'All-sky Search for Time-integrated Neutrino Emission from Astrophysical Sources with 7 yr of IceCube Data'

[16]: Blaufuss et al. (2019), 'The Next Generation of IceCube Real-time Neutrino Alerts'

Integrating the neutrino spectra shown in Figure 7.7 with the total duration of each gamma-ray state listed in Tab. 7.1, we obtain the total neutrino fluences shown in Figure 7.9 (*left* panel). Here, is shown for comparison the IceCube discovery potential at Dec = 0° from [244]. Only the fluence of the hard flaring state in the leptohadronic scenario has the best fit results above the discovery potential in a smaller energy range around the peak. The leptohadronic quiescent and soft flaring states marginally intercept the discovery potential with their 1 σ uncertainty band. However, it is important to remember that PKS 1502+106 is at Dec ~ 10, therefore neutrino events arriving from its direction will suffer more absorption in the Earth and the correspondent discovery potential will be higher than the one shown in Figure 7.9.
Despite the higher relative fluence, the flaring states in the proton synchrotron scenario never reach the discovery potential. At the energies where the neutrino spectra peak in this model, the effect of absorption inside the Earth strongly affects the discovery potential steepening its

energy dependence.
The total number of expected neutrino events is shown in the right panel of Figure 7.9 and Tab. 7.2, with shaded bands reflecting the variation of the power in accelerated protons and correspondent uncertainty band of the neutrino spectrum. When comparing the two different models, because of the arguments discussed above, the expected number of neutrinos is significantly different. For instance, during all the hard flaring states, the total number of expected events is $10.94^{+6.56}_{-5.84}$, among which $7.97^{-4.25}_{+4.78}$ are expected only in the IC86 season. Even in the lowest expectation of 3.72 events this quite high neutrino efficiency would be in mild tension with the non-detection of events during hard flaring states with a p-value of 2.4% (from Poisson statistics).
On the contrary, the quiescent state of the leptohadronic scenario is statistically compatible with the observation of a single neutrino in 11 years of observations. Even in the highest level of expectation of ~ 10 events, its overall compatibility with a leptonic dominated scenario could be interpreted as having the source with only occasional periods of efficient states of hadronic acceleration, without affecting significantly the multi-wavelength picture. This would be consistent with having observed a single high-energy neutrino from the source during one of its quiescent periods.
A similar argument can be made for all states in the proton synchrotron scenario. However, here the proton acceleration must happen continuously, since in this scenario the quiescent-state SED is partially explained by hadronic emission. Although the number of predicted neutrinos (that ranges from 0.03 to 0.17) is statistically consistent with the observation of a single event, the model is probably somewhat disfavoured by the high physical luminosity in protons that would be required from the source during long quiescent periods (20-200 times the Eddington limit). Similar issues were found in [108], where the sustainability of a persistent proton-synchrotron emission in bright gamma-ray detected blazars is disfavoured by the energetics available for these systems.

[108]: Liodakis et al. (2020), 'Proton Synchrotron Gamma-Rays and the Energy Crisis in Blazars'

7.5 Summary

In this chapter, I have first presented an analysis of the gamma-ray emission of the blazar PKS 1502+106 [227, 228], which was found in coincidence with IceCube-190730A. I then showed how that data, together with other simultaneous data observed across the electromagnetic spectrum, can be explained in the context of leptohadronic interactions [228]. These interaction models can also help to shed light on the neutrino emission from the source, potentially explaining the IceCube coincidence. Despite the source was not found in a flaring state at the detection of the neutrino and seems to destabilise the picture of the prototype neutrino blazar, several elements of this coincidence and the source itself make it an outstanding science case.
A remarkable factor is that the Gold alert IceCube-190730A, with its 67% signalness, is one of the events with the highest probability of being of cosmic origin, compared to only 51% signalness in the case of IceCube-170922A coincident with TXS 0506+056. The event has a good angular reconstruction that identifies the gamma-ray blazar as the only high-energy candidate. The present gamma-ray analysis and previous

[227]: Franckowiak et al. (2020), 'Patterns in the Multiwavelength Behavior of Candidate Neutrino Blazars'
[228]: Rodrigues et al. (2021), 'Multi-wavelength and Neutrino Emission from Blazar PKS 1502 + 106'

works at several wavelengths have shown the remarkable characteristics of PKS 1502+106 that, other than being the $15th$ brightest blazar observed by *Fermi*-LAT, has shown a broad variety of flaring activities and long (but still detectable with sufficient statistics) quiescent states that make this source a unique laboratory for the study of blazars even at its high redshift of $z = 1.84$. This incredible amount of information obtained from the source, has lead me to collaborate in a broad study that combined synergies from both the experimental and phenomenological sides. Our results revealed how the environment of a source with characteristics of PKS 1502+106 can be a site for cosmic-ray acceleration and high-energy neutrino production. Furthermore, our study underlined the importance of gamma-ray and X-ray observations in the identification of features typical of hadronic emission in blazars, only possible thanks to the characterization of each emission state with the resolution achievable by the *Fermi*-LAT for this source.

Other works have studied the source in the context of the coincidence with IceCube-190730A. A recent study with VLBI and gamma-ray data [245] at 15 GHz and 8 GHz, found evidence for a radio ring structure, that can be explained by the existence of a precessing jet. A correlation study between the radio and gamma-ray observations has constrained also in this case the location of the gamma-ray emission region within the BLR at sub-parsec distances, close to the jet launching region itself. However, resolving such a compact environment at high redshift is still very challenging with available observations, and the site of hadronic interactions cannot be strongly constrained and could be also compatible with being outside the BLR or even at distances of less dense NLR material (~300 pc).

[245]: Britzen et al. (2021), 'A ring accelerator? Unusual jet dynamics in the IceCube candidate PKS 1502+106'

Assumptions of an interaction site located far beyond the BLR within the dusty torus were made by the study [246], where also in this case the expected neutrino production is compatible with the observation of a single high-energy event in a decade of observations.

[246]: Oikonomou et al. (2021), 'Multi-messenger emission from the parsec-scale jet of the flat-spectrum radio quasar PKS 1502+106 coincident with high-energy neutrino IceCube-190730A'

We are still at the first attempts to describe a neutrino blazar candidate like PKS 1502+106. The compatibility in the final results of these different approaches reveals, also in this case, that the model assumptions for these environments may be too simplistic and do not necessarily describe the system in a complete way. Observational studies are in fact revealing complex structures, that might be one of the keys to solve many of the problems still open.

Finally, the findings presented in this chapter reveal a relationship between multi-wavelength and neutrino emission from PKS 1502+106 that is quite different from the two blazars discussed previously in this thesis (TXS 0506+056 and GB6 J1040+0617). This highlights the diversity among the blazar population and the importance of considering the physical properties of each source when considering its potential as a neutrino candidate. Motivated by this, in the next chapter we turn from individual source to the entire blazar population.

Variability study of gamma-ray Blazars

A decade of gamma-ray variability in Blazar

8

From our studies on TXS 0506+056, GB6 J1040+0617 and PKS 1502+106 as candidate neutrino counterparts, we soon realize that the variability in blazars could play a crucial role also in the identification of fundamental features in the environment of the blazar emission region, and therefore give important insights about possible identification of high-energy neutrino blazar counterparts in terms of their variability properties.
While trying to have a broader view of the behaviour of the gamma-ray emission observed in blazars over time, we've soon realised that the majority of blazar flares systematically studied in the literature was from a limited sample of exceptionally bright blazars. I have therefore dedicated part of my PhD project to build a large (more than 250 sources) sample of gamma-ray light curves from blazars detected by *Fermi*-LAT in a decade of observations. Along with this, in order to exploit all the available physical information that these time series could provide, I have developed a pipeline for the temporal modelling of the flaring activities. This chapter gives an overview of a subset of the results from this study, oriented to the comparison between the variability properties of the candidate neutrino blazars studied in the previous chapters and those of the larger sample of gamma-ray blazars.
I will first give an overview on the sample selection, then I will present an exploratory analysis of the the global variability properties of the light curves. I will then present the modelling pipeline and the results from the application to our neutrino blazar candidate and to the whole sample.

8.1 A sample of bright blazars detected by *Fermi*-LAT 115
8.2 Modelling the flaring activities 124
8.3 Results 129
8.4 Summary 139

Contributions to the work presented in this chapter

The work presented in this Chapter is from a publication in preparation, for which I am the leading author. My contribution to this work is the production of the light curves sample, the developing of the flare modelling code and the analysis of the results. The developing and application of the HOP algorithm in the sample (Sec. 7.2) is a contribution to the project by M. Meyer and S. M. Wagner.

8.1 A sample of bright blazars detected by *Fermi*-LAT

The selection of the blazar sample for this variability study is driven by the method chosen for the computing of the light curves. Since the choice of the temporal binning size is strongly dependent to the specific transient (i.e. its duration and photon statistics), we use in this work the adaptive-binning method [162]. This method (already introduced in the previous chapters) allows to achieve a good resolution in the periods of enhanced activity by the source for a broad range of durations of the transients, down to very short variability timescales. At the same time, the absence of an a priori arbitrary size for the time binning, allows to

[162]: Lott et al. (2012), 'An adaptive-binning method for generating constant-uncertainty/constant-significance light curves with Fermi-LAT data'

increase the integration time as much as needed during periods of fainter emission, in order to avoid upper limits in the time series.
That said, we select the sources classified as blazar in the 4LAC [148] by ranking them following their average detection significance in 4LAC. This allows to exploit the adaptive-binning method, maximizing the number of adaptive bins calculated for each lightcurve. We select all 4LAC blazars that have an average detection significance $\sigma_{av} > 40$. The choice of this specific threshold is a result of a trade-off between having a large sample of bright blazars and a balanced representation among the different blazar classes, and is not motivated by additional properties of the sources listed in the 4LAC. Figure 8.1 shows the distribution of the average detection significance (σ_{av}) for all blazar in 4LAC, with the orange dashed line marking the cut at $\sigma_{av} = 40$.

[148]: Ajello et al. (2020), 'The Fourth Catalog of Active Galactic Nuclei Detected by the Fermi Large Area Telescope'

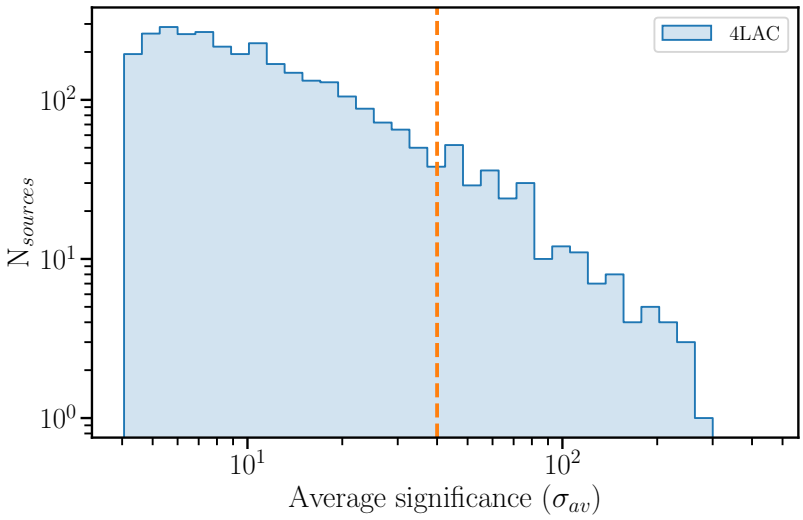

Figure 8.1: Distribution of the average detection significance of blazars listed in 4LAC. The dashed orange line marks the selection cut at $\sigma_{av} = 40$.

A total of 257 sources pass the selection cut, among which 236 are from the high-latitude sample ($|b| > 10°$) and 21 from the low-latitude sample ($|b| \leq 10°$) in Galactic coordinates. As for the classification of their optical spectra, 123 sources are classified as FSRQ, 125 as BL Lac and the remaining 9 are blazars of uncertain type (BCU). Following the classification in [62] based on the synchrotron-peak frequency, 170 sources are classified as low synchrotron peaked (LSP), 28 as intermediate synchrotron peaked (ISP) and 39 are high synchrotron peaked (HSP). The remaining 10 objects have no classification.
The left panel of Figure 8.2 shows the energy flux of the selected sources. The distributions for each optical class behave in a similar way. Only 211 sources in the sample have measured redshifts, and their distributions for each class are shown in the right panel of Figure 8.2. As already shown in Chapter 2, the nearby universe is populated mostly by BL Lac objects and the FSRQ spread up to the highest redshifts reached by gamma-ray observations.

[62]: Abdo et al. (2010), 'The Spectral Energy Distribution of Fermi Bright Blazars'

8.1.1 The light curve sample

In this work, we use *Fermi*-LAT Pass 8 data observed from August 4, 2008 to November 21, 2019. The details of the analysis configuration are described in Appendix A, and a common analysis approach is used for all sources.

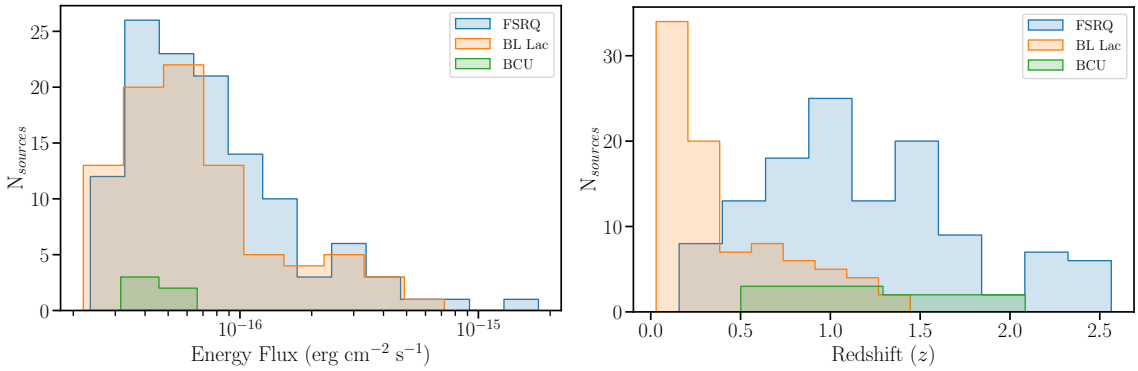

Figure 8.2: Distributions of the energy fluxes (*left*) and redshift (*right*) of the selected sample. Only 210 sources out of 257 have a measured redshift in [148].

To optimize the computational efficiency of such a large light curve sample, I have developed a pipeline that is structured in 3 main steps:

1. Running a binned likelihood analysis of the full-time period in a ROI centered at the catalog position of each target source, to obtain the best-fit models of our targets. Once obtained the best-fit spectral model, the adaptive bins method from [162] is applied to compute the temporal binning scheme for each light curve.
2. After the computation of the adaptive bins widths, a dedicated likelihood analysis is performed for each time bin. As already described in Chapter 3, `fermipy` libraries can serialize the execution of the likelihood analyses of each time bin. However, for large numbers (> 100) of bins, the pipeline splits the light curve in batches of maximum 100 bins each to be executed in parallel and optimize the computational demands. In addition, a power-law spectral model is always assumed for the target source (even when a curved spectrum is significantly preferred in the full analysis) because a curved spectrum is not usually statistically preferred at the shorter timescales of each bin, and this allows us to obtain a light curve for the spectral index along with the one for the integrated flux.
3. Once the previous step delivers the light curve, a sanity check searching for upper limits is performed in each time series. After performing the full likelihood analysis in each bin, upper limits might arise in time periods where also bright nearby sources are in high-state. The adaptive-bins method from [162], uses a simplified version of the *Fermi*-LAT likelihood approach that only includes the target source and one additional nearby object, in order to speed up the computation of each interval. Therefore, issues from source confusion might arise locally. The sanity-check routine looks for upper limits and, if found, merges the corresponding intervals with the adjacent bin with the lowest TS_{det} iteratively, until a minimum of $TS_{det} = 9$ is reached. The light curve is then re-computed with the updated binning scheme.

[162]: Lott et al. (2012), 'An adaptive-binning method for generating constant-uncertainty/constant-significance light curves with Fermi-LAT data'

The number of bins per light curve obtained from our sample of 257 sources ranges from a minimum of 10 bins per source to a maximum of 2890 bins for the most populated one (the FSRQ 3C 454.3), with a median value of 105 bins (Figure 8.3, *left* panel). The width of these time bins ranges from a minimum duration of ~5 minutes up to a maximum

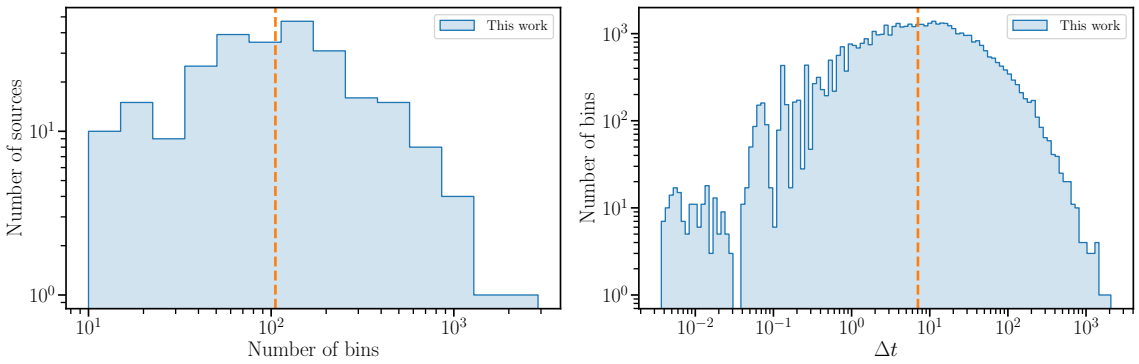

Figure 8.3: Distribution of the number of adaptive bins for each source in the sample (*left*) and time durations of each adaptive bin (*right*). The orange dashed lines indicate the median value of each distribution.

duration of ~5.7 years, with a median value of 7 days (Figure 8.3, *right* panel).
For the purpose of this chapter, that is also to compare the variability properties of the three neutrino blazar candidates studied in Chapters 5-7, I consider also the light curve of GB6 J1040+0617 described in Chapter 6 that, unlike TXS 0506+056 and PKS 1502+106, does not pass the selection cut on σ_{av}.

Sample variability

A first important thing to assess for the sample is a metric to quantify the variability of each source. We adopt the same approach used for the first time in the 2FGL catalog [247], that consists of a statistical test between the observed light curve and a null hypothesis that describes a constant flux model. The test statistic TS_{var} is defined as twice the difference of the log-likelihood under the alternate hypothesis (where the best-fit flux in each bin is calculated) and the value of the log-likelihood in the hypothesis of a constant flux across the full time period

[247]: Nolan et al. (2012), 'Fermi Large Area Telescope Second Source Catalog'

$$TS_{var} = 2\sum_{i}^{N}\left[log\frac{\mathscr{L}_i(F_i)}{\mathscr{L}_i(F_{glob})}\right] \tag{8.1}$$

where $\log\mathscr{L}(F_i)$ is the log-likelihood in the individual time bin i. In [141], a correction term is applied to this definition to correct for the difference between the flux obtained in the analysis integrated in the whole time range F_{glob} and the average flux F_{av} from the lightcurve bins

[141]: Abdollahi et al. (2020), 'Fermi Large Area Telescope Fourth Source Catalog'

$$TS_{var} = 2\sum_{i}^{N}\left[log\frac{\mathscr{L}_i(F_i)}{\mathscr{L}_i(F_{glob})}\right] - max(\chi^2(F_{glob}) - \chi^2(F_{av}), 0) \tag{8.2}$$

where the *max* argument considers the correction term only when positive. TS_{var} follows a χ^2 distribution with N-1 degrees of freedom (*dof*), where N is the number of bins of the light curve. In [141], a TS_{var} threshold of 18.48 is considered to distinguish variable from unlikely-variable sources, calculated over 12 intervals (yearly binned light curves) and

corresponding to a p-value of 1% for a χ^2 distribution with N-1 = 7 *dof* . According to the TS_{var} reported in 4FGL[141], 17 sources in our selection have a p-value > 1% of being consistent with the steady-source hypothesis. We apply the same variability test on our sample, to investigate whether a subsample of our light curves is compatible with a steady-source hypothesis. Since the number of light curve bins N is different for each source in our sample, we compare the p-values corresponding to a χ^2 distribution with N-1 *dof*. We find 7 sources with p-value > 1%, all included in the sample of 17 candidate steady sources from the variability test in 4FGL. From an inspection of the 10 remaining objects, we find for all of them some sporadic variability at timescales shorter than 1-year, that is likely not resolved in the 4FGL light curves due to their fixed binning choice. The 7 sources are listed in Tab. 8.1 with their TS_{var} and corresponding p-value.

Name	N_{bins}	TS_{var}	p-value
4FGLJ0957.6+5523	298	347.4	0.02
4FGLJ1243.2+3627	20	31.6	0.03
4FGLJ1120.8+4212	13	20.6	0.06
4FGLJ1607.0+1550	58	76.5	0.04
4FGLJ2121.0+1901	54	76.3	0.02
4FGLJ0008.0+4711	34	36.9	0.29
4FGLJ0718.6-4319	21	32.2	0.04

Table 8.1: Sources with p > 1% from variability test.

Detecting local variability: Bayesian Blocks representation

After assessing the global variability properties of the sample, the next step is to quantify the local variations in the time series. As already shown in the previous chapter, a flux measurement in each light curve bin comes with an uncertainty (like any scientific measurement) regardless of the technique used. Variations in the best-fit value of each measurement could be either due to a real change in the emission pattern from the object or merely to fluctuations introduced by experimental factors, like different exposures or observing conditions.

The Bayesian Block (BB) algorithm, first introduced in [194], provides an objective approach to detect local significant variations in the light curve measurements. The algorithm can be applied to either evenly and unevenly spaced observations and divides the light curve in blocks of adjacent data points where the signal is statistically compatible to a constant level. The prior in this bayesian approach can be used to calibrate the sensitivity of the method to variations at different significance levels, and is calibrated by means of Monte Carlo simulations in [194]. Throughout the analysis presented in this chapter, all BB representations have a prior corresponding to a false positive rate of 0.05, corresponding to a 2σ significance for the detected variations in the light curve.

[194]: Scargle et al. (2013), 'Studies in Astronomical Time Series Analysis. VI. Bayesian Block Representations'

After the application of the BBs to our light curve sample, we can start to quantify the shortest variability timescales, which can be significantly measured with the adaptive binning method.

A commonly used quantity is the timescale for the flux to double or to be reduced by half of its value. This is calculated for each pair of adjacent measurements that mark a significant variation of the flux level [248] with the expression

[248]: Saito et al. (2015), 'Time-dependent Modeling of Gamma-Ray Flares in Blazar PKS1510–089'

$$\tau_d = (t_2 - t_1)\frac{ln2}{ln(F_2/F_1)} \tag{8.3}$$

where (t_1,F_1) and (t_2,F_2) are the central time and the flux measurements for each pair of adjacent bins considered.

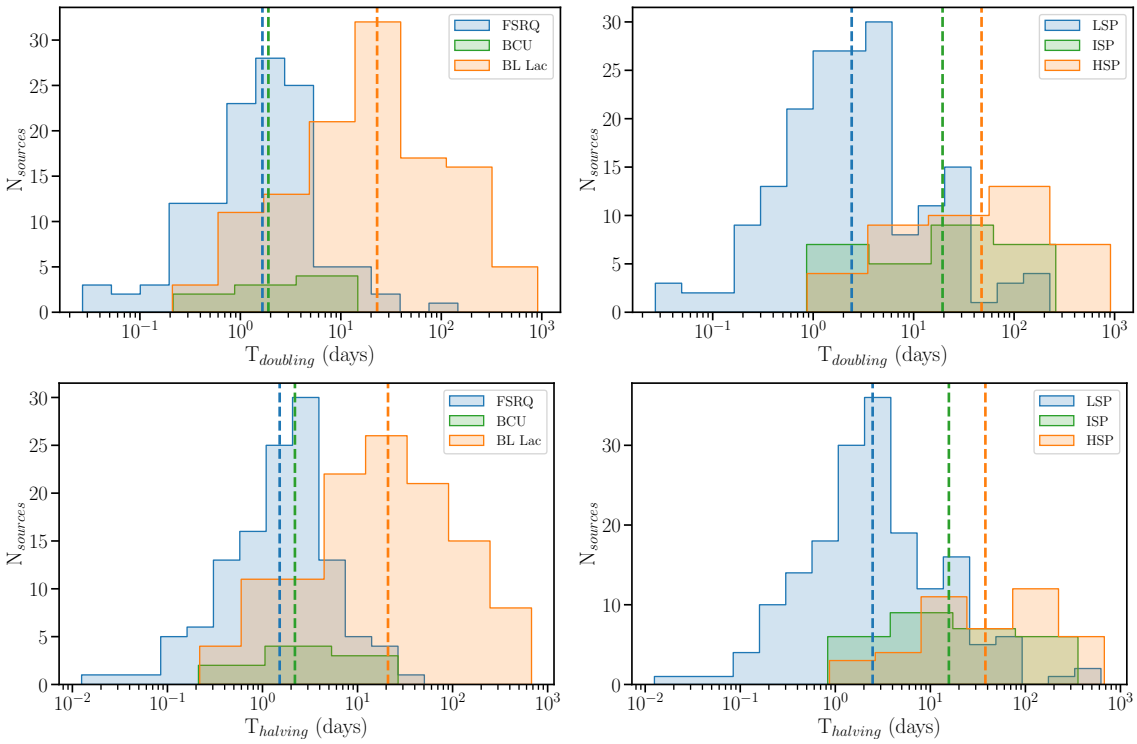

Figure 8.4: Distributions of the doubling (*upper row*) and halving (*lower row*) timescales divided by optical class (*left column*) and synchrotron peak frequency (*right column*). The dashed coloured lines mark the median value of each distribution.

Figure 8.4 shows the distributions of the doubling time (upper panels) and halving time (lower panels) for each optical (left column panels) and synchrotron peak class (right column panels). Half of the LSP sample has a $T_{doubling/halving} < 2$ days, with some sources at timescales as short as ∼ 30 minutes, while the distributions of ISP and HSP sources have median values ∼10 times higher and have the shortest $T_{doubling/halving}$ time scales at ∼ 1 day. When the optical classification is considered, the median values of FSRQs and BL Lacs show a similar difference, while in this case the distributions are generally more overlapped.

[249]: Abdo et al. (2010), 'Gamma-ray Light Curves and Variability of Bright Fermi-detected Blazars'

Following the approach in [249], I investigate the possibility of increasing the separation power between the different subclasses using a bi-variate representation of the dataset in the $T_{doubling/halving}$ vs redshift space (only for sources with a measured redshift).

Figure 8.5 shows the distributions of the doubling time (upper panels) and halving time (lower panels) in the comoving frame, versus the redshift. The colour scheme follows the optical classification of blazars in the left-column panels and the classification based on the synchrotron peak frequency in the right-column panels. The three neutrino candidate sources from Chapters 5 (TXS 0506+056), 6 (GB6 J1040+0617) and 7 (PKS 1502+106) are marked with red, brown and purple star, respectively. In order to understand if this bi-variate representation of the sample shows some separation power between the different subclasses of blazars,

I apply a *Support Vector Machines* (SVMs) classifier algorithm [250] to the dataset. The SVMs are a set of algorithms that use a subset of training points from the dataset (called support vectors) to optimize the parameters of an objective function (in our case, a linear function) that maximizes the separation power between a number of subclasses in the dataset. For this dataset, I apply the SVMs classifier to calculate the optimal separation boundary between 2 classes for each dataset: the FSRQ and BL Lac for the optical classification and the LSP and HSP for the synchrotron peak classification. I do not consider the BCU and ISP classes because the former is supposed to be a mixture of the other two optical classes, and the latter to have a better focus on the separation of the two extreme ends of the synchrotron peak classification. The solid black lines show the best-fit linear kernel that marks the optimal separation between the two subclasses, while the dashed black lines mark the width of the decision margin. Ideally, the algorithm would maximize the width of the decision margin and no data points should fall within the margin itself. In our case, where there is only a moderate separation power between the subclasses, the best-fit decision margin can be interpreted as an uncertainty region for the classification method where there is significant overlap between the subclasses.

[250]: Schölkopf et al. (2000), 'New Support Vector Algorithms'

The best-fit SVM kernels in the four panels of Figure 8.5 show that the bulk of the 2-D distributions for each of the selected classes can be separated with moderate efficiency using a simple linear cut (solid black line). The decision margin (dashed black lines) still includes a significant amount of the two subclasses which appear to be in a transition region between the two classifications.
Contrary to PKS 1502+106 that is well located within the bulk of FSRQ and LSP objects, TXS 0506+056 and GB6 J1040+0617 are located in this transition region, but still consistent with a BL Lac classification. This might support the recent tentative classification of TXS 0506+056 and GB6 J1040+0617 among a special subclass of BL Lac objects called *masquerading BL Lacs* [61, 251]. As already introduced in Chapters 2 and 5, these objects are intrinsically FSRQs for which the lack of emission lines in the spectrum is supposed to be due to the bright emission of the relativistic jet, that saturates the observed optical spectrum.
In [249] the maximum ratio of flux variations in adjacent weekly bins versus the redshift is used for the brightest 53 objects in the sample to test the separation between the FSRQ and BL Lac classes. A possible separation boundary was suggested in the 2-D representation, and also in that case the separation was not sharp. Even with a much smaller sample, an handful of sources was sharing properties with a different class like in our case.

[61]: Padovani et al. (2019), 'TXS 0506+056, the first cosmic neutrino source, is not a BL Lac'
[251]: Padovani et al. (2022), 'The spectra of IceCube neutrino (SIN) candidate sources - II. Source characterization'

Duty cycle

Another useful metric to quantify the activity of an astrophysical source is the duty cycle. It is defined as the ratio between the sum of each period spent by the source in an active state (δt_i) and the total observation time T_{obs}

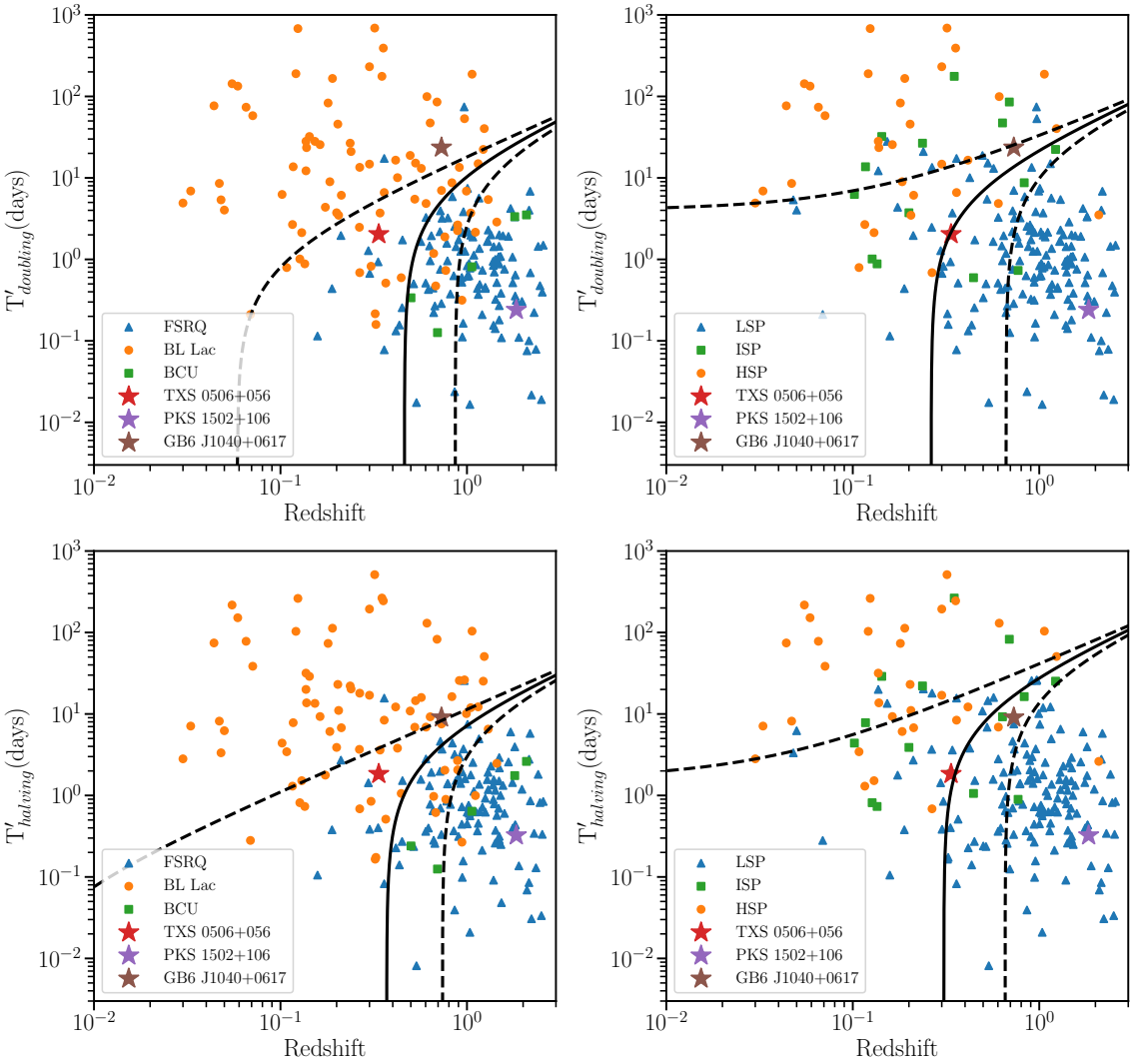

Figure 8.5: Scatter plots of the doubling (upper row) and halving (lower row) timescales in the comoving frame, versus redshift. The distributions are divided following the optical classification (left column) and synchrotron peak classification (right column). The solid and dashed black lines mark the decision boundaries of the SVMs classifier best-fit results. The star-shaped markers are used for the three candidate neutrino blazars.

$$D = \frac{\sum_i \Delta t_i}{T_{obs}}. \tag{8.4}$$

The choice of the optimal threshold is a critical point that has seen several approaches in literature, like the choice of a value equal or proportional to the average observed flux [252], from fitting the distribution of the observed fluxes [253], iterative methods [254] and several others. I will return to the challenging disentanglement of the flaring states from the quiescent periods in the next section, where I will describe a method specifically oriented to the purpose of the modelling of flaring states. For the estimation of the duty cycle, I exploit once again the properties of the BB representation and tailor the method to the characteristics of the adaptively-binned light curves.

I adopt the same approach described in Chapter 7 for PKS 1502+106, where the flux threshold F_{th} is the average of all flux measurements in the light curve weighted with the duration of each time bin (δt_i)

[252]: Vercellone et al. (2004), 'On the duty-cycle of γ-ray blazars'

[253]: Tluczykont et al. (2010), 'Long-term lightcurves from combined unified very high energy γ-ray data'

[254]: Nalewajko (2013), 'The brightest gamma-ray flares of blazars'

$$F_{th} = \frac{\sum_i F_i \Delta t_i}{\sum_i \Delta t_i}. \tag{8.5}$$

The periods of active state are then defined as all the groups of adjacent BBs with average flux

$$\overline{F} > F_{th} + \Delta F_{th} \tag{8.6}$$

where ΔF_{th} is the error on the average flux, calculated through the error propagation of the uncertainties on each measurement. The BBs that are not exceeding the threshold level are considered quiescent states of the source. This selection, based on the BB representation of the light curve, ensures that only states significantly higher than F_{th} are being selected. Figure 8.6 shows the results of the selection of active states for the light curve of GB6 J1040+0617. The green horizontal line and shaded area represent the threshold F_{th} and its uncertainty, while the orange shaded areas mark the BBs selected as active states.

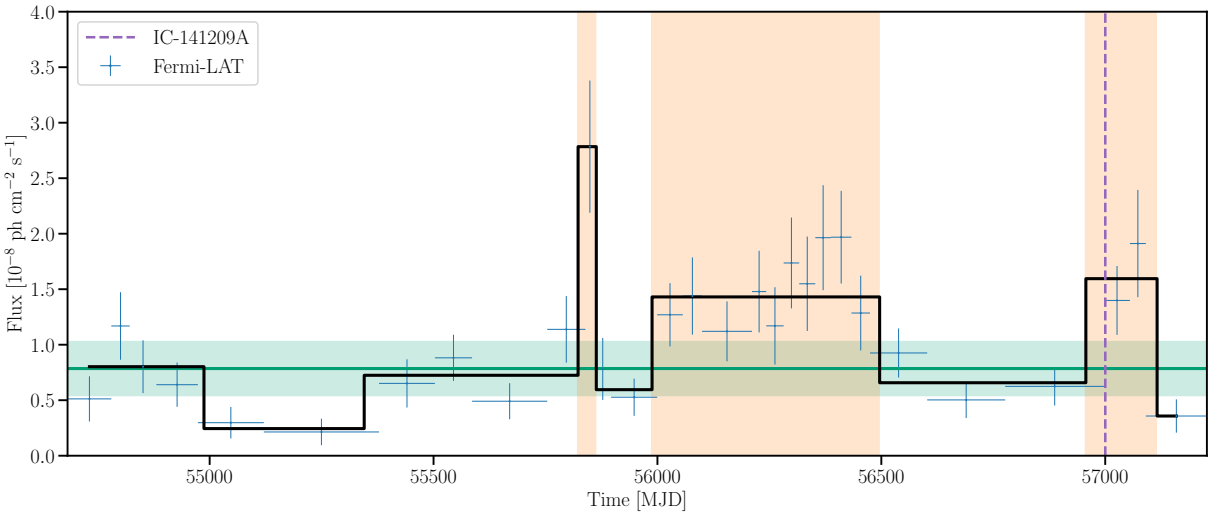

Figure 8.6: Active states in the light curve of GB6 J1040+0617. The green horizontal line and shaded area represent the threshold F_{th} and its uncertainty, while the orange shaded areas mark the BBs selected as active states.

The distributions of duty cycles for all the light curves in the sample (excluded those not showing variability) are plotted in Figure 8.7, divided following the optical classification (left panel) and the synchrotron peak classification (right panel). The median values for each sub-class are shown with a dashed line following the color scheme. For the distributions of the optical classes, the median values are very similar at ~23-24%, consistent with recent findings from [255] and a Kolmogorov-Smirnov (KS) test [256] shows a moderate tension between the FSRQ and BL Lac samples, where the null hypothesis (i.e. the two samples are drawn from the same distribution) can be rejected at 2.8 σ level. The samples based on the synchrotron-peak classification have also very similar median values, and the KS test shows a similar tension at 2.1 σ level between the LSP and HSP classes.

Table 8.2 lists the results for our blazar neutrino candidates. The blazar TXS 0506+056 and GB6 J1040+0617 show similar values of the duty cycle of 19-20%, while PKS 1502+106 is at 29%.

[255]: Sacahui et al. (2021), 'Study of Blazar Activity in 10 year Fermi-LAT Data and Implications for TeV Neutrino Expectations'

[256]: Hodges (1958), 'The significance probability of the smirnov two-sample test'

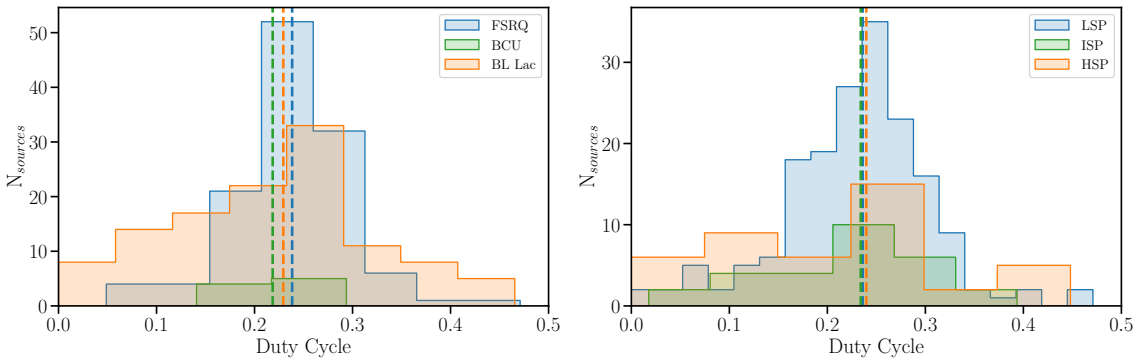

Figure 8.7: Distributions of duty cycles divided following the optical classification (left panel) and the synchrotron peak classification (right panel). The dashed colored lines mark the median value of each distribution.

In the next section, I will focus on the definition of flaring activity, and on the development of a pipeline to model the temporal evolution of the gamma-ray emission of blazar during these exceptional states.

Table 8.2: Doubling and halving time scales (in the comoving frame) and duty cycle (DC) of the three neutrino blazar candidates.

4LAC Name	Source	T'_D (days)	T'_H (days)	DC
4FGL J0509.4+0542	TXS 0506+056	2.0	1.8	0.19
4FGL J1504.4+1029	PKS 1502+106	0.24	0.32	0.29
4FGL J1040.5+0617	GB6 J1040+0617	23.6	9.1	0.20

8.2 Modelling the flaring activities

In the previous sections, I have presented an overview of the global variability properties of the light curve sample. The subsequent step, fundamental to extract their physical properties, is a proper characterization that consists of an analytical modelling of the temporal evolution of each flaring activity.
As already shown for the estimation of the duty cycle, the first critical point is to answer the question "*what is a flare?*". From decades of blazars observations, we know that the variation in their radiative emission spans over several orders of magnitude and throughout the whole energy spectrum, but the mechanisms behind this phenomena are still one of the main topic of study. From a pure empirical perspective, the fact that blazars show flaring activities interspersed by periods of low (apparently constant) activity has established the dichotomy between the concepts of *flaring* and *quiescent* states. However, this separation between the two states is often very difficult to be determined in an objective way, and it is strongly dependent on the observed source. The true nature of the flaring episodes is still under debate, and the possible scenarios include exceptional injections of particles in the jet, with subsequent acceleration and cooling phase [257], magnetohydrodynamic instabilities in the jet [258] or magnetic reconnection [94], among the various models proposed. Several of these scenarios do not agree with the existence of a stable quiescent state, but rather with a superimposition of many flaring episodes at different temporal timescales, among which those we call *flares* are just shorter, exceptionally bright episodes that happen on top of fainter and slow-varying class of flares that determine the observed

[257]: Ghisellini et al. (2002), 'Low power BL Lacertae objects and the blazar sequence. Clues on the particle acceleration process'

[258]: Raiteri et al. (2017), 'Blazar spectral variability as explained by a twisted inhomogeneous jet'

[94]: Shukla et al. (2020), 'Gamma-ray flares from relativistic magnetic reconnection in the jet of the quasar 3C 279'

quiescent level.

Identification of flaring periods

To identify distinct periods of flaring activity in each light curve, we adopt a modified version of the method in [92], that combines the Bayesian Block (BB) algorithm from [194] and the hill-climbing HOP algorithm from [259]. The methods consists of two steps:

1. Identify a BB that is higher than both the two adjacent blocks as a peak;
2. Proceed downward from the peak in both directions, as long as the blocks are higher than the average observed flux of the whole light curve, weighted by the duration of each bin.

[92]: Meyer et al. (2019), 'Characterizing the Gamma-Ray Variability of the Brightest Flat Spectrum Radio Quasars Observed with the Fermi LAT'

[194]: Scargle et al. (2013), 'Studies in Astronomical Time Series Analysis. VI. Bayesian Block Representations'

[259]: Eisenstein et al. (1998), 'HOP: A New Group-Finding Algorithm for N-Body Simulations'

This identifies the HOP blocks that contain single or multiple flaring activities to be modelled. Figure 8.8 shows the HOP blocks (shaded coloured areas) identified in the light curve of the source MG1 J123931+0443.
I will now present an overview of the modelling pipeline that I have developed for the characterization of the flares in each HOP block selected in this work.

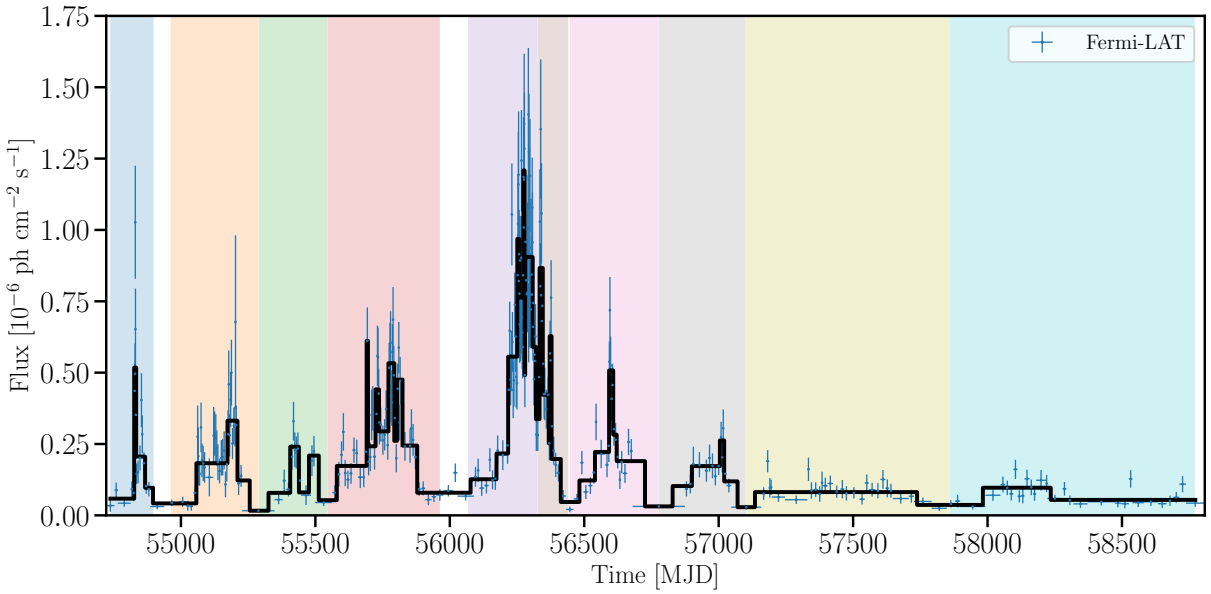

Figure 8.8: HOP blocks (shaded coloured areas) identified in the light curve of MG1 J123931+0443. The solid black line shows the BB representation of the light curve.

Non-parametric modelling with Gaussian Process Regressor

Astronomical time series present several challenges in their use and interpretation, mostly because of their quality that strongly depends on instrumental limitations during observations. Light curves represent a discrete representation of a continuous quantity (the emission from the source) and therefore the first problem concerns the cadence of

observations. As already described at the beginning of this chapter, we adopt the adaptive method for the light curve sampling, in order to mitigate the effects of an a priori choice of the binning. However, this is not enough to reach a clean description of the emission because of the limited sensitivity of the instrument and therefore we obtain an uneven sampling of the target emission. Modelling this emission with analytical functions involves making assumptions e.g. on the number of flares to be modelled and the intrinsic noisy behaviour of unevenly sampled astronomical time series can make this task quite difficult when one wants to have a common, objective approach over a large sample of observations.

In order to obtain a first guess on the true shape of the light curve, trying to avoid as much as possible the introduction of a bias from model assumptions, I have developed as first step of the pipeline a Gaussian Process regression. A Gaussian Process (GP) regressor is part of the wider branch of Bayesian Modelling algorithms and is defined as *"a collection of random variables, any finite number of which have a joint Gaussian distribution"* [260]. In more practical terms, it is a non-parametrical approach for data regression that, instead of assuming a particular function to be fitted over data, assigns a prior probability to a wide class of smooth functions that could be used to describe the data to then obtain the posterior probability given the data, as for a canonical Bayesian approach.

[260]: Rasmussen et al. (2006), *Gaussian Processes for Machine Learning*

Introducing a minimal mathematical formalism to this definition, there are 3 key elements in the GP approach: the training data, the covariance kernel and the learning process. The data in our case is a set $\mathcal{D}$ of n observations

$$\mathcal{D} = \{(x_i, y_i, \sigma_i), i = 1, ..., n\} \tag{8.7}$$

where the x_i are the central times of each bin, y_i the integrated flux measurements and the σ_i the errors on the flux. The dataset can be in general multidimensional, but in our specific problem it is a simple one-dimensional distribution.

The covariance kernel is the term that quantifies the differences between the function value evaluated at two points $k(x_i,x_j)$, and embeds the choice of the prior on the set of functions that constitute the GP. The covariance kernel has several mathematical properties (see [260] for a detailed overview on the mathematical formalism), among which their additive and multiplicative properties allow to construct complex kernels from the combination of simple ones. In our one-dimensional problem, the chosen kernel can be written as [260]

$$k_y(x_i, x_j) = \sigma_f^2 exp\left(-\frac{1}{2l^2}(x_i - x_j)^2\right) + \sigma_n^2 \delta_{ij} \tag{8.8}$$

where σ_f^2 and l are the signal variance and length-scale respectively, and are the only two so-called *hyperparameters* of the kernel, that define the properties of the prior distribution over the function. In the right-end of Equation 8.8, the first term is called *Squared Exponential (SE)* kernel and was chosen because every function in its prior has infinitely many derivatives and can therefore provide a smooth model for our light curves. The SE kernel however, does not take into account the so-called noise variance on data points (σ_f^2, the error on the flux measurements), and therefore the additional term $\sigma_n^2 \delta_{ij}$ (where δ_{ij} is the Kronecker delta)

takes also in account the error associated to each data point.
The flux measurements in the light curve (and their error) are used as training data to get the best set of hyperparameters for the kernel. The selection among all the possible functions embedded in the prior is performed via Bayesian model selection and constitutes the learning process of the algorithm. A detailed mathematical discussion is described in [260], and for the implementation in this thesis work I used the tools in the python library `scikit-learn`[i][261].
Figure 8.9 shows the modelling results with GP for one of the HOP blocks of the source S5 0716+71. The purple solid line is the best-fit function, while the shaded area marks the 95% confidence level from all the functions sampled in the posterior distribution.

[261]: Pedregosa et al. (2012), 'Scikit-learn: Machine Learning in Python'

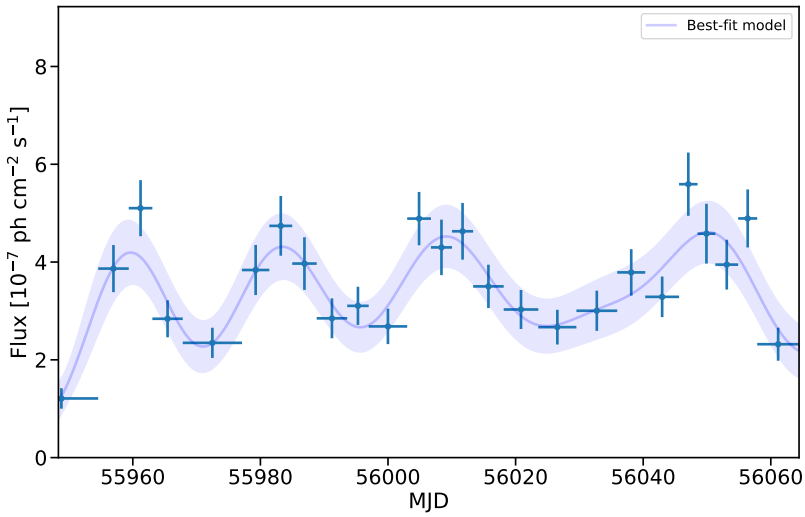

Figure 8.9: Best fit from Gaussian Process regression (solid purple curve) and 95% confidence level from the posterior distribution (shaded area).

The non-parametric modelling approach with the GP regression technique gives an accurate description of astronomical time series, and this is confirmed by the recent growth in its use on variability studies in astronomy (see [262–264] among recent works) and its wide application in machine learning for time series analysis and forecast.

[262]: Griffiths et al. (2021), 'Modeling the Multiwavelength Variability of Mrk 335 Using Gaussian Processes'
[263]: Willecke Lindberg et al. (2019), 'A Bayesian Method for Inferring Asteroid Properties from Sparse Light Curves'
[264]: Karamanavis (2017), 'Gaussian Processes for Blazar Variability Studies'

The double-exponential profile

The non-parametric modelling seen in the previous section has several advantages compared to more canonical interpolation methods of time series (e.g. spline interpolation), from the lack of assumptions on the specific signal shape to the handling of the uncertainties on the data points, that play an important role in the separation between significant and non-significant variability features in the light curve. The downside of such an approach is the non-trivial interpretation of the physical properties of the flares we are modelling. Since our ultimate goal is to have a physical characterization of these flares, the GP modelling is just the first step of the modelling pipeline, that tries to overcome the issue of the sparse distribution of data over time.
Each HOP block is ultimately modelled as the superimposition of a certain number of flaring activity on top of a background emission. The functional form used to describe the time profile of each single flare is the commonly used double-exponential profile [249]

[249]: Abdo et al. (2010), 'Gamma-ray Light Curves and Variability of Bright Fermi-detected Blazars'

[i] `https://scikit-learn.org/`

$$F(t) = F_0 \left(e^{\frac{t_0 - t}{T_r}} + e^{\frac{t - t_0}{T_f}} \right) \tag{8.9}$$

where F_0 is the amplitude of the flare, T_r and T_f are the rising and falling times, respectively, and the peak time of the flare can be calculated as

$$t_m = t_0 + \frac{T_r T_f}{T_r + T_f} ln \left(\frac{T_f}{T_r} \right) \tag{8.10}$$

that is equal to the parameter t_0 for perfectly symmetric flares.
Once the analytical function that will be used to describe each flare is determined, the next problem is to identify the number of flares that contribute to the whole HOP block. For this purpose, I have developed a peak finding procedure that exploits the information from the GP model and from the BB representation. The procedure finds peaks in the GP model that are located within a BB whose level is higher than the two adjacent ones (similar to the approach in the HOP algorithm), in order to only select peaks in the GP model that result also in significant variations of the measured flux. This procedure, once the preliminary position of the peaks is determined, can also extract preliminary guesses about rising/falling time to be used as initial values for the fitting of the double-exponential profiles where the model for the whole HOP block will be

$$F_{HOP}(t) = \sum_{i=0}^{N_{flares}} F_i(t) + F_{bkg} \tag{8.11}$$

where N_{flares} is the number of valid peaks found in the GP model and F_{bkg} is a constant background level.
The last step is the model fitting, that is initially performed via log likelihood minimization with the Nelder-Mead method [265, 266] and then with an extensive sampling of the parameter space using the Markov Chain Monte Carlo (MCMC) sampling technique with the `emcee` library [267]. From the posterior distribution of each parameter, the median value and the +1σ and -1σ errors are extracted (generally asymmetric). Figure 8.10 shows the final best-fit model (orange solid curve) and the single best-fit models of each flare (dashed green lines) and the constant background level (dashed red line).

[265]: Nelder et al. (1965), 'A Simplex Method for Function Minimization'
[266]: Newville et al. (2014), *LMFIT: Non-Linear Least-Square Minimization and Curve-Fitting for Python*
[267]: Foreman-Mackey et al. (2013), 'emcee: The MCMC Hammer'

Error propagation via bootstrapping

Due to the generally asymmetric nature of the errors extracted from the posterior distributions, I have implemented a Monte Carlo code to estimate errors on quantities derived by the fitted parameters of each flare (e.g. flare duration, symmetry etc.). The procedure consists of the following steps, for each derived quantity:

- Let us assume that the quantity Y is calculated from a series of parameters, each one defined as (x_i,-$\delta_{i,m}$, +$\delta_{i,p}$) where m and p denote the negative and positive error, respectively.

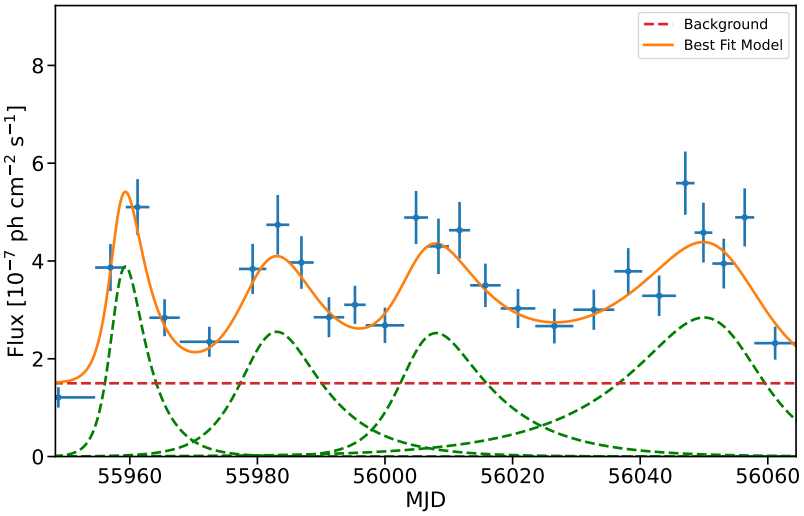

Figure 8.10: Global fit of the HOP block from Figure 8.9. The solid orange curve shows the best-fit total model, while the green and red dashed curves show the single-flare models and constant background, respectively.

- For each flare parameter, the algorithm randomly draws N times from two half-normal distributions with standard deviations $\delta_{i,m}$ and $\delta_{i,p}$.
- At each random draw, the quantity Y is calculated.
- The mean and standard deviation of the distribution of all the values calculated for Y are extracted.

For each parameter, N = 5000 random values are drawn every time and the same procedure is adopted from here on for the estimation of quantities (and their error) derived from the results of the modelling.

8.3 Results

In this section I will give an overview of the results from the modelling of the flares in the light curve sample. A total of 3453 flares are modelled in the sample, with 3322 of these flares belonging to sources with a measured redshift. In this results section, I will refer to the sample of 3322 flares from sources with associated redshift, for which these quantities can be converted into the comoving frame of the source.

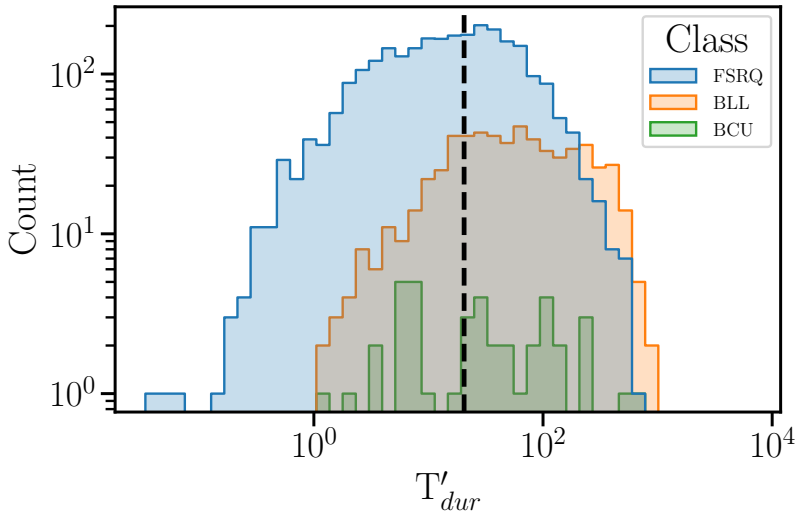

Figure 8.11: Flare duration distributions of the 3322 modelled flares in the comoving frame for each optical class. The black dashed line marks the median value of the total sample at 20.4 days.

Figure 8.11 shows the distribution of the flare total duration in the comoving frame calculated as $T'_{dur} = 2(T_r + T_f)/(1+z)$, for each optical class. The black dashed line marks the median of the total distribution at $T'_{dur} = 20.4$ days, that spans from a minimum duration of $T'_{dur,min} = 49$ minutes up to a maximum of $T'_{dur,max} \sim 2.7$ years.
The tails of this distribution cannot may include observational biases. The shortest observed durations are limited by the AB algorithm and the LAT sensitivity. Shortest duration flares may still be found by tuning the condition used for the computing of the adaptive bins on a source-by-source base, or by zooming into the brightest intervals of the lightcurve like the approach in [92]. A part of the flares with the longest durations could be the result of the too simple assumptions on the background level, and the necessity for the model to include a slow-varying component to describe the activity in the HOP block. In the future, an upgrade of the modelling pipeline will include the possibility of testing more sophisticated background models.

[92]: Meyer et al. (2019), 'Characterizing the Gamma-Ray Variability of the Brightest Flat Spectrum Radio Quasars Observed with the Fermi LAT'

Flare symmetry

A first interesting quantity that can provide a hint on the particle acceleration and cooling is the flare symmetry ξ, defined as in [249]

$$\xi = \frac{T_d - T_r}{T_d + T_r}. \tag{8.12}$$

[249]: Abdo et al. (2010), 'Gamma-ray Light Curves and Variability of Bright Fermi-detected Blazars'

The values of ξ range from -1 to 1, where $\xi = 0$ indicate perfectly symmetric flares. Values of $\xi > 0$ indicate flares with fast-rise exponential-decay (FRED) profile, that can be due to an acceleration timescale of emitting particles much shorter than the radiative cooling timescales. As shown in [268], this profile is mostly determined by a change in the bulk Lorentz factor or by the width of the emission region. On the other side, values of $\xi < 0$ indicate flares with slower rise than falling time, possibly due to a gradual acceleration of particles consistent with a first-order Fermi mechanism [135] and a faster cooling timescale [268].

[268]: Roy et al. (2019), 'Probing the jets of blazars using the temporal symmetry of their multiwavelength outbursts'

[135]: Fermi (1949), 'On the Origin of the Cosmic Radiation'

[268]: Roy et al. (2019), 'Probing the jets of blazars using the temporal symmetry of their multiwavelength outbursts'

As shown in the previous section, the durations of the more than 3000 flares modelled in the sample span over a few orders of magnitude, therefore the presentation of these results has to be necessarily split among different subsets of relatively comparable flare durations.
From a global inspection of the modelling results, it is evident that the short and medium-duration flares are well localized and describe distinct structures in the light curves. As mentioned in the previous section, flares of long duration (> 100 days) describe slowly varying periods and sometimes span for a large portion of the HOP block to compensate our simple assumptions on the shape of the background emission model, that would require additional slow-varying components.
A first, strict cut of $T'_{dur} < 1$ day can be applied to select the flares with shortest durations in the source frame. Only 113 flares pass the selection, all belonging to 19 sources of the FSRQ class and of LSP type. The distribution of ξ for the selected flares is shown in Figure 8.12.

The average symmetry for the 114 flares is $\xi = -0.01 \pm 0.02$, where the nominal value is indicated with a solid black line and the error range with dashed black lines. A fraction of (26.2 ± 2.1) % of these flares show

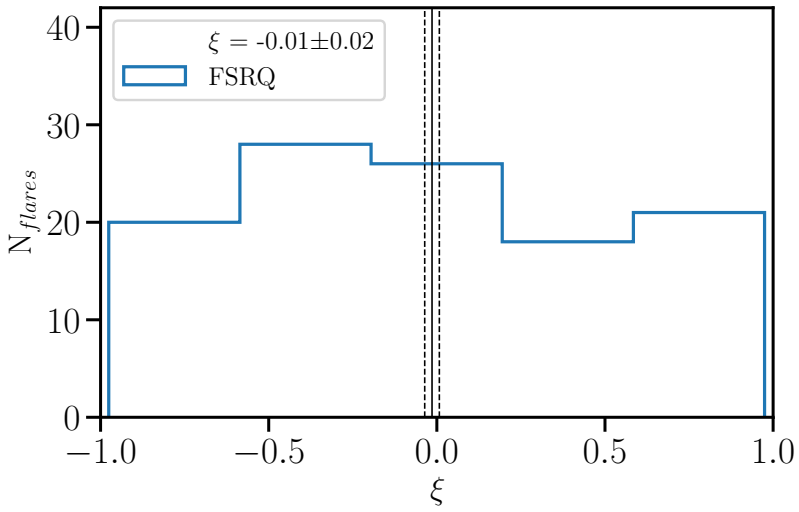

Figure 8.12: Distribution of the symmetry parameter ξ for flares with T'_{dur} < 1 day. The solid and dashed vertical lines marks the average value and 1σ uncertainty calculated with the bootstrap method.

a FRED-type profile (ξ > 0.5), and (29.2 ± 2.3) % have ξ < -0.5.
It is useful to consider the average value of ξ per source in this sample of fast flares. Figure 8.13 shows the average value and error of ξ for the 12 sources that have at least 3 flares with T'_{dur} < 1 day as a function of the redshift. Interestingly, we observe subsets of sources that show markedly different average behaviours at these short timescales. PKS 1510-089, 3C 279, 3C 454.3, B2 0218+357 and PKS 1824-582 show average values towards a FRED-type profile, while 4C+21.35, CTA 102, 4C+71.07 and PKS 1830-211 show the opposite profile with faster cooling timescale. The three sources NRAO 676, 4C+01.02 and PKS 1329-049 show instead an average value consistent with ξ = 0 within the uncertainties. This marked average behaviour observed from each source could be an important signature for the mechanisms behind the flares at these timescales, and might reveal more information about the specific source environment.

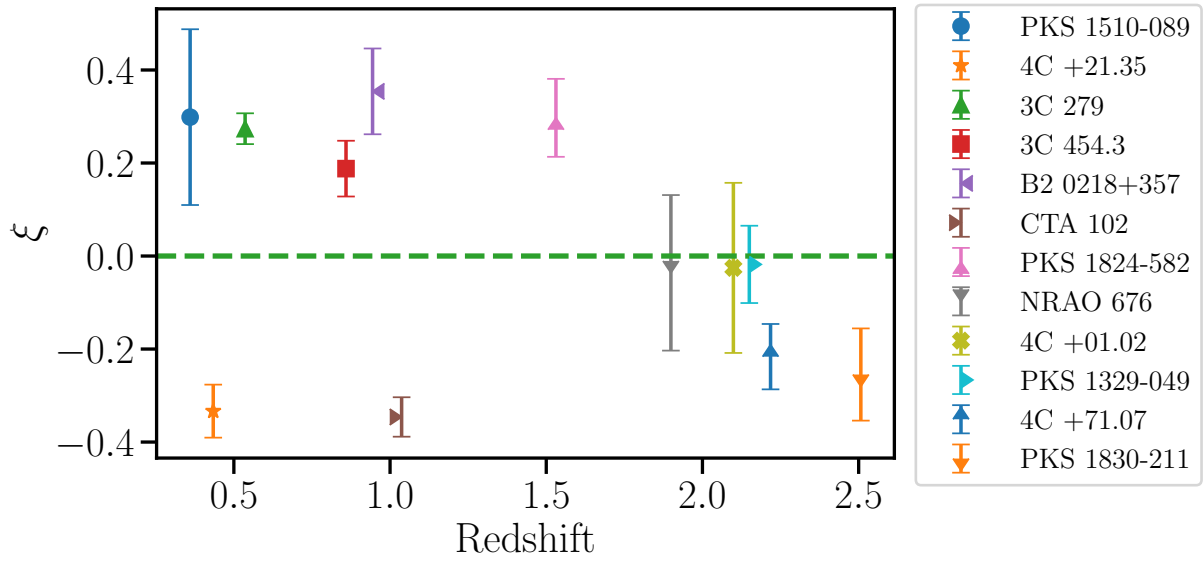

Figure 8.13: Average symmetry parameter ξ (and error) for sources with at least 3 flares with T'_{dur} < 1 day as a function of redshift.

Given the symmetric shape of the flare durations distribution in Figure 8.11, we divide the sample in two considering a selection cut at the median

value of the distribution of T'_{dur} = 20.4 days. Among the subsample with duration less than 20.4 days, 1490 belong to FSRQ sources and 155 to BL Lacs, while the remaining 16 flares belong to sources classified as BCU. Figure 8.14 shows the distributions of the selected flares for FSRQ sources (left) and BL Lac (right) with their respective average values. With the adding of longer duration flares, the amount of more symmetric flares increases, and the fractions of highly asymmetric flares is reduced in total to ~25-30% for both samples. The average values for the distribution are both consistent with the pure symmetric value of $\xi = 0$, confirmed by a K-S test between the two distributions with a p-value of 0.15.

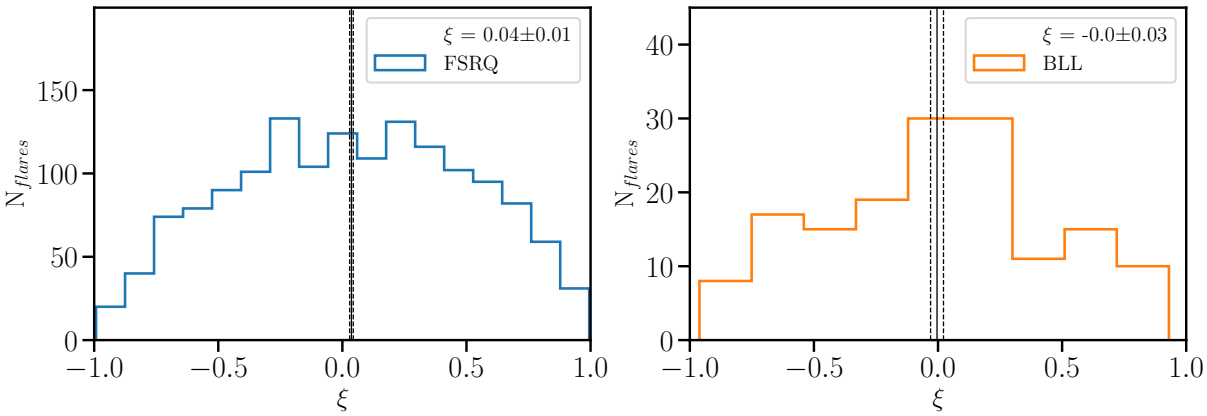

Figure 8.14: Distribution of the symmetry parameter ξ for flares with T'_{dur} < 20.4 days for FSRQs (left panel) and BL Lacs (right panel). The solid and dashed vertical lines marks the average value and 1σ uncertainty calculated with the bootstrap method.

The second half of the sample covers flares with duration in the comoving frame longer than 20.4 days, and therefore flares of medium-long durations within almost two orders of magnitude. It is composed by 1180 flares from FSRQs, 458 from BL Lacs and 25 from BCUs. The distributions of ξ for FSRQ and BL Lac (Figure 8.15) show similar characteristics compared to the first half of the sample, although the durations in this latter subsample span over more than an order of magnitude.

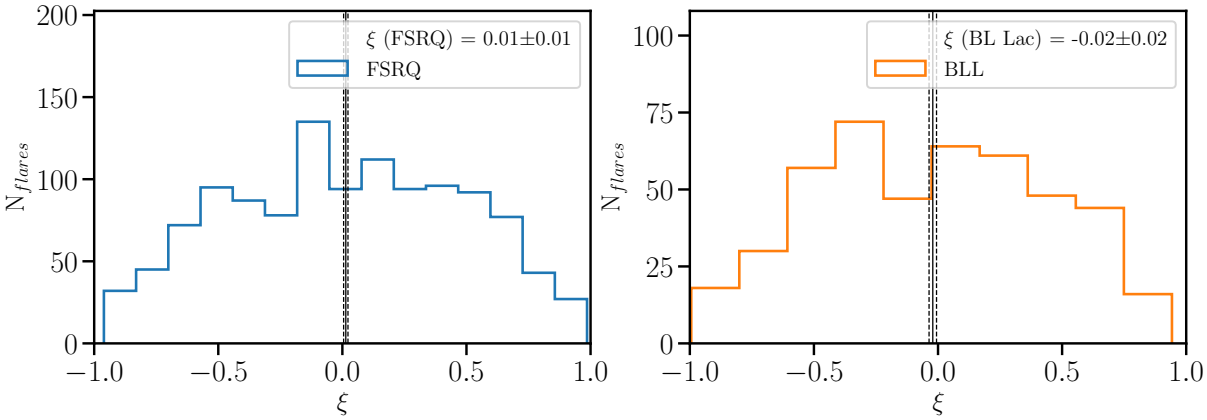

Figure 8.15: Distribution of the symmetry parameter ξ for flares with T'_{dur} > 20.4 days for FSRQs (left panel) and BL Lacs (right panel). The solid and dashed vertical lines marks the average value and 1σ uncertainty calculated with the bootstrap method.

These results are consistent with results from previous studies where a much smaller sample of blazar sources was used. Among these, [268] found similar distributions with the longer-term flares being mostly symmetric. This can be explained by the fact that long-term flares are

[268]: Roy et al. (2019), 'Probing the jets of blazars using the temporal symmetry of their multiwavelength outbursts'

dominated by the radiation crossing time through the emission region, and not by the cooling timescale of the radiating particles.

Size of the gamma-ray emission region

In the simple assumption of a single-zone model, another useful quantity that could be estimated is the size of the blob responsible for the observed gamma-ray emission. Once the shortest variability timescale t_{var} during the flaring activity is measured, an upper limit can be placed on the radius of a spherical blob in the comoving frame [269]

$$R'_b \leq \frac{c t_{var} \Gamma}{1+z} \tag{8.13}$$

were c is the speed of light, z the redshift and Γ is the bulk Lorentz factor of the flow and the relation uses the typical approximation $\delta_D \sim \Gamma \sim 10$ for blazars mentioned in Chapter 2.
The shortest variability timescale for each flare can be calculated following the relation used in [92, 269]

$$t_{var,ij} = \frac{F_i + F_j}{2} \left| \frac{t_i - t_j}{F_i - F_j} \right| \tag{8.14}$$

where i and j are the indices of two measurements F_i and F_j measured at the central times t_i and t_j. In order to select pairs of measurements with significant variations we use again the BB representation, limiting the portion of the light curve to the interval considered as total flare duration (t_m - $2T_r$, t_m + $2T_f$). The shortest variability timescale t_{var} is then the smallest $t_{var,ij}$ calculated within the flare duration.

[269]: Begelman et al. (2008), 'Implications of very rapid TeV variability in blazars'

[92]: Meyer et al. (2019), 'Characterizing the Gamma-Ray Variability of the Brightest Flat Spectrum Radio Quasars Observed with the Fermi LAT'
[269]: Begelman et al. (2008), 'Implications of very rapid TeV variability in blazars'

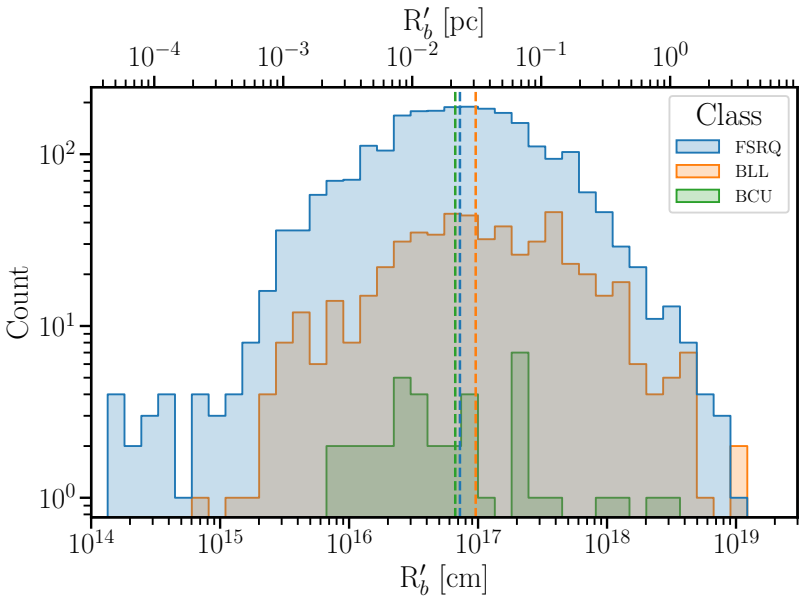

Figure 8.16: Distributions of the blob radius size R'_b (in the comoving frame) of each flare, for each optical class. The dashed coloured lines mark the median values of each distribution.

Figure 8.16 shows the distribution of the blob radius size R'_b (in the comoving frame) of each flare in centimeters and parsecs, for each optical

class. The values span across five orders of magnitude, from $\sim 10^{14}$ cm (3.24×10^{-5} pc) to $\sim 10^{19}$ cm (3.24 pc). The median values of each optical class (coloured dashed lines) are very similar, with 7.7×10^{16} cm for FSRQs, 1.1×10^{17} cm for BL Lacs and 6.9×10^{16} cm for BCUs.
A K-S tests strongly excludes the hypothesis that the FSRQ and BL Lac samples are drawn from the same distribution, with a p-value of 4×10^{-6}.

The TXS 0506+056 flare in September 2017

I will briefly report the results from the modelling of the two flaring activities described in Chapters 5 and 6, starting from the gamma-ray flare of TXS 0506+056 observed in coincidence with the detection of IceCube-170922A.

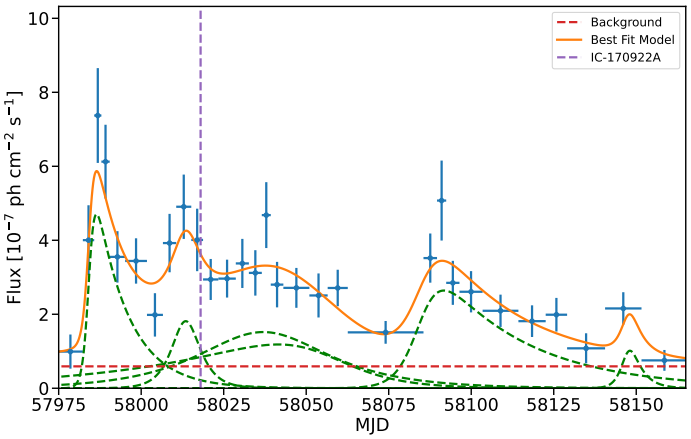

Figure 8.17: Best-fit model for the HOP block of TXS 0506+056 coincident with the arrival of IceCube-170922A (purple dashed line). The solid orange curve shows the best-fit total model, while the green and red dashed curves show the single-flare models and constant background, respectively.

Figure 8.17 shows the HOP block that includes the detection of IceCube-170922A, that spans between MJD (57973.8, 58158.3) . The best-fit combination that models the whole block has six flares in addition to a constant background. The brightest flare is the first one of the series in the HOP block (Flare 1), with a rise time $T'_{r,1} = 0.8^{+0.6}_{-0.4}$ days and a falling time $T'_{f,1} = 7^{+2}_{-2}$ days ($\xi_1 = 0.78 \pm 0.12$), for a total duration of $T'_{dur,1} = 16 \pm 4$ days (in the comoving frame) .
At the arrival of IceCube-170922A, three concurrent flares contribute to the observed flux points. The first one (Flare 2) is the shortest in duration ($T'_{dur,2} = 7 \pm 5$ days) and stronger in magnitude (~5 times the average flux), while the other two (Flare 3 and 4) are on their rising phase and only partially overlapping with Flare 2. Their durations are $T'_{dur,3} = 55 \pm 17$ days and $T'_{dur,4} = 84 \pm 33$ days.
The peak of Flare 2 is on MJD (58014 ± 5), 4 days before the arrival of IceCube-170922A at nominal value, and has a symmetric profile with $\xi_2 = 0.03 \pm 0.45$ (not well constrained because of the relatively large uncertainties on the best-fit flare parameters). The shortest variability timescale detected during these flares is of 5.5 days and is associated with the gamma-ray emission region responsible for Flare 2, for which the limit on the size would be $R'_b \leq 1.4{\times}10^{17}$ cm ($4.5{\times}10^{-2}$ pc). Flare 3 and Flare 4 show variability timescales of 12 and 24 days, respectively, and correspondent limits on the emission region size of $3.2{\times}10^{17}$ cm and $6.4{\times}10^{17}$ cm.

The best-fit parameters and errors for all six flares are listed in Tab. 8.3 and the distribution of the symmetry parameter ξ and the sizes of the gamma-ray emission region for all the 14 flares modelled in the light curve of TXS 0506+056 are shown in Figure 8.18. The left panel of Figure 8.18 shows the flare symmetry, with its average $\xi_{av} = 0.04 \pm 0.09$ that denotes a quite balanced distribution among the different flare profiles,

Table 8.3: Best fit parameters and derived quantities of the six flares in the HOP block of TXS 0506+056 coincident with the arrival of IceCube-170922A.

Flare	t_{peak} [MJD]	T'_r [d]	T'_f [d]	T'_{dur} [d]	ξ	t'_{var} [d]	R'_b [cm]
1	57986 ± 1	$0.8^{+0.6}_{-0.4}$	7^{+2}_{-2}	16±4	0.8±0.1	20.9	5.4×10^{17}
2	58013 ± 5	3^{+3}_{-2}	3^{+4}_{-2}	16±7	0.03±0.45	5.5	1.4×10^{17}
3	58037 ± 12	13^{+7}_{-7}	13^{+6}_{-6}	55±13	0.02±0.34	12.3	3.2×10^{17}
4	58040 ± 16	31^{+18}_{-17}	8^{+3}_{-5}	84±33	-0.5±0.3	24.7	6.4×10^{17}
5	58091 ± 5	3^{+4}_{-2}	20^{+4}_{-6}	48±11	0.6±0.2	5.2	1.3×10^{17}
6	58161 ± 23	$1.4^{+2.0}_{-0.9}$	2^{+2}_{-2}	10±5	0.2±0.4	5.2	1.3×10^{17}

with Flare 1 as the most extreme observed profile. On the right panel, the orange dashed line shows the estimated size of the blob radius in the comoving frame $R'_b \leq 1.4\times10^{17}$ cm, that falls among the most compact observed values for the source, ~2 times smaller than the median of the distribution.

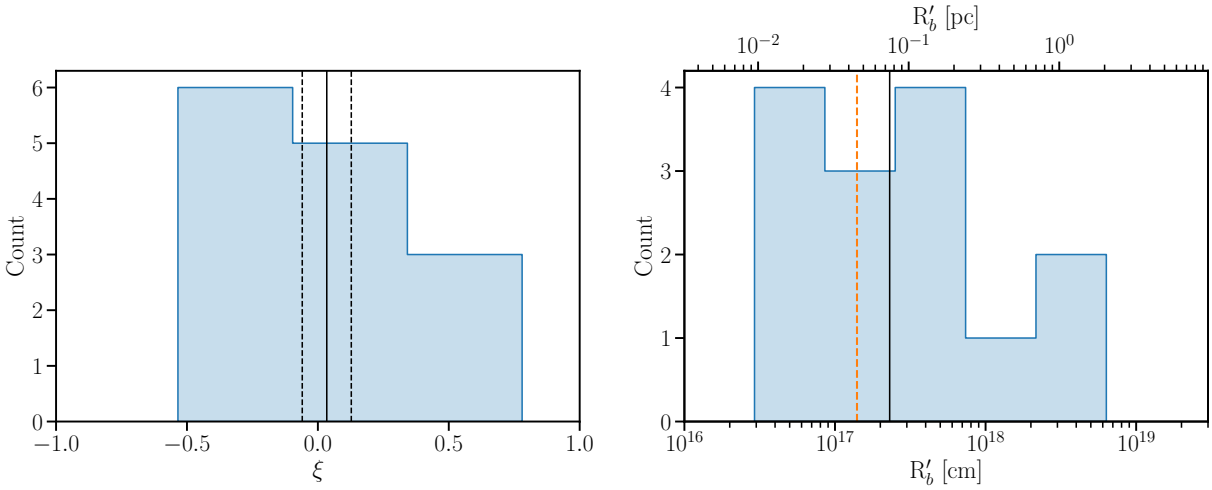

Figure 8.18: Distribution of ξ (*left*) and emission region size R'_b (*right*) for all the modelled flares in the light curve of TXS 0506+056. The orange dashed line marks the emission blob size of the flare coincident with the detection of IceCube-170922A.

The GB6 J1040+0617 flare in December 2014

As already shown in Fig. 8.6, the light curve of GB6 J1040+0617 shows activity at a level higher than average only in 3 periods, that can be grouped in the two flaring periods described in Chapter 6. In order to model the flaring emission coincident with the detection of GB6 J1040+0617, I select a 700-day interval from MJD 56600 - 57300 (Figure 8.19).

The activity is modelled with a single flare (green dashed line) plus a constant background (red dashed line) and the final best-fit model is shown as solid orange line. The flare peaks at MJD 57062^{+34}_{-51} and has a slow rising time in the observer frame $T_r = 86^{+49}_{-48}$ days and a faster falling time of $T_f = 16^{+27}_{-12}$ days, for a total duration $T_{dur} = 191 \pm 84$ days. The symmetry parameter for the flare is ξ = -0.5 ± 0.4 (the large uncertainty is due to the uncertainties on the raising and fall times) and, based on our results over the BL Lac sources in our sample. Profiles with symmetry larger than this one are observed only in ~23% of cases for flares in this

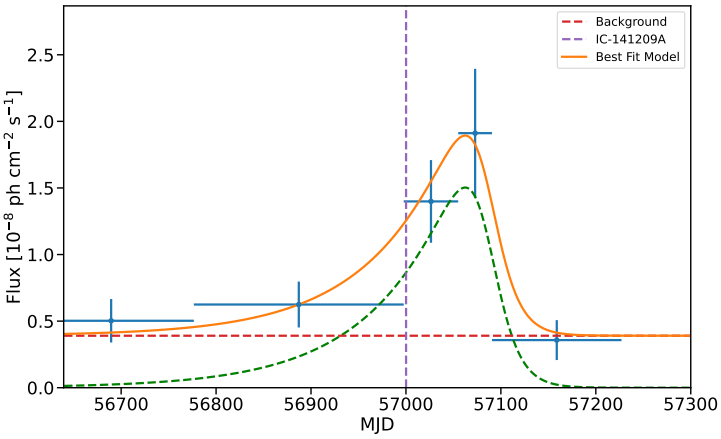

Figure 8.19: Best-fit model for the HOP block of GB6 J1040+0617 coincident with the arrival of IceCube-141209A (purple dashed line). The solid orange curve shows the best-fit total model, while the green and red dashed curves show the single-flare model and constant background, respectively.

range of durations (Figure 8.15).
The detection of the high-energy neutrino IceCube-141209A happens during the rising phase of the flare, ~70 days before the peak. In the comoving frame, the flare has a duration T'_{dur} = 190 ± 48 days and the shortest variability timescale is τ'_{var} = 36.2 days, that places a quite large limit on the blob radius of $R'_b \leq 9.4\times10^{17}$ cm, about 7 times larger than the limit we could place for TXS 0506+056.

The flaring history of PKS 1502+106

As already discussed in Chapter 7, the peculiar spatial coincidence of IceCube-190730A with PKS 1502+106 was not accompanied by a flaring activity of the source at gamma rays. It is interesting however to investigate the flaring history of the source to compare the variability properties with those of the other two neutrino candidates and the entire sample.
A total of 41 flares are modelled in the light curve of PKS 1502+106, with durations that range from $T'_{dur,min}$ = 20 ± 7 hours to $T'_{dur,max}$ = 112 ± 20 days in the comoving frame. The distribution of the symmetry parameter for all the modelled flares is shown in Figure 8.20 (*left*). The average value of the distribution is ξ_{av} = -0.06 ± 0.05, and the most extreme values observed are $\xi \simeq \pm 0.9$, denoting extremely asymmetric profiles. However, the bulk of the observed flares have values of ξ distributed between (-0.5, 0.5) denoting moderately asymmetric flares and without a mareked preference for symmetric shapes.

As for the previous sources, we can obtain the corresponding estimated sizes of the blob radius R'_b (Figure 8.20, *right*). The observation of variability timescales as fast as ~25 minutes in the comoving frame identifies very compact emission regions, and allows to set limits on the radius down to milli-parsec scales, with the smallest value at $R'_b \leq 1.4\times10^{-4}$ pc . The median value of the distribution for all 41 flares is 1.0×10^{17} cm (3.24×10^{-2} pc), with the largest blob radius of 0.6 pc.
Another interesting quantity that can be inferred from the variability timescales that is interesting for a FSRQ like PKS 1502+106 is the distance of the gamma-ray emission region from the central SMBH. One of the most debated argument about the gamma-ray emission in blazar jets is

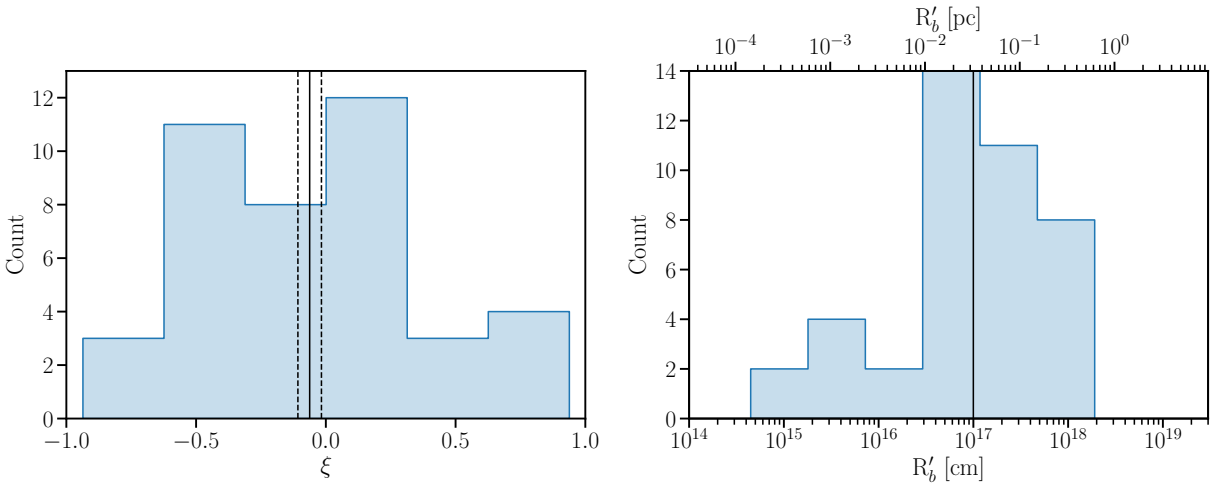

Figure 8.20: Distribution of ξ (*left*) and emission region size R'_b (*right*) for all the modelled flares in the light curve of PKS 1502+106.

the location of the blazar zone since observations show that the blob can be localized on source-by-source and flare-by-flare basis either within or beyond the BLR [270]. This is of great importance in the context of leptohadronic scenarios where the BLR can serve as main target for proton interactions.

[270]: Costamante et al. (2018), 'The blazar zone: Issues and recent developments'

Once we have calculated the minimum variability timescale using Eq. 8.14, the distance of the gamma-ray emission zone can be calculated following the approach in [245]

[245]: Britzen et al. (2021), 'A ring accelerator? Unusual jet dynamics in the IceCube candidate PKS 1502+106'

$$d_\gamma \sim 2c\Gamma^2\tau'_{var} \tag{8.15}$$

where τ'_{var} is the minimum variability timescale in the comoving frame and Γ is the bulk Lorentz factor. In their work, [245] find values for the bulk Lorentz factor $\Gamma \sim 1.5$ - 4.0 from their precessing-jet models. Here I consider the value $\Gamma = 4.0$ to obtain more conservative estimations of d_γ.

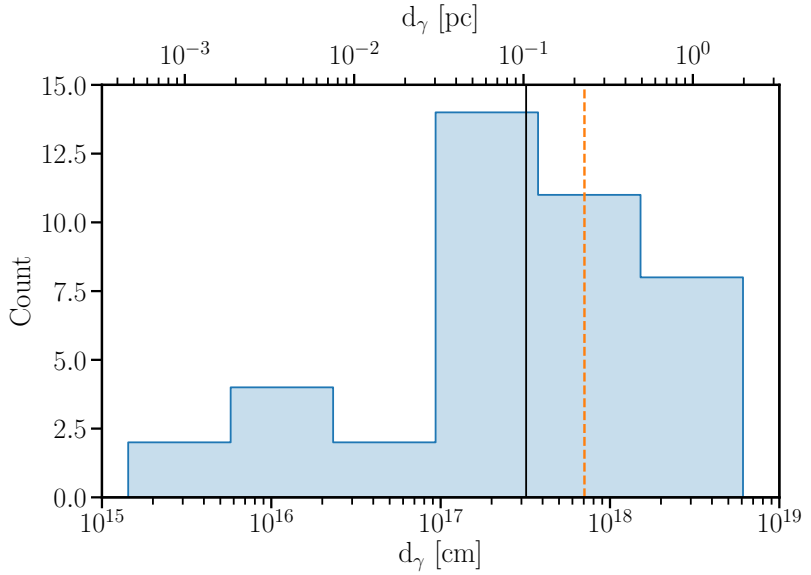

Figure 8.21: Distribution of the distance of the gamma-ray emission region from the central SMBH. The solid black line marks the median value of the distirbution, while the orange dashed line marks the radius of the BLR derived in Chapter 7.

The distribution of d_γ is shown in Figure 8.21. The median value of 0.1 pc

(solid black line) is well within the radius of the BLR derived in Chapter 7 (dashed orange line) and the maximum value observed is within ~10 times the BLR radius. A fraction of 70% of the flaring blobs have $d_\gamma < r_{BLR}$, reaching 97% when the lowest value of $\Gamma = 1.5$ from one of the jet models from [245] is used.
These results are in agreement with the findings in [245], and they are consistent with the location of the gamma-ray blob within the BLR. The different approach in this work consists in considering not only the fastest variability timescale observed in the light curve of PKS 1502+106 (and therefore the most compact emission region), but in considering each single flare separately to have an overview of the statistical properties of the gamma-ray emitting regions in the jet of this powerful blazar.
Comparing the derived distances d_γ with the Schwarzschild radius (R_S) of the SMBH calculated in Chapter 7, we find that our distribution spans over 3 orders of magnitude from $\sim 1\ R_S$ to $10^3\ R_S$. In particular, for the bright outburst of PKS 1502+106 in 2008-10 at the beginning of the *Fermi*-LAT mission, the smallest value for $d_\gamma = 4.3{\times}10^{-4}$ pc $= 4.5\ R_S$ is in agreement with previous results [239, 245].

[239]: Abdo et al. (2010), 'PKS 1502+106: A New and Distant Gamma-ray Blazar in Outburst Discovered by the Fermi Large Area Telescope'
[245]: Britzen et al. (2021), 'A ring accelerator? Unusual jet dynamics in the IceCube candidate PKS 1502+106'

8.4 Summary

In this chapter I have presented an overview on the characterization of the variability of a large sample of bright blazars observed by *Fermi*-LAT in more than a decade of operations. The sample of ~250 light curves obtained with the adaptive binning method gives noteworthy resolution of variable behaviour of the sources, and already from the variability timescales observed for each source, we obtain an interesting picture of differences and similarities within the different subclasses of blazars.
The major challenge of this work was to develop a general method for the identification and characterization of the flaring activities shown by the sources. The code that I have developed identifies and models successfully more than 3000 flares, making this so far the largest sample of gamma-ray flares ever studied in a single work.
The detailed characterization of each flaring activity gives interesting insights on the possible nature of the mechanisms behind the flares. In particular, the much larger sample of flares obtained in this work, shows that a significant portion of the observed flares have a marked asymmetric profile. Among the sources that show flaring activities with the shortest intrinsic durations (< 1 day), a significant fraction shows an average asymmetric profile in their flaring activities. This might be an hint of possible alternative classification of blazars based on their variability and therefore on the properties of their emission regions. A larger sample of sources that exhibit flares of very short duration will be crucial to probe the existence of different blazar types based on their variability.
A special focus in this chapter is given to the characterization of the neutrino blazar candidates from Chapters 5, 6 and 7. This has confirmed the compact nature of the emission region possibly associated with the observation of IceCube-170922A from TXS 0506+056, and a similar limit on the emission blob size (within one order of magnitude) can be derived for the flare of GB6 J1040+0617 coincident with IceCube-141209A.
In the case of PKS 1502+106, that does not show a gamma-ray flare at the

time of the observation of IceCube-190730A, it is interesting to notice that the distribution of the 41 flares modelled is more populated by very compact emission regions, down to milli-parsec scales in the source frame. Furthermore, an estimate on the distance of the emission blob from the central SMBH shows that in the majority of cases this is within or compatible with the BLR radius, confirming our assumptions in the modelling presented in Chapter 7 where the emission region was placed at the border of the BLR.

Several new features are planned in the future to improve this variability analysis. The first one will be the implementation of different models for the flares profile and for the background. We've seen that in several cases the flaring regions include in the best-fit models flares of long duration that contribute to the description of a slowly-varying component of the background, poorly described by a constant background level. Improvements in the fitting strategy and a better understanding of the performance of the modelling pipeline can be achieved by a dedicated application on simulated light curves. This will be also crucial to understand the biases introduced by the algorithm.

A population of neutrino blazar candidates

Realtime follow-up activities with *Fermi*-LAT

9

In this Chapter, I present an overview of the follow-up strategies and activities to realtime neutrino alerts with the *Fermi*-LAT, highlighting some interesting coincidences observed with gamma-ray sources that were not treated in the previous chapters. Since the start of my PhD fellowship in 2018, I have conducted follow-ups of more than 60 realtime neutrino alerts, the results of which were published systematically a few hours after each observations by means of rapid publications like circulars for the Gamma-ray Coordinates Network (GCN) and Astronomer's Telegram (ATel). I will start with the description of the analysis strategy and the correspondent follow-up pipeline that I have implemented for the Flare Advocates working group of the *Fermi*-LAT Collaboration, and I will discuss the properties of the observed alerts and their possible gamma-ray counterparts as presented in [271]. I will then present the results of a recent analysis [227], where my collaborators and I compared the gamma-ray properties of neutrino blazar candidates with the whole population of gamma-ray detected blazars by *Fermi*-LAT. Compared to the publication [227], this chapter will consist of a more updated analysis, which includes also coincidences after October 2019, in order to test a broader range of correlations between the neutrino and gamma-ray properties of these sources. At the end of the chapter, I also briefly present the results on the population of neutrino flare blazar candidates published in [227], with a focus on the only source that shows gamma-ray activity coincident with the neutrino flare detection.

9.1 Follow-up observations with *Fermi*-LAT 144
9.2 A population of neutrino blazar candidates 148
9.3 Results and discussion . . 155
9.4 Neutrino flare candidates 158

[271]: Garrappa et al. (2021), '*Fermi*-LAT realtime follow-ups of high-energy neutrino alerts'

[227]: Franckowiak et al. (2020), 'Patterns in the Multiwavelength Behavior of Candidate Neutrino Blazars'

Contributions to the work presented in this chapter

The work presented in this Chapter is from two publications for which I am corresponding author and also includes new results from a paper that is currently in preparation. The first part is from the Proceedings of Science of the ICRC 2021 (*Garrappa et al. 2021* [271]) and several rapid publications (ATel, GCN). I have developed the follow-up pipeline described here for the Flare Advocates group of the *Fermi*-LAT Collaboration, of which I am coordinator since 2020 and I have performed the majority of the realtime follow-ups to high-energy neutrino alerts during the time of my PhD. I am also the author of the analysis of neutrino-blazar coincidences. The second part of the Chapter is from the paper *Franckowiak et al. 2020* [227] in which I am the author of the *Fermi*-LAT spectral and temporal analysis of all 16 sources studied in the paper, and I have contributed to the collection of multiwavelength archival observations. The population study presented in [227] was made by A. Franckowiak and here I present an updated version of this study performed by me on a larger sample of sources and a broader set of statistical hypothesis.

9.1 Follow-up observations with *Fermi*-LAT

Analysis strategy

Since the start of the IceCube Realtime Alert Stream described in Chapter 4, the *Fermi*-LAT follow-up strategy to neutrino alerts has been consisting of a systematic, full-likelihood analysis of the sky region around the neutrino arrival direction, that contains the neutrino best-fit localisation and its 90% error contour. The follow-up strategy described in this section aims to look for transient emission from known catalogued LAT sources or new gamma-ray emitters at timescales that range from hours up to the full set of archival observations provided by the LAT over the entire mission.
To improve the standardisation and time-efficiency of the follow-up procedure, I have developed a semi-automatic follow-up pipeline that reduces the user time in setting-up the analysis to a minimum and significantly reduces the computing time needed for the longest integration timescales.
During a first standard follow-up analysis at the moment of the alert reception, we investigate 3 different timescales with respect to the arrival time T_0 of the neutrino:

- **1 day before T_0**: sensitive to the detection of fast, bright transients, down to few-hours duration.
- **1 month before T_0**: sensitive to the detection of recent transients from the sources of interest.
- **Full-mission data up to T_0**: to study long-term behaviour of LAT catalog sources and detect weak gamma-ray emitters not significantly detected and listed in the LAT catalogs.

The choice of these timescales is motivated by a trade-off between the detection sensitivity of the LAT for typical blazar-like transients at different timescales and the expected time lag between gamma-ray and neutrino emission from time-dependent studies of blazars (see [272] for an application to the gamma-ray flare of TXS 0506+056 contemporaneous to IceCube-170922A).

[272]: Gao et al. (2019), 'Modelling the coincident observation of a high-energy neutrino and a bright blazar flare'

The computational cost of a typical analysis of LAT data is proportional (among other factors) to the chosen integration time. For an analysis over the full mission data and a typical ROI size of 10°- 15°, the average computational time on a typical single-core process is between ∼30 min up to ∼ 1 hour per year of data, only to compute the *livetime cube* (see Chapter 3) . Under these computational demands, the investigation of the full-mission data (which currently amount to more than 13 years of observations) becomes prohibitive when the main purpose of the follow-up activities is to promptly report the observation of transients to the astronomical community.
To overcome this issue, I have adopted a modular approach in the follow-up pipeline, from the database managing to the analysis products. Fig. 9.1 illustrates the workflow of the pipeline. The first part of it consists in the update and preprocessing of the database with the most recent observations, representing the first and most crucial part for the optimization of the computational cost.
In the first step, weekly FT1 and FT2 all-sky files (see Chapter 3) are downloaded directly from the FSSC [1] and they are individually preprocessed,

1: *Fermi Science Support Center*

removing low energy events and the time intervals coincident with the detection of bright GRBs and Solar Flares. After the preprocessing, a *livetime cube* is computed for each weekly file (taking a few minutes for each week of data) and then they are subsequently all merged in a single file to be used as a pre-computed *livetime cube* for the analysis of the full-mission data. This cancels completely the time needed to compute each time the *livetime cube*, since now it will be computed only for newly added data at each update. As a result, the three analyses will take approximately the same running time.

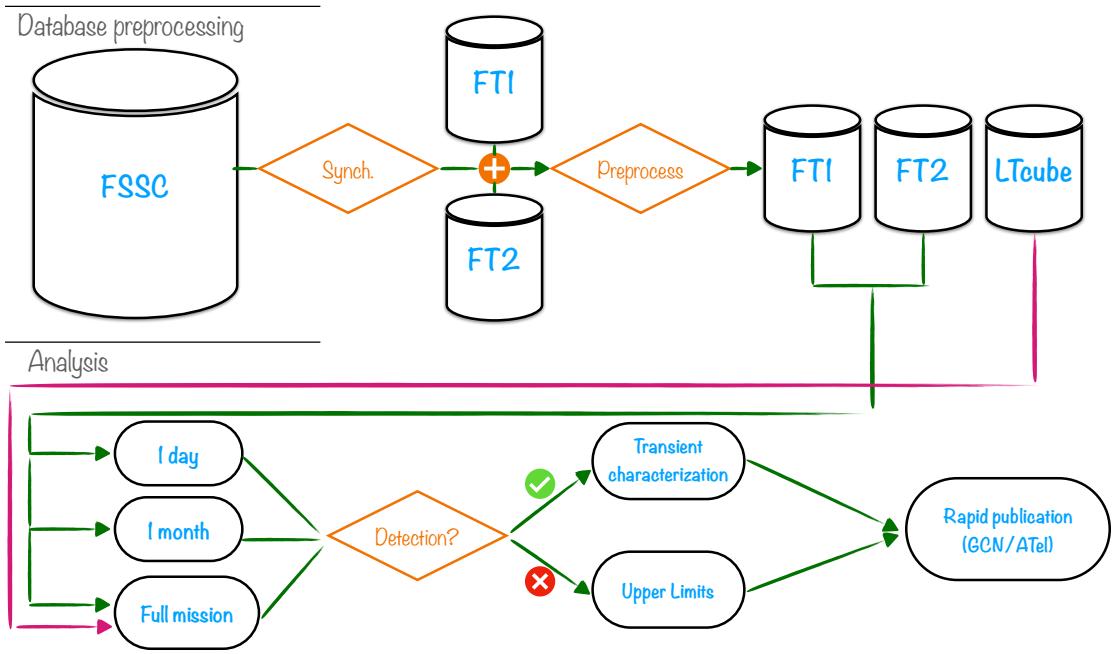

Figure 9.1: Scheme of the follow-up pipeline developed for *Fermi*-LAT data. The upper panel shows the synchronization and preprocessing of events (FT1) and spacecraft pointings (FT2) files, with the production of the *livetime cubes*. The lower panel shows the analysis workflow.

As standard configuration for the LAT follow-up analysis, we select photons from the point-source event class in the energy range from 100 MeV up to 1 TeV, binned into 10 logarithmically spaced energy intervals per decade. Depending on the extension of the IceCube error contour, we select a ROI of at least 15°×15°binned in 0.1°size pixel and centered at the neutrino best-fit arrival direction. The binning is made on a Hammer-Aitoff projection applied in celestial coordinates. In addition to the standard quality cuts discussed in Chapter 3, we remove time periods with the Sun within 15°distance from the ROI center.
After performing the analysis at all timescales, we check in the analysis products for sources in active state (or new transients) at short (1-day) and medium (1-month) timescales and for new gamma-ray emitters in the full-mission data. The latter might point to recently awakened sources or faint sources that reached a significant detection only adding up data after the set used for the most recent catalogs. If these detections are found, we perform a dedicated lightcurve analysis on the transient to assess the temporal evolution and its possible association with the neutrino detection. In case the excess was not previously listed in a LAT catalog, we also perform a search in the multiwavelength archive for observations of sources consistent with the LAT localisation of the transient.

After collecting all the results, we report our findings by means of rapid publications via GCN circulars and ATels. In the next section I give an overview of the results from the follow-up activities up to June 2021 published in [271].

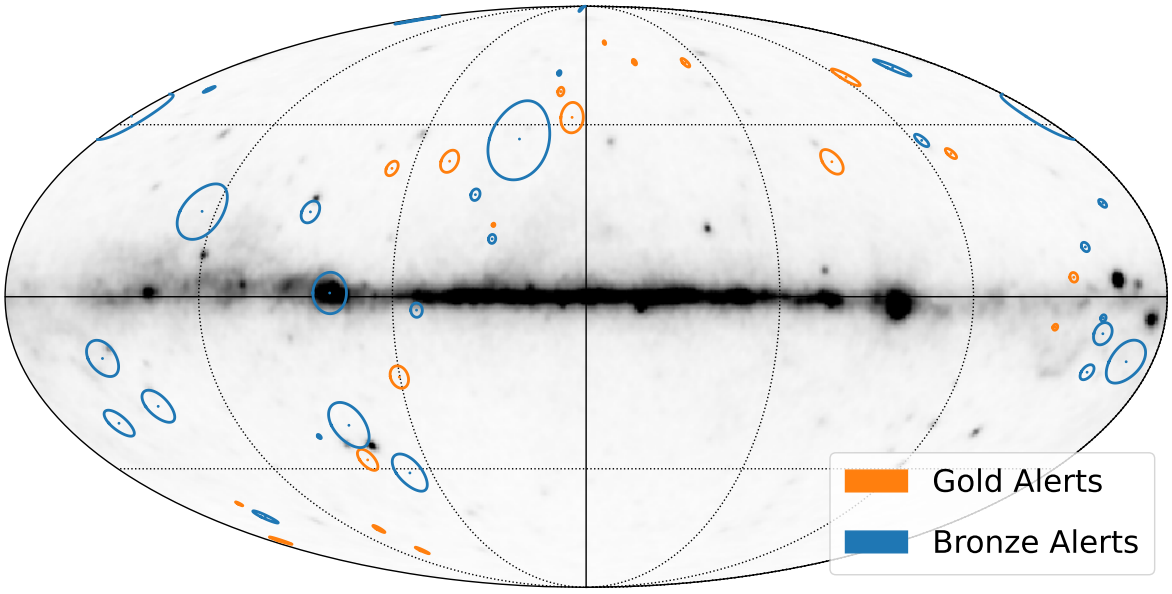

Figure 9.2: All-sky map in in Galactic coordinates from [271] showing the best-fit positions and 90% containment regions (approximated to circles) of the new IceCube Realtime Alert Stream in Galactic coordinates. *Gold* alerts are shown in orange and *Bronze* alerts in blue.

[271]: Garrappa et al. (2021), '*Fermi*-LAT realtime follow-ups of high-energy neutrino alerts'

Follow-up results

At the time of the most recent work, published as proceedings of science and presented at the $37th$ International Cosmic Ray Conference (July 2021) [271], the *Fermi*-LAT observed all the 46 alerts issued by the IceCube Realtime Stream 2.0 (see Chapter 4). Among these alerts, 19 were classified as *Gold* and 27 as *Bronze*. Figure 9.2 shows the best-fit localisations of the aforementioned events with their 90% error contours with *Gold* alerts shown in orange and *Bronze* alerts in blue. The sky-map is made with an healpix pixelization scheme of $N_{side} = 12$ in Galactic coordinates, with photon counts from LAT data as background in greyscale.
From an exploratory analysis of the properties of these alerts, we can observe that the distribution of the areas of the 90% containment regions is quite wide, and ranges from localisations reconstructed with an uncertainty as low as 0.57 sq. deg up to 385 sq. deg. In the left panel of Fig. 9.3 I show the distributions of the containment regions for each alert classification, separately. The median extension for the full sample is shown with a dashed black line at 11.4 sq. deg. This value differs significantly from the median of each sub-sample, amounting to 5.6 sq. deg. for the *Gold* sample (orange dashed line) and 13.4 sq. deg for the *Bronze* sample (blue dashed line).

The right panel of Fig. 9.3 shows the number of coincidences with sources from the 4FGL-DR2. For about 43% of the alerts sample, that consists of 20 alerts, there are no 4FGL-DR2 sources consistent with the neutrino localisation. There is a single 4FGL-DR2 candidate for 7 events, while the remaining 19 have several sources coincident due to the poor localisation of a substantial part of the sample.

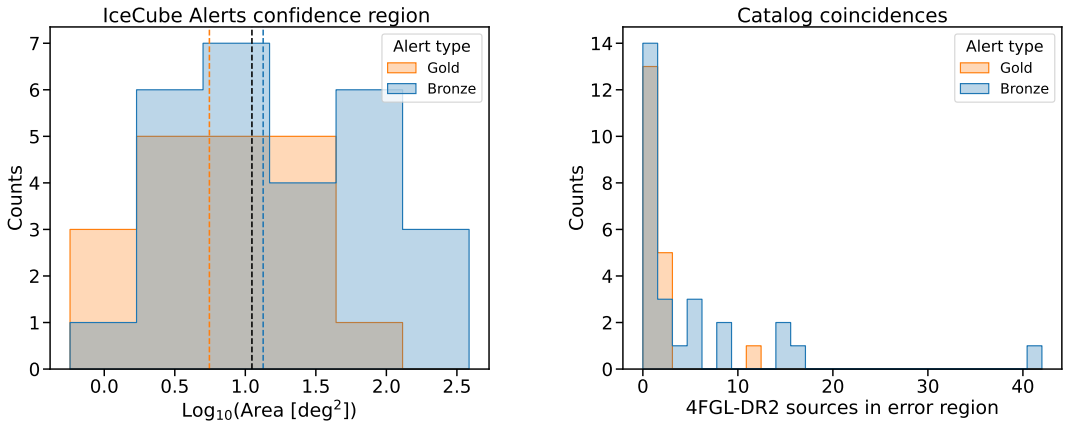

Figure 9.3: Distribution of the 90% containment regions (*left*) and number of 4FGL sources coincident (*right*) divided by alert type from [271]. The black dashed line in the *left* plot shows the median extension for the full sample, while the orange and blue dashed lines show the median extensions for the Gold and Bronze alerts, respectively.

When we consider the most recent version of the 4LAC catalog, that includes only AGN detected in gamma rays by *Fermi*-LAT, we have an average source density in the sky of ~0.07 deg^{-2} (~0.12 deg^{-2} if we consider the whole 4FGL), assuming an isotropic distribution of the sources. Considering the median value of 11.4 sq. deg for the neutrino error contour extension, on average we expect a 36% probability of observing 1 coincident source by chance (following a Poisson distribution). This is still a non-negligible rate of random chance coincidences of catalog sources with neutrino alerts, even with the gamma-ray detections of AGN-type sources being more rare than at lower frequencies. This high rate of chance coincidences is also due to the poor reconstruction of a significant part of the observed neutrino events.
In order to select coincidences only from a smaller sample of relatively well-reconstructed neutrino alerts, and improve the quality of our candidate associations, I select alerts that have an extension below the median value of 11.4 sq. deg.
Of the remaining 23 alerts after the selection cut, 12 of these are of the *Gold* class and 11 of the *Bronze*. Only 7 of them have at least one 4FGL-DR2 coincidence and one of them has 2 (Tab. 9.1). Six of these objects are identified as blazar while 4FGL J1747.6+0324 is an unidentified gamma-ray source.

Table 9.1: Selection of 4FGL-DR2 sources coincident with well-reconstructed realtime events from [271].

4FGL Name	Class	E.Flux [erg cm^{-2} s^{-1}]	Redshift	Event	Type	Sig.
J1504.4+1029	FSRQ	$(1.9 \pm 0.02)\times10^{-10}$	1.84	IC190730A	Gold	0.67
J0946.2+0104	BL Lac	$(2.55 \pm 0.55)\times10^{-12}$	0.577	IC190819A	Bronze	0.29
J1003.4+0205	BCU	$(1.64 \pm 0.39)\times10^{-12}$	2.075	IC190819A	Bronze	0.29
J0658.6+0636	BCU	$(3.7 \pm 0.73)\times10^{-12}$	-	IC201114A	Gold	0.56
J0206.4-1151	FSRQ	$(1.22 \pm 0.06)\times10^{-11}$	1.663	IC201130A	Gold	0.15
J1342.7+0505	BL Lac	$(2.98 \pm 0.49)\times10^{-12}$	0.13663	IC210210A	Gold	0.65
J1747.6+0324	unid.	$(7.03 \pm 0.92)\times10^{-12}$	-	IC210510A	Bronze	0.28

9.2 A population of neutrino blazar candidates

As shown in the previous section, the identification of the electromagnetic counterparts is very challenging for the majority of the high-energy neutrinos starting from the spatial association of the reconstructed directions. The high density of the point sources resolved throughout the electromagnetic spectrum and the poor resolution of neutrino telescopes, both pose a limitation to neutrino astronomy.

[227]: Franckowiak et al. (2020), 'Patterns in the Multiwavelength Behavior of Candidate Neutrino Blazars'

Along with the study of the multiwavelength behaviour of individual sources, in the work [227] we show a study of blazars coincident with high energy neutrinos as a population, and compare their average gamma-ray properties with those of the entire sample of gamma-ray resolved blazars. In order to select a clean sample of reasonable candidates, we have to somehow reduce the chance coincidence of sources falling in the neutrino localisation regions. We apply a selection cut that includes only neutrino events with angular uncertainty smaller than 5 sq. deg, with the prescriptions already adopted in [38]. The selection cut at 5 sq. deg comes from the median extension of the alerts issued in the first version of the realtime stream, that consisted in an error radius of 1.2°in their approximation to perfect circles. This selection reduces the amount of poorly reconstructed events that would lead to no significant association. After the cut, we are left with the following samples:

[38]: Garrappa et al. (2019), 'Investigation of Two Fermi-LAT Gamma-Ray Blazars Coincident with High-energy Neutrinos Detected by IceCube'

- From the archival events not included in the realtime system, observed between 2010 September and 2016 May: 28 neutrinos out of 40.
- From events observed and issued by the Realtime Alert Stream between 2016 April and 2019 October: 16 neutrinos out of 35.

Among the remaining samples of well reconstructed events, we identify 3 new coincidences in addition to the already discussed ones with TXS 0506+056, GB6 J1040+0617 and PKS 1502+106. The first one is a coincidence of the HESE event IceCube-190221A with two 4FGL sources, 4FGL J1758.7–1621 and 4FGL J1750.4–172. The first one is associated with the blazar of uncertain type AT20G J175841–161703, while the second is an unassociated source. The reconstructed direction of this event points to a region right in the Galactic plane with a high source density and large diffuse emission that makes detection and association very challenging. Since our search is targeted to blazar objects, we considered only AT20G J175841–161703 as a candidate counterpart. The other two coincidences are 4FGL J1258.7–0452, associated with the BL Lac object RBS 1194 and consistent with the position of IceCube-150926A, and 4FGL J0244.7+1316, associated with the blazar of uncertain type GB6 J0244+1320 and within the localisation of IceCube-161103A. These last two coincidences were not

found in the previous search performed in [38] because the sources were only listed in the more recent 4LAC catalog, that was only published later.
We compared the gamma-ray energy flux distributions of this sample of selected neutrino blazar candidates with the whole blazar sample listed in 4LAC. The energy flux of the neutrino blazar candidates is used in this case to probe the more general relation

$$L_\nu \propto L_\gamma^\alpha \tag{9.1}$$

between the correspondent average neutrino and gamma luminosities (L_ν and L_γ, respectively). To do so, we apply a Kolmogorov-Smirnov (*K-S*) test [256] to compare the two samples and statistically quantify how likely they belong to the same population. The null hypothesis here is that the two distributions are identical, and we have tested the samples of gamma-ray energy fluxes in 3 different scenarios:

[256]: Hodges (1958), 'The significance probability of the smirnov two-sample test'

- **Uncorrelated (α=0)**: all neutrino blazar coincidences occur by chance. In this case we expect the distribution of selected coincidences to be well compatible with the whole 4LAC population.
- **Linear correlation (α=1)**: the neutrino flux is proportional to the gamma-ray flux. In this case we expect the neutrino blazar to have a higher gamma-ray energy flux.
- **Quadratical correlation (α=2)**: the neutrino flux is proportional to the square of the gamma-ray energy flux. In this case we expect the neutrino blazars distribution to have a stronger dependence on the gamma-ray energy flux.

Sample	Uncorrelated (α=0)	Linear ($\alpha = 1$)	Quadratic ($\alpha = 2$)
BL Lac	0.32	0.45	0.0013
FSRQ	0.10	0.36	0.28
All Blazar	0.13	0.64	0.00032

Table 9.2: The *p*-values from the K-S test on the different classes and the whole sample of candidate neutrino blazars from [227].

The *p*-values from each test, for each source class and for the whole sample are listed in Tab. 9.2. For the scenario of linearly correlated fluxes we find a *p*-value of 0.64 indicating that the neutrino blazars distribution is well described by this hypothesis. They show instead a mismatch with the quadratical correlation with a *p*-value of 0.03%. The test in the uncorrelated scenario gives a *p*-value of 0.13 for the whole neutrino blazar sample, that makes it a more unlikely scenario that cannot however be strongly excluded. We can then repeat the same tests also for the classes of BL Lac and FSRQ objects separately, although the further reduction of the sample statistics leaves space to higher statistical fluctuations. The p-values for the single classes listed in Tab. 9.2 reflect the general behaviour of the whole neutrino blazar sample, which also includes blazars of uncertain type (BCU).
After the publication of the study in [227], there have been subsequent realtime alerts that are not included in the analysis. In Sec. 9.3 I present an updated analysis that I performed based on this new data. Before that, I will give a brief summary of the coincidences that will be included in the sample, with a focus on the source properties and the findings at the time of the detection. The selection criteria for the *Gold/Bronze* alerts used for the updated test is the observed median value of 5.56 sq. deg for

the Gold alerts, very similar to the selection cut of 5 sq. deg used in the previous works. Of the 17 alerts passing the selection cut, only 4 Gold alerts (included IceCube-190730A) have a coincident 4LAC source. This is compatible with the number of expected random coincidences (~3.4) for the whole area covered by the alerts passing the selection cut, assuming a uniform distribution of 4LAC-DR2 sources. Outside the selection from realtime alerts, I have also included two additional blazar-neutrino coincidences motivated by strong multiwavelength coincidences found among neutrino detections published in various samples of IceCube data:

- The FRSQ PKS 1424-41 coincident with IceCube-35 [35];
- The BL Lac MG3 J225517+2409 coincident with IceCube-100608A and an hot spot of a point source search from ANTARES in the directions of *Fermi*-LAT blazars [273].

[35]: Kadler et al. (2016), 'Coincidence of a high-fluence blazar outburst with a PeV-energy neutrino event'

[273]: Albert et al. (2021), 'ANTARES Search for Point Sources of Neutrinos Using Astrophysical Catalogs: A Likelihood Analysis'

Below I present a summary of these alerts in chronological order.

PKS 1424-41 and IceCube-35

The event IceCube-35 is part of the PeV neutrinos sample detected by IceCube in the first 3 years of observations [180]. It was detected on 2012 Dec 4 and classified as HESE with a cascade topology. The estimated energy of the parent neutrino was of 2004^{+236}_{-262} TeV with a best fit arrival direction at Ra = 208.4°and Dec = -55.8 °(J2000) and a 50% containment region of r_{50} = 15.9°. Among the several gamma-ray objects located in its large uncertainty region, the FSRQ PKS 1424-41 at redshif z = 1.522 [274] was found by [35] in a major outburst in gamma-ray, X-ray, optical and radio wavelengths. The chance probability for this coincidence was estimated at 5%. PKS 1424-21 is the $4th$ brightest blazar detected by *Fermi*-LAT in terms of gamma-ray energy flux.

[180]: Aartsen et al. (2014), 'Observation of High-Energy Astrophysical Neutrinos in Three Years of IceCube Data'

[274]: White et al. (1988), 'Redshifts of Southern Radio Sources. VII.'

[35]: Kadler et al. (2016), 'Coincidence of a high-fluence blazar outburst with a PeV-energy neutrino event'

MG3 J225517+2409 and IceCube-100608A

In a point sources search from the ANTARES collaboration [273] at the positions of *Fermi*-LAT sources listed in the 3LAC, one of the most significant hotspots reported was from the direction of 4FGL J2255.2+2411, associated with the BL Lac object MG3 J225517+2409 (lower limit at redshift z > 0.86 [275], z = 1.37 estimated from the SDSS survey and listed in 4LAC [148]). MG3 J225517+2409 is the $528th$ brightest blazar detected by *Fermi*-LAT in terms of gamma-ray energy flux. The gamma-ray source is also coincident with the neutrino event IceCube-100608A listed in [276]. The event is part of the sample used for the measurement and characterization of the diffuse astrophysical flux, has a signalness of 65% and an estimated energy of 340 TeV. The neutrino event has a 90% angular uncertainty region of 30 sq. deg (see Fig.9.4), and therefore it would not have been included in our searches for counterparts of well-reconstructed events.

[275]: Paiano et al. (2019), 'Spectroscopic lower limit to the redshift (z>0.863) of the BL Lac object 4FGL J2255.1+2411, a possible neutrino source'

[148]: Ajello et al. (2020), 'The Fourth Catalog of Active Galactic Nuclei Detected by the Fermi Large Area Telescope'

[276]: Aartsen et al. (2016), 'Observation and Characterization of a Cosmic Muon Neutrino Flux from the Northern Hemisphere Using Six Years of IceCube Data'

At the time of the arrival of IceCube-100608A, MG3 J225517+2409 was observed in high gamma-ray state by *Fermi*-LAT and we study in detail its temporal and spectral behaviour in [227]. During the gamma-ray flare

[227]: Franckowiak et al. (2020), 'Patterns in the Multiwavelength Behavior of Candidate Neutrino Blazars'

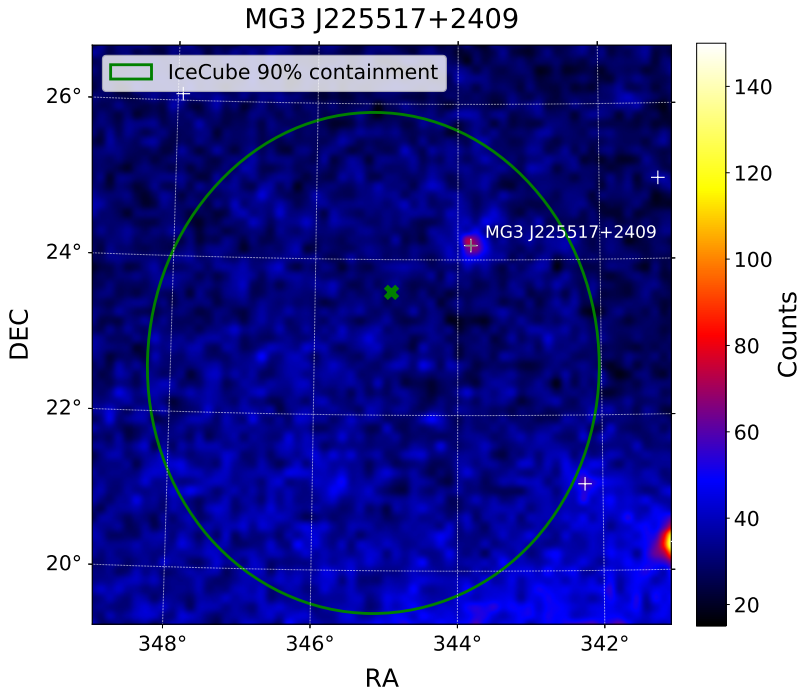

Figure 9.4: *Fermi*-LAT counts map of IceCube-100608A with the 90% angular uncertainty.

coincident with the IceCube event, the gamma-ray flux reaches a peak level of F = $(3.5 \pm 1.0) \times 10^{-8}$ ph cm^{-2} s^{-1}. From the lightcurve analysis of 11 years of *Fermi*-LAT data, we find that this high level of gamma-ray emission lasted for about 140 days (Fig. 9.5). After defining the frequentist p-value for the source of being observed in a higher gamma-ray state compared to the flux measured at the time of the neutrino arrival ($F_{\gamma,\nu}$):

$$p_\gamma(F_{\gamma,\nu}) = \frac{\int_{-\infty}^{\infty} \left(\sum_i t_i \int_{F_x}^{\infty} \mathcal{N}(x, F_i, \sigma_i) dx \right) \mathcal{N}(F_x, F_{\gamma,\nu}, \sigma_{\gamma,\nu}) dF_x}{\sum_i t_i} \quad (9.2)$$

we estimate a chance coincidence for the neutrino to be associated with the gamma-ray flare of $p_\gamma = 4\%$. In Eq. 9.2, $\mathcal{N}$ is a Gaussian function with mean $F_{\gamma,\nu}$ and standard deviation $\sigma_{\gamma,\nu}$ evaluated at F_x (we are assuming a gaussian distribution for the flux uncertainties). The index i identifies the time bins of the lightcurve of duration t_i. The lower the value of p_γ, the lower the probability of finding the source in a higher or equal gamma-ray state during the whole observation time. From the multiwavelength data collected from CSS observations, the source shows an enhancing also in the optical emission. The observations from ASAS-SN cover the time window only starting from 2012, and they show a good correlation with the gamma rays. Data from the OVRO monitoring start only few months after the neutrino arrival, and they show a descending phase with a much slower decaying of the flux compared to the other wavelengths, also for flux variations observed in the following years.

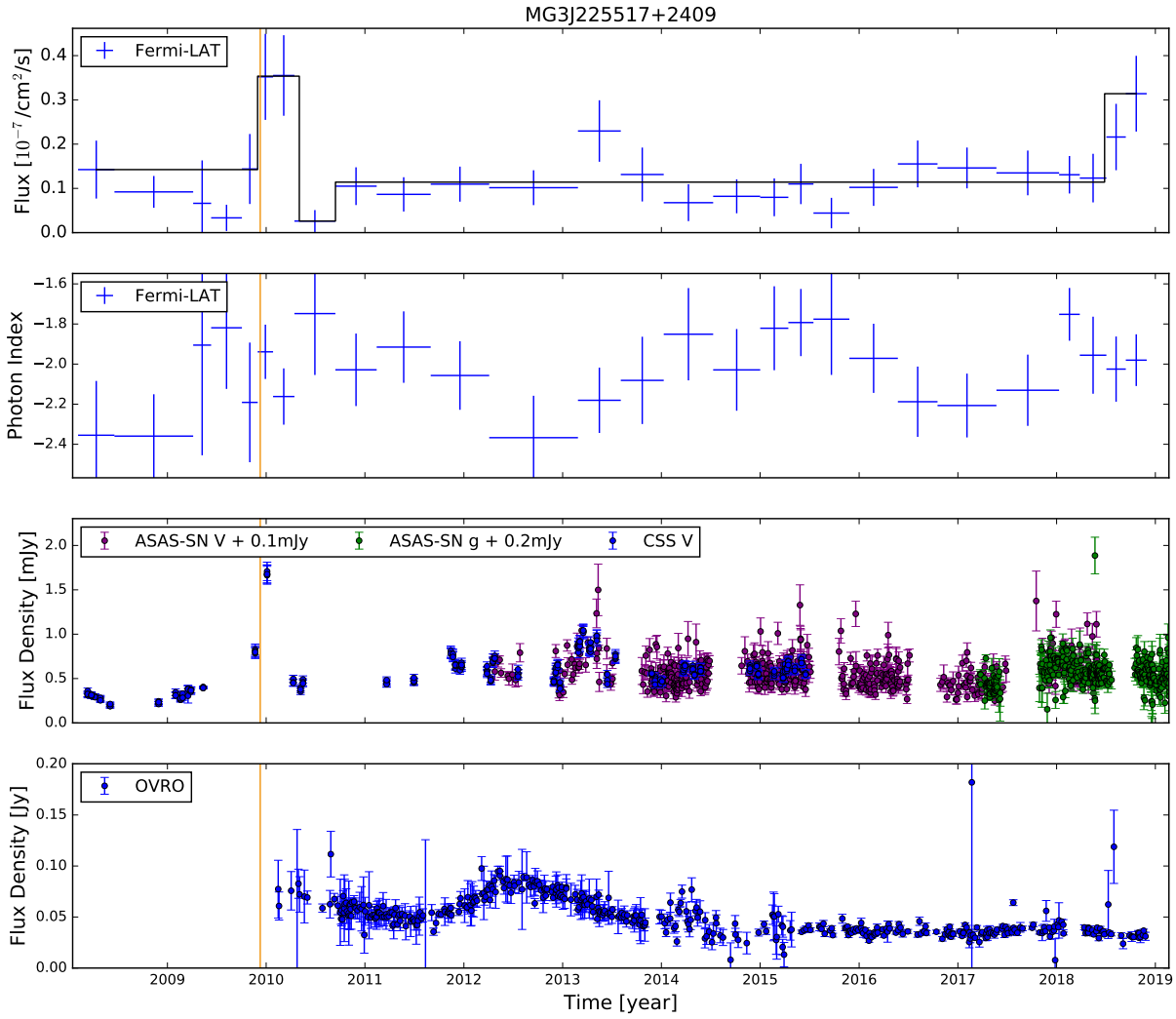

Figure 9.5: Multiwavelength lightcurves of MG3 J225517+2409

4FGL J0658.6+0636 and IceCube-201114A

On November 11 2020, IceCube reported the observation of a high-energy neutrino of the *Gold* type with a 56% signalness and a well-reconstructed arrival direction at Ra = $105.25^{\circ}{}^{+1.28}_{-1.12}$ Dec = $6.05^{\circ}{}^{+0.95}_{-0.95}$ J2000. Only one *Fermi*-LAT source is consistent with the 4.56 sq. deg extension of the 90% containment region. This is 4FGL J0658.6+0636 (also listed in the 3FHL catalog[144]) located 0.81°away from the neutrino best-fit arrival direction and associated with the high-synchrotron peaked blazar NVSS J065844+063711 [277], at unknown redshift. NVSS J065844+063711 is the 1628th brightest blazar detected by *Fermi*-LAT in terms of energy flux. In the follow-up analysis with *Fermi*-LAT observations after issuing the realtime alert, the source was not significantly detected at 1-day and 1-month timescales before the neutrino arrival time [278]. From more extensive analysis of the source, we found VHE gamma-ray emission from the source up to 155 GeV [279] during 12 years of *Fermi*-LAT observations. A rich multi-wavelength campaign from radio to IACT observations was triggered to get quasi-simultaneous data of the source right after the neutrino detection [280]. However, no remarkable activity is shown by the source at the time of the neutrino arrival, and the source is not

[144]: Ajello et al. (2017), '3FHL: The Third Catalog of Hard Fermi-LAT Sources'

[277]: Condon et al. (1998), 'The NRAO VLA Sky Survey'

[278]: Garrappa et al. (2020), 'Fermi-LAT Gamma-ray Observations of IceCube-201114A'

[279]: Buson et al. (2020), 'Fermi-LAT evidence for VHE emission from NVSS J065844+063711'

[280]: Menezes et al. (2021), 'Multi-Messenger observations of the Fermi-LAT blazar 4FGL J0658.6+0636 consistent with an IceCube high-energy neutrino'

detected by IACT facilities. Figure 9.6 shows a counts map of *Fermi*-LAT data of the IceCube-201130A region with its best-fit arrival direction and 90% angular uncertainty.

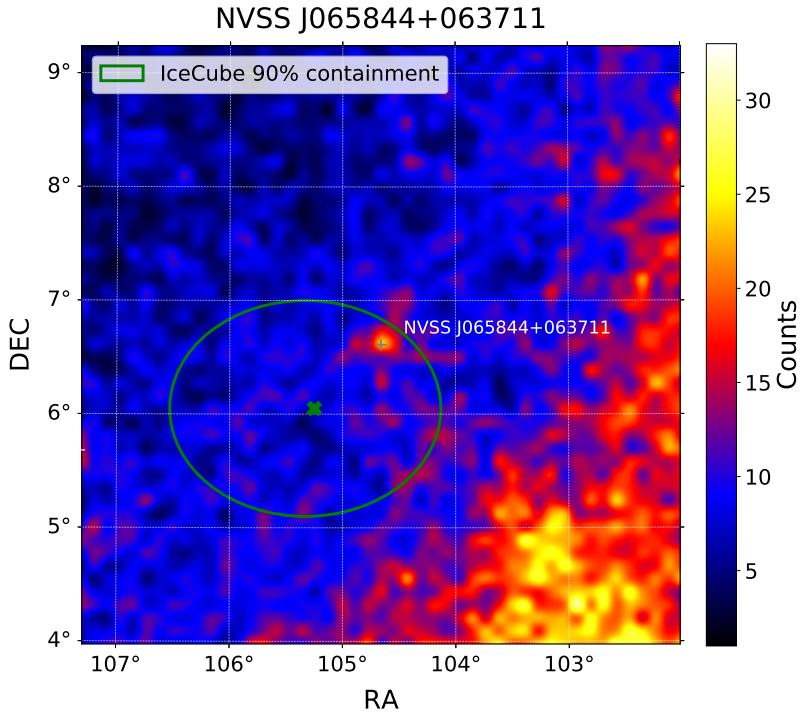

Figure 9.6: *Fermi*-LAT countmap of the IceCube-201114A with its best-fit localization (green *x*) and 90% angular uncertainty (green circle). The bright diffuse emission in the lower right corner is due to the Galactic Plane.

4FGL J0206.4-1151 and IceCube-201130A

On November 30 2020, IceCube reported the observation of a high-energy neutrino of the *Gold* type with a 15% signalness and best-fit arrival direction at RA = $30.54^{\circ}{}^{+1.13}_{-1.31}$, Dec = $-12.10^{\circ}{}^{+1.15}_{-1.13}$. One *Fermi*-LAT source is located within the 90% IceCube-201130A localisation. This is the source 4FGL J0206.4-1151, associated with the FSRQ object PMN J0206-1150 [281] at redshift z = 1.663 [146]. The 4FGL best-fit position is at Ra = 31.6018°and Dec = -11.8576°(J2000), at 1.1°distance from IceCube-201130A. The average measured energy flux is $(1.41 \pm 0.06) \times 10^{-11}$ MeV cm^{-2} s^{-1}, making it the 472*th* brightest *Fermi*-LAT blazar in terms of energy flux. Its spectrum is well described by a simple power-law model with spectral index $\Gamma = 2.40 \pm 0.03$.
During the realtime follow-up analysis with *Fermi*-LAT data, we found no significant ($> 5\,\sigma$) detection of the source over the timescales of 1-day and 1-month prior the neutrino arrival [282]. Figure 9.7 shows a counts map of *Fermi*-LAT data of the IceCube-201130A region with its best-fit arrival direction and 90% angular uncertainty.

[281]: Griffith et al. (1994), 'The Parkes-MIT-NRAO (PMN) Surveys. III. Source Catalog for the Tropical Survey (-29 degrees < delta < -9 degrees -3pt.5)'

[146]: Healey et al. (2008), 'CGRaBS: An All-Sky Survey of Gamma-Ray Blazar Candidates'

[282]: Garrappa et al. (2020), 'Fermi-LAT Gamma-ray Observations of IceCube-201130A'

4FGL J1342.7+0505 and IceCube-210210A

On February 10 2021, IceCube reported the observation of a high-energy neutrino of the *Gold* type with a 65% signalness and best-fit arrival direction at RA = $206.06^{\circ}{}^{+1.40}_{-0.95}$, Dec = $4.78^{\circ}{}^{+0.62}_{-0.56}$. One *Fermi*-LAT source is located within the 90% IceCube-210210A localisation.

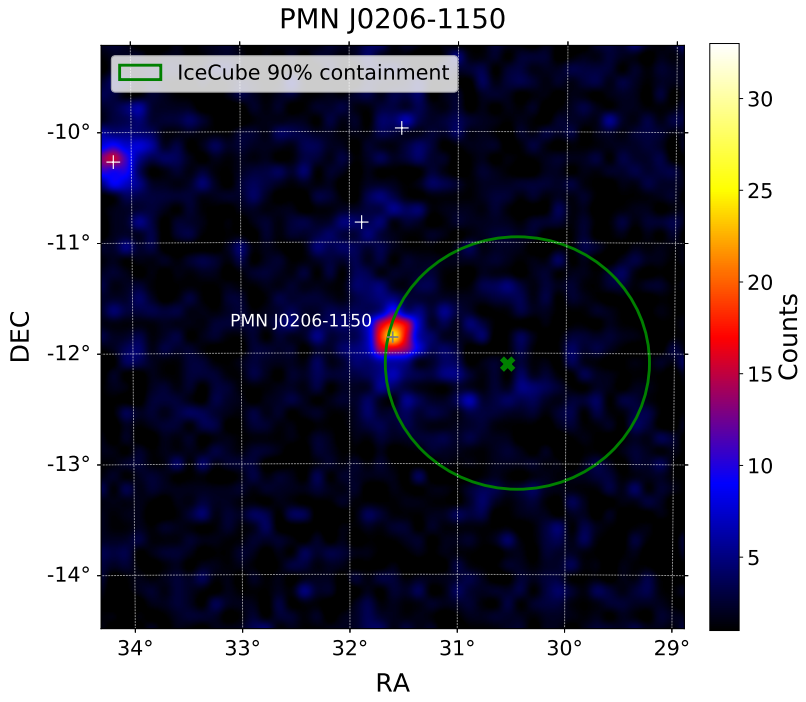

Figure 9.7: *Fermi*-LAT counts map of the IceCube-201130A with its best-fit localization (green *x*) and 90% angular uncertainty (green circle).

This is the source 4FGL J1342.7+0505, associated with the BL Lac object 4C +05.57 [283], at redshift z = 0.13663 [284]. The source is also classified as broad-line radio galaxy [285].

The 4FGL best-fit position is at Ra = 205.685°and Dec = 5.0904°(J2000), at 0.5°distance from IceCube-210210A. The average measured energy flux is $(3.0 \pm 0.4) \times 10^{-12}$ MeV cm^{-2} s^{-1}, making it the 1959th brightest *Fermi*-LAT blazar in terms of energy flux. Its spectrum is well described by a simple power-law model with spectral index $\Gamma = 2.4 \pm 0.1$.
During the realtime follow-up analysis with *Fermi*-LAT data, we found no significant ($> 5\ \sigma$) detection of the source over the timescales of 1-day and 1-month prior the neutrino arrival [286]. Figure 9.8 shows a counts map of *Fermi*-LAT data of the IceCube-210210A region with its best-fit arrival direction and 90% angular uncertainty.

[283]: Bolton et al. (1975), 'The Parkes 2700 MHz Survey (Seventh Part): Supplementary Catalogue for the Declination zone -4^{o} to -30^{o}'

[284]: Hewett et al. (2010), 'Improved redshifts for SDSS quasar spectra'

[285]: Grandi (1983), 'Spectroscopic observations of southern N-galaxy candidates.'

[286]: Garrappa et al. (2021), 'Fermi-LAT Gamma-ray Observations of IceCube-210210A'

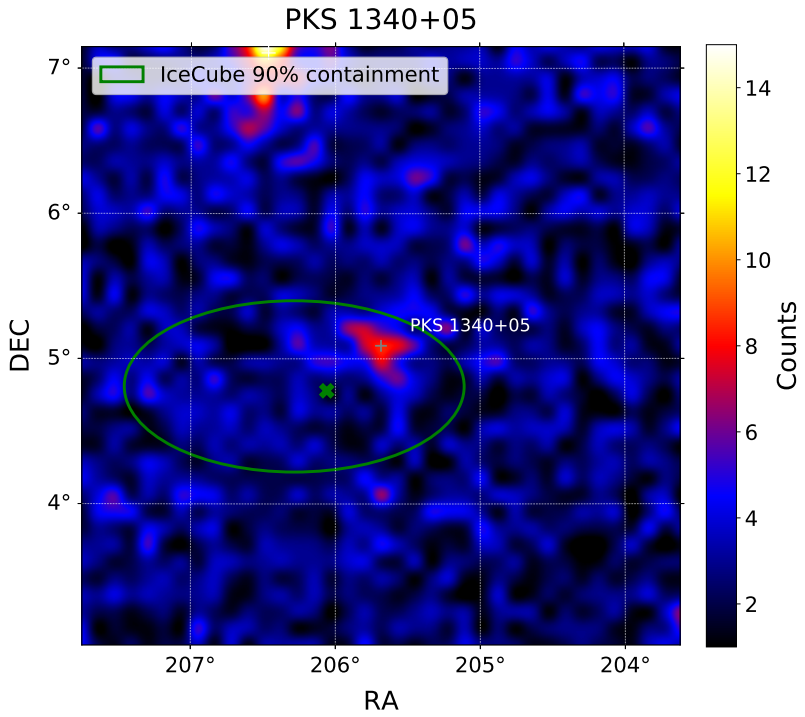

Figure 9.8: *Fermi*-LAT counts map of the IceCube-210210A with its best-fit localization (green x) and 90% angular uncertainty (green circle).

9.3 Results and discussion

I have repeated the K-S test against the whole population of blazars in the 4LAC, with the new sample of neutrino blazar candidates that now includes:

- Three Flat Spectrum Radio Quasars;
- Five BL Lac;
- Three blazars of uncertain type (BCU);

In addition to the tests described in the previous section (see [227]), in order to test a broader range of possible correlations between the energy flux distributions, I have now considered a range of values for the correlation power (α) from 0 (correlation with the random distribution) to 2 (quadratical correlation) with steps of 0.25. The p-values in function of the correlation power α are shown with solid lines in Fig. 9.9.

[227]: Franckowiak et al. (2020), 'Patterns in the Multiwavelength Behavior of Candidate Neutrino Blazars'

The p-values for the two blazar classes peak at very different values, with the FSRQs (green line) having the highest p-value of 0.95 for $\alpha = 1.25$ and the BL Lacs (orange line) peaking at a p-value of 0.92 for $\alpha = 0.5$. For the distribution that includes together BL Lacs, FSRQs and BCUs the peak is for $\alpha = 0.75$ with a p-value of 0.88 . The quadratical correlation ($\alpha = 2.0$) can be strongly excluded when considering the distribution of all blazars with a p-value of $6{\times}10^{-6}$, and with p-values of $7{\times}10^{-4}$ and 0.1 for the single distributions of BL Lacs and FSRQs, respectively. Similar behaviour is observed when testing against the random distribution ($\alpha = 0$) of 4LAC blazars, with p-values of 0.02 and 0.06 for the whole candidates sample and the FSRQs, respectively, while BL Lacs have a higher p-value of 0.31 .
I have performed a sanity check with a control sample of randomized data in order to verify the robustness of the p-values from the K-S tests and exclude possible biases. To do so, for each value of α I repeated the

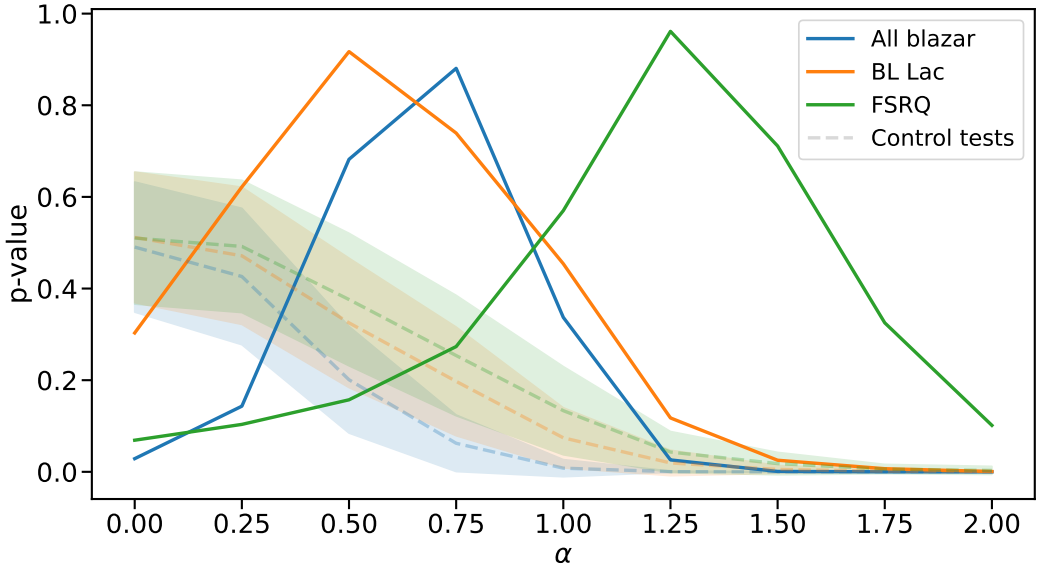

Figure 9.9: p-values from the KS tests in function of the index α from Eq. 9.1. The solid lines show the results for the neutrino blazar candidates sample for each class. The dashed lines show the results for the test performed on the control samples, with the shaded areas marking the 1σ uncertainty regions from the N = 1000 Monte Carlo samples drawn for each α and source class.

test on 10^3 randomly drawn samples of objects with the same size of the original samples of identified neutrino blazar candidates. The evolution of the average p-values from each set of 10^3 K-S tests and the relative $\pm 1\sigma$ dispersion are shown in Fig. 9.9 with dashed lines and shaded bands. The average p-values of the control tests are all well described by a random distribution ($\alpha = 0$) with a fast decreasing trend for higher values of α that confirm the robustness of the test.

Several works in the literature have discussed the relation between the neutrino and gamma-ray luminosity in astrophysical sources, that in general can be expressed in the form of Eq. 9.1,where α is the power index used in our K-S test. In the work [111], the theoretical expectations of this functional dependence for different classes of cosmic neutrino sources are discussed in detail. Interestingly, for environments typical of FSRQs, the neutrino production is expected to be dominated by the interaction of high-energy protons with the external photon fields of the broad line region, accretion disk and dust torus, as we have already discussed in our modelling of PKS 1502+106 in Chapter 7 (see also [287] and [288]). In [113], the photomeson production efficiency $f_{p\gamma}$ from optical and infrared data was found proportional to $L_{AD}^{1/2}$, where L_{AD} is the accretion disk luminosity. Therefore, using the simple assumption that the cosmic ray luminosity L_{CR} is proportional to L_{AD}, then

[287]: Atoyan et al. (2001), 'High-Energy Neutrinos from Photomeson Processes in Blazars'

[288]: Atoyan et al. (2003), 'Neutral Beams from Blazar Jets'

$$L_\nu \propto L_{CR} \cdot L_{AD}^{1/2} \propto L_\gamma^{3/2}. \tag{9.3}$$

so the theoretically predicted value for FSRQs would be $\alpha = 1.5$. Although the highest p-value in our FSRQ sample is obtained for $\alpha = 1.25$, a value of $\alpha = 1.5$ is actually compatible as well, with a high p-value of 0.7.

For BL Lac neutrino candidates, theoretical predictions are less constrained. Given the absence of external photon fields, the main target is

represented by the synchrotron photons in the blazar jet and therefore the luminosity dependence usually expected for these objects can be anything between $\alpha = 1$ (the target photons from the low-frequency bump do not increase with the high-frequency bump) and $\alpha = 2$ (target photons are proportional to L_γ) [111–114].

For $\alpha = 1$, the analysis shows a good compatibility (p-value of 0.45), with a maximum p-value reached for $\alpha = 0.5$. It is important to stress that our sample of neutrino blazar candidates is still very limited on a small number of objects, which could make this statistical tests vulnerable to statistical fluctuations. In addition, considered the average signalness of the neutrino events of these coincidences, we expect our sample to be contaminated by some random coincidences that would affect the true shape of the distribution in a significant way given the low statistics. This might also explain why the subsample of BL Lac objects has still a non-negligible p-value of 0.29 from the K-S test against the random distribution ($\alpha = 0$).

That said, these results on a preliminary small sample of neutrino blazar candidates can be considered a promising first step in the characterisation of the gamma-ray/neutrino connection in the sources of high-energy neutrinos.

Figure 9.10 shows the distribution of the candidate neutrino blazars (with measured redshift) described in this chapter (coloured points) compared to the whole 4LAC catalog in a 2-D space of gamma-ray energy flux versus redshift. In the side plots, the values for the energy flux and redshift of the neutrino source candidates (with multiwavelenght motivations) are highlighted over the quantile function and the counts distribution, respectively.

[111]: Murase et al. (2016), 'Constraining high-energy cosmic neutrino sources: Implications and prospects'

[112]: Tavecchio et al. (2015), 'High-energy cosmic neutrinos from spine-sheath BL Lac jets'

[113]: Murase et al. (2014), 'Diffuse neutrino intensity from the inner jets of active galactic nuclei: Impacts of external photon fields and the blazar sequence'

[114]: Petropoulou et al. (2015), 'Photohadronic origin of γ-ray BL Lac emission: implications for IceCube neutrinos'

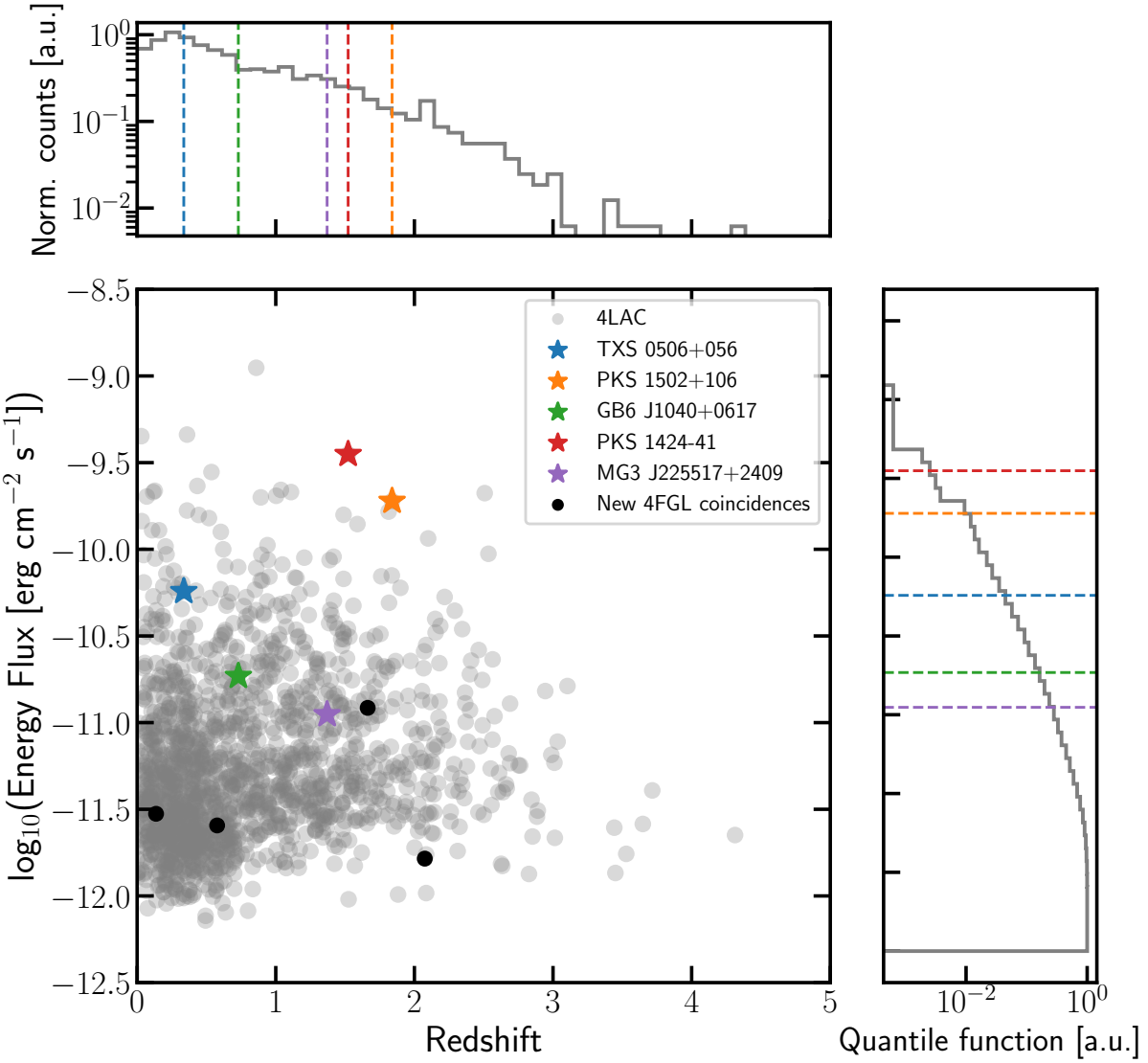

Figure 9.10: Comparison of candidate neutrino blazars with all blazars in the 4LAC AGN sample adapted from [227]. Star-shaped markers indicate candidate neutrino blazars already studied in the literature and black circles show the new coincident sources (with an identified counterpart) from Table 9.1

9.4 Neutrino flare candidates

The final section of this chapter is dedicated to the studies conducted on the sources that have been associated to the most significant neutrino flares observed by IceCube up to 2019. A search for neutrino flare was motivated in IceCube after the archival excess of neutrinos found in 2014/15 for TXS 0506+056 (for which the term *neutrino flare* was coined). This search, reported in [289], targeted all the positions of sources in the 3LAC catalog located in the northern sky (Dec > -5°, for a total of 1023 objects), searching for an excess of neutrino emission in the time period from 2012 April 26 to 2017 May 11.

In the work [227], my collaborators and I have studied the multiwavelength behaviour of the most significant sources reported by [289], associated with a neutrino flare.

[289]: O'Sullivan et al. (2019), 'Searching for Time-Dependent Neutrino Emission from Blazars'

[227]: Franckowiak et al. (2020), 'Patterns in the Multiwavelength Behavior of Candidate Neutrino Blazars'

Table 9.3: Neutrino flare candidates from [289].

Source Name	4FGL Name	Class	redshift	T_0 [MJD]	T_w [days]
4C +20.25	J1125.9+2005	FSRQ	0.133	56464.1	5.2
CRATES J112916+370317	J1129.1+3703	BL Lac	0.445	56501.385	6.0×10^{-2}
MG2 J112758+3620	J1127.8+3618	FSRQ	0.884	56501.385	6.0×10^{-2}
TXS 0506+056	J0509.4+0542	BL Lac	0.336	57000	120
1H 0323+342	J0324.8+3412	NLSY1	0.061	57326.2938	1.7×10^{-3}
RBS 1467	J1508.8+2708	BL Lac	0.27	57440	170
S4 1716+68	J1716.1+6836	FSRQ	0.777	57469.17919	5.4×10^{-5}
M 87	J1230.8+1223	radio galaxy	0.00428	57730.0307	2.7×10^{-3}
GB6 J0929+5013	J0929.3+5014	BL Lac	0.37	57758.0	1.2
1ES 0927+500	J0930.5+4951	BL Lac	0.187	57758.0	1.2

We have studied in details the temporal behaviour in gamma rays and other available data from different wavelengths (radio, optical and X-ray) of the 11 reported sources listed in Tab. 9.3. None of these sources was found in temporal coincidence with a gamma-ray flare during the observation of the neutrino excess, with the exception of one source, the narrow-line Seyfert 1 galaxy 1H 0323+342, for which a dedicated paragraph will follow.
We have performed a K-S test also for the candidate neutrino flare source, with the same prescriptions described in the previous section. Differently from the single high-energy neutrino candidates, this sample shows a good match with the random distribution, with a p-value ranging from 39% to 98% and it shows a small K-S p-value of 0.4% and 2.1% for the linear and quadratical correlations, respectively.
This test shows that these neutrino flare candidates are compatible with the background hypothesis and that a correlation with the gamma-ray energy flux (and hence, between the neutrino and gamma-ray luminosity) is not supported by data, also in the search for a temporal coincidence of multiwavelength activity contemporaneous to the neutrino flares. This could indicate two possible scenarios:

- The measured neutrino excesses are dominated by statistical fluctuations of the background, and therefore the coincidence with the gamma-ray sources are of random nature. This would be supported by the fact that the highest significance measured is the 3.5σ for the TXS 0506+056 neutrino flare, while the rest of the sample has lower significances down to $\sim 2\sigma$.
- The neutrino flares are not observed along with gamma-ray outburst of the sources, or their sources are in general environments with suppressed gamma-ray emission.

The second scenario in particular, is currently matter of speculation (see [290] for a review) and would support more efficient target for neutrino production in these cosmic accelerators, in a so called *beam dump* scenario in environments like galaxy mergers or heavily obscured sources.

[290]: Halzen (2021), 'The Observation of High-Energy Neutrinos from the Cosmos: Lessons Learned for Multimessenger Astronomy'

The case of 1H 0323+342

The only object in our sample of sources that we found on enhanced gamma-ray activity in the time window of the neutrino excess, is the

radio-loud narrow-line Seyfert 1 galaxy 1H 0323+342. The source is located at a redshift of $z = 0.061$ [291] [292] and detected in the 4FGL-DR2 as 4FGL J0324.8+3412 at Ra = 51.2058°and Dec = 34.2119°(J2000). A countmap of *Fermi*-LAT gamma-ray data in a region centered at 1H 0323+342, is shown in Fig. 9.11.

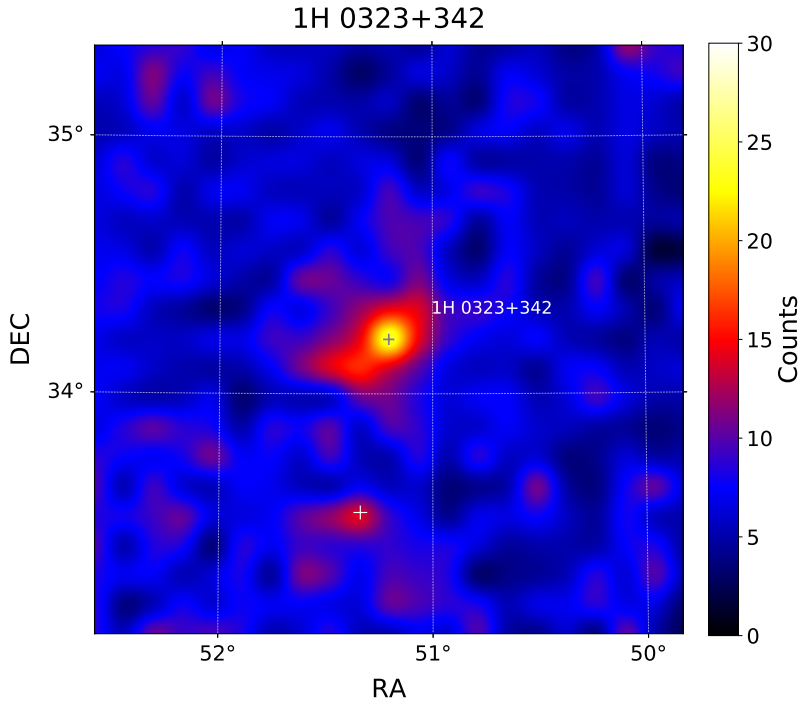

Figure 9.11: *Fermi*-LAT countmap of the nlsy1 galaxy 1H 0323+342 (4FGL J0324.8+3412).

The neutrino flare time window is centered at MJD 57326.2938 and is only ~150 s wide (~2.5 min). During the neutrino flare time window, the source shows a distinct flare that peaks at $F_\gamma^{peak} = (2.8 \pm 0.7) \times 10^{-7}$ ph cm^{-2} s^{-1} and lasts for approximately 30 days. The neutrino flaring window is much shorter compared to the gamma-ray flare, and is observed in the descending phase of the gamma-ray flare ~2 days after the peak flux. If we calculate the same p-values used in Eq. 9.2 ,the chance probability to find the neutrino in a period of flaring activity at a level equal or higher than F_γ^{peak} is $p_\gamma = 8\%$. The gamma-ray flare happens about 1-2 months after enhanced activities observed in X-ray, UV and optical ([227] for further details on the observations) that seems not correlated with the observations in gamma rays. Figure 9.12 shows the multi-wavelength light curve of 1H 0323+342 with data from radio observations (OVRO), optical (ASAS-SN, CSS and *Swift*-UVOT), X-rays (*Swift*-XRT) and gamma rays from *Fermi*-LAT. The poor sampling of multiwavelength data, however, does not give a good description of the flaring periods across all bands and makes the correlation studies challenging.

Previous SED modelling of the source in literature suggest that the gamma-ray emission region lies within the BLR, in the vicinity of the central black hole [292] [293] [294]. This makes 1H 0323+342 an interesting candidate for neutrino production, with the characteristic X-ray photon field from the corona as main target for photohadronic interactions. However, with the p-value of 8%, the chance temporal coincidence between the gamma-ray and the neutrino flares cannot be excluded.

[291]: Zhou et al. (2007), 'A Narrow-Line Seyfert 1-Blazar Composite Nucleus in 2MASX J0324+3410'

[292]: Abdo et al. (2009), 'Radio-Loud Narrow-Line Seyfert 1 as a New Class of Gamma-Ray Active Galactic Nuclei'

[293]: Paliya et al. (2014), 'The Peculiar Radio-loud Narrow Line Seyfert 1 Galaxy 1H 0323+342'

[294]: Kynoch et al. (2018), 'The relativistic jet of the γ-ray emitting narrow-line Seyfert 1 galaxy 1H 0323+342'

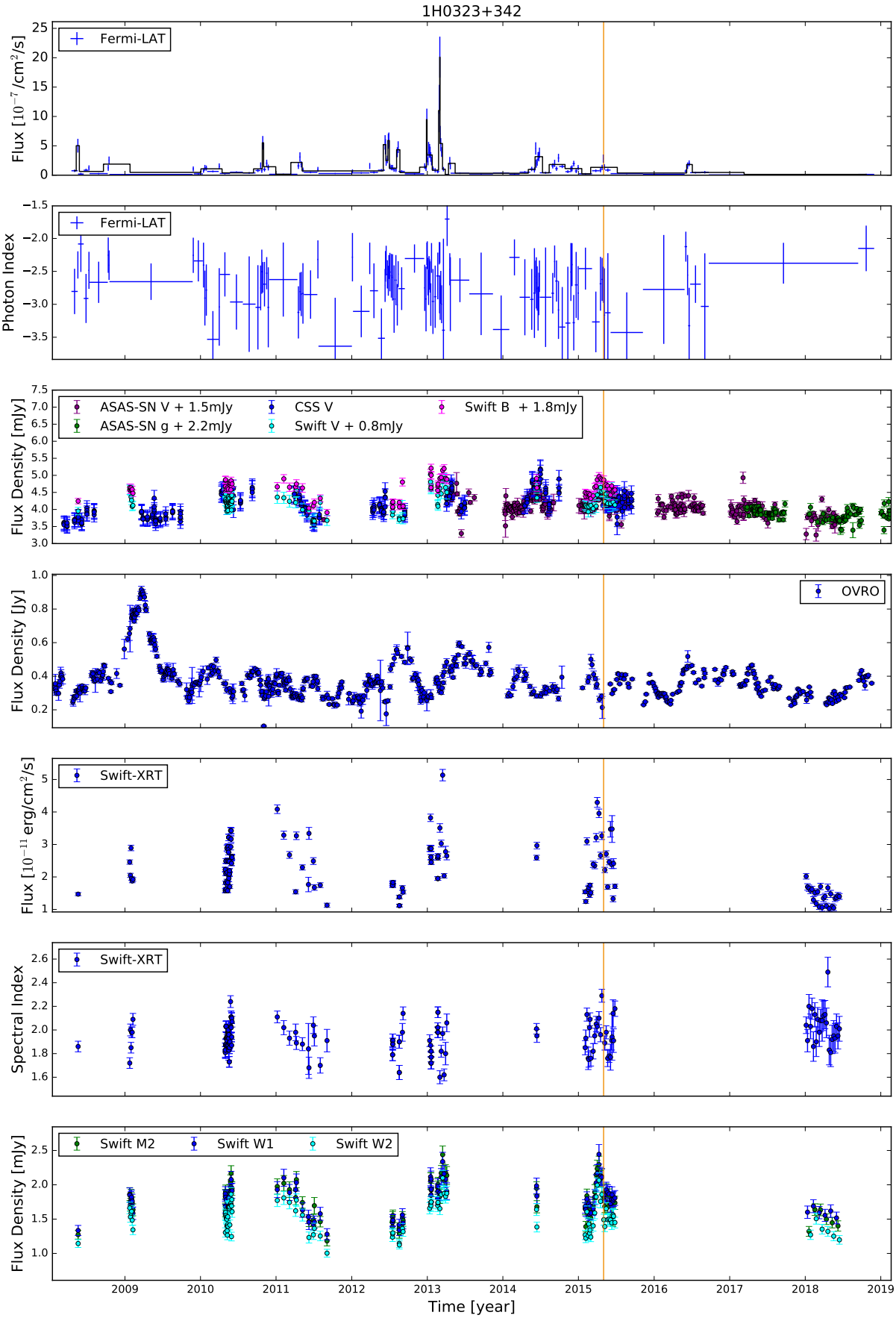

Figure 9.12: Multi-wavelength light curve of 1H 0323+342 from [227]. The duration of the neutrino flare is short (T_w = 147 s) and its arrival time is shown as an orange line. An excess in gamma rays is found coincident with the neutrino arrival time and an excess in X-ray emission is visible roughly one month before the neutrino arrival time. The *Fermi*-LAT gamma-ray light curve covers the energy range from 100 MeV to 800 GeV, the *Swift* X-ray light curve from 0.3 to 10 keV and the OVRO radio data is at 15 GHz

Conclusion

Summary and outlook | 10

In this thesis I have presented the analyses of gamma-ray blazar candidate counterparts to high-energy neutrino events with *Fermi*-LAT data and other multiwavelength observations. The remarkable coincidence between the ~290 TeV neutrino IceCube-170922A and the flaring blazar TXS 0506+056 that motivated this thesis has been the first case study of this work. In the analysis presented in Chapter 5 we show that at the time of the detection of IceCube-170922A, the blazar was undergoing a major, prolonged gamma-ray outburst phase. This outburst is characterised by fast flux variations on weekly timescales and reaches the highest flux levels ever observed by *Fermi*-LAT for this source. However, we find that during the time of the 2014/15 neutrino flare detection, the source shows a completely different behaviour. The flux levels are among the lowest ever observed for the source and we are able to constrain any spectral variation or excess in the emission of high-energy photons in this period. From this study we realised that the connection between gamma rays and neutrinos in this source may not be trivial, and the casual connection between the two messengers might be strongly dependent on the specific properties of the emission region.

The work that followed the investigation of TXS 0506+056 as neutrino counterpart was driven by a compelling question: *Are there more coincidences between flaring gamma-ray sources and high-energy neutrinos?*.

We found a first answer to this question when looking into the archival IceCube observations of single high-energy neutrinos. Among the few spatial coincidences with blazar sources, one (GB6 J1040+0617) was showing gamma-ray activity at the time of the neutrino arrival, similar to what observed for TXS 0506+056. In Chapter 6 we study the gamma-ray emission of the BL Lac object GB6 J1040+0617, in spatial coincidence with the neutrino event IceCube-141209A, in detail. The identification of the gamma-ray counterpart presented several challenges because of another bright gamma-ray emitter at a distance of 0.2°. A detailed gamma-ray analysis of the region allowed to disentangle the two emissions and we proposed GB6 J1040+0617 as neutrino blazar candidate for the first time. Although the post-trial spatial chance coincidence is at ~30%, the gamma-ray properties make GB6 J1040+0617 a plausible neutrino-source candidate, which is also supported by simultaneous bright optical activity in ASAS-SN observations.

A second way to answer the question comes from the realtime follow-up activities done in this years with the *Fermi*-LAT. As part of the technical work developed in this thesis, the semi-automatic pipeline described in Chapter 9 performs analysis of the regions around the neutrino localisations when a realtime alert is issued. The gamma-ray analysis is performed at different timescales, and targets transient gamma-ray activity from known gamma-ray sources and possible newly detected emitters.

An outstanding spatial coincidence is found between the blazar PKS 1502+106 and the ~300 TeV neutrino event IceCube-190730A. PKS 1502+106 is the 15^{th} brightest out of the almost 3000 blazars detected by *Fermi*-LAT and represents a unique laboratory because of the rich multiwave-

length archive of observations. Unlike the cases of TXS 0506+056 and GB6 J1040+0617, the source is not showing enhanced gamma-ray activity at the arrival of the neutrino, but is observed in a long-term quiescent state. However, when we combine our experimental results with numerical simulations, we find that the environment of a source with the characteristics of PKS 1502+106 is suitable for cosmic-rays acceleration and is consistent with the observation of the high-energy neutrino. Furthermore, thanks to the spectral resolution achieved by the *Fermi*-LAT for this source, we have been able to assess the importance of observation in the gamma-ray and X-ray bands to identify typical features of hadronic emission in blazars.

The variability of blazars is an important tool to better understand the underlying processes, which also play a crucial role for the neutrino production in the source. Therefore an additional technical effort in this thesis work was devoted to the production and characterisation of a large sample of ∼250 light curves of bright *Fermi*-LAT blazars observed in more than a decade. The modelling pipeline developed for this purpose (described in Chapter 8) identified and characterized more than 3000 single flares. This allowed to obtain interesting insights on the physical properties of the emission regions, that could lead to the identification of different mechanisms behind these flares. As for the purposes of this thesis work, the variability of the three neutrino blazar candidates was characterised and compared to the larger population. The flaring activities of TXS 0506+056 and GB6 J1040+0617 observed in coincidence with the neutrino detections point to sizes of the emission regions similar to the average value observed for the large sample ($R'_b \sim 10^{17}$ cm). The simultaneous flare of TXS 0506+056 shows a symmetric profile, while the simultaneous flare of GB6 J1040+0617 shows a marked asymmetric profile with slow rise and fast decay. However, the statistic of coincident flares is still too low to draw some conclusions on the identification of a class of neutrino blazars based on the variability properties or on the flare profiles. A larger number of flares simultaneous to neutrino detections might be helpful in the future to address this point.

Interesting information can be extracted from the variability of PKS 1502+106. Although the source was not showing activity simultaneous with the neutrino detection, the large sample of 41 flares modelled by the pipeline shows that the localization of the emission regions of a significant fraction of these flares can be constrained at distances comparable or lower than the radius of the BLR. This is important in light of leptohadronic models, in which the BLR represents an efficient target for photo-meson production.

Two main things will help in the future to improve the variability study. The first one is the implementation of different analytical models to be tested both for the flares and the background emission. The second one will be the application of the modelling pipeline on simulated light curves, which will be crucial to understand the performance on different type of flares.

Finally, in Chapter 9 I present a population study to compare the gamma-ray properties of the sample of neutrino blazar candidates to the entire population of blazars detected by *Fermi*-LAT. We find that the single blazar neutrino candidates may be compatible with the correlation hypothesis, and show different dependencies for the FSRQ and BL Lac classes. The non-correlation hypothesis for this sample however, cannot

still be completely excluded. At the same time, the candidate neutrino flare sources show a good match with the non-correlation hypothesis and are less well described by the correlation hypothesis. Although this test is performed with the small available sample of neutrino coincidences, the preliminary results can be considered a promising first step towards the characterisation of the gamma-ray/neutrino connection in the sources of high-energy neutrinos.

The results of this thesis work point to the importance of gamma-rays and the key role of *Fermi*-LAT observations to identify candidate neutrino counterparts among blazars. However, although the gamma-ray properties of these source might help to identify plausible neutrino sources, the signatures in the observed gamma-ray emission simultaneous to the neutrino production may not be trivial and be strongly dependent on the source environment. Lower-energy photons produced in the interaction of gamma rays within the source may also be considered important tracers of neutrino emission. It will be crucial in the future to improve the synergies between the broad-band multi-wavelength and multimessenger observations with numerical simulations, to identify the observational signatures expected in specific models.

Furthermore, a lesson learned from the *Fermi*-LAT observational strategy is the importance of having a continuous coverage of the sky or, alternatively, a fast response to multi-messenger transients. The strategy that will be adopted by future observatories like the Cherenkov Telescope Array (CTA) [295] will be important to provide a full multi-wavelength picture of the source simultaneous to the neutrino detection. CTA will provide unprecedented sensitivities for the observations of extragalactic sources in the range between few tens of GeV up to tens of TeV. In the soft X-ray band (< 10 keV), the Neil Gehrels *Swift* observatory is the principal instrument used for neutrino follow-up observations thanks to its capabilities to respond promptly to target of opportunity (ToO) requests [296]. A future mission with similar capabilities of fast ToOs is SVOM [297], that will carry multiple detectors on board to cover energies from the visible to gamma rays. In the hard X-rays (> 10 keV) *NuSTAR* is the most sensitive instrument [298]. A major contribution in the X-ray band will be given by the all-sky surveys of *eROSITA*, that will provide a census of the X-ray sky with unprecedented sensitivity [299].

One major lack in multi-wavelength observations is represented by the gap in the MeV band, which is expected to be covered in the next decades by missions like COSI [300] and AMEGO-X [301].

Another important improvement in the search of neutrino counterparts will come from the new generation of neutrino observatories, starting from IceCube-*Gen2* [302] that will increase the current 1 km^3 extension of IceCube to a total of 7.9 km^3, with a gain in sensitivity of about ∼5 times at all declinations. In the Mediterranean sea, KM3NeT-ARCA [303] is expected to be completed in the following decade and with its ∼km^3 of instrumented volume will be able to provide additional sensitivity at declination were IceCube is less sensitive. The improvements in sensitivity and the angular resolution for track-like neutrino events that will be introduced by the next generation of neutrino telescopes will be of extreme importance for neutrino astronomy. This will help to reduce the number of candidate sources in the uncertainty region of the arrival direction, and have more significant associations.

[295]: Cherenkov Telescope Array Consortium et al. (2019), *Science with the Cherenkov Telescope Array*

[296]: Evans et al. (2015), 'Swift follow-up of IceCube triggers, and implications for the Advanced-LIGO era'

[297]: Godet et al. (2012), 'The Chinese-French SVOM Mission: studying the brightest astronomical explosions'

[298]: Harrison et al. (2013), 'The Nuclear Spectroscopic Telescope Array (NuSTAR) High-energy X-Ray Mission'

[299]: Predehl et al. (2021), 'The eROSITA X-ray telescope on SRG'

[300]: Tomsick et al. (2022), 'The Compton Spectrometer and Imager Project for MeV Astronomy'

[301]: Fleischhack et al. (2022), 'AMEGO-X: MeV gamma-ray Astronomy in the Multi-messenger Era'

[302]: Aartsen et al. (2021), 'IceCube-Gen2: the window to the extreme Universe'

[303]: Adrian-Martinez et al. (2016), 'Letter of intent for KM3NeT 2.0'

Appendix

Fermi-LAT Analysis configurations

A

A.1 TXS 0506+056 analysis in Chapter 5

The following is the main configuration for the *Fermi*-LAT analysis of TXS 0506+056 reported in [38].
In this study we use 9.6 years of Pass 8 *Fermi*-LAT data collected between 2008 August 4 and 2018 March 16 (MJD 54682-58193), selecting photons from the event class developed for point source analyses[i]. We perform a likelihood analysis[ii], binned in space and energy, using the standard *Fermi*-LAT ScienceTools package version v11r5p3 available from the *Fermi* Science Support Center[iii] (FSSC) and the P8R2_SOURCE_V6 instrument response functions, together with the fermipy package v0.16.0 [156]. We analyze data in the energy range from 100 MeV to 1 TeV binned into eight logarithmically-spaced energy intervals per decade. To minimize the contamination from gamma rays produced in the Earth's upper atmosphere, we apply an instrument zenith angle cut of $\theta < 90°$. We use the standard data quality cuts $(DATA\_QUAL > 0)\&\&(LAT\_CONFIG == 1)$ and we remove time periods coinciding with solar flares and gamma-ray bursts detected by the LAT. The effect of energy dispersion is included in the fits performed with the *Fermi*-LAT ScienceTools.
For each source, we select a $10° \times 10°$ region of interest (ROI) centered on the source position, binned in 0.1°size pixels. The binning is applied in celestial coordinates using a Hammer-Aitoff projection. The input model for the ROI includes all known gamma-ray sources from the 3FGL catalog in a region of $15° \times 15°$, slightly larger than the ROI, and the isotropic and Galactic diffuse gamma-ray emission models provided by the standard templates iso_P8R2_SOURCE_V6_v06.txt (extrapolated linearly in the logarithm up to 1 TeV) and gll_iem_v06.fits[iv].
We compute the light curve for each source using the adaptive binning algorithm from [162] with the prescriptions outlined in [38], in order to better resolve flaring activities of the target sources. Statistically-significant variations in the light curve's behavior are detected in this work with the Bayesian Blocks algorithm [194] for which we use its Astropy implementation[v]. We adopt a prior that makes the algorithm sensitive to variations that are significant at 95% confidence level.

[i] http://fermi.gsfc.nasa.gov/ssc/data/analysis/documentation/Pass8_usage.html
[ii] We use MINUIT as optimizer with 10^{-3} tolerance
[iii] http://fermi.gsfc.nasa.gov/ssc/data/analysis/
[iv] https://fermi.gsfc.nasa.gov/ssc/data/access/lat/BackgroundModels.html
[v] http://docs.astropy.org/en/stable/api/astropy.stats.bayesian_blocks.html

A.2 GB6 J1040+0617 analysis in Chapter 6

The following is the main configuration for the *Fermi*-LAT analysis of TXS 0506+056 reported in [38].
In this study we use 9.6 years of Pass 8 *Fermi*-LAT data collected between 2008 August 4 and 2018 March 16 (MJD 54682-58193), selecting photons from the event class developed for point source analyses[vi]. We perform a likelihood analysis[vii], binned in space and energy, using the standard *Fermi*-LAT ScienceTools package version v11r5p3 available from the *Fermi* Science Support Center[viii] (FSSC) and the P8R2_SOURCE_V6 instrument response functions, together with the fermipy package v0.16.0 [156]. We analyze data in the energy range from 100 MeV to 1 TeV binned into eight logarithmically-spaced energy intervals per decade. To minimize the contamination from gamma rays produced in the Earth's upper atmosphere, we apply an instrument zenith angle cut of $\theta < 90°$. We use the standard data quality cuts $(DATA\_QUAL > 0)\&\&(LAT\_CONFIG == 1)$ and we remove time periods coinciding with solar flares and gamma-ray bursts detected by the LAT. The effect of energy dispersion is included in the fits performed with the *Fermi*-LAT ScienceTools.
For each source, we select a $10° \times 10°$ region of interest (ROI) centered on the source position, binned in 0.1°size pixels. The binning is applied in celestial coordinates using a Hammer-Aitoff projection. The input model for the ROI includes all known gamma-ray sources from the 3FGL catalog in a region of $15° \times 15°$, slightly larger than the ROI, and the isotropic and Galactic diffuse gamma-ray emission models provided by the standard templates iso_P8R2_SOURCE_V6_v06.txt (extrapolated linearly in the logarithm up to 1 TeV) and gll_iem_v06.fits[ix].
An additional data cut is applied to remove the time periods when the Sun was located less than 15°from the source position. This additional cut is necessary because GB6 J1040+0617 lies very close to the ecliptic.
We compute the light curve for each source using the adaptive binning algorithm from [162] with the prescriptions outlined in [38], in order to better resolve flaring activities of the target sources. Statistically-significant variations in the light curve's behavior are detected in this work with the Bayesian Blocks algorithm [194] for which we use its Astropy implementation[x]. We adopt a prior that makes the algorithm sensitive to variations that are significant at 95% confidence level.

[vi] http://fermi.gsfc.nasa.gov/ssc/data/analysis/documentation/Pass8_usage.html
[vii] We use MINUIT as optimizer with 10^{-3} tolerance
[viii] http://fermi.gsfc.nasa.gov/ssc/data/analysis/
[ix] https://fermi.gsfc.nasa.gov/ssc/data/access/lat/BackgroundModels.html
[x] http://docs.astropy.org/en/stable/api/astropy.stats.bayesian_blocks.html

A.3 Analyses in Chapters 7 and 9

The following is the main configuration for the *Fermi*-LAT analysis of PKS 1502+106 reported in [227].
In this study we use almost 11 years of Pass 8 *Fermi*-LAT data collected between 2008 August 4 and 2019 July 31 (MJD 54682-58695), selecting photons from the event class developed for point source analyses[xi]. We perform a likelihood analysis[xii], binned in space and energy, using the standard *Fermi*-LAT *fermitools* package version v1.0.1 [304] available from the *Fermi* Science Support Center[xiii] (FSSC) and the P8R3_SOURCE_V2 instrument response functions, together with the fermipy package v0.17.4 [156]. We analyze data in the energy range from 100 MeV to 800 GeV binned into eight logarithmically-spaced energy intervals per decade. To minimize the contamination from gamma rays produced in the Earth's upper atmosphere, we apply an instrument zenith angle cut of $\theta < 90°$. We use the standard data quality cuts $(DATA\_QUAL > 0)\&\&(LAT\_CONFIG == 1)$ and we remove time periods coinciding with solar flares and gamma-ray bursts detected by the LAT. The effect of energy dispersion is included in the fits performed with the *Fermi*-LAT ScienceTools.
For each source, we select a $15° \times 15°$ region of interest (ROI) centered on the source position, binned in 0.1°size pixels. The binning is applied in celestial coordinates using a Hammer-Aitoff projection. The input model for the ROI includes all known gamma-ray sources from the 4FGL catalog in a region of $20° \times 20°$, slightly larger than the ROI, and the isotropic and Galactic diffuse gamma-ray emission models provided by the standard templates iso_P8R3_SOURCE_V2_v01.txt (extrapolated linearly in the logarithm up to 1 TeV) and gll_iem_v07.fits[xiv].
We compute the light curve for each source using the adaptive binning algorithm from [162] with the prescriptions outlined in [38], in order to better resolve flaring activities of the target sources. Statistically-significant variations in the light curve's behavior are detected in this work with the Bayesian Blocks algorithm [194] for which we use its Astropy implementation[xv]. We adopt a prior that makes the algorithm sensitive to variations that are significant at 95% confidence level.

[xi] http://fermi.gsfc.nasa.gov/ssc/data/analysis/documentation/Pass8_usage.html
[xii] We use MINUIT as optimizer with 10^{-3} tolerance
[xiii] http://fermi.gsfc.nasa.gov/ssc/data/analysis/
[xiv] https://fermi.gsfc.nasa.gov/ssc/data/access/lat/BackgroundModels.html
[xv] http://docs.astropy.org/en/stable/api/astropy.stats.bayesian_blocks.html

A.4 Analyses in Chapter 8

In this study we use more than 11 years of Pass 8 *Fermi*-LAT data collected between 2008 August 4 and 2019 November 21 (MJD 54682-58695), selecting photons from the event class developed for point source analyses[xvi]. We perform a likelihood analysis[xvii], binned in space and energy, using the standard *Fermi*-LAT *fermitools* package version v1.0.1 [304] available from the *Fermi* Science Support Center[xviii] (FSSC) and the P8R3_SOURCE_V2 instrument response functions, together with the fermipy package v0.17.4 [156]. We analyze data in the energy range from 100 MeV to 800 GeV binned into eight logarithmically-spaced energy intervals per decade. To minimize the contamination from gamma rays produced in the Earth's upper atmosphere, we apply an instrument zenith angle cut of $\theta < 90°$. We use the standard data quality cuts $(DATA\_QUAL > 0)\&\&(LAT\_CONFIG == 1)$ and we remove time periods coinciding with solar flares and gamma-ray bursts detected by the LAT. The effect of energy dispersion is included in the fits performed with the *Fermi*-LAT ScienceTools.

For each source, we select a $15° \times 15°$ region of interest (ROI) centered on the source position, binned in 0.1°size pixels. The binning is applied in celestial coordinates using a Hammer-Aitoff projection. The input model for the ROI includes all known gamma-ray sources from the 4FGL catalog in a region of $20° \times 20°$, slightly larger than the ROI, and the isotropic and Galactic diffuse gamma-ray emission models provided by the standard templates iso_P8R3_SOURCE_V2_v01.txt (extrapolated linearly in the logarithm up to 1 TeV) and gll_iem_v07.fits[xix].

An additional data cut is applied to remove the time periods when the Sun was located less than 15°from the source position. This additional cut is necessary for sources that lay close to the ecliptic.

We compute the light curve for each source using the adaptive binning algorithm from [162] with the prescriptions outlined in [38], in order to better resolve flaring activities of the target sources. Statistically-significant variations in the light curve's behavior are detected in this work with the Bayesian Blocks algorithm [194] for which we use its Astropy implementation[xx]. We adopt a prior that makes the algorithm sensitive to variations that are significant at 95% confidence level.

[xvi] http://fermi.gsfc.nasa.gov/ssc/data/analysis/documentation/Pass8_usage.html

[xvii] We use MINUIT as optimizer with 10^{-3} tolerance

[xviii] http://fermi.gsfc.nasa.gov/ssc/data/analysis/

[xix] https://fermi.gsfc.nasa.gov/ssc/data/access/lat/BackgroundModels.html

[xx] http://docs.astropy.org/en/stable/api/astropy.stats.bayesian_blocks.html

IceCube Realtime Alerts | B

B.1 IceCube Realtime Stream 1.0 (April 2016 - May 2019)

Table B.1: Alerts from the IceCube Realtime Stream 1.0. Alerts that have been retracted are not shown.

Name	Signalness	Class	Ra (J2000)	Dec (J2000)
IC-190504A	63 %	HESE	65.77	−37.44
IC-190503A	36.6 %	EHE	$120.28^{+0.57}_{-0.77}$	$6.35^{+0.76}_{-0.70}$
IC-190331A	57 %	HESE	$337.68^{+0.23}_{-0.34}$	$-20.70^{+0.30}_{-0.48}$
IC-190221A	37 %	HESE	$268.81^{+1.2}_{-1.8}$	$-17.04^{+1.3}_{-0.5}$
IC-190124A	91 %	HESE	$307.40^{+0.8}_{-0.9}$	$-32.18^{+0.7}_{-0.7}$
IC-190104A	35 %	HESE	$357.98^{+2.3}_{-2.1}$	$-26.65^{+2.2}_{-2.5}$
IC-181023A	28.0 %	EHE	$270.18^{+2.00}_{-1.70}$	$-8.57^{+1.25}_{-1.30}$
IC-181014A	10 %	HESE	$225.15^{+1.40}_{-2.85}$	$-34.80^{+1.15}_{-1.85}$
IC-180908A	34.4 %	EHE	$144.58^{+1.55}_{-1.45}$	$-2.13^{+0.9}_{-1.2}$
IC-171106A	74.6 %	EHE	$340.00^{+0.70}_{-0.50}$	$+7.40^{+0.35}_{-0.25}$
IC-171015A	51 %	HESE	$162.86^{+2.60}_{-1.70}$	$-15.44^{+1.60}_{-2.00}$
IC-170922A	56.5 %	EHE	$77.43^{+1.30}_{-0.80}$	$5.72^{+0.70}_{-0.40}$
IC-170321A	28.0 %	EHE	$98.30^{+1.2}_{-1.2}$	$-15.02^{+1.2}_{-1.2}$
IC-170312A	78 %	HESE	$305.15^{+0.5}_{-0.5}$	$-26.61^{+0.5}_{-0.5}$
IC-161210A	49.0 %	EHE	$46.58^{+1.10}_{-1.00}$	$14.98^{+0.45}_{-0.40}$
IC-161103A	30 %	HESE	$40.83^{+1.10}_{-0.70}$	$12.56^{+1.10}_{-0.65}$
IC-160814A	12 %	HESE	$200.3^{+2.43}_{-3.03}$	$-32.4^{+1.39}_{-1.21}$
IC-160806A	28.0 %	EHE	$122.81^{+0.5}_{-0.5}$	$-0.81^{+0.5}_{-0.5}$
IC-160731A	84.9 %	EHE/HESE	$214.5^{+0.75}_{-0.75}$	$-0.33^{+0.75}_{-0.75}$
IC-160427A	92 %	HESE	$240.57^{+0.6}_{-0.6}$	$9.34^{+0.6}_{-0.6}$

B.2 IceCube Realtime Stream 2.0 (Up to June 2021)

Table B.2: Alerts from the IceCube Realtime Stream 2.0. Alerts that have been retracted are not shown.

Name	Signalness	Class	Ra (J2000)	Dec (J2000)
IC-190619A	55 %	GOLD	$343.26^{+4.08}_{-2.63}$	$10.73^{+1.51}_{-2.61}$
IC-190629A	34 %	BRONZE	$27.22^{+10.0}_{-10.0}$	$84.33^{+4.95}_{-3.13}$
IC-190704A	49 %	BRONZE	$161.85^{+2.16}_{-4.33}$	$27.11^{+1.81}_{-1.83}$
IC-190712A	30 %	BRONZE	$76.46^{+5.09}_{-6.83}$	$13.06^{+4.48}_{-3.44}$
IC-190730A	67 %	GOLD	$225.79^{+1.28}_{-1.43}$	$10.47^{+1.14}_{-0.89}$
IC-190819A	29 %	BRONZE	$148.8^{+2.07}_{-3.24}$	$1.38^{+1.0}_{-0.75}$
IC-190922A	20 %	GOLD	$167.43^{+3.4}_{-2.63}$	$-22.39^{+2.88}_{-2.89}$
IC-190922B	51 %	GOLD	$5.76^{+1.19}_{-1.37}$	$-1.57^{+0.93}_{-0.82}$
IC-191001A	59 %	GOLD	$314.08^{+6.56}_{-2.26}$	$12.94^{+1.5}_{-1.47}$
IC-191119A	45 %	GOLD	$230.1^{+4.76}_{-6.48}$	$3.17^{+3.36}_{-2.09}$
IC-191122A	33 %	BRONZE	$27.25^{+1.7}_{-2.9}$	$-0.04^{+1.17}_{-1.49}$
IC-191204A	33 %	BRONZE	$79.72^{+3.2}_{-1.74}$	$2.8^{+1.12}_{-1.23}$
IC-191215A	47 %	BRONZE	$285.87^{+2.88}_{-3.19}$	$58.92^{+1.85}_{-2.25}$
IC-191231A	46 %	BRONZE	$46.36^{+4.27}_{-3.47}$	$20.42^{+2.11}_{-2.8}$
IC-200109A	77 %	GOLD	$164.49^{+4.94}_{-4.19}$	$11.87^{+1.16}_{-1.36}$
IC-200117A	38 %	BRONZE	$116.24^{+0.71}_{-1.24}$	$29.14^{+0.9}_{-0.78}$
IC-200227A	35 %	BRONZE	$348.26^{+0.5}_{-0.5}$	$21.32^{+0.5}_{-0.5}$
IC-200410A	31 %	BRONZE	$242.58^{+14.05}_{-13.35}$	$11.61^{+7.87}_{-6.21}$
IC-200421A	33 %	BRONZE	$87.93^{+3.44}_{-2.83}$	$8.23^{+2.09}_{-1.84}$
IC-200512A	32 %	BRONZE	$295.18^{+1.72}_{-2.26}$	$15.79^{+1.26}_{-1.29}$
IC-200523A	25 %	BRONZE	$338.64^{+10.77}_{-6.07}$	$1.75^{+1.84}_{-3.54}$
IC-200530A	59 %	GOLD	$255.37^{+2.48}_{-2.56}$	$26.61^{+2.33}_{-3.28}$

Table B.3: (Continuing of Tab B.2) Alerts from the IceCube Realtime Stream 2.0. Alerts that have been retracted are not shown.

Name	Signalness	Class	Ra (J2000)	Dec (J2000)
IC-200614A	42 %	BRONZE	$33.84^{+4.77}_{-6.39}$	$31.61^{+2.75}_{-2.28}$
IC-200615A	83 %	GOLD	$142.95^{+1.18}_{-1.45}$	$3.66^{+1.19}_{-1.06}$
IC-200806A	40 %	BRONZE	$157.25^{+1.21}_{-0.89}$	$47.75^{+0.65}_{-0.64}$
IC-200911A	41 %	BRONZE	$51.11^{+4.42}_{-11.01}$	$38.11^{+2.35}_{-1.99}$
IC-200916A	32 %	BRONZE	$109.78^{+1.08}_{-1.44}$	$14.36^{+0.88}_{-0.85}$
IC-200921A	41 %	BRONZE	$195.29^{+2.35}_{-1.73}$	$26.24^{+1.51}_{-1.77}$
IC-200926A	44 %	GOLD	$96.46^{+0.73}_{-0.55}$	$-4.33^{+0.61}_{-0.76}$
IC-200926B	43 %	BRONZE	$184.75^{+3.64}_{-1.55}$	$32.93^{+1.15}_{-0.91}$
IC-200929A	47 %	GOLD	$29.53^{+0.53}_{-0.53}$	$3.47^{+0.71}_{-0.35}$
IC-201007A	88 %	GOLD	$265.17^{+0.52}_{-0.52}$	$5.34^{+0.32}_{-0.23}$
IC-201014A	41 %	BRONZE	$221.22^{+1.0}_{-0.75}$	$14.44^{+0.67}_{-0.46}$
IC-201021A	30 %	BRONZE	$260.82^{+1.73}_{-1.68}$	$14.55^{+1.35}_{-0.74}$
IC-201114A	56 %	GOLD	$105.25^{+1.28}_{-1.12}$	$6.05^{+0.95}_{-0.95}$
IC-201115A	46 %	GOLD	$195.12^{+1.27}_{-1.49}$	$1.38^{+1.3}_{-1.11}$
IC-201120A	50 %	BRONZE	$307.53^{+5.34}_{-5.59}$	$40.77^{+4.97}_{-2.8}$
IC-201130A	15 %	GOLD	$30.54^{+1.13}_{-1.31}$	$-12.1^{+1.15}_{-1.13}$
IC-201209A	19 %	GOLD	$6.86^{+1.02}_{-1.22}$	$-9.25^{+0.99}_{-1.14}$
IC-201221A	56 %	GOLD	$261.69^{+2.29}_{-2.5}$	$41.81^{+1.29}_{-1.2}$
IC-201222A	53 %	GOLD	$206.37^{+0.9}_{-0.8}$	$13.44^{+0.55}_{-0.38}$
IC-210210A	65 %	GOLD	$206.06^{+1.4}_{-0.95}$	$4.78^{+0.62}_{-0.56}$
IC-210503A	41 %	BRONZE	$143.53^{+7.71}_{-5.16}$	$41.81^{+5.02}_{-5.68}$
IC-210510A	28 %	BRONZE	$268.42^{+1.47}_{-1.6}$	$3.81^{+0.68}_{-0.64}$
IC-210516A	29 %	BRONZE	$91.76^{+1.05}_{-0.97}$	$9.52^{+0.5}_{-0.58}$
IC-210608A	31 %	BRONZE	$337.41^{+4.89}_{-11.64}$	$18.37^{+3.75}_{-3.24}$

B.3 Archival high-energy neutrino events

Table B.4: Archival high-energy neutrino events from https://icecube.wisc.edu/science/data/TXS0506_alerts.

Name	Class	Ra (J2000)	Dec (J2000)
IC-160510A	EHE	$352.34^{+1.63}_{-1.31}$	$2.09^{+0.99}_{-0.85}$
IC-160128A	EHE	$263.40^{+1.35}_{-1.18}$	$-14.79^{+0.99}_{-1.02}$
IC-151207A	HESE	–	–
IC-151122A	EHE	$262.18^{+0.90}_{-1.21}$	$-2.38^{+0.73}_{-0.43}$
IC-150926A	EHE	$194.50^{+0.76}_{-1.21}$	$-4.34^{+0.70}_{-0.95}$
IC-150923A	EHE	$103.27^{+0.70}_{-1.36}$	$3.88^{+0.59}_{-0.71}$
IC-150911A	HESE	$240.20^{+1.29}_{-1.38}$	$-0.45^{+1.17}_{-1.23}$
IC-150831A	EHE	$54.85^{+0.94}_{-0.98}$	$33.96^{+1.07}_{-1.19}$
IC-150812A	EHE	$328.19^{+1.01}_{-1.03}$	$6.21^{+0.44}_{-0.49}$
IC-150428A	HESE	$80.77^{+1.12}_{-1.23}$	$-20.75^{+0.45}_{-0.83}$
IC-141209A	HESE	$160.05^{+0.84}_{-1.04}$	$6.57^{+0.64}_{-0.56}$
IC-141109A	HESE	$55.63^{+0.79}_{-1.53}$	$-16.50^{+0.81}_{-0.68}$
IC-140923A	EHE	$169.72^{+0.91}_{-0.86}$	$-1.34^{+0.73}_{-0.66}$
IC-140611A	EHE	$110.30^{+0.66}_{-0.45}$	$11.57^{+0.14}_{-0.24}$
IC-140420A	HESE	$238.98^{+1.81}_{-1.91}$	$-37.73^{+1.47}_{-1.31}$
IC-140203A	EHE	$349.54^{+2.21}_{-1.97}$	$-13.71^{+1.23}_{-1.38}$
IC-140122A	HESE	$219.64^{+5.16}_{-4.16}$	$-86.16^{+0.55}_{-0.60}$
IC-140109A	EHE	$292.85^{+0.87}_{-0.94}$	$33.06^{+0.50}_{-0.46}$
IC-140108A	EHE	$344.53^{+0.67}_{-0.48}$	$1.57^{+0.35}_{-0.32}$
IC-131204A	EHE	$289.16^{+1.08}_{-0.94}$	$-14.25^{+0.91}_{-0.81}$
IC-131202A	HESE	$206.63^{+2.04}_{-1.56}$	$-22.02^{+1.69}_{-1.04}$
IC-131023A	EHE	$301.82^{+1.10}_{-0.93}$	$11.49^{+1.19}_{-1.09}$
IC-130907A	EHE	$129.81^{+0.48}_{-0.28}$	$-10.36^{+0.36}_{-0.31}$

Table B.5: (Continuing of Tab. B.4). Archival high-energy neutrino events from https://icecube.wisc.edu/science/data/TXS0506_alerts.

Name	Class	Ra (J2000)	Dec (J2000)
IC-130627A	HESE	$93.43^{+0.80}_{-0.85}$	$14.02^{+0.72}_{-0.75}$
IC-130408A	HESE	$167.17^{+2.87}_{-1.90}$	$20.67^{+1.15}_{-0.89}$
IC-121011A	EHE	$205.22^{+0.59}_{-0.65}$	$-2.39^{+0.51}_{-0.57}$
IC-120922A	EHE	$70.75^{+1.56}_{-1.63}$	$19.79^{+1.37}_{-0.68}$
IC-120523A	EHE	$171.03^{+0.81}_{-0.90}$	$26.36^{+0.49}_{-0.30}$
IC-120501A	HESE	–	–
IC-120301A	EHE	$238.01^{+0.60}_{-0.59}$	$18.60^{+0.46}_{-0.39}$
IC-111228A	HESE	–	–
IC-110930A	EHE	$266.48^{+2.09}_{-1.55}$	$-4.41^{+0.59}_{-0.86}$
IC-110714A	HESE	$67.86^{+0.51}_{-0.72}$	$40.32^{+0.73}_{-0.25}$
IC-110304A	EHE	$116.37^{+0.73}_{-0.73}$	$-10.72^{+0.57}_{-0.65}$
IC-110216A	HESE	–	–
IC-110128A	EHE	$307.53^{+0.82}_{-0.81}$	$1.19^{+0.35}_{-0.32}$
IC-101112A	HESE	$110.56^{+0.80}_{-0.37}$	$-0.37^{+0.48}_{-0.65}$
IC-101028A	EHE	$88.68^{+0.54}_{-0.55}$	$0.46^{+0.33}_{-0.27}$
IC-101009A	EHE	$331.09^{+0.56}_{-0.72}$	$11.10^{+0.48}_{-0.58}$
IC-100912A	HESE	–	–

Acknowledgements

This years of PhD have been overall a wonderful experience. With this thesis, I hope to return at least a small fraction of the treasure of knowledge and experience that I had the fortune to collect from the people that shared this journey with me.

First of all, I would like to thank Anna for giving me the opportunity to be one of the first members of her group. I will always be grateful for the trust you put in me since the first day and everything I learned from you. Your passion for science and your way of being a group leader are an inspiration to me.

These years have been special also because of all the amazing people met here at DESY. It will be very hard in the future to find something even just similar to the atmosphere made by people in this place, so I thank you for all the memories that now I carry with me.

I would like to thank my thesis readers Anna, Federica, Xavier, Jannis, Richard, Cristina and Christoph. Your comments during the preparation of this manuscript have been precious for the final result.

A special thank goes to my office mates, in particular to Federica and Robert for the countless days of great time spent together.

I would like to thank the amazing fellows of the bands NuInTown and NuInTown-Gen2. Playing music together has been one of the most surprisingly beautiful things I couldn't ever expect to find in a workplace.

I would like to particularly thank Federica, not only for being the best colleague one could have, but also a great friend.

A special thank to Marlene, for being my strength and my safe place.

E infine, grazie alla mia famiglia, perchè è grazie al vostro incondizionato supporto che ogni volta riesco ad aggiungere qualcosa. Una dedica speciale per quest'ultima avventura va ai miei nonni, che ne hanno visto l'inizio ma non hanno potuto attenderne il finale.

Bibliography

Here are the references in citation order.

[1] V. F. Hess. 'Über Beobachtungen der durchdringenden Strahlung bei sieben Freiballonfahrten'. In: *Phys. Z.* 13 (1912), pp. 1084–1091 (cited on page 1).

[2] D. Pacini. 'La radiazione penetrante alla superficie ed in seno alle acque'. In: *Il Nuovo Cimento* 3.1 (Dec. 1912), pp. 93–100. DOI: 10.1007/BF02957440 (cited on page 1).

[3] P. A. Zyla et al. 'Review of Particle Physics'. In: *PTEP* 2020.8 (2020), p. 083C01. DOI: 10.1093/ptep/ptaa104 (cited on page 2).

[4] A. Aab et al. 'An Indication of Anisotropy in Arrival Directions of Ultra-high-energy Cosmic Rays through Comparison to the Flux Pattern of Extragalactic Gamma-Ray Sources'. In: *ApJ* 853.2, L29 (Feb. 2018), p. L29. DOI: 10.3847/2041-8213/aaa66d (cited on page 2).

[5] R. Davis. 'Solar Neutrinos. II. Experimental'. In: *Phys. Rev. Lett.* 12 (11 Mar. 1964), pp. 303–305. DOI: 10.1103/PhysRevLett.12.303 (cited on page 3).

[6] A. M. Brown. 'The ANTARES neutrino telescope: Status and first results'. In: *5th International Workshop on the Dark Side of the Universe*. Ed. by C. Balazs and F. Wang. Vol. 1178. American Institute of Physics Conference Series. Oct. 2009, pp. 76–82. DOI: 10.1063/1.3264559 (cited on page 3).

[7] V. A. Allakhverdyan et al. 'The Baikal-GVD neutrino telescope: search for high-energy cascades'. In: *arXiv e-prints*, arXiv:2108.01894 (Aug. 2021), arXiv:2108.01894 (cited on page 3).

[8] M. G. Aartsen et al. 'The IceCube Neutrino Observatory: instrumentation and online systems'. In: *Journal of Instrumentation* 12.3 (Mar. 2017), P03012. DOI: 10.1088/1748-0221/12/03/P03012 (cited on pages 3, 57, 58).

[9] IceCube Collaboration. 'Evidence for High-Energy Extraterrestrial Neutrinos at the IceCube Detector'. In: *Science* 342.6161, 1242856 (Nov. 2013), p. 1242856. DOI: 10.1126/science.1242856 (cited on pages 3, 57, 85).

[10] M. G. Aartsen et al. 'Atmospheric and astrophysical neutrinos above 1 TeV interacting in IceCube'. In: *Phys. Rev. D* 91 (2 Jan. 2015), p. 022001. DOI: 10.1103/PhysRevD.91.022001 (cited on page 3).

[11] M. G. Aartsen et al. 'Observation and Characterization of a Cosmic Muon Neutrino Flux from the Northern Hemisphere using six years of IceCube data'. In: *Astrophys. J.* 833.1 (2016), p. 3. DOI: 10.3847/0004-637X/833/1/3 (cited on page 3).

[12] M. G. Aartsen et al. 'All-sky Search for Time-integrated Neutrino Emission from Astrophysical Sources with 7 yr of IceCube Data'. In: *Astrophys. J.* 835.2 (2017), p. 151. DOI: 10.3847/1538-4357/835/2/151 (cited on page 3).

[13] M. G. Aartsen et al. 'Searches for Time-dependent Neutrino Sources with IceCube Data from 2008 to 2012'. In: *ApJ* 807, 46 (July 2015), p. 46. DOI: 10.1088/0004-637X/807/1/46 (cited on page 3).

[14] K. Murase. 'Multi-Messenger Connections among High-Energy Cosmic Particles'. In: *36th International Cosmic Ray Conference (ICRC2019)*. Vol. 36. International Cosmic Ray Conference. July 2019, 965, p. 965 (cited on pages 3, 4).

[15] M. G. Aartsen et al. 'The IceCube realtime alert system'. In: *Astroparticle Physics* 92 (June 2017), pp. 30–41. DOI: 10.1016/j.astropartphys.2017.05.002 (cited on pages 4, 64, 65, 71, 86).

[16] E. Blaufuss et al. 'The Next Generation of IceCube Real-time Neutrino Alerts'. In: *36th International Cosmic Ray Conference (ICRC2019)*. Vol. 36. International Cosmic Ray Conference. July 2019, 1021, p. 1021 (cited on pages 4, 65–67, 109).

[17] Y. T. Tanaka, S. Buson, and D. Kocevski. 'Fermi-LAT detection of increased gamma-ray activity of TXS 0506+056, located inside the IceCube-170922A error region.' In: *The Astronomer's Telegram* 10791 (Sept. 2017) (cited on page 4).

[18] M. G. Aartsen, M. Ackermann, J. Adams, et al. 'Multi-messenger observations of a flaring blazar coincident with high-energy neutrino IceCube-170922A'. In: *Science* 361 (2018), eaat1378 (cited on pages 4, 85, 86, 94).

[19] S. Ansoldi et al. 'The Blazar TXS 0506+056 Associated with a High-energy Neutrino: Insights into Extragalactic Jets and Cosmic-Ray Acceleration'. In: A*pJ* 863, L10 (Aug. 2018), p. L10. DOI: 10.3847/2041-8213/aad083 (cited on pages 4, 72, 81, 82).

[20] A. U. Abeysekara et al. 'VERITAS Observations of the BL Lac Object TXS 0506+056'. In: A*pJ* 861, L20 (July 2018), p. L20. DOI: 10.3847/2041-8213/aad053 (cited on pages 4, 72).

[21] F. W. Stecker et al. 'High-energy neutrinos from active galactic nuclei'. In: *Physical Review Letters* 66 (May 1991), pp. 2697–2700. DOI: 10.1103/PhysRevLett.66.2697 (cited on pages 4, 5).

[22] R. J. Protheroe and A. P. Szabo. 'High energy cosmic rays from active galactic nuclei'. In: *Physical Review Letters* 69 (Nov. 1992), pp. 2885–2888. DOI: 10.1103/PhysRevLett.69.2885 (cited on pages 4, 5).

[23] K. Mannheim. 'The proton blazar'. In: A*&A* 269 (Mar. 1993), pp. 67–76 (cited on pages 4, 5).

[24] A. P. Szabo and R. J. Protheroe. 'Implications of particle acceleration in active galactic nuclei for cosmic rays and high energy neutrino astronomy'. In: *Astroparticle Physics* 2 (Oct. 1994), pp. 375–392. DOI: 10.1016/0927-6505(94)90027-2 (cited on pages 4, 5).

[25] K. Mannheim. 'High-energy neutrinos from extragalactic jets'. In: *Astroparticle Physics* 3 (May 1995), pp. 295–302. DOI: 10.1016/0927-6505(94)00044-4 (cited on pages 4, 5).

[26] A. Mastichiadis. 'The Hadronic Model of Active Galactic Nuclei'. In: S*pace Sci. Rev.* 75 (Jan. 1996), pp. 317–329. DOI: 10.1007/BF00195042 (cited on pages 4, 5).

[27] R. J. Protheroe. 'High energy neutrino astrophysics'. In: *Nuclear Physics B Proceedings Supplements* 77 (May 1999), pp. 465–473. DOI: 10.1016/S0920-5632(99)00468-5 (cited on pages 4, 5).

[28] W. Bednarek and R. J. Protheroe. 'Gamma-ray and neutrino flares produced by protons accelerated on an accretion disc surface in active galactic nuclei'. In: M*NRAS* 302 (Jan. 1999), pp. 373–380. DOI: 10.1046/j.1365-8711.1999.02132.x (cited on pages 4, 5).

[29] A. Mücke and R. J. Protheroe. 'A proton synchrotron blazar model for flaring in Markarian 501'. In: *Astroparticle Physics* 15 (Mar. 2001), pp. 121–136. DOI: 10.1016/S0927-6505(00)00141-9 (cited on pages 4, 5).

[30] K. Mannheim, R. J. Protheroe, and J. P. Rachen. 'Cosmic ray bound for models of extragalactic neutrino production'. In: P*hys. Rev. D* 63.2, 023003 (Jan. 2001), p. 023003. DOI: 10.1103/PhysRevD.63.023003 (cited on pages 4, 5).

[31] A. Atoyan and C. D. Dermer. 'High-Energy Neutrinos from Photomeson Processes in Blazars'. In: *Physical Review Letters* 87.22, 221102 (Nov. 2001), p. 221102. DOI: 10.1103/PhysRevLett.87.221102 (cited on pages 4, 5).

[32] C. D. Dermer et al. 'Ultra-high-energy cosmic rays from black hole jets of radio galaxies'. In: *New Journal of Physics* 11.6, 065016 (June 2009), p. 065016. DOI: 10.1088/1367-2630/11/6/065016 (cited on pages 4, 5).

[33] M. Böttcher et al. 'Leptonic and Hadronic Modeling of Fermi-detected Blazars'. In: A*pJ* 768, 54 (May 2013), p. 54. DOI: 10.1088/0004-637X/768/1/54 (cited on pages 4, 5).

[34] F. Halzen. 'Pionic photons and neutrinos from cosmic ray accelerators'. In: *Astroparticle Physics* 43 (Mar. 2013), pp. 155–162. DOI: 10.1016/j.astropartphys.2011.10.003 (cited on pages 4, 5).

[35] M. Kadler et al. 'Coincidence of a high-fluence blazar outburst with a PeV-energy neutrino event'. In: *Nature Physics* 12 (Aug. 2016), pp. 807–814. DOI: 10.1038/nphys3715 (cited on pages 4, 5, 85, 150).

[36] M. Ahlers and F. Halzen. 'Opening a New Window onto the Universe with IceCube'. In: *Prog. Part. Nucl. Phys.* 102 (2018), pp. 73–88. DOI: 10.1016/j.ppnp.2018.05.001 (cited on pages 4, 5).

[37] M. G. Aartsen, M. Ackermann, J. Adams, et al. 'Neutrino emission from the direction of the blazar TXS 0506+056 prior to the IceCube-170922A alert'. In: *Science* 361 (2018), pp. 147–151 (cited on pages 4, 5, 72, 73).

[38] S. Garrappa et al. 'Investigation of Two Fermi-LAT Gamma-Ray Blazars Coincident with High-energy Neutrinos Detected by IceCube'. In: A*pJ* 880.2, 103 (Aug. 2019), p. 103. DOI: 10.3847/1538-4357/ab2ada (cited on pages 4, 5, 71, 73–77, 79–81, 85–90, 92, 94, 95, 148, 149, 171–174).

[39] R. Stein et al. 'A tidal disruption event coincident with a high-energy neutrino'. In: *Nature Astronomy* 5 (Feb. 2021), pp. 510–518. DOI: 10.1038/s41550-020-01295-8 (cited on page 5).

[40] S. Reusch et al. 'The candidate tidal disruption event AT2019fdr coincident with a high-energy neutrino'. In: *arXiv e-prints*, arXiv:2111.09390 (Nov. 2021), arXiv:2111.09390 (cited on page 5).

[41] S. van Velzen et al. 'Establishing accretion flares from massive black holes as a major source of high-energy neutrinos'. In: *arXiv e-prints*, arXiv:2111.09391 (Nov. 2021), arXiv:2111.09391 (cited on page 5).

[42] M. G. Aartsen et al. 'Time-Integrated Neutrino Source Searches with 10 Years of IceCube Data'. In: P*hys. Rev. Lett.* 124.5, 051103 (Feb. 2020), p. 051103. DOI: 10.1103/PhysRevLett.124.051103 (cited on page 5).

[43] C. K. Seyfert. 'Nuclear Emission in Spiral Nebulae.' In: A*pJ* 97 (Jan. 1943), p. 28. DOI: 10.1086/144488 (cited on page 9).

[44] E. Y. Khachikian and D. W. Weedman. 'An atlas of Seyfert galaxies.' In: A*pJ* 192 (Sept. 1974), pp. 581–589. DOI: 10.1086/153093 (cited on page 9).

[45] V. Beckmann and C. R. Shrader. *Active Galactic Nuclei*. 2012 (cited on pages 10, 11, 13–16, 22, 23).

[46] D. E. Osterbrock. 'Spectrophotometry of Seyfert 1 galaxies.' In: A*pJ* 215 (Aug. 1977), pp. 733–745. DOI: 10.1086/155407 (cited on page 10).

[47] D. E. Osterbrock and R. W. Pogge. 'The spectra of narrow-line Seyfert 1 galaxies.' In: A*pJ* 297 (Oct. 1985), pp. 166–176. DOI: 10.1086/163513 (cited on page 10).

[48] B. L. Fanaroff and J. M. Riley. 'The morphology of extragalactic radio sources of high and low luminosity'. In: M*NRAS* 167 (May 1974), 31P–36P. DOI: 10.1093/mnras/167.1.31P (cited on page 10).

[49] A. S. Bennett. 'The revised 3C catalogue of radio sources.' In: M*mRAS* 68 (Jan. 1962), p. 163 (cited on page 10).

[50] M. Schmidt. '3C 273 : A Star-Like Object with Large Red-Shift'. In: N*ature* 197.4872 (Mar. 1963), p. 1040. DOI: 10.1038/1971040a0 (cited on page 10).

[51] J. S. Ulvestad, R. R. J. Antonucci, and R. Barvainis. 'VLBA Imaging of Central Engines in Radio-Quiet Quasars'. In: A*pJ* 621.1 (Mar. 2005), pp. 123–129. DOI: 10.1086/427426 (cited on page 11).

[52] J. L. Schmitt. 'BL Lac identified as a Radio Source'. In: N*ature* 218.5142 (May 1968), p. 663. DOI: 10.1038/218663a0 (cited on page 11).

[53] J. M. MacLeod and B. H. Andrew. 'The Radio Source VRO 42.22.01'. In: A*strophys. Lett.* 1 (Jan. 1968), p. 243 (cited on page 11).

[54] P. Padovani et al. 'Active galactic nuclei: what's in a name?' In: A*&A Rev.* 25.1, 2 (Aug. 2017), p. 2. DOI: 10.1007/s00159-017-0102-9 (cited on page 11).

[55] R. D. Blandford and M. J. Rees. 'Extended and compact extragalactic radio sources: interpretation and theory.' In: P*hys. Scr* 17 (Mar. 1978), pp. 265–274. DOI: 10.1088/0031-8949/17/3/020 (cited on page 11).

[56] R. Antonucci. 'Unified models for active galactic nuclei and quasars.' In: A*RA&A* 31 (Jan. 1993), pp. 473–521. DOI: 10.1146/annurev.aa.31.090193.002353 (cited on page 12).

[57] C. M. Urry and P. Padovani. 'Unified Schemes for Radio-Loud Active Galactic Nuclei'. In: P*ASP* 107 (Sept. 1995), p. 803. DOI: 10.1086/133630 (cited on page 12).

[58] J. Thorne et al. *AGN Unification Diagram*. Was originally created to be included in the introduction of Thorne J. E., et al., 2022, MNRAS, 509, 4940. Mar. 2022. DOI: 10.5281/zenodo.6381013. URL: https://doi.org/10.5281/zenodo.6381013 (cited on page 12).

[59] A. A. Abdo et al. 'Fermi Large Area Telescope Observations of Markarian 421: The Missing Piece of its Spectral Energy Distribution'. In: A*pJ* 736.2, 131 (Aug. 2011), p. 131. DOI: 10.1088/0004-637X/736/2/131 (cited on page 13).

[60] J. T. Stocke, C. W. Danforth, and E. S. Perlman. 'Broad Lyα Emission from Three Nearby BL Lacertae Objects'. In: A*pJ* 732.2, 113 (May 2011), p. 113. DOI: 10.1088/0004-637X/732/2/113 (cited on page 13).

[61] P. Padovani et al. 'TXS 0506+056, the first cosmic neutrino source, is not a BL Lac'. In: M*NRAS* 484.1 (Mar. 2019), pp. L104–L108. DOI: 10.1093/mnrasl/slz011 (cited on pages 13, 74, 121).

[62] A. A. Abdo et al. 'The Spectral Energy Distribution of Fermi Bright Blazars'. In: A*pJ* 716.1 (June 2010), pp. 30–70. DOI: 10.1088/0004-637X/716/1/30 (cited on pages 14, 47, 116).

[63] G. Fossati et al. 'A unifying view of the spectral energy distributions of blazars'. In: M*NRAS* 299.2 (Sept. 1998), pp. 433–448. DOI: 10.1046/j.1365-8711.1998.01828.x (cited on page 14).

[64] G. Ghisellini et al. 'The Fermi blazar sequence'. In: M*NRAS* 469.1 (July 2017), pp. 255–266. DOI: 10.1093/mnras/stx806 (cited on page 14).

[65] X. Rodrigues et al. 'Neutrinos and Ultra-high-energy Cosmic-ray Nuclei from Blazars'. In: A*pJ* 854.1, 54 (Feb. 2018), p. 54. DOI: 10.3847/1538-4357/aaa7ee (cited on page 14).

[66] A. Einstein. 'Die Feldgleichungen der Gravitation'. In: *Sitzungsberichte der Königlich Preußischen Akademie der Wissenschaften (Berlin* (Jan. 1915), pp. 844–847 (cited on page 14).

[67] R. P. Kerr. 'Gravitational Field of a Spinning Mass as an Example of Algebraically Special Metrics'. In: P*hys. Rev. Lett.* 11.5 (Sept. 1963), pp. 237–238. DOI: 10.1103/PhysRevLett.11.237 (cited on page 15).

[68] C. T. Bolton. 'Identification of Cygnus X-1 with HDE 226868'. In: N*ature* 235.5336 (Feb. 1972), pp. 271–273. DOI: 10.1038/235271b0 (cited on page 15).

[69] B. L. Webster and P. Murdin. 'Cygnus X-1-a Spectroscopic Binary with a Heavy Companion ?' In: N*ature* 235.5332 (Jan. 1972), pp. 37–38. DOI: 10.1038/235037a0 (cited on page 15).

[70] R. A. Remillard and J. E. McClintock. 'X-Ray Properties of Black-Hole Binaries'. In: *Annual Review of Astronomy and Astrophysics* 44.1 (2006), pp. 49–92. DOI: 10.1146/annurev.astro.44.051905.092532 (cited on page 15).

[71] E. E. Salpeter. 'Accretion of Interstellar Matter by Massive Objects.' In: A*pJ* 140 (Aug. 1964), pp. 796–800. DOI: 10.1086/147973 (cited on page 15).

[72] D. Lynden-Bell. 'Galactic Nuclei as Collapsed Old Quasars'. In: N*ature* 223.5207 (Aug. 1969), pp. 690–694. DOI: 10.1038/223690a0 (cited on page 15).

[73] H. Bondi. 'On spherically symmetrical accretion'. In: M*NRAS* 112 (Jan. 1952), p. 195. DOI: 10.1093/mnras/112.2.195 (cited on page 15).

[74] N. I. Shakura and R. A. Sunyaev. 'Black holes in binary systems. Observational appearance.' In: A*&A* 24 (Jan. 1973), pp. 337–355 (cited on page 16).

[75] H. Netzer. *The Physics and Evolution of Active Galactic Nuclei*. 2013 (cited on page 16).

[76] R. Narayan and I. Yi. 'Advection-dominated Accretion: A Self-similar Solution'. In: A*pJ* 428 (June 1994), p. L13. DOI: 10.1086/187381 (cited on page 17).

[77] R. Narayan and I. Yi. 'Advection-dominated Accretion: Underfed Black Holes and Neutron Stars'. In: A*pJ* 452 (Oct. 1995), p. 710. DOI: 10.1086/176343 (cited on page 17).

[78] MAGIC Collaboration et al. 'Detection of the blazar S4 0954+65 at very-high-energy with the MAGIC telescopes during an exceptionally high optical state'. In: A*&A* 617, A30 (Sept. 2018), A30. DOI: 10.1051/0004-6361/201832624 (cited on page 17).

[79] Event Horizon Telescope Collaboration et al. 'First M87 Event Horizon Telescope Results. IV. Imaging the Central Supermassive Black Hole'. In: A*pJ* 875.1, L4 (Apr. 2019), p. L4. DOI: 10.3847/2041-8213/ab0e85 (cited on page 17).

[80] S. W. Davis and A. Tchekhovskoy. 'Magnetohydrodynamics Simulations of Active Galactic Nucleus Disks and Jets'. In: A*RA&A* 58 (Aug. 2020), pp. 407–439. DOI: 10.1146/annurev-astro-081817-051905 (cited on pages 18, 19).

[81] R. D. Blandford and R. L. Znajek. 'Electromagnetic extraction of energy from Kerr black holes.' In: M*NRAS* 179 (May 1977), pp. 433–456. DOI: 10.1093/mnras/179.3.433 (cited on page 19).

[82] C. W. Misner, K. S. Thorne, and J. A. Wheeler. *Gravitation*. 1973 (cited on page 19).

[83] J. C. McKinney, A. Tchekhovskoy, and R. D. Blandford. 'General relativistic magnetohydrodynamic simulations of magnetically choked accretion flows around black holes'. In: M*NRAS* 423.4 (July 2012), pp. 3083–3117. DOI: 10.1111/j.1365-2966.2012.21074.x (cited on page 19).

[84] M. J. Rees. 'Appearance of Relativistically Expanding Radio Sources'. In: N*ature* 211.5048 (July 1966), pp. 468–470. DOI: 10.1038/211468a0 (cited on page 19).

[85] R. D. Blandford, C. F. McKee, and M. J. Rees. 'Super-luminal expansion in extragalactic radio sources'. In: N*ature* 267.5608 (May 1977), pp. 211–216. DOI: 10.1038/267211a0 (cited on page 19).

[86] J.-Y. Kim et al. 'Event Horizon Telescope imaging of the archetypal blazar 3C 279 at an extreme 20 microarcsecond resolution'. In: A*&A* 640, A69 (Aug. 2020), A69. DOI: 10.1051/0004-6361/202037493 (cited on page 20).

[87] R. Blandford, D. Meier, and A. Readhead. 'Relativistic Jets from Active Galactic Nuclei'. In: A*RA&A* 57 (Aug. 2019), pp. 467–509. DOI: 10.1146/annurev-astro-081817-051948 (cited on pages 20, 21).

[88] L. Sironi, A. Spitkovsky, and J. Arons. 'The Maximum Energy of Accelerated Particles in Relativistic Collisionless Shocks'. In: A*pJ* 771.1, 54 (July 2013), p. 54. DOI: 10.1088/0004-637X/771/1/54 (cited on page 21).

[89] A. R. Bell et al. 'Cosmic-ray acceleration by relativistic shocks: limits and estimates'. In: M*NRAS* 473.2 (Jan. 2018), pp. 2364–2371. DOI: 10.1093/mnras/stx2485 (cited on page 21).

[90] M. Meyer, M. Petropoulou, and I. M. Christie. 'The Observability of Plasmoid-powered γ-Ray Flares with the Fermi Large Area Telescope'. In: A*pJ* 912.1, 40 (May 2021), p. 40. DOI: 10.3847/1538-4357/abedab (cited on page 21).

[91] N. F. Loureiro et al. 'Magnetic reconnection and stochastic plasmoid chains in high-Lundquist-number plasmas'. In: *Physics of Plasmas* 19.4 (Apr. 2012), pp. 042303–042303. DOI: 10.1063/1.3703318 (cited on page 21).

[92] M. Meyer, J. D. Scargle, and R. D. Blandford. 'Characterizing the Gamma-Ray Variability of the Brightest Flat Spectrum Radio Quasars Observed with the Fermi LAT'. In: A*pJ* 877.1, 39 (May 2019), p. 39. DOI: 10.3847/1538-4357/ab1651 (cited on pages 21, 125, 130, 133).

[93] S. Appl and M. Camenzind. 'The structure of relativistic MHD jets: a solution to the nonlinear Grad-Shafranov equation.' In: A*&A* 274 (July 1993), pp. 699–706 (cited on page 21).

[94] A. Shukla and K. Mannheim. 'Gamma-ray flares from relativistic magnetic reconnection in the jet of the quasar 3C 279'. In: *Nature Communications* 11, 4176 (Aug. 2020), p. 4176. DOI: 10.1038/s41467-020-17912-z (cited on pages 21, 124).

[95] F. Tavecchio and G. Ghisellini. 'On the magnetization of BL Lac jets'. In: M*NRAS* 456.3 (Mar. 2016), pp. 2374–2382. DOI: 10.1093/mnras/stv2790 (cited on page 22).

[96] G. Ghisellini et al. 'A theoretical unifying scheme for gamma-ray bright blazars'. In: M*NRAS* 301.2 (Dec. 1998), pp. 451–468. DOI: 10.1046/j.1365-8711.1998.02032.x (cited on page 23).

[97] M. Spurio. *Particles and Astrophysics*. 2015 (cited on pages 24–26).

[98] J. D. Finke, S. Razzaque, and C. D. Dermer. 'Modeling the Extragalactic Background Light from Stars and Dust'. In: A*pJ* 712.1 (Mar. 2010), pp. 238–249. DOI: 10.1088/0004-637X/712/1/238 (cited on page 24).

[99] A. Dominguez et al. 'Extragalactic background light inferred from AEGIS galaxy-SED-type fractions'. In: M*NRAS* 410.4 (Feb. 2011), pp. 2556–2578. DOI: 10.1111/j.1365-2966.2010.17631.x (cited on page 24).

[100] R. C. Gilmore et al. 'Semi-analytic modelling of the extragalactic background light and consequences for extragalactic gamma-ray spectra'. In: M*NRAS* 422.4 (June 2012), pp. 3189–3207. DOI: 10.1111/j.1365-2966.2012.20841.x (cited on page 24).

[101] H. E. S. S. Collaboration et al. 'Measurement of the EBL spectral energy distribution using the VHE gamma-ray spectra of H.E.S.S. blazars'. In: A*&A* 606, A59 (Oct. 2017), A59. DOI: 10.1051/0004-6361/201731200 (cited on page 25).

[102] V. A. Acciari et al. 'Measurement of the extragalactic background light using MAGIC and Fermi-LAT gamma-ray observations of blazars up to z = 1'. In: M*NRAS* 486.3 (July 2019), pp. 4233–4251. DOI: 10.1093/mnras/stz943 (cited on page 25).

[103] A. U. Abeysekara et al. 'Measurement of the Extragalactic Background Light Spectral Energy Distribution with VERITAS'. In: A*pJ* 885.2, 150 (Nov. 2019), p. 150. DOI: 10.3847/1538-4357/ab4817 (cited on page 25).

[104] K. Murase and F. W. Stecker. 'High-Energy Neutrinos from Active Galactic Nuclei'. In: *arXiv e-prints*, arXiv:2202.03381 (Feb. 2022), arXiv:2202.03381 (cited on pages 26, 29).

[105] X. Rodrigues et al. 'Leptohadronic Blazar Models Applied to the 2014-2015 Flare of TXS 0506+056'. In: A*pJ* 874.2, L29 (Apr. 2019), p. L29. DOI: 10.3847/2041-8213/ab1267 (cited on pages 27, 82).

[106] X. Rodrigues. 'Blazars as Sources of Neutrinos and Ultra-high-energy Cosmic Rays'. PhD thesis. Humboldt University of Berlin, Germany, Aug. 2019 (cited on pages 27, 28).

[107] A. Mücke and R. J. Protheroe. 'A proton synchrotron blazar model for flaring in Markarian 501'. In: *Astroparticle Physics* 15.1 (Mar. 2001), pp. 121–136. DOI: 10.1016/S0927-6505(00)00141-9 (cited on page 27).

[108] I. Liodakis and M. Petropoulou. 'Proton Synchrotron Gamma-Rays and the Energy Crisis in Blazars'. In: A*pJ* 893.1, L20 (Apr. 2020), p. L20. DOI: 10.3847/2041-8213/ab830a (cited on pages 27, 110).

[109] M. Ajello et al. 'The Origin of the Extragalactic Gamma-Ray Background and Implications for Dark Matter Annihilation'. In: A*pJ* 800.2, L27 (Feb. 2015), p. L27. DOI: 10.1088/2041-8205/800/2/L27 (cited on page 28).

[110] M. Di Mauro and F. Donato. 'Composition of the Fermi-LAT isotropic gamma-ray background intensity: Emission from extragalactic point sources and dark matter annihilations'. In: P*hys. Rev. D* 91.12, 123001 (June 2015), p. 123001. DOI: 10.1103/PhysRevD.91.123001 (cited on page 28).

[111] K. Murase and E. Waxman. 'Constraining high-energy cosmic neutrino sources: Implications and prospects'. In: P*hys. Rev. D* 94.10, 103006 (Nov. 2016), p. 103006. DOI: 10.1103/PhysRevD.94.103006 (cited on pages 28, 29, 156, 157).

[112] F. Tavecchio and G. Ghisellini. 'High-energy cosmic neutrinos from spine-sheath BL Lac jets'. In: M*NRAS* 451 (Aug. 2015), pp. 1502–1510. DOI: 10.1093/mnras/stv1023 (cited on pages 28, 157).

[113] K. Murase, Y. Inoue, and C. D. Dermer. 'Diffuse neutrino intensity from the inner jets of active galactic nuclei: Impacts of external photon fields and the blazar sequence'. In: P*hys. Rev. D* 90.2, 023007 (July 2014), p. 023007. DOI: 10.1103/PhysRevD.90.023007 (cited on pages 28, 156, 157).

[114] M. Petropoulou et al. 'Photohadronic origin of γ -ray BL Lac emission: implications for IceCube neutrinos'. In: M*NRAS* 448.3 (Apr. 2015), pp. 2412–2429. DOI: 10.1093/mnras/stv179 (cited on pages 28, 157).

[115] M. G. Aartsen et al. 'Differential limit on the extremely-high-energy cosmic neutrino flux in the presence of astrophysical background from nine years of IceCube data'. In: P*hys. Rev. D* 98.6, 062003 (Sept. 2018), p. 062003. DOI: 10.1103/PhysRevD.98.062003 (cited on page 29).

[116] M. Aartsen et al. 'The contribution of Fermi-2LAC blazars to the diffuse TeV-PeV neutrino flux'. In: *Astrophys. J.* 835.1 (2017), p. 45. DOI: 10.3847/1538-4357/835/1/45 (cited on page 29).

[117] C. Yuan, K. Murase, and P. Mészáros. 'Complementarity of Stacking and Multiplet Constraints on the Blazar Contribution to the Cumulative High-energy Neutrino Intensity'. In: A*pJ* 890.1, 25 (Feb. 2020), p. 25. DOI: 10.3847/1538-4357/ab65ea (cited on page 29).

[118] D. J. Thompson et al. 'Calibration of the Energetic Gamma-Ray Experiment Telescope (EGRET) for the Compton Gamma-Ray Observatory'. In: A*pJS* 86 (June 1993), p. 629. DOI: 10.1086/191793 (cited on page 33).

[119] W. L. Kraushaar and G. W. Clark. 'Search for Primary Cosmic Gamma Rays with the Satellite Explorer XI'. In: P*hys. Rev. Lett.* 8.3 (Feb. 1962), pp. 106–109. DOI: 10.1103/PhysRevLett.8.106 (cited on page 33).

[120] W. L. Kraushaar et al. 'High-Energy Cosmic Gamma-Ray Observations from the OSO-3 Satellite'. In: A*pJ* 177 (Nov. 1972), p. 341. DOI: 10.1086/151713 (cited on page 33).

[121] C. E. Fichtel et al. 'High-energy gamma-ray results from the second Small Astronomy Satellite.' In: A*pJ* 198 (May 1975), pp. 163–182. DOI: 10.1086/153590 (cited on page 33).

[122] L. Scarsi et al. 'The Cos-B Experiment and Mission'. In: *Recent Advances in Gamma-Ray Astronomy*. Ed. by R. D. Wills and B. Battrick. Vol. 124. ESA Special Publication. July 1977, p. 3 (cited on page 33).

[123] C. Meegan et al. 'The Fermi Gamma-ray Burst Monitor'. In: A*pJ* 702.1 (Sept. 2009), pp. 791–804. DOI: 10.1088/0004-637X/702/1/791 (cited on page 33).

[124] W. B. Atwood et al. 'The Large Area Telescope on the Fermi Gamma-Ray Space Telescope Mission'. In: A*pJ* 697.2 (June 2009), pp. 1071–1102. DOI: 10.1088/0004-637X/697/2/1071 (cited on pages 36, 37).

[125] A. A. Moiseev et al. 'Observation and simulations of the backsplash effects in high-energy γ-ray telescopes containing a massive calorimeter'. In: *Astroparticle Physics* 22.3-4 (Nov. 2004), pp. 275–283. DOI: 10.1016/j.astropartphys.2004.07.008 (cited on page 37).

[126] W. Atwood et al. 'Pass 8: Toward the Full Realization of the Fermi-LAT Scientific Potential'. In: *arXiv e-prints*, arXiv:1303.3514 (Mar. 2013), arXiv:1303.3514 (cited on pages 37, 38).

[127] M. Ackermann et al. 'The Fermi Large Area Telescope on Orbit: Event Classification, Instrument Response Functions, and Calibration'. In: A*pJS* 203.1, 4 (Nov. 2012), p. 4. DOI: 10.1088/0067-0049/203/1/4 (cited on page 38).

[128] I. King. 'The structure of star clusters. I. an empirical density law'. In: A*J* 67 (Oct. 1962), p. 471. DOI: 10.1086/108756 (cited on page 41).

[129] Student. 'The probable error of a mean'. In: *Biometrika* (1908), pp. 1–25 (cited on page 41).

[130] G. P. Ginet et al. 'Proton Flux Anisotropy in Low Earth Orbit'. In: *IEEE Transactions on Nuclear Science* 54.6 (Dec. 2007), pp. 1975–1980. DOI: 10.1109/TNS.2007.910041 (cited on page 43).

[131] G. Cowan. 'Statistics'. In: *Handbook of Particle Detection and Imaging*. Ed. by I. Fleck et al. 2021, pp. 117–143. DOI: 10.1007/978-3-319-93785-4_5 (cited on page 43).

[132] E. Massaro et al. 'Log-parabolic spectra and particle acceleration in the BL Lac object Mkn 421: Spectral analysis of the complete BeppoSAX wide band X-ray data set'. In: A*&A* 413 (Jan. 2004), pp. 489–503. DOI: 10.1051/0004-6361:20031558 (cited on page 45).

[133] P. Bak, C. Tang, and K. Wiesenfeld. 'Self-organized criticality: An explanation of the 1/f noise'. In: P*hys. Rev. Lett.* 59.4 (July 1987), pp. 381–384. DOI: 10.1103/PhysRevLett.59.381 (cited on page 45).

[134] P. Lipari. 'The origin of the power-law form of the extragalactic gamma-ray flux'. In: *Astroparticle Physics* 125, 102507 (Feb. 2021), p. 102507. DOI: 10.1016/j.astropartphys.2020.102507 (cited on page 45).

[135] E. Fermi. 'On the Origin of the Cosmic Radiation'. In: *Physical Review* 75.8 (Apr. 1949), pp. 1169–1174. DOI: 10.1103/PhysRev.75.1169 (cited on pages 45, 130).

[136] E. Massaro et al. 'Fine phase resolved spectroscopy of the X-ray emission of the Crab pulsar (PSR B0531+21) observed with BeppoSAX'. In: A*&A* 361 (Sept. 2000), pp. 695–703 (cited on page 46).

[137] P. Giommi et al. 'A Catalog of 157 X-ray Spectra and 84 Spectral Energy Distributions of Blazars Observed with BeppoSAX'. In: *Blazar Astrophysics with BeppoSAX and Other Observatories*. Ed. by P. Giommi, E. Massaro, and G. Palumbo. Jan. 2002, p. 63 (cited on page 46).

[138] G. Boella et al. 'BeppoSAX, the wide band mission for X-ray astronomy'. In: A*&AS* 122 (Apr. 1997), pp. 299–307. DOI: 10.1051/aas:1997136 (cited on page 46).

[139] A. A. Abdo et al. 'Fermi/Large Area Telescope Bright Gamma-Ray Source List'. In: A*pJS* 183.1 (July 2009), pp. 46–66. DOI: 10.1088/0067-0049/183/1/46 (cited on page 46).

[140] J. Ballet et al. 'Fermi Large Area Telescope Fourth Source Catalog Data Release 2'. In: *arXiv e-prints*, arXiv:2005.11208 (May 2020), arXiv:2005.11208 (cited on page 46).

[141] S. Abdollahi et al. 'Fermi Large Area Telescope Fourth Source Catalog'. In: A*pJS* 247.1, 33 (Mar. 2020), p. 33. DOI: 10.3847/1538-4365/ab6bcb (cited on pages 46, 50, 118, 119).

[142] G. Principe et al. 'The first catalog of Fermi-LAT sources below 100 MeV'. In: A*&A* 618, A22 (Oct. 2018), A22. DOI: 10.1051/0004-6361/201833116 (cited on page 46).

[143] M. Ackermann et al. 'The First Fermi-LAT Catalog of Sources above 10 GeV'. In: A*pJS* 209.2, 34 (Dec. 2013), p. 34. DOI: 10.1088/0067-0049/209/2/34 (cited on page 46).

[144] M. Ajello et al. '3FHL: The Third Catalog of Hard Fermi-LAT Sources'. In: A*pJS* 232.2, 18 (Oct. 2017), p. 18. DOI: 10.3847/1538-4365/aa8221 (cited on pages 46, 73, 74, 85, 86, 152).

[145] M. Ackermann et al. '2FHL: The Second Catalog of Hard Fermi-LAT Sources'. In: A*pJS* 222.1, 5 (Jan. 2016), p. 5. DOI: 10.3847/0067-0049/222/1/5 (cited on page 46).

[146] S. E. Healey et al. 'CGRaBS: An All-Sky Survey of Gamma-Ray Blazar Candidates'. In: A*pJS* 175.1 (Mar. 2008), pp. 97–104. DOI: 10.1086/523302 (cited on pages 47, 153).

[147] T. R. Monroe et al. 'The UV-bright Quasar Survey (UVQS): DR1'. In: A*J* 152.1, 25 (July 2016), p. 25. DOI: 10.3847/0004-6256/152/1/25 (cited on page 47).

[148] M. Ajello et al. 'The Fourth Catalog of Active Galactic Nuclei Detected by the Fermi Large Area Telescope'. In: A*pJ* 892.2, 105 (Apr. 2020), p. 105. DOI: 10.3847/1538-4357/ab791e (cited on pages 47–50, 99, 116, 117, 150).

[149] B. Lott, D. Gasparrini, and S. Ciprini. 'The Fourth Catalog of Active Galactic Nuclei Detected by the Fermi Large Area Telescope – Data Release 2'. In: *arXiv e-prints*, arXiv:2010.08406 (Oct. 2020), arXiv:2010.08406 (cited on pages 47, 50).

[150] L. Petrov et al. 'The Second LBA Calibrator Survey of southern compact extragalactic radio sources - LCS2'. In: M*NRAS* 485.1 (May 2019), pp. 88–101. DOI: 10.1093/mnras/stz242 (cited on page 47).

[151] E. Massaro et al. 'The 5th edition of the Roma-BZCAT. A short presentation'. In: A*p&SS* 357.1, 75 (May 2015), p. 75. DOI: 10.1007/s10509-015-2254-2 (cited on page 47).

[152] S. E. Healey et al. 'CRATES: An All-Sky Survey of Flat-Spectrum Radio Sources'. In: A*pJS* 171.1 (July 2007), pp. 61–71. DOI: 10.1086/513742 (cited on pages 47, 98).

[153] M. Ackermann et al. 'The Third Catalog of Active Galactic Nuclei Detected by the Fermi Large Area Telescope'. In: A*pJ* 810, 14 (Sept. 2015), p. 14. DOI: 10.1088/0004-637X/810/1/14 (cited on pages 49, 85).

[154] C. D. Dermer et al. 'Near-equipartition Jets with Log-parabola Electron Energy Distribution and the Blazar Spectral-index Diagrams'. In: A*pJ* 809.2, 174 (Aug. 2015), p. 174. DOI: 10.1088/0004-637X/809/2/174 (cited on page 49).

[155] J. J. Ruan et al. 'The Nature of Transition Blazars'. In: A*pJ* 797.1, 19 (Dec. 2014), p. 19. DOI: 10.1088/0004-637X/797/1/19 (cited on page 49).

[156] M. Wood et al. 'Fermipy: An open-source Python package for analysis of Fermi-LAT Data'. In: *PoS* ICRC2017 (2018). [35,824(2017)], p. 824. DOI: 10.22323/1.301.0824 (cited on pages 51, 171–174).

[157] A. A. Abdo et al. 'Fermi large area telescope observations of the cosmic-ray induced γ-ray emission of the Earth's atmosphere'. In: P*hys. Rev. D* 80.12, 122004 (Dec. 2009), p. 122004. DOI: 10.1103/PhysRevD.80.122004 (cited on page 51).

[158] T. A. Porter, G. Johannesson, and I. V. Moskalenko. 'The GALPROP Cosmic-ray Propagation and Non-thermal Emissions Framework: Release v57'. In: *arXiv e-prints*, arXiv:2112.12745 (Dec. 2021), arXiv:2112.12745 (cited on page 52).

[159] K. M. Górski et al. 'HEALPix: A Framework for High-Resolution Discretization and Fast Analysis of Data Distributed on the Sphere'. In: A*pJ* 622.2 (Apr. 2005), pp. 759–771. DOI: 10.1086/427976 (cited on pages 52, 66).

[160] F. James and M. Roos. 'Minuit - a system for function minimization and analysis of the parameter errors and correlations'. In: *Computer Physics Communications* 10.6 (Dec. 1975), pp. 343–367. DOI: 10.1016/0010-4655(75)90039-9 (cited on page 53).

[161] J. R. Mattox et al. 'The Likelihood Analysis of EGRET Data'. In: A*pJ* 461 (Apr. 1996), p. 396. DOI: 10.1086/177068 (cited on pages 54, 79).

[162] B. Lott et al. 'An adaptive-binning method for generating constant-uncertainty/constant-significance light curves with Fermi-LAT data'. In: A*&A* 544, A6 (Aug. 2012), A6. DOI: 10.1051/0004-6361/201218873 (cited on pages 56, 76, 100, 115, 117, 171–174).

[163] A. Cooper-Sarkar, P. Mertsch, and S. Sarkar. 'The high energy neutrino cross-section in the Standard Model and its uncertainty'. In: *Journal of High Energy Physics* 2011, 42 (Aug. 2011), p. 42. DOI: 10.1007/JHEP08(2011)042 (cited on page 57).

[164] A. Roberts. 'The birth of high-energy neutrino astronomy: A personal history of the DUMAND project'. In: *Reviews of Modern Physics* 64.1 (Jan. 1992), pp. 259–312. DOI: 10.1103/RevModPhys.64.259 (cited on page 57).

[165] E. Andres et al. 'The AMANDA neutrino telescope: principle of operation and first results'. In: *Astroparticle Physics* 13.1 (Mar. 2000), pp. 1–20. DOI: 10.1016/S0927-6505(99)00092-4 (cited on page 57).

[166] R. Abbasi et al. 'Calibration and characterization of the IceCube photomultiplier tube'. In: *Nuclear Instruments and Methods in Physics Research A* 618.1-3 (June 2010), pp. 139–152. DOI: 10.1016/j.nima.2010.03.102 (cited on page 58).

[167] R. Abbasi et al. 'IceTop: The surface component of IceCube'. In: *Nuclear Instruments and Methods in Physics Research A* 700 (Feb. 2013), pp. 188–220. DOI: 10.1016/j.nima.2012.10.067 (cited on page 58).

[168] J. A. Formaggio and G. P. Zeller. 'From eV to EeV: Neutrino cross sections across energy scales'. In: *Reviews of Modern Physics* 84.3 (July 2012), pp. 1307–1341. DOI: 10.1103/RevModPhys.84.1307 (cited on page 59).

[169] M. G. Aartsen et al. 'Energy reconstruction methods in the IceCube neutrino telescope'. In: *Journal of Instrumentation* 9.3, P03009 (Mar. 2014), P03009. DOI: 10.1088/1748-0221/9/03/P03009 (cited on pages 61, 66).

[170] J. G. Learned and S. Pakvasa. 'Detecting ν_τ oscillations at PeV energies'. In: *Astroparticle Physics* 3.3 (May 1995), pp. 267–274. DOI: 10.1016/0927-6505(94)00043-3 (cited on page 61).

[171] R. Abbasi et al. 'Measurement of Astrophysical Tau Neutrinos in IceCube's High-Energy Starting Events'. In: *arXiv e-prints*, arXiv:2011.03561 (Nov. 2020), arXiv:2011.03561 (cited on page 61).

[172] S. L. Glashow. 'Resonant Scattering of Antineutrinos'. In: *Physical Review* 118.1 (Apr. 1960), pp. 316–317. DOI: 10.1103/PhysRev.118.316 (cited on page 61).

[173] M. G. Aartsen et al. 'Detection of a particle shower at the Glashow resonance with IceCube'. In: N*ature* 591.7849 (Mar. 2021), pp. 220–224. DOI: 10.1038/s41586-021-03256-1 (cited on page 62).

[174] R. Gandhi et al. 'Neutrino interactions at ultrahigh energies'. In: P*hys. Rev. D* 58.9, 093009 (Nov. 1998), p. 093009. DOI: 10.1103/PhysRevD.58.093009 (cited on page 62).

[175] F. Bradascio. 'Searches for cross-correlations between IceCube neutrinos and Active Galactic Nuclei selected in various bands of the electromagnetic spectrum'. PhD thesis. Humboldt University of Berlin, Germany, Jan. 2021 (cited on page 62).

[176] T. K. Gaisser et al. 'Generalized self-veto probability for atmospheric neutrinos'. In: P*hys. Rev. D* 90.2, 023009 (July 2014), p. 023009. DOI: 10.1103/PhysRevD.90.023009 (cited on page 63).

[177] V. S. Vorobev and A. A. Petrukhin. 'Review of Investigations of Muon Bundles Generated by Very-High-Energy Cosmic Rays'. In: *Physics of Atomic Nuclei* 84.6 (Nov. 2021), pp. 934–940. DOI: 10.1134/S1063778821130408 (cited on page 63).

[178] R. Abbasi et al. 'Improved Characterization of the Astrophysical Muon-Neutrino Flux with 9.5 Years of IceCube Data'. In: *arXiv e-prints*, arXiv:2111.10299 (Nov. 2021), arXiv:2111.10299 (cited on page 64).

[179] R. Abbasi et al. 'IceCube high-energy starting event sample: Description and flux characterization with 7.5 years of data'. In: P*hys. Rev. D* 104.2, 022002 (July 2021), p. 022002. DOI: 10.1103/PhysRevD.104.022002 (cited on page 64).

[180] M. G. Aartsen et al. 'Observation of High-Energy Astrophysical Neutrinos in Three Years of IceCube Data'. In: P*hys. Rev. Lett.* 113.10, 101101 (Sept. 2014), p. 101101. DOI: 10.1103/PhysRevLett.113.101101 (cited on pages 64, 150).

[181] M. G. Aartsen et al. 'Characteristics of the diffuse astrophysical electron and tau neutrino flux with six years of IceCube high energy cascade data'. In: *arXiv e-prints*, arXiv:2001.09520 (Jan. 2020), arXiv:2001.09520 (cited on page 64).

[182] R. Abbasi et al. 'A muon-track reconstruction exploiting stochastic losses for large-scale Cherenkov detectors'. In: *Journal of Instrumentation* 16.8, P08034 (Aug. 2021), P08034. DOI: 10.1088/1748-0221/16/08/P08034 (cited on page 66).

[183] T. Kintscher. 'Searching for Transient Neutrino Sources with IceCube in Real-Time'. In: *XXVIII International Conference on Neutrino Physics and Astrophysics*. June 2018, 294, p. 294. DOI: 10.5281/zenodo.1300867 (cited on page 66).

[184] C. Haack, C. Wiebusch, and IceCube Collaboration. 'A measurement of the diffuse astrophysical muon neutrino flux using eight years of IceCube data.' In: *35th International Cosmic Ray Conference (ICRC2017)*. Vol. 301. International Cosmic Ray Conference. Jan. 2017, 1005, p. 1005 (cited on page 66).

[185] M. W. E. Smith et al. 'The Astrophysical Multimessenger Observatory Network (AMON)'. In: *Astroparticle Physics* 45 (May 2013), pp. 56–70. DOI: 10.1016/j.astropartphys.2013.03.003 (cited on page 67).

[186] IceCube Coll. et al. 'Multimessenger observations of a flaring blazar coincident with high-energy neutrino IceCube-170922A'. In: *Science* 361.6398, eaat1378 (July 2018), eaat1378. DOI: 10.1126/science.aat1378 (cited on pages 71, 72, 81).

[187] Y. T. Tanaka, S. Buson, and D. Kocevski. 'Fermi-LAT detection of increased gamma-ray activity of TXS 0506+056, located inside the IceCube-170922A error region.' In: *The Astronomer's Telegram* 10791 (Sept. 2017), p. 1 (cited on page 72).

[188] D. Dornic and A. Coleiro. 'Search for counterpart to IceCube-170922A with ANTARES'. In: *The Astronomer's Telegram* 10773 (Sept. 2017), p. 1 (cited on page 72).

[189] M. Ajello et al. 'The Cosmic Evolution of Fermi BL Lacertae Objects'. In: A*pJ* 780, 73 (Jan. 2014), p. 73. DOI: 10.1088/0004-637X/780/1/73 (cited on page 74).

[190] S. Paiano et al. 'The Redshift of the BL Lac Object TXS 0506+056'. In: A*pJ* 854, L32 (Feb. 2018), p. L32. DOI: 10.3847/2041-8213/aaad5e (cited on page 74).

[191] M. .-. Véron-Cetty and P. Véron. 'A catalogue of quasars and active nuclei: 12th edition'. In: A*&A* 455.2 (Aug. 2006), pp. 773–777. DOI: 10.1051/0004-6361:20065177 (cited on page 74).

[192] P. Padovani et al. 'Dissecting the region around IceCube-170922A: the blazar TXS 0506+056 as the first cosmic neutrino source'. In: M*NRAS* 480 (Oct. 2018), pp. 192–203. DOI: 10.1093/mnras/sty1852 (cited on pages 75, 79).

[193] Y.-F. Liang et al. 'Search for GeV flare coincident with the IceCube neutrino flare'. In: (2018) (cited on page 75).

[194] J. D. Scargle et al. 'Studies in Astronomical Time Series Analysis. VI. Bayesian Block Representations'. In: A*pJ* 764, 167 (Feb. 2013), p. 167. DOI: 10.1088/0004-637X/764/2/167 (cited on pages 76, 101, 119, 125, 171–174).

[195] Astropy Collaboration et al. 'Astropy: A community Python package for astronomy'. In: A*&A* 558, A33 (Oct. 2013), A33. DOI: 10.1051/0004-6361/201322068 (cited on page 76).

[196] A. M. Price-Whelan et al. 'The Astropy Project: Building an Open-science Project and Status of the v2.0 Core Package'. In: A*J* 156, 123 (Sept. 2018), p. 123. DOI: 10.3847/1538-3881/aabc4f (cited on page 76).

[197] S. S. Wilks. 'The Large-Sample Distribution of the Likelihood Ratio for Testing Composite Hypotheses'. In: *Ann. Math. Statist.* 9.1 (Mar. 1938), pp. 60–62. DOI: 10.1214/aoms/1177732360 (cited on page 79).

[198] S. Gao et al. 'Interpretation of the coincident observation of a high energy neutrino and a bright flare'. In: *Nat. Astron.* 3.1 (2019), pp. 88–92. DOI: 10.1038/s41550-018-0610-1 (cited on page 82).

[199] A. Keivani et al. 'A Multimessenger Picture of the Flaring Blazar TXS 0506+056: Implications for High-energy Neutrino Emission and Cosmic-Ray Acceleration'. In: A*pJ* 864, 84 (Sept. 2018), p. 84. DOI: 10.3847/1538-4357/aad59a (cited on page 82).

[200] M. Cerruti et al. 'Leptohadronic single-zone models for the electromagnetic and neutrino emission of TXS 0506+056'. In: M*NRAS* 483 (Feb. 2019), pp. L12–L16. DOI: 10.1093/mnrasl/sly210 (cited on page 82).

[201] N. L. Strotjohann, M. Kowalski, and A. Franckowiak. 'Eddington Bias for Cosmic Neutrino Sources'. In: (2018) (cited on pages 82, 95).

[202] R.-Y. Liu et al. 'Hadronuclear interpretation of a high-energy neutrino event coincident with a blazar flare'. In: P*hys. Rev. D* 99.6, 063008 (Mar. 2019), p. 063008. DOI: 10.1103/PhysRevD.99.063008 (cited on page 82).

[203] R. Xue et al. 'A Two-zone Model for Blazar Emission: Implications for TXS 0506+056 and the Neutrino Event IceCube-170922A'. In: A*pJ* 886.1, 23 (Nov. 2019), p. 23. DOI: 10.3847/1538-4357/ab4b44 (cited on page 82).

[204] K. Wang et al. 'Jet-cloud/star interaction as an interpretation of neutrino outburst from the blazar TXS 0506+056'. In: *arXiv e-prints*, arXiv:1809.00601 (Sept. 2018), arXiv:1809.00601 (cited on page 82).

[205] S. Britzen et al. 'A cosmic collider: Was the IceCube neutrino generated in a precessing jet-jet interaction in TXS 0506+056?' In: A*&A* 630, A103 (Oct. 2019), A103. DOI: 10.1051/0004-6361/201935422 (cited on page 82).

[206] E. Ros et al. 'Apparent superluminal core expansion and limb brightening in the candidate neutrino blazar TXS 0506+056'. In: A*&A* 633, L1 (Jan. 2020), p. L1. DOI: 10.1051/0004-6361/201937206 (cited on page 82).

[207] M. Petropoulou et al. 'Multi-epoch Modeling of TXS 0506+056 and Implications for Long-term High-energy Neutrino Emission'. In: A*pJ* 891.2, 115 (Mar. 2020), p. 115. DOI: 10.3847/1538-4357/ab76d0 (cited on page 82).

[208] A. Reimer, M. Böttcher, and S. Buson. 'Cascading Constraints from Neutrino-emitting Blazars: The Case of TXS 0506+056'. In: A*pJ* 881.1, 46 (Aug. 2019), p. 46. DOI: 10.3847/1538-4357/ab2bff (cited on page 82).

[209] F. Halzen et al. 'On the Neutrino Flares from the Direction of TXS 0506+056'. In: A*pJ* 874.1, L9 (Mar. 2019), p. L9. DOI: 10.3847/2041-8213/ab0d27 (cited on page 82).

[210] F. Acero et al. 'Fermi Large Area Telescope Third Source Catalog'. In: A*pJS* 218, 23 (June 2015), p. 23. DOI: 10.1088/0067-0049/218/2/23 (cited on pages 85, 87).

[211] IceCube Collaboration et al. 'The IceCube Neutrino Observatory - Contributions to ICRC 2017 Part II: Properties of the Atmospheric and Astrophysical Neutrino Flux'. In: *ArXiv e-prints* (Oct. 2017) (cited on page 86).

[212] M. Ackermann et al. '2FHL: The Second Catalog of Hard Fermi-LAT Sources'. In: A*pJS* 222, 5 (Jan. 2016), p. 5. DOI: 10.3847/0067-0049/222/1/5 (cited on page 86).

[213] C. P. Ahn et al. 'The Ninth Data Release of the Sloan Digital Sky Survey: First Spectroscopic Data from the SDSS-III Baryon Oscillation Spectroscopic Survey'. In: A*pJS* 203, 21 (Dec. 2012), p. 21. DOI: 10.1088/0067-0049/203/2/21 (cited on page 87).

[214] A. Maselli et al. 'New blazars from the cross-match of recent multi-frequency catalogs'. In: *Astrophys. Space Sci.* 357.2 (2015), p. 141. DOI: 10.1007/s10509-015-2372-x (cited on page 87).

[215] S. Paiano et al. 'The spectra of IceCube neutrino candidate sources - I. Optical spectroscopy of blazars'. In: M*NRAS* 504.3 (July 2021), pp. 3338–3353. DOI: 10.1093/mnras/stab1034 (cited on page 87).

[216] I. A. G. Snellen et al. 'Automated optical identification of a large complete northern hemisphere sample of flat-spectrum radio sources with S_{6cm}>200 mJy'. In: M*NRAS* 329 (Feb. 2002), pp. 700–746. DOI: 10.1046/j.1365-8711.2002.05049.x (cited on page 87).

[217] P. C. Gregory et al. 'The GB6 Catalog of Radio Sources'. In: A*pJS* 103 (Apr. 1996), p. 427. DOI: 10.1086/192282 (cited on page 88).

[218] S. B. Lambert and A. .-. Gontier. 'On radio source selection to define a stable celestial frame'. In: A*&A* 493 (Jan. 2009), pp. 317–323. DOI: 10.1051/0004-6361:200810582 (cited on page 88).

[219] B. J. Shappee et al. 'The Man behind the Curtain: X-Rays Drive the UV through NIR Variability in the 2013 Active Galactic Nucleus Outburst in NGC 2617'. In: A*pJ* 788, 48 (June 2014), p. 48. DOI: 10.1088/0004-637X/788/1/48 (cited on page 93).

[220] C. S. Kochanek et al. 'The All-Sky Automated Survey for Supernovae (ASAS-SN) Light Curve Server v1.0'. In: P*ASP* 129.10 (Oct. 2017), p. 104502. DOI: 10.1088/1538-3873/aa80d9 (cited on page 93).

[221] A. J. Drake et al. 'First Results from the Catalina Real-Time Transient Survey'. In: A*pJ* 696 (May 2009), pp. 870–884. DOI: 10.1088/0004-637X/696/1/870 (cited on page 93).

[222] R. R. Laher et al. 'IPAC Image Processing and Data Archiving for the Palomar Transient Factory'. In: P*ASP* 126 (July 2014), p. 674. DOI: 10.1086/677351 (cited on page 93).

[223] F. J. Masci et al. 'The IPAC Image Subtraction and Discovery Pipeline for the Intermediate Palomar Transient Factory'. In: P*ASP* 129.1 (Jan. 2017), p. 014002. DOI: 10.1088/1538-3873/129/971/014002 (cited on page 93).

[224] I. Liodakis et al. 'Probing Blazar Emission Processes with Optical/Gamma-Ray Flare Correlations'. In: A*pJ* 880.1, 32 (July 2019), p. 32. DOI: 10.3847/1538-4357/ab26b7 (cited on page 93).

[225] H. Zhang, K. Fang, and H. Li. 'Variability and Optical Polarization Can Probe the Neutrino and Electromagnetic Emission Mechanisms of TXS˜0506+056'. In: *ArXiv e-prints* (July 2018) (cited on page 93).

[226] A. A. Abdo et al. 'Fermi Large Area Telescope Observations of Two Gamma-Ray Emission Components from the Quiescent Sun'. In: A*pJ* 734.2, 116 (June 2011), p. 116. DOI: 10.1088/0004-637X/734/2/116 (cited on page 94).

[227] A. Franckowiak et al. 'Patterns in the Multiwavelength Behavior of Candidate Neutrino Blazars'. In: A*pJ* 893.2, 162 (Apr. 2020), p. 162. DOI: 10.3847/1538-4357/ab8307 (cited on pages 97, 99, 101, 102, 104, 105, 110, 143, 148–150, 155, 158, 160, 161, 173).

[228] X. Rodrigues et al. 'Multiwavelength and Neutrino Emission from Blazar PKS 1502 + 106'. In: A*pJ* 912.1, 54 (May 2021), p. 54. DOI: 10.3847/1538-4357/abe87b (cited on pages 97, 100–102, 104–110).

[229] J. H. Crowther and R. W. Clarke. 'A pencil-beam radio telescope operating at 178 Mc/s'. In: M*NRAS* 132 (Jan. 1966), p. 405. DOI: 10.1093/mnras/132.3.405 (cited on page 98).

[230] P. J. S. Williams, S. Kenderdine, and J. E. Baldwin. 'A survey of radio sources and background radiation at 38 Mc/s'. In: M*mRAS* 70 (Jan. 1966), pp. 53–110 (cited on page 98).

[231] G. A. Day et al. 'The Parkes catalogue of radio sources, declination zone 0° to +20°'. In: *Australian Journal of Physics* 19 (Feb. 1966), p. 35. DOI: 10.1071/PH660035 (cited on page 98).

[232] L. T. Fitch, R. S. Dixon, and J. D. Kraus. 'A high-sensitivity 1415-MHz survey between declinations of 0 and 20 north.' In: A*J* 74 (June 1969), pp. 612–688. DOI: 10.1086/110844 (cited on page 98).

[233] J. K. Adelman-McCarthy et al. 'The Sixth Data Release of the Sloan Digital Sky Survey'. In: A*pJS* 175.2 (Apr. 2008), pp. 297–313. DOI: 10.1086/524984 (cited on page 98).

[234] V. D'Elia, P. Padovani, and H. Landt. 'The disc-jet relation in strong-lined blazars'. In: M*NRAS* 339.4 (Mar. 2003), pp. 1081–1094. DOI: 10.1046/j.1365-8711.2003.06255.x (cited on page 98).

[235] Y. Shen et al. 'A Catalog of Quasar Properties from Sloan Digital Sky Survey Data Release 7'. In: A*pJS* 194.2, 45 (June 2011), p. 45. DOI: 10.1088/0067-0049/194/2/45 (cited on page 99).

[236] G. Ghisellini and F. Tavecchio. 'Canonical high-power blazars'. In: M*NRAS* 397.2 (Aug. 2009), pp. 985–1002. DOI: 10.1111/j.1365-2966.2009.15007.x (cited on pages 99, 105).

[237] S. Ciprini. 'GLAST LAT detection of a possible new gamma-ray flaring blazar: PKS 1502+106'. In: *The Astronomer's Telegram* 1650 (Aug. 2008), p. 1 (cited on page 99).

[238] D. Horan and E. Hays. 'Fermi-LAT detection of renewed activity from the blazar PKS 1502+106'. In: *The Astronomer's Telegram* 1905 (Jan. 2009), p. 1 (cited on page 99).

[239] A. A. Abdo et al. 'PKS 1502+106: A New and Distant Gamma-ray Blazar in Outburst Discovered by the Fermi Large Area Telescope'. In: A*pJ* 710.1 (Feb. 2010), pp. 810–827. DOI: 10.1088/0004-637X/710/1/810 (cited on pages 99, 100, 139).

[240] V. Karamanavis et al. 'PKS 1502+106: A high-redshift Fermi blazar at extreme angular resolution. Structural dynamics with VLBI imaging up to 86 GHz'. In: A*&A* 586, A60 (Feb. 2016), A60. DOI: 10.1051/0004-6361/201527225 (cited on page 99).

[241] S. Garrappa, S. Buson, and D. Gasparrini. 'Fermi-LAT Gamma-ray Observations of IceCube-190730A'. In: *The Astronomer's Telegram* 12972 (July 2019), p. 1 (cited on page 99).

[242] Fermi-LAT Collaboration et al. 'A gamma-ray determination of the Universe's star formation history'. In: *Science* 362.6418 (Nov. 2018), pp. 1031–1034. DOI: 10.1126/science.aat8123 (cited on pages 102, 104).

[243] J. E. Greene and L. C. Ho. 'Estimating Black Hole Masses in Active Galaxies Using the Hα Emission Line'. In: A*pJ* 630.1 (Sept. 2005), pp. 122–129. DOI: 10.1086/431897 (cited on page 105).

[244] M. G. Aartsen et al. 'All-sky Search for Time-integrated Neutrino Emission from Astrophysical Sources with 7 yr of IceCube Data'. In: *The Astrophysical Journal* 835.2 (2017), p. 151. DOI: 10.3847/1538-4357/835/2/151 (cited on page 109).

[245] S. Britzen et al. 'A ring accelerator? Unusual jet dynamics in the IceCube candidate PKS 1502+106'. In: M*NRAS* 503.3 (May 2021), pp. 3145–3178. DOI: 10.1093/mnras/stab589 (cited on pages 111, 138, 139).

[246] F. Oikonomou et al. 'Multi-messenger emission from the parsec-scale jet of the flat-spectrum radio quasar PKS 1502+106 coincident with high-energy neutrino IceCube-190730A'. In: J. *Cosmology Astropart. Phys.* 2021.10, 082 (Oct. 2021), p. 082. DOI: 10.1088/1475-7516/2021/10/082 (cited on page 111).

[247] P. L. Nolan et al. 'Fermi Large Area Telescope Second Source Catalog'. In: A*pJS* 199.2, 31 (Apr. 2012), p. 31. DOI: 10.1088/0067-0049/199/2/31 (cited on page 118).

[248] S. Saito et al. 'Time-dependent Modeling of Gamma-Ray Flares in Blazar PKS1510–089'. In: A*pJ* 809.2, 171 (Aug. 2015), p. 171. DOI: 10.1088/0004-637X/809/2/171 (cited on page 119).

[249] A. A. Abdo et al. 'Gamma-ray Light Curves and Variability of Bright Fermi-detected Blazars'. In: A*pJ* 722.1 (Oct. 2010), pp. 520–542. DOI: 10.1088/0004-637X/722/1/520 (cited on pages 120, 121, 127, 130).

[250] B. Schölkopf et al. 'New Support Vector Algorithms'. In: *Neural Computation* 12.5 (2000), pp. 1207–1245. DOI: 10.1162/089976600300015565 (cited on page 121).

[251] P. Padovani et al. 'The spectra of IceCube neutrino (SIN) candidate sources - II. Source characterization'. In: M*NRAS* 510.2 (Feb. 2022), pp. 2671–2688. DOI: 10.1093/mnras/stab3630 (cited on page 121).

[252] S. Vercellone et al. 'On the duty-cycle of γ-ray blazars'. In: M*NRAS* 353.3 (Sept. 2004), pp. 890–902. DOI: 10.1111/j.1365-2966.2004.08119.x (cited on page 122).

[253] M. Tluczykont et al. 'Long-term lightcurves from combined unified very high energy γ-ray data'. In: A*&A* 524, A48 (Dec. 2010), A48. DOI: 10.1051/0004-6361/201015193 (cited on page 122).

[254] K. Nalewajko. 'The brightest gamma-ray flares of blazars'. In: M*NRAS* 430.2 (Apr. 2013), pp. 1324–1333. DOI: 10.1093/mnras/sts711 (cited on page 122).

[255] J. R. Sacahui et al. 'Study of Blazar Activity in 10 year Fermi-LAT Data and Implications for TeV Neutrino Expectations'. In: R*ev. Mexicana Astron. Astrofis.* 57 (Oct. 2021), pp. 251–268. DOI: 10.22201/ia.01851101p.2021.57.02.01 (cited on page 123).

[256] J. L. Hodges. 'The significance probability of the smirnov two-sample test'. In: *Arkiv för Matematik* 3.5 (1958), pp. 469–486. DOI: 10.1007/BF02589501 (cited on pages 123, 149).

[257] G. Ghisellini, A. Celotti, and L. Costamante. 'Low power BL Lacertae objects and the blazar sequence. Clues on the particle acceleration process'. In: A&A 386 (May 2002), pp. 833–842. DOI: 10.1051/0004-6361:20020275 (cited on page 124).

[258] C. M. Raiteri et al. 'Blazar spectral variability as explained by a twisted inhomogeneous jet'. In: N*ature* 552.7685 (Dec. 2017), pp. 374–377. DOI: 10.1038/nature24623 (cited on page 124).

[259] D. J. Eisenstein and P. Hut. 'HOP: A New Group-Finding Algorithm for N-Body Simulations'. In: A*pJ* 498.1 (May 1998), pp. 137–142. DOI: 10.1086/305535 (cited on page 125).

[260] C. E. Rasmussen and C. K. I. Williams. *Gaussian Processes for Machine Learning*. 2006 (cited on pages 126, 127).

[261] F. Pedregosa et al. 'Scikit-learn: Machine Learning in Python'. In: *arXiv e-prints*, arXiv:1201.0490 (Jan. 2012), arXiv:1201.0490 (cited on page 127).

[262] R.-R. Griffiths et al. 'Modeling the Multiwavelength Variability of Mrk 335 Using Gaussian Processes'. In: A*pJ* 914.2, 144 (June 2021), p. 144. DOI: 10.3847/1538-4357/abfa9f (cited on page 127).

[263] C. Willecke Lindberg et al. 'A Bayesian Method for Inferring Asteroid Properties from Sparse Light Curves'. In: *American Astronomical Society Meeting Abstracts #233*. Vol. 233. American Astronomical Society Meeting Abstracts. Jan. 2019, 302.04, p. 302.04 (cited on page 127).

[264] V. Karamanavis. 'Gaussian Processes for Blazar Variability Studies'. In: *Galaxies* 5.1 (Mar. 2017), p. 19. DOI: 10.3390/galaxies5010019 (cited on page 127).

[265] J. A. Nelder and R. Mead. 'A Simplex Method for Function Minimization'. In: *The Computer Journal* 7.4 (Jan. 1965), pp. 308–313. DOI: 10.1093/comjnl/7.4.308 (cited on page 128).

[266] M. Newville et al. *LMFIT: Non-Linear Least-Square Minimization and Curve-Fitting for Python*. Version 0.8.0. Sept. 2014. DOI: 10.5281/zenodo.11813 (cited on page 128).

[267] D. Foreman-Mackey et al. 'emcee: The MCMC Hammer'. In: P*ASP* 125.925 (Mar. 2013), p. 306. DOI: 10.1086/670067 (cited on page 128).

[268] N. Roy et al. 'Probing the jets of blazars using the temporal symmetry of their multiwavelength outbursts'. In: M*NRAS* 482.1 (Jan. 2019), pp. 743–757. DOI: 10.1093/mnras/sty2748 (cited on pages 130, 132).

[269] M. C. Begelman, A. C. Fabian, and M. J. Rees. 'Implications of very rapid TeV variability in blazars'. In: M*NRAS* 384.1 (Feb. 2008), pp. L19–L23. DOI: 10.1111/j.1745-3933.2007.00413.x (cited on page 133).

[270] L. Costamante, S. Cutini, and G. Tosti. 'The blazar zone: Issues and recent developments'. In: *Fourteenth Marcel Grossmann Meeting - MG14*. Ed. by M. Bianchi, R. T. Jansen, and R. Ruffini. Jan. 2018, pp. 3080–3085. DOI: 10.1142/9789813226609_0390 (cited on page 138).

[271] S. Garrappa et al. '*Fermi*-LAT realtime follow-ups of high-energy neutrino alerts'. In: *arXiv e-prints*, arXiv:2112.11586 (Dec. 2021), arXiv:2112.11586 (cited on pages 143, 146–148).

[272] S. Gao et al. 'Modelling the coincident observation of a high-energy neutrino and a bright blazar flare'. In: *Nature Astronomy* 3 (Jan. 2019), pp. 88–92. DOI: 10.1038/s41550-018-0610-1 (cited on page 144).

[273] A. Albert et al. 'ANTARES Search for Point Sources of Neutrinos Using Astrophysical Catalogs: A Likelihood Analysis'. In: A*pJ* 911.1, 48 (Apr. 2021), p. 48. DOI: 10.3847/1538-4357/abe53c (cited on page 150).

[274] G. L. White et al. 'Redshifts of Southern Radio Sources. VII.' In: A*pJ* 327 (Apr. 1988), p. 561. DOI: 10.1086/166216 (cited on page 150).

[275] S. Paiano et al. 'Spectroscopic lower limit to the redshift (z>0.863) of the BL Lac object 4FGL J2255.1+2411, a possible neutrino source'. In: *The Astronomer's Telegram* 13202 (Oct. 2019), p. 1 (cited on page 150).

[276] M. G. Aartsen et al. 'Observation and Characterization of a Cosmic Muon Neutrino Flux from the Northern Hemisphere Using Six Years of IceCube Data'. In: A*pJ* 833.1, 3 (Dec. 2016), p. 3. DOI: 10.3847/0004-637X/833/1/3 (cited on page 150).

[277] J. J. Condon et al. 'The NRAO VLA Sky Survey'. In: A*J* 115.5 (May 1998), pp. 1693–1716. DOI: 10.1086/300337 (cited on page 152).

[278] S. Garrappa and S. Buson. 'Fermi-LAT Gamma-ray Observations of IceCube-201114A'. In: *The Astronomer's Telegram* 14188 (Nov. 2020), p. 1 (cited on page 152).

[279] S. Buson, S. Garrappa, and C. C. Cheung. 'Fermi-LAT evidence for VHE emission from NVSS J065844+063711'. In: *The Astronomer's Telegram* 14200 (Nov. 2020), p. 1 (cited on page 152).

[280] R. de Menezes et al. 'Multi-Messenger observations of the Fermi-LAT blazar 4FGL J0658.6+0636 consistent with an IceCube high-energy neutrino'. In: *PoS* ICRC2021 (2021), p. 955. DOI: 10.22323/1.395.0955 (cited on page 152).

[281] M. R. Griffith et al. 'The Parkes-MIT-NRAO (PMN) Surveys. III. Source Catalog for the Tropical Survey (-29 degrees < delta < -9 degrees -3pt.5)'. In: A*pJS* 90 (Jan. 1994), p. 179. DOI: 10.1086/191863 (cited on page 153).

[282] S. Garrappa et al. 'Fermi-LAT Gamma-ray Observations of IceCube-201130A'. In: *GRB Coordinates Network* 28978 (Dec. 2020), p. 1 (cited on page 153).

[283] J. G. Bolton, A. J. Shimmins, and J. V. Wall. 'The Parkes 2700 MHz Survey (Seventh Part): Supplementary Catalogue for the Declination zone -4^o to -30^o'. In: *Australian Journal of Physics Astrophysical Supplement* 34 (Jan. 1975), p. 1 (cited on page 154).

[284] P. C. Hewett and V. Wild. 'Improved redshifts for SDSS quasar spectra'. In: M*NRAS* 405.4 (July 2010), pp. 2302–2316. DOI: 10.1111/j.1365-2966.2010.16648.x (cited on page 154).

[285] S. A. Grandi. 'Spectroscopic observations of southern N-galaxy candidates.' In: M*NRAS* 204 (Aug. 1983), pp. 691–697. DOI: 10.1093/mnras/204.3.691 (cited on page 154).

[286] S. Garrappa et al. 'Fermi-LAT Gamma-ray Observations of IceCube-210210A'. In: *GRB Coordinates Network* 29473 (Feb. 2021), p. 1 (cited on page 154).

[287] A. Atoyan and C. D. Dermer. 'High-Energy Neutrinos from Photomeson Processes in Blazars'. In: *Phys. Rev. Lett.* 87 (22 Nov. 2001), p. 221102. DOI: 10.1103/PhysRevLett.87.221102 (cited on page 156).

[288] A. M. Atoyan and C. D. Dermer. 'Neutral Beams from Blazar Jets'. In: A*pJ* 586 (Mar. 2003), pp. 79–96. DOI: 10.1086/346261 (cited on page 156).

[289] E. O'Sullivan and C. Finley. 'Searching for Time-Dependent Neutrino Emission from Blazars'. In: *36th International Cosmic Ray Conference (ICRC2019)*. Vol. 36. International Cosmic Ray Conference. July 2019, 973, p. 973 (cited on pages 158, 159).

[290] F. Halzen. 'The Observation of High-Energy Neutrinos from the Cosmos: Lessons Learned for Multimessenger Astronomy'. In: *arXiv e-prints*, arXiv:2110.01687 (Oct. 2021), arXiv:2110.01687 (cited on page 159).

[291] H. Zhou et al. 'A Narrow-Line Seyfert 1-Blazar Composite Nucleus in 2MASX J0324+3410'. In: A*pJ* 658.1 (Mar. 2007), pp. L13–L16. DOI: 10.1086/513604 (cited on page 160).

[292] A. A. Abdo et al. 'Radio-Loud Narrow-Line Seyfert 1 as a New Class of Gamma-Ray Active Galactic Nuclei'. In: A*pJ* 707.2 (Dec. 2009), pp. L142–L147. DOI: 10.1088/0004-637X/707/2/L142 (cited on page 160).

[293] V. S. Paliya et al. 'The Peculiar Radio-loud Narrow Line Seyfert 1 Galaxy 1H 0323+342'. In: A*pJ* 789.2, 143 (July 2014), p. 143. DOI: 10.1088/0004-637X/789/2/143 (cited on page 160).

[294] D. Kynoch et al. 'The relativistic jet of the γ-ray emitting narrow-line Seyfert 1 galaxy 1H 0323+342'. In: M*NRAS* 475.1 (Mar. 2018), pp. 404–423. DOI: 10.1093/mnras/stx3161 (cited on page 160).

[295] Cherenkov Telescope Array Consortium et al. *Science with the Cherenkov Telescope Array*. 2019 (cited on page 167).

[296] P. A. Evans et al. 'Swift follow-up of IceCube triggers, and implications for the Advanced-LIGO era'. In: M*NRAS* 448.3 (Apr. 2015), pp. 2210–2223. DOI: 10.1093/mnras/stv136 (cited on page 167).

[297] O. Godet et al. 'The Chinese-French SVOM Mission: studying the brightest astronomical explosions'. In: *Space Telescopes and Instrumentation 2012: Ultraviolet to Gamma Ray*. Ed. by T. Takahashi, S. S. Murray, and J.-W. A. den Herder. Vol. 8443. Society of Photo-Optical Instrumentation Engineers (SPIE) Conference Series. Sept. 2012, 84431O, 84431O. DOI: 10.1117/12.925171 (cited on page 167).

[298] F. A. Harrison et al. 'The Nuclear Spectroscopic Telescope Array (NuSTAR) High-energy X-Ray Mission'. In: A*pJ* 770.2, 103 (June 2013), p. 103. DOI: 10.1088/0004-637X/770/2/103 (cited on page 167).

[299] P. Predehl et al. 'The eROSITA X-ray telescope on SRG'. In: *Astron. Astrophys.* 647 (2021), A1. DOI: 10.1051/0004-6361/202039313 (cited on page 167).

[300] J. Tomsick and COSI Collaboration. 'The Compton Spectrometer and Imager Project for MeV Astronomy'. In: *37th International Cosmic Ray Conference. 12-23 July 2021. Berlin*. Mar. 2022, 652, p. 652 (cited on page 167).

[301] H. Fleischhack and Amego X Team. 'AMEGO-X: MeV gamma-ray Astronomy in the Multi-messenger Era'. In: *37th International Cosmic Ray Conference. 12-23 July 2021. Berlin*. Mar. 2022, 649, p. 649 (cited on page 167).

[302] M. G. Aartsen et al. 'IceCube-Gen2: the window to the extreme Universe'. In: *Journal of Physics G Nuclear Physics* 48.6, 060501 (June 2021), p. 060501. DOI: 10.1088/1361-6471/abbd48 (cited on page 167).

[303] S. Adrian-Martinez et al. 'Letter of intent for KM3NeT 2.0'. In: *Journal of Physics G Nuclear Physics* 43.8, 084001 (Aug. 2016), p. 084001. DOI: 10.1088/0954-3899/43/8/084001 (cited on page 167).

[304] Fermi Science Support Development Team. *Fermitools: Fermi Science Tools*. Astrophysics Source Code Library, record ascl:1905.011. May 2019 (cited on pages 173, 174).

I declare that I have completed the thesis independently using only the aids and tools specified. I have not applied for a doctor's degree in the doctoral subject elsewhere and do not hold a corresponding doctor's degree. I have taken due note of the Faculty of Mathematics and Natural Sciences PhD Regulations, published in the Official Gazette of Humboldt-Universität zu Berlin no. 42/2018 on 11/07/2018.

Berlin May 4, 2022

Simone Garrappa